

UC San Diego

UC San Diego Electronic Theses and Dissertations

Title

Novel Methods and Materials for Additive Manufacturing

Permalink

<https://escholarship.org/uc/item/3nm388g3>

Author

Wirth, David M.

Publication Date

2022

Peer reviewed|Thesis/dissertation

UNIVERSITY OF CALIFORNIA SAN DIEGO

Novel Methods and Materials for Additive Manufacturing

A dissertation submitted in partial satisfaction of the
requirements for the degree
Doctor of Philosophy

in

NanoEngineering

by

David M. Wirth

Committee in charge:

Professor Jonathan K. Pokorski, Chair
Professor Shaochen C. Chen, Co-Chair
Professor Shengqiang Cai
Professor Susan S. Golden
Professor Ping Liu

2022

The dissertation of David M. Wirth is approved,
and it is acceptable in quality and form for publi-
cation on microfilm and electronically.

University of California San Diego

2022

EPIGRAPH

“Ordering matter was the sole endeavor of Life, whether it was a jumble of self-replicating molecules in the primordial ocean, or a steam-powered English mill turning weeds into clothing, or Fiona lying in her bed turning air into Fiona . . . We ignore the blackness of outer space and pay attention to the stars, especially if they seem to order themselves into constellations.”

—*Neal Stephenson*

TABLE OF CONTENTS

	Dissertation Approval Page	iii
	Epigraph	iv
	Table of Contents	v
	List of Figures	x
	List of Tables	xvii
	Acknowledgements	xix
	Dedication	xxii
	Vita	xxiii
	Abstract of the Dissertation	xxiv
Chapter 1	Introduction	1
	1.1 Objectives of this work	1
	1.2 Scope of the document	2
	1.3 Background	3
	1.3.1 History of AM	3
	1.3.2 Proposed Definition and Classification of Manufacturing Techniques	6
	1.3.3 Major Limitations of AM Systems	7
	1.3.4 General Trends in AM Systems - Volumetric Build Rate vs. Minimum Feature Size	7
	1.4 The Conversion Rate of Digital Information to Granular Physical Structures in Top-Down AM Systems	9
	1.4.1 Derivation of the Relationship Between V_s and r_x for Top-Down AM Systems	10
	1.4.2 Limitations of Memory Retrieval (Bottleneck 1)	13
	1.4.3 Limitations of Machine Response (Bottleneck 2)	13
	1.4.4 Limitations of Material Response (Bottleneck 3)	14
	1.4.5 Tradeoffs in Top-Down AM: Size, Resolution, and Speed	15
	1.4.6 Towards a Bottom-Up Paradigm: Quasi-Volumetric Systems	15
	1.5 A Proposed Model for Bottom-Up AM systems	16
	1.5.1 Self-replication of of Notional Bottom-Up Assembly System	16
	1.5.2 Comparison Between Top-Down and Bottom-Up Assembly Systems	17
	1.5.3 A Forward Look at Biological Self-Assembly as a Possible Manufacturing System	20

	1.6	Conclusion	20
	1.7	Supplemental Tables	21
	1.8	Acknowledgements	26
Chapter 2		Self-Expansion of Additively Manufactured Polymeric Structures . .	27
	2.1	Introduction	27
	2.2	Background	28
	2.3	Results and Discussion	30
	2.3.1	Optimization of Monomer	30
	2.3.2	Optimization of Photoinitiator	32
	2.3.3	Optimization of Blowing Agent and Foaming Resin Com- position	33
	2.3.4	Characterization of the Presence and Impact of Added Crosslinkers	36
	2.3.5	3D Printing of Expandable HEMA/BOC ₂ O Resin	37
	2.3.6	Digital Control of Expansion Ratio and Cellular Structure	39
	2.3.7	Mechanical Testing of 3D Printed Foams	43
	2.3.8	Applied Technology Demonstration	44
	2.4	Conclusion	45
	2.5	Experimental Section	46
	2.5.1	Materials	46
	2.5.2	Equipment	46
	2.5.3	Instrumentation	47
	2.5.4	NMR Analysis	47
	2.6	Supplemental Figures	48
	2.7	Supplemental Tables	57
	2.8	Acknowledgements	62
Chapter 3		Development and Applications of High Strength Photo-curable Poly- mers	63
	3.1	Introduction	63
	3.2	Background	64
	3.3	Results and Discussion	66
	3.3.1	Advantages of Isotropically Expanded Foams	66
	3.3.2	Initial Exploration of Alternate Foam Resin Compositions	68
	3.3.3	Exploration of High Strength Foam Coating Materials .	69
	3.3.4	Mechanical Tensile Characterization of High Toughness S100 Resin	71
	3.3.5	Compression Testing of Foam/Resin Composite Samples	74
	3.3.6	Spray Coating of Foam/Resin Composite Samples	76
	3.3.7	Applied Technical Demonstration	79
	3.4	Conclusion	81
	3.5	Experimental Section	81
	3.5.1	Materials	81
	3.5.2	Equipment	82
	3.5.3	Instrumentation	83

	3.5.4	Synthesis of 1,6-Bis(maleimido)hexane	83
	3.5.5	Synthesis of 1,3-Bis(maleimido)pentane	84
	3.6	Supplemental Figures	85
	3.7	Supplemental Tables	96
	3.8	Acknowledgements	101
Chapter 4		Design and Fabrication of a Pilot-Scale Melt Processing System . . .	102
	4.1	Introduction	102
	4.2	Background	103
	4.3	Results and discussion	104
	4.3.1	Injection Molding of Polymer Composites	104
	4.3.2	Characterization of Composite Samples	104
	4.3.3	<i>In-silico</i> Simulation of Shear Forces Within a Polymer Extrusion Nozzle	107
	4.3.4	Mechanical Characterization of Injection Molded Poly- mer Samples	109
	4.4	Conclusion	110
	4.5	Experimental section	112
	4.5.1	Benchtop Injection Molding Instrument Fabrication . .	112
	4.5.2	Injection Mold Fabrication	113
	4.5.3	Polymer Composite Fabrication	113
	4.5.4	Suggested Print Bed Layouts	118
	4.5.5	Mechanical Assembly	119
	4.5.6	Electrical Assembly	123
	4.5.7	Materials	126
	4.5.8	Instrumentation	126
	4.6	Supplemental Figures	127
	4.7	Supplemental Tables	128
	4.8	Acknowledgements	131
Chapter 5		Design and Fabrication of a Pilot-Scale Injection Molding Instrument for Rapid Prototyping of High Precision Parts	132
	5.1	Introduction	132
	5.2	Background	133
	5.3	Results and discussion	135
	5.3.1	Design and Construction of a Pilot-Scale Injection Mold- ing System	135
	5.3.2	Polymer Blend Formulation	137
	5.3.3	Injection Mold Insert Fabrication	138
	5.3.4	Injection Molding Procedure	140
	5.3.5	Method of Fabrication of Microneedle Insert Molds . . .	140
	5.3.6	Polymer Blend Characterization and Testing	143
	5.3.7	Characterization of Microneedle Arrays	144
	5.3.8	Delivery of Microneedle Payload	148
	5.3.9	Characterization of Microparticles	149
	5.4	Conclusion	151

5.5	Experimental Section	152
5.5.1	Materials	152
5.5.2	Equipment/Instrumentation	152
5.5.3	Mechanical Assembly	154
5.5.4	Electrical Assembly	156
5.5.5	Pneumatic Assembly	157
5.6	Supplemental Figures	159
5.7	Supplemental Tables	165
5.8	Acknowledgements	170
Chapter 6	Directed Biological Polymerization of Aniline	171
6.1	Introduction	171
6.2	Background	172
6.2.1	Engineered Living Materials	173
6.2.2	Biosynthetic Conductive Materials	173
6.2.3	Polymerization of Aniline	175
6.2.4	Biological Peroxidase Enzymes	178
6.2.5	Cyanobacteria Photo-Induced Production of Reactive Oxygen Species	180
6.2.6	Bottom-Up Manufacture of Polyaniline Conductive Struc- tures	183
6.3	Results and Discussion	185
6.3.1	Investigation of Polyaniline Precursor Solution	185
6.3.2	Optimizing Cyanobacterial Production of H ₂ O ₂ in Re- sponse to Light	189
6.3.3	Recombinant Engineering of <i>PCC 7942</i> Cyanobacteria and Knock-Out of Catalase-Peroxidase	194
6.3.4	Utilization of ETC Inhibitors to Increase H ₂ O ₂ Produc- tion of KOCO	197
6.3.5	Transformation of Synthetic HRP-Coding Plasmid into <i>E. Coli</i> and Quantification of Peroxidase Expression	202
6.3.6	Expression of APEX2 in <i>E. Coli</i>	204
6.3.7	Attempts at Recombinant Engineering of <i>PCC 7942</i> to Express Peroxidase Enzymes	206
6.4	Conclusion	206
6.5	Experimental Section	207
6.5.1	Method of ABTS Assay for Quantification of Enzymatic Peroxidase Activity	207
6.5.2	Method of ABTS Assay for Quantification of Enzymatic Peroxidase Activity	207
6.5.3	Method of Scopoletin Assay for Quantification of Hy- drogen Peroxide Production	208
6.5.4	Preparation of BG-11 Media	209
6.5.5	Materials	209
6.5.6	Instrumentation	210
6.6	Acknowledgements	210

Chapter 7	Conclusions and future work	211
	7.1 Future Work on Self-expanding AM Polymeric Structures . . .	212
	7.1.1 Pushing the Envelope of Volumetric Build Rate for AM Systems	212
	7.1.2 Improving the Strength of Expanded Polymeric Structures	213
	7.1.3 Novel Applications for Expanded Polymeric Structures .	214
	7.2 Injection Molding of Controlled Release Devices	215
	7.2.1 Efficacy of drug and vaccine loaded polymeric devices .	215
	7.2.2 Improving Sharpness of Injection Molded Microneedles .	215
	7.3 Directed Biological Polymerization of Conductive Polymers . .	216
	7.3.1 Cyanobacterial metabolic engineering	216
	7.3.2 Reductive Capabilities of <i>E. coli</i>	217
	7.3.3 Final Thoughts	218
	Bibliography	219

LIST OF FIGURES

Figure 1.1: A proposed method of classifying structural manufacturing techniques	6
Figure 1.2: Scatter plot of modern AM technologies	8
Figure 1.3: Notional diagrams of various AM processes and their associated generalized parameters	10
Figure 1.4: A notional system of self-replicating, self assembling volumetric assemblers and associated parameters	16
Figure 1.5: Volume of a notional self-replicating system with respect to time compared with conventional top-down assembly methods	18
Figure 2.1: Procedure used for experimentally determining cure time of polymer samples	32
Figure 2.2: Procedure used for experimentally determining the expansion ratio of small samples of foaming polymer	36
Figure 2.3: Overview of high expansion 3D printable foaming polymer manufacturing process	38
Figure 2.4: Samples shown before and after expansion at 200 °C for 10 minutes.	40
Figure 2.5: Diagram of the process used to evaluate the expansion ratio of various print parameters	42
Figure 2.6: Mechanical compressive analysis and summary of physical properties of foam polymer samples	44
Figure 2.7: Nuclear Magnetic Resonance of samples in CDCl ₃	48
Figure 2.8: Nuclear Magnetic Resonance of monomer samples in DMSO-d ₆	49
Figure 2.9: Photographs of the effect of long print times and high light doses on undesirable extraneous polymerization of the resin bath.	50
Figure 2.10: Test prints of lattice structure	51
Figure 2.11: Photograph showing a comparison of selected foam samples: A) resin sample C3, B) resin sample B31, and C) resin sample B22.	51
Figure 2.12: Thermo-gravimetric Analysis (TGA) of A) BOC ₂ O and B) polymerized HEMA samples.	52

Figure 2.13: GC-MS processed chromatogram of m/z 55-57 showing retention times of BOC ₂ O, t-Butanol and foam sample expanded immediately prior to gas sampling via headspace.	52
Figure 2.14: GC-MS total ion concentration vs retention time plot	53
Figure 2.15: GC-MS total ion concentration vs retention time plot	54
Figure 2.16: A) Raw FTIR data used in determination of cure time and B) representative photograph of HEA (left) and HEMA (right) samples after curing.	54
Figure 2.17: Example of cylindrical test samples	55
Figure 2.18: Contour surface plot of mean anisotropy of 10x10 mm cylindrical test samples after expansion.	56
Figure 3.1: Test samples printed to assess compression strength of foam coatings.	67
Figure 3.2: Diagram representation of our method to produce high strength 3D printable foam-based structures.	70
Figure 3.3: Summary of results from mechanical testing of preliminary resin samples	72
Figure 3.4: Confirmatory tests S100 resin printed articles	73
Figure 3.5: Compression tests of S100-coated HEMA foam samples	76
Figure 3.6: Compression testing of S100 resin spray-coated HEMA foam samples under different illumination sources	78
Figure 3.7: Applied technology demonstration of improved strength coating on expandable HEMA foams	80
Figure 3.8: Nuclear Magnetic Resonance of synthesized (top) 1,6-Bis(maleimido)hexane and (bottom) commercial N,N' - (4,4'- Diphenylmethane) bis-maleimide in CDCl ₃	84
Figure 3.9: Nuclear Magnetic Resonance of synthesized 1,3-Bis(maleimido)hexane in CDCl ₃	85
Figure 3.10: Method of testing and optimizing various coating chemical compositions for optimal mechanical properties.	86
Figure 3.11: Preliminary test sample mold print layout printed on Anycubic Mono X.	87

Figure 3.12: Photographs of preliminary resin test samples. A) Samples 1-21, B) Samples 24-31. Scale bars: 10mm.	88
Figure 3.13: Components of S100 resin	89
Figure 3.14: Confirmatory tensile test dogbone dimensions, created according to ASTM D638-IV.	89
Figure 3.15: Confirmatory tensile test dogbone dimensions, created according to ASTM D638-IV.	90
Figure 3.16: Testing procedure for S100 resin spray coated tissue paper strips . . .	91
Figure 3.17: Photographs of the tensile failure mode of each group of samples: A) Group 1, B) Group 2, C) Group 3, D) Group 4.	91
Figure 3.18: Results of tensile analysis performed on the S100 coated tissue paper strips	92
Figure 3.19: Scanning electron micrographs of sections of tissue paper test samples shown in figure 3.16/3.17	93
Figure 3.20: Scanning electron micrographs of S100 resin coated foam samples showing coating thickness and surface morphology.	94
Figure 3.21: Colorized scanning electron micrograph of a S100 resin spray coated onto HEMA foam sample, 3 layers sequentially coated with 60 s UV cure for each layer. Scale bar: 500 μm	95
Figure 3.22: Plot of compressive yield strength vs layers of S100 spray coating . . .	96
Figure 4.1: A) Mechanical design of pneumatic injection system, B) digital image of micro-injection molding instrument.	104
Figure 4.2: Electron micrographs of PLA-based injection molded samples	105
Figure 4.3: Electron micrographs of PCL-based injection molded samples	106
Figure 4.4: Energy dispersive X-ray spectrographic (EDS) maps of injection molded composite samples	106
Figure 4.5: <i>in-silico</i> shear force simulation of a polymer hot melt extrusion nozzle	107
Figure 4.6: Mechanical properties of injection molded composite samples as a function of processing temperature and use of solvent during pre-processing.	109
Figure 4.7: Design schematic of bench-top polymer melt processing system	113

Figure 4.8: Mini melt processing extruder CAD, injection molding dies and assembly	114
Figure 4.9: Melt processed polymer samples	116
Figure 4.10: Melt processed polymer dog bone tensile test samples	116
Figure 4.11: Recommended printbed layout #1	118
Figure 4.12: Recommended printbed layout #2	118
Figure 4.13: Mark FRP base plate as shown above	119
Figure 4.14: Deep countersunk holes in base plate using step drill or countersink drill	120
Figure 4.15: Insert rail fasteners into rail	120
Figure 4.16: Tighten screws to secure rail in place	121
Figure 4.17: Finished sliding gusset	121
Figure 4.18: Both gussets mounted to rail	122
Figure 4.19: Cylinder mounted in place	122
Figure 4.20: Cylinder secured using included nut	122
Figure 4.21: 7/16-20 threaded shaft collar	123
Figure 4.22: Gauge pin inserted into shaft collar with threaded 8-32 thumb screws securing it in place	123
Figure 4.23: Diagram showing pneumatic connections between switch, regulator and cylinder	124
Figure 4.24: Photograph of pneumatic manifold and regulator	124
Figure 4.25: Wiring diagram of the electrical system	125
Figure 4.26: Raw stress-strain curves for mechanically tested samples.	127
Figure 4.27: Additional SEM and EDS data for tensile tested samples	128
Figure 5.1: Pilot-scale injection molding system design	136
Figure 5.2: Procedure for forming insert injection molds for implants, scaffolds and other arbitrary shapes	139

Figure 5.3: Procedure for forming injection molded microneedle patches with micron-scale features.	143
Figure 5.4: Rheometer viscosity profiles of various polymer compositions with respect to temperature.	144
Figure 5.5: Effect of processing parameters on microneedle patch tip sharpness .	146
Figure 5.6: EDS and SEM characterization of injection molded microneedles . .	147
Figure 5.7: Demonstration of dissolvable microparticle-laden microneedles fabricated via an injection molding approach.	149
Figure 5.8: SEM micrographs of PLGA microparticles prior to microneedle tests	150
Figure 5.9: SEM micrographs of PLGA microparticles after microneedle tests . .	150
Figure 5.10: Photographs and computer aided drafting models of the heated barrel and assembly procedure. All scale bars: 15 mm.	154
Figure 5.11: Photographs and computer aided drafting models of the assembled mechanical structure of the injection molding system.	156
Figure 5.12: Wiring diagram of the electrical system	157
Figure 5.13: Diagram showing pneumatic connections between switch, regulator and cylinder	158
Figure 5.14: Diagram showing mold pre-vacuum system	159
Figure 5.15: Differential scanning calorimetric results showing amorphous character of PLGA AP041 polymer	160
Figure 5.16: Photographs of the preparation of PDMS mold tooling for epoxy casting	161
Figure 5.17: Photographs of the preparation of High Temperature epoxy mold tooling	162
Figure 5.18: Electron micrographs of microneedles fabricated using different processing parameters	162
Figure 5.19: Mechanical testing of microneedle patches.	163
Figure 5.20: SEM images of IM and solvent cast MN patches before and after mechanical testing	164
Figure 6.1: The photopatterning of polyaniline via UV exposure and oxidation with silver nitrate	176

Figure 6.2: H ₂ O ₂ production by cyanobacteria in response to light as classified by Stevens et al.	181
Figure 6.3: The molecular structures of MV and DCMU	182
Figure 6.4: Proposed method for the photodirected biosynthetic fabrication of polyaniline wires	184
Figure 6.5: Optimization of the enzymatic preconductive polymer solution component concentrations	186
Figure 6.6: Morphological differences in enzymatically produced PANI	188
Figure 6.7: Direct ink writing of enzymatically crosslinked PANI precursor hydrogels	189
Figure 6.8: Design and construction of a high intensity LED light exposure chamber for the evaluation of cyanobacterial production of H ₂ O ₂	190
Figure 6.9: Evidence of ABTS as an unsuitable test for <i>in-situ</i> H ₂ O ₂ production of biological organisms	191
Figure 6.10: The molecular structures of scopoletin and ABTS	192
Figure 6.11: H ₂ O ₂ production of WT 7942 cyanobacteria over time as a function of light intensity	193
Figure 6.12: Evidence of enzymatic oxidative polymerization of aniline into PANI:PSS via HRP and photo-induced cyanobacterial biosynthesis of H ₂ O ₂	194
Figure 6.13: Optical micrographs of KOCO colonies grown on agar with varying concentrations of sodium thiosulfate	195
Figure 6.14: H ₂ O ₂ production of WT 7942 vs KOCO cyanobacterial cells after exposure to 246 mW/cm ² light over the course of 60 minutes	196
Figure 6.15: Preliminary studies on the H ₂ O ₂ production of WT 7942 in the presence of ETC inhibitors during exposure to 246 mW/cm ²	197
Figure 6.16: H ₂ O ₂ production of WT 7942 vs KOCO cyanobacterial cells after exposure to 246 mW/cm ² light over the course of 60 minutes	198
Figure 6.17: H ₂ O ₂ production of WT 7942 vs KOCO cyanobacterial cells in the presence of 25 μM DCMU after exposure to 492 mW/cm ² (4.5 mmol PPFD) light for 60 and 120 minutes	199
Figure 6.18: H ₂ O ₂ production of WT 7942 and KOCO cyanobacterial cells in the presence of 25 μM DCMU and 1000nM MV after exposure to 656 mW/cm ² (6 mmol PPFD) light for 90 min	200

Figure 6.19: H ₂ O ₂ production of WT 7942 vs KOCO cyanobacterial cells in the presence of 25-100nM MV after exposure to 656 mW/cm ² (6 mmol PPFD) light for 90 min	201
Figure 6.20: PANI production of WT 7942 vs KOCO cyanobacterial cells in the presence of 50 nM MV, and HRP 48 hrs after exposure to 656 mW/cm ² (6 mmol PPFD) light for 60 min	201
Figure 6.21: Synthetic pET-26b(+) construct for expression of functional HRP protein in <i>E. coli</i>	203
Figure 6.22: ABTS assay activity of expressed HRP protein in <i>E. coli</i>	204
Figure 6.23: ABTS assay activity of expressed peroxidase enzyme activity in <i>E. coli</i>	205
Figure 7.1: Scatter plot of modern AM technologies comparing volumetric build rate, minimum feature size and SPR	212
Figure 7.2: Growth of NIH 3T3 cells on pHEMA foams incorporating 0.1 wt% GRGDS-Acrylate	214
Figure 7.3: Fluorescence micrograph of <i>E. coli</i> expressing HRP in a scopoletin/H ₂ O ₂ solution	218

LIST OF TABLES

Table 1.1: Systems plotted in Figure 1.2 and associated references.	22
Table 1.2: Equivalent parameters for 0D, 1D, 2D, and tomographic volumetric AM processes	25
Table 2.1: Composition of blowing agents explored in the current study.	34
Table 2.2: Composition of various samples tested for cure time in the current study	58
Table 2.3: Composition of non-BOC ₂ O samples tested for curing time and expansion ratio in the current study.	59
Table 2.4: Comparison of formulations containing BOC ₂ O as a blowing agent exploring the effect of BOC ₂ O concentration	61
Table 2.5: Comparison of formulations containing BOC ₂ O as a blowing agent exploring the effect of crosslinker	62
Table 3.1: List of alternate monomers explored in the current study and their respective cure times, qualitative hydrophilicity, qualitative gas trapping properties and solubility with maleimide precursors.	69
Table 3.2: List of selected relevant resin formulations explored or discussed in the current study and their respective cure times.	97
Table 4.1: Average values of properties for tensile test samples prepared with and without solvent	110
Table 4.2: Composition of samples prepared for injection molding	115
Table 4.3: Composition of samples prepared for mechanical testing	117
Table 4.4: Bill of Materials (BOM) for construction of benchtop melt-processing system	129
Table 5.1: Composition of samples prepared for injection molding.	137
Table 5.2: Bill of materials for construction of pilot-scale injection molding system.	166
Table 5.3: Bill of machined parts for construction of pilot-scale injection molding system.	168
Table 5.4: Selected unsuccessful polymer formulations used for microneedle injection molds.	169

Table 6.1:	List of preconductive monomers suitable for enzymatic oxidative polymerization, oxidation potentials and conductivities of resultant polymers	177
Table 6.2:	List of peroxidase enzymes, oxidation potentials, and activities	179
Table 6.3:	Design space for polyaniline precursor solution	188

ACKNOWLEDGEMENTS

First I would like to thank Jon for accepting me into his research group back in 2018, for believing in me, being patient with me, always giving me guidance when I was confused, and allowing me to chase crazy ideas, even if they didn't always work out.

Justin- thank you for putting up with all my antics: Cowboy Chemistry, wrangling Mass Spec fairies, showing me the wonders of microwave sterile technique, and opening my eyes to the fact that grown men still play Runescape. But most of all- for always being someone I could talk to, and for teaching me so much about organic chemistry.

Trinity- you are the most creative person I've ever met and it's been an honor to work with you. Your quotables always brighten my day and your ideas are always amazing. Every time I talk with you, you're always coming up with new ways to do things and new perspectives. I know you'll do great things.

Debika- you are way better with cyanobacteria than I will ever be. Hopefully you will be able to finish some of the things I attempted and succeed where I could not. I wish you all the best!

Derek- thank you for being a great post-doc, for teaching me how to do HPLC, GPC, SDS-PAGE and half a dozen other techniques. Hope you're enjoying industry.

Sam Shifron, I honestly don't know what I would have done without you. Thank you for being someone I could bounce ideas off of, always count on, and never shy away from a challenge.

Susan Golden, David Welkie, Elliot Weiss and Marie Adomako - Thank you for introducing me to biology, genetic engineering and recombinant techniques. My time working in your lab has opened my eyes to just how challenging biology can be and how much skill it takes to do it well. I'm honored I got the chance to learn from the best.

Hayden Taylor, James Tour, Ajax Peris, Klint Simon, Adrian Pelkus, Laura Barnes, Morley Stone - Without each of your help, I probably wouldn't have ended up at UCSD pursuing this degree. Words cannot express my gratitude. Thank you so much for taking the time to advise me, for steering me in this direction and for helping a young aspiring scientist find his way.

Sofia and Anna- thank you for being great summer interns, I hope the paper you co-authored helps advance both of your careers.

Lenny - I am always impressed by your passion for science, dedication and a drive

to learn and advance technology. I have no doubt you will make a great applied scientist if that is the path you choose.

Finally, everyone else in the Pokorski, Steinmetz and Golden labs, co-authors, reviewers, and publishers, who helped me on innumerable occasions - if I listed each of them here, this page would be its own separate chapter. I'd just like to say: thank you for sharing your time, your knowledge, and your patience.

I wish you all *way more than luck*.

.....

Chapter 1, in part, is currently being prepared for submission for publication of the material. Wirth, David M.; Li, Chi C.; Pokorski, Jonathan K.; Taylor, Hayden K.; Shusteff, Maxim. The dissertation author was the primary investigator and author of this material.

Chapter 2, in full, is a reprint of the material as it appears in “Highly Expandable Foam for Lithographic 3D Printing”, Wirth, David M.; Jacquez, Anna; Gandarilla, Sofia; Hochberg, Justin D.; Church, Derek C.; Pokorski, Jonathan K. ACS Appl. Mater. Interfaces 2020, 12, 16, 19033–19043. The dissertation author was the primary investigator and author of this paper. This work was supported by the National Science Foundation (OISE 1844463) and the ENLACE program at UCSD which provided research support.

Chapter 3, in full, is currently being prepared for submission for publication of the material. Wirth, David M.; Hochberg, Justin, D.; Pokorski, Jonathan K. The dissertation author was the primary investigator and author of this material. This work was supported by the National Science Foundation (OISE 1844463).

Chapter 4, in part, is a reprint of the material as it appears in “Design and fabrication of a low-cost pilot-scale melt-processing system”, Wirth, David M.; Pokorski, Jonathan K. Polymer, 181, 121802, 2019. The dissertation author was the primary investigator and author of this paper. This work was supported by the National Science Foundation (OISE 1844463) and UCSD.

Chapter 5, in part, has been submitted for publication of the material as it may appear in “Fabrication of an Inexpensive Injection Molding Instrument for Rapid Prototyping of High Precision Parts”, Wirth, David M.; McCline, Leonard G.; Pokorski, Jonathan K., Polymer, 2022. The dissertation author was the primary investigator and author of this paper. This work was sponsored in part by the UC San Diego Materials Research Science and Engineering Center (UCSD MRSEC), supported by the National

Science Foundation (Grant DMR-2011924), as well as NSF awards OISE 184463 and CMMI 2027668.

Chapter 6, is coauthored with Weiss, Elliot T.; Welkie, David; Pokorski, Jonathan K. The dissertation author was the primary investigator and author of this material.

DEDICATION

To my good friends.
To Anna and Milton.
And of course, Jon.

VITA

2012	Bachelor of Science in Aerospace Engineering, <i>cum laude</i> , University of California Los Angeles
2012	Master of Science in Aerospace Engineering, University of California Los Angeles
2012-2016	U.S. Air Force
2016-2018	Fabric8Labs
2022	Doctor of Philosophy in NanoEngineering, University of California San Diego

PUBLICATIONS

- “Experimental Study on the Aerospace Applications of Photoreactive Nanomaterials”, M.S. Thesis, *University of California, Los Angeles*, 2012.
- “Three dimensional additive manufacturing of metal objects by stereo-electrochemical deposition”, 2017, US Patent 9,777,385
- “Design and fabrication of a low-cost pilot-scale melt-processing system”, *Polymer*, 181, 121802, 2019
- “Apparatus for electrochemical additive manufacturing”, 2019, US Patent 10,465,307
- “Highly expandable foam for lithographic 3D printing”, *ACS Applied Materials and Interfaces*, 12, 16, 19033-19043, 2020
- “COVID-19 vaccine development and a potential nanomaterial path forward”, *Nature Nanotechnology*, 15, 8, 646-655, 2020
- “Matrix-controlled printhead for an electrochemical additive manufacturing system”, 2020, US Patent 10,724,146
- “Clamped quasi-resonant step-up inverter”, 2020, US Patent 10,811,995
- “Electrochemical layer deposition by controllable anode array”, 2021, US Patent 10,975,485
- “Strong, Ductile MOF–Poly (urethane urea) Composites”, *Chemistry of Materials*, 33, 9, 3164-3171, 2021
- “Electrochemical Layer Deposition”, 2021, US Patent App. 17/227,726
- “High-Throughput Manufacturing of Antibacterial Nanofibers by Melt Coextrusion and Post-Processing Surface-Initiated Atom Transfer Radical Polymerization”, *ACS Appl. Polym. Mater.*, 4, 1, 260–269, 2022

ABSTRACT OF THE DISSERTATION

Novel Methods and Materials for Additive Manufacturing

by

David M. Wirth

Doctor of Philosophy in NanoEngineering

University of California San Diego, 2022

Professor Jonathan K. Pokorski, Chair

Professor Shaochen C. Chen, Co-Chair

Additive Manufacturing (AM) is a process most commonly defined by the addition of material to an object, specified by digital instructions, typically in a layer-by-layer fashion. It offers numerous advantages over conventional manufacturing processes since it can be used to form objects that would otherwise be difficult or impossible to fashion. It also allows for the on-demand production of parts which would otherwise require large, bulky mass production tooling. However, AM is subject to many of the same limitations as other “Top-Down” manufacturing processes: the objects produced by an AM system (or conventional manufacturing system) must be smaller than the system’s build volume.

A method to circumvent this limitation is described which utilizes a photopolymer resin incorporating a soluble blowing agent. This resin can be patterned into a desired structure using a commercially available Masked Stereolithography (MSLA) printer. The printed structures may then be thermally expanded to produce objects up to 40x larger than the original printed parts, and which retain their expanded shape and size after

cooling. Using this method, production of objects larger than the printer itself is demonstrated. These isotropically expanded structures can subsequently be sprayed with a low-viscosity isocyanyl acrylate-based photocurable resin to enhance their mechanical properties for structural applications. Mechanical tensile and compression analysis of the novel resin and composite foam/resin structures is presented.

The construction, testing and characterization of a small format bench-scale polymer melt processing system is documented as well as the design, fabrication and testing of a bench-scale injection molding system. Such devices enable the lab-scale production of customizable solvent-free polymeric implants and microneedle patches. Characterization of the fabricated polymer devices via Scanning Electron Microscopy (SEM), Energy-Dispersive X-ray spectroscopy (EDX), and fluorescence micrography is documented.

Fundamental scaling relationships of AM, and bottom-up biosynthetic approaches to AM are also explored.

Chapter 1

Introduction

1.1 Objectives of this work

The aims of this work are to discover, characterize, and apply novel methods and materials to the field of additive manufacturing for the purposes of aerospace exploration, scalable manufacturing, biomedical drug delivery, and rapid pandemic response. This work aims to advance the state of the art in an interdisciplinary pursuit of pure and applied science; straddling the fields of biology, chemistry, mechanical engineering, biomedical engineering, and nanoengineering.

Advancement in the field of additive manufacturing bridges the gap between mass production and mass customization, allowing for the rapid production of customized devices for use in specialized tasks. The objectives of the present study are as follows:

1. To derive a generalized model for the fundamental scaling relationships in additive manufacturing and their implications for future manufacturing systems
2. To develop novel materials which expand the application space for additively manufactured devices
3. To explore novel pathways to increase the volumetric build rate of additively manufactured structures
4. To develop rapid, scalable, and solvent free additive manufacturing processes for biomedical devices
5. To explore novel methods to harness biological mechanisms in order to construct devices from the bottom-up

1.2 Scope of the document

Chapter 1 focuses on the fundamental scaling relationships behind manufactured structures and what these fundamental physical laws imply about the future developments in this field of additive manufacturing. Specifically, an attempt will be made derive a mathematical model for the theoretical limitations of both top-down and bottom-up additive manufacturing, focusing first on the former, and then proceeding to apply these insights to the latter.

Chapter 2 describes a highly expandable 2-hydroxyethyl methacrylate-based foaming resin which was developed for commercial off the shelf lithographic additive manufacturing systems. This novel resin is photocurable and isotropically expands up to 40x its original volume, when heated above its blowing agent decomposition point, allowing users to create structures which exceed the printer's build volume, greatly expanding the application space of additive manufacturing with respect to part geometry.

Chapter 3 describes a novel tris-isocyanyl acrylate-based photocurable polymeric resin with low viscosity suitable for spray coating and sunlight curing. The novel resin possesses high strength and fast curing properties. This novel resin augments the work in Chapter 2 and allows for the creation of lightweight, strong, and high strength to weight ratio structures from the previously mentioned expanding foam.

Chapter 4 describes the construction, testing and characterization of a small format bench-scale polymer melt processing system and Chapter 5 describes the design, fabrication and testing of a bench-scale injection molding system. Such systems are highly economical and are designed to ease access to polymer melt processing for small academic labs, with the goal of increasing innovation and access to this versatile solvent-free manufacturing process.

Chapter 6 describes a novel approach to bottom-up biomanufacturing of an electrically conductive poly(aniline) device using self-assembling recombinant *Synechococcus elongatus* (*PCC 7942*) as a means to facilitate light responsive generation of hydrogen peroxide in desired patterns.

Chapter 7 summarizes our findings and proposes recommendations for future work.

1.3 Background

AM, also known as 3D printing, is most commonly defined as a process of successively adding material to an object, specified by digital data from a 3D model, typically in a layer-by-layer fashion. AM is usually contrasted with subtractive manufacturing methods, in which material is cut away from a larger bulk volume, or formative methods, in which it is shaped or molded. Since Charles Hull’s invention of the process known today as stereolithography (SLA) in 1984 [1], nearly four decades of progress have brought about a great variety of AM methods, printer systems, and materials. [2–4] Given the degree to which these technologies have matured, it has become possible to identify their common principles and extract generalized parameters that lend themselves to a universal description.

Taking stock of the totality of AM approaches elucidates the fundamental limitations that may constrain their further development. Therefore a universal framework is proposed which describes the speed of AM as it scales with feature resolution and overall structure size. This allows the evaluation of the inherent trade-offs and limitations that are implied by this universal description, and its consequences for the scalability of AM as a manufacturing paradigm. AM approaches that aren’t neatly described by the model provide clues to possible directions for future research and development to overcome the inherent limitations.

1.3.1 History of AM

In order to understand the theoretical limitations of both top-down and bottom-up additive manufacturing, it is important to highlight an overview of the field as a whole.

Historically, “rapid prototyping” was developed in 1980 by Charles Hull [5], and commercialized by DTM Inc. in 1988 (later acquired by 3D Systems) using a process known as Stereolithography (SLA). [6] This process utilized a vat of photopolymer resin with a movable platform upon which layers of material were selectively cured using a focused light source (such as a fiber-coupled short arc lamp, UV or blue-violet laser). Once a layer was cured, the platform would be moved a fixed distance (the layer height), and the next layer of material would then be cured on top of it.

This process was notably slow and messy. It required a large bath of resin and its speed was limited by the cure rate of the photopolymer, the power of the laser, and

the speed at which the laser could be scanned across the build surface. The layer height in early SLA systems was approximately 50-200 μm .

Modern SLA-type systems can achieve layer heights from 500 μm down to as small as 1 μm . This has been enabled using either focusing optics [7] to reduce feature size, or oxygen inhibition to eliminate the need to debind each layer from the build window. [8]

In recent years, advances have been made in control systems and advanced SLA technologies, such as digital light projection (DLP), masked SLA (MSLA), and continuous layer interface production (CLIP). [8] DLP uses a micro-mirror array to create and direct many independently controlled pixels of light at a resin bath simultaneously, exposing an entire layer of print at a time.

While scanning-based SLA might be preferable for sparse geometries or very thin parts, the use of multiple simultaneous deposition paths reduces the print time dramatically for the majority of practical parts by eliminating the time required for the laser to scan the surface of complex objects. MSLA optimizes this technology- using a LCD screen (instead of a DLP micro-mirror array) which reduces cost and complexity, bringing the total system cost to under \$300 and opening up this technology to the mass market. However, such a system is limited to a lower light intensity on target due to the limited transmissibility of the LCD screen, thereby reducing print speed.

Finally, some advanced resin-based systems (such as CLIP) also incorporate an oxygen-permeable window which creates a “dead zone”, preventing the print from sticking to the bottom of the projection window. This allows prints to be formed in a quasi-continuous motion, varying only the light exposure with changes in z-dimension, allowing for very high z-resolution and much faster effective print speeds. In contrast, SLA/MSLA/DLP systems without oxygen permeable windows require a careful peeling procedure after each exposure to ensure the previous layer has detached from the projection window, necessitating larger z-steps to achieve practical print times.

A further advancement to this technology was made in 2019, high-area rapid printing (HARP) [9] uses a film of fluorinated oil between the projection window and the printed object to not only allow for continuous formation of the printed object, but also to dissipate the heat generated by rapid photopolymerization which can degrade the materials used for ordinary projection windows. Extremely rapid print times of large objects (up to $10^8 \text{ mm}^3/\text{hr}$) can be achieved with this method. However, the original

authors noted that the useful resolution of such printers is limited to 100-300 μm [9] and significant roughness is encountered at resolutions below 1000 μm .

One final advancement to the photopolymer additive manufacturing regime is computed axial lithography (CAL). [10] Distinct from all other forms of additive manufacturing, CAL uses tomographic reconstruction to expose all points in a desired volume of resin to a measured dose of light by rotating the volume in an index matched medium while illuminating the photopolymer with the corresponding projection of a computer-optimized pattern of light. This method allows complex and soft objects to be printed without the use of support material, and very rapidly in comparison to many other AM methods.

Other forms of AM include laser sintering (including selective laser sintering (SLS), and direct metal laser sintering (DMLS)), and laser melting (SLM) which employ lasers to sinter or melt polymer layer-by-layer into the desired form rather than curing it chemically. Polyjet [11] which uses a print head with one or more linear arrays of nozzles (similar to an inkjet) to deposit photopolymer in a desired layer and cure it using a flood UV illuminator. And binder jetting [12], which uses a similar print head to Polyjet but which deposits adhesive material onto a metal or polymer powder which is then baked and/or infused in a secondary post processing step.

While all of the above methods have enjoyed some measure of academic, industrial or commercial success in their various respective fields, fused deposition modeling (FDM) is perhaps most responsible for the widespread availability and adoption of 3D printing as a manufacturing process. FDM emerged in the early 1990's as a more versatile form of AM [13] without the requirement for hazardous chemical vats and expensive laser galvanometers. It uses a heated nozzle which extrudes molten thermoplastic polymer through a precise circular orifice in a heated nozzle which is controlled by a simple three axis CNC stage.

FDM promised clean, high speed, and economical 3D printing as well as the intriguing notion of a 'self-replicating' machine: the "Rep-Rap". [14] While the Rep-Rap was not truly self-replicating (it still required commercial off the shelf computers, ready-rods, stepper motors, wires and metal parts for the thermal extruder), it demonstrated a device which could produce all the custom parts needed to produce a copy of itself. While the Rep-Rap project garnered a sizable community, one could posit that it was not just due to its *open source hardware*, but because the idea of a *self-replicating assembler*

attracted the attention of hobbyists and the “maker” community at large. Such a “self-replicating assembler” was perhaps so captivating to engineers and project supporters because it mirrored, at least in principle, the mechanics of living systems. Which, as will be investigated herein, may be a paradigm better suited to additive manufacturing than the conventional (top-down) assemblers which have dominated the field of AM to this day.

1.3.2 Proposed Definition and Classification of Manufacturing Techniques





		SOURCE OF INFORMATION	
		Bottom-Up	Top-Down
MATERIAL FLOW	Additive		
	Subtractive		

Figure 1.1: A proposed method of classifying structural manufacturing techniques with regards to the size of assemblers in relation to the finished object, and whether material is added to or removed from the structure as it progresses towards a final form.

Techniques of manufacturing can be classified as either *top down* or *bottom up*, which will define for the remainder of this chapter in reference to to the size of the machines involved in assembly in relation the size of the final structure. One can also

choose to think about the various paradigms for manufacturing in terms of two parameters: the direction of the flow of matter (additive vs. subtractive), and the direction of the flow of information (from within the assembling structure vs. from without). Figure 1.1 depicts this foundational classification with illustrations. Top-down subtractive manufacturing is represented by conventional machining, bottom-up subtractive techniques are represented by bacterial/fungal/insect excavation of natural materials into colonies, bottom-up additive manufacturing is represented by living materials, and finally top-down additive manufacturing is represented by 3D printing.

Rather than a binary, it is hypothesized that there exists a continuum between a purely top-down assembler (such as a conventional 3D printer or MEMS reactive ion etching machine) which may be anywhere from a few volume % larger than the structure being assembled, or many orders of magnitude larger- to hybrid assemblers (such as those described in Chapters 2 and 3) which can produce structures a few volume % larger than the assembler's build volume, to perhaps 40x the volume of the original assembler's build plate. Finally there are purely bottom-up assemblers such as the self-assembly and growth of cells or seeds into living organisms.

1.3.3 Major Limitations of AM Systems

With this definition in place, it is important to note that top-down manufacturing systems have a few glaring limitations:

1. They are limited by the build volume of the assembler's travel range.
2. Their resolution is limited by the voxel size: comprising the *metamorphic area* (the smallest cross-sectional area through which material can be either added or removed from the structure) times the layer height.
3. Their speed of assembly (i.e. volumetric build rate) is fixed with respect to the hardware configuration of the assembler (i.e. the size and speed of travel of the toolpath).

1.3.4 General Trends in AM Systems - Volumetric Build Rate vs. Minimum Feature Size

When the volumetric build rate of various additive manufacturing (AM) systems is plotted against minimum feature size on a log-log plot, a roughly cubic (slope=3) trend

emerges among various (seemingly unrelated) classes of systems. A plot of this nature was first compiled by M. Shusteff [7] to demonstrate the advantages of tomographic projection-based volumetric printers, also known as Computed Axial Lithography (CAL) systems. [10] However, the relationship between volumetric build rate (V_s) and minimum feature size r_x was not explicitly investigated. A similar plot was constructed by Hahn et al. [15] who chose to examine the relationship between a “voxel rate” and the minimum voxel size (1/pixel size), with contours of volumetric build rate. However, such a plot when presented using the metrics chosen by Hahn et al. did not elucidate any correlation between the variables. In Figure 1.2 the data from Hahn et al. is reproduced along with additional points from Shusteff, comparing (V_s) and r_x on a log-log axes in order to elucidate this overarching trend. Examining this chart, a roughly linear (cubic) trend emerges among various classes of systems.

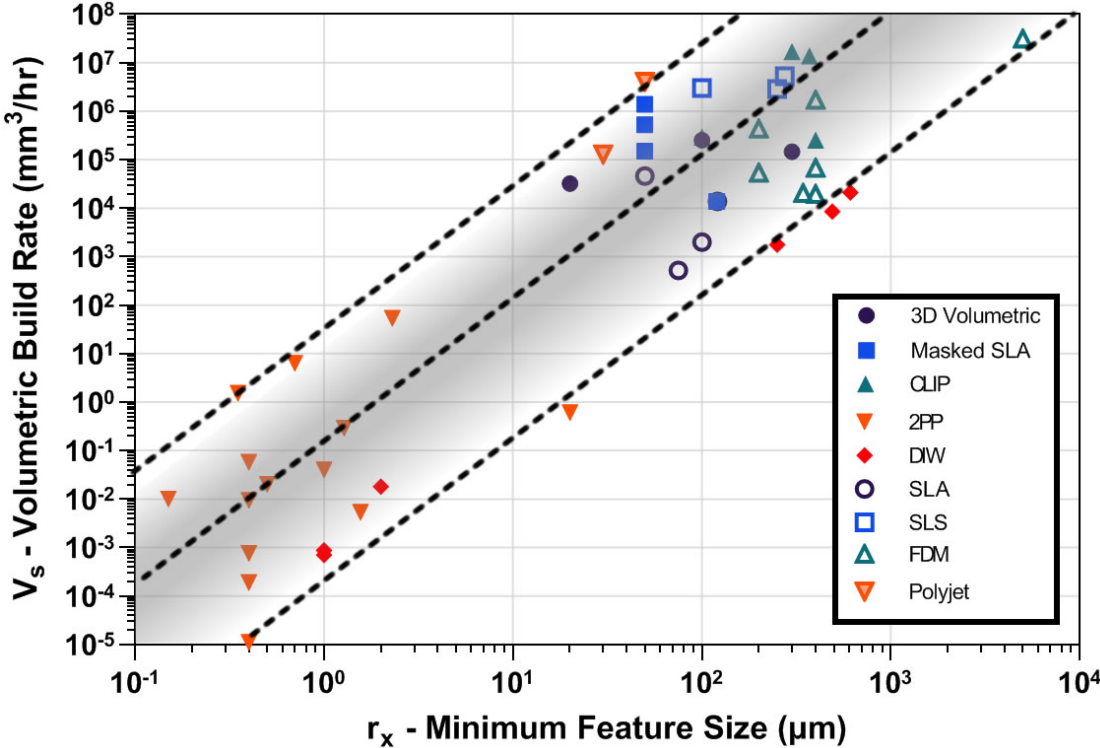


Figure 1.2: Scatter plot of selected AM technologies demonstrating of various technologies demonstrates a roughly cubic relationship between minimum feature size and volumetric build rate. The selected datapoints were chosen to demonstrate the rough order of magnitude envelope of each AM technology and the full details for the selected AM systems can be found in Tables 1.1.

While a general trend is observed in this chart (Figure 1.2), there are a number of incongruities with a strictly cubic relationship between V_s (volumetric build rate) and r_x (minimum feature size) – firstly, it must be noted that disparate classes of AM systems employ different methods of depositing material. For instance, 2PP, 3D Volumetric, CLIP, MSLA, SLA, and Polyjet use chemical photopolymerization while FDM, SLS and DIW generally use single point deposition via extrusion or thermal melting/sintering of material. The implications of this are discussed in detail. Secondly, a general trend can be observed in similar classes of system: FDM and SLS which both employ thermal melting of polymer material. FDM and DIW are both in general mechanically driven/Cartesian gantry systems with generally a single point of deposition which is easily scalable by the nozzle through with material is fed. 3D Volumetric, MSLA and CLIP systems all employ a 2D plane, comprising a matrix of pixels where material change via photopolymerization is occurring. SLA, SLS, and 2PP all employ scanning lasers with a metamorphic area dependent on the focal point of the laser.

1.4 The Conversion Rate of Digital Information to Granular Physical Structures in Top-Down AM Systems

The conversion rate of digital information to physical structures is the slowest of three bottlenecks, which can be summarized as the following:

1. Memory retrieval: The rate at which structural information can be retrieved from memory and passed to the metamorphic area to toggle the deposition or removal of material
2. Machine response: The rate at which the assembler’s metamorphic area can move (v_t)
3. Material response: The rate at which the material inside the metamorphic voxel can accept information and undergo conformational change

This work will focus primarily on additive rather than subtractive manufacturing systems, but it is important to note that the above bottlenecks can be applied to both. Focusing chiefly on the machine response (the limiting case for many systems), we can attempt to derive a relationship which we hypothesize underlies the cubic relationship observed in Figure 1.2.

1.4.1 Derivation of the Relationship Between V_s and r_x for Top-Down AM Systems

It is perhaps most intuitive to start by creating a generalized model of an AM system, for which we can define the various physical dimensions and parameters (Figure 1.3).

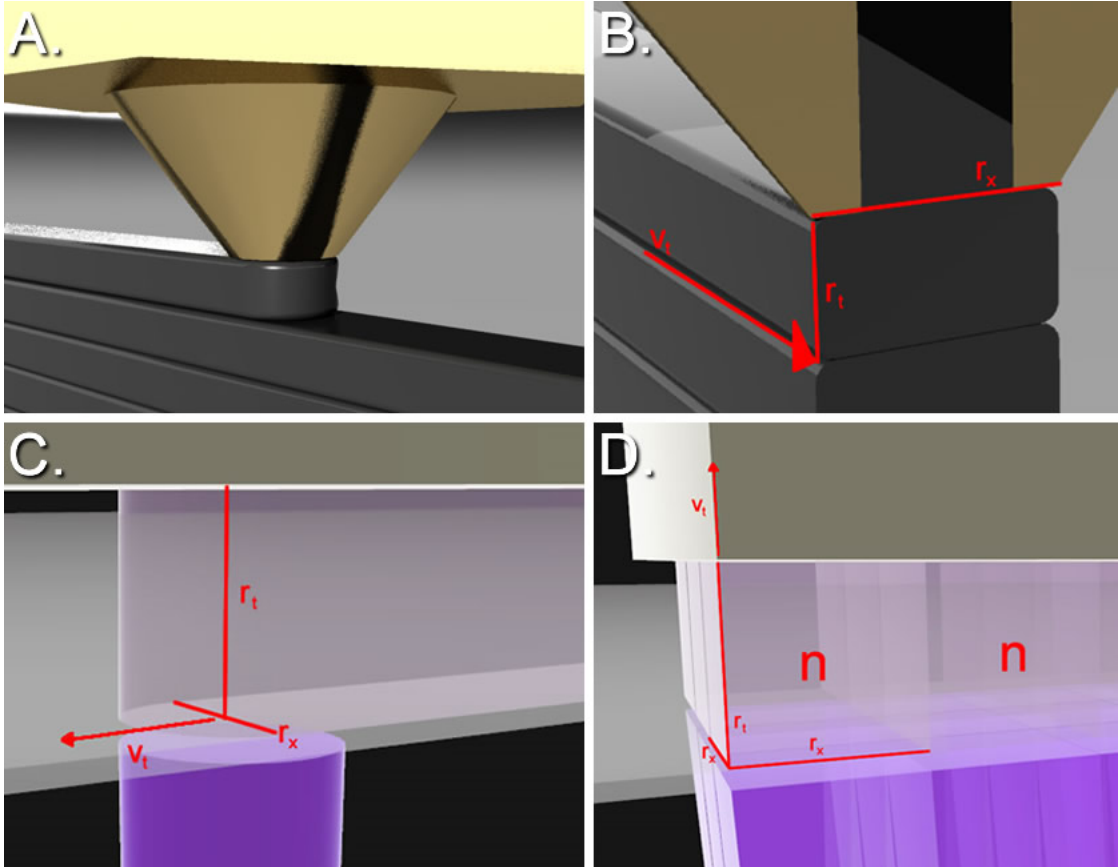


Figure 1.3: Notional diagrams of various AM processes including: A-B) FDM, C) SLA, and D) DLP/CLIP/MSLA and associated key geometric parameters noting the similarities between each process. Each process has (n) deposition paths, each depositing material in a volume of $(cl_t r_x^2)$ at a toolpath speed of (v_t) .

Derivation of Total Build Time from V_s and Voxel Parameters

We can obtain the volumetric build rate (V_s) of the generalized model by dividing the voxel size $v_0 = c(r_x r_x r_t)$ by the required for the system to move to the next voxel's position (t_l). The constant (c) is related to the packing fraction. If we envision one

voxel as a cube, $c = 1$ would yield the correct deposition volume. If there is void space in between deposition paths, c would be less than 1, and would equate to the packing fraction of the assembled structure. In the case of an infill structure, we could also define c as the infill percentage (0-100%).

If we define the time required to move one voxel as (t_l) where $t_l = r_x/v_t$ in the case of FDM/SLA or $t_l = r_t/v_t$ in the case of DLP/CLIP/MSLA. It is important to note that the time to advance one layer includes any recoating or “down” time included in t_l (for DLP/MSLA/SLS systems). We arrive at Equation 1.1 for the volumetric build rate (V_s).

If we assume a toolpath radius r_x , we can generalize the cross sectional area $c * r_x^2$ of the toolpath normal to the velocity vector (v_t) of structural formation. This relationship holds for both circular and square toolpaths, where in the case of a circular toolpath, $c = \pi$ and in the case of a square toolpath, $c = 4$.

We can obtain the volumetric material deposition rate V_s by simple multiplication of this cross sectional area by the layer thickness r_t and dividing this volume by the time required to move one toolpath radius $t_l = (r_x/v_t)$, as shown in Equation 1.1.

$$V_s = \frac{c r_t r_x^2}{t_l} \quad (1.1)$$

If we define the deposition aspect ratio as $d_r = r_t/r_x$, then V_s can be expressed in the following Equation 1.2.

$$V_s = \frac{d_r c r_x^3}{t_l} \quad (1.2)$$

Therefore, the time (T) to print an arbitrary object with a volume V_0 can be expressed as Equation 1.3.

$$T = \frac{V_0}{V_s} = \frac{V_0 t_l}{c d_r r_x^3} \quad (1.3)$$

Taking into account the fact that some systems may have multiple (n) deposition paths or printheads acting simultaneously, the total deposition rate becomes Equation 1.4.

$$V_s = \frac{n d_r c r_x^3}{t_l} \quad (1.4)$$

And the minimum time to print an object becomes Equation 1.5.

$$T = \frac{V_0 t_l}{n d_r c r_x^3} \quad (1.5)$$

The Structural Patterning Rate (SPR)

With these definitions in place, we can also construct a parameter which represents the rate of structural information processing, which we can define as the structural patterning rate (SPR), with units of 1/s (Hz). It is the information processing rate necessary to build a structure at a volumetric build rate V_s [mm³/s] with a voxel volume v_0 [mm³], expressed in Equation 1.6, which represents V_s/v_0 (volumetric material deposition rate divided by the voxel volume, $v_0 = d_r c r_x^3$).

$$SPR = \frac{V_s}{v_0} = \frac{V_s}{d_r c r_x^3} = \frac{n}{t_l} \quad (1.6)$$

SPR can also be arrived at by dividing the number of simultaneous deposition paths by the time required to pattern each voxel.

Defining a “Printer Constant” (k)

We can define (k) as the “printer constant” which encompasses nozzle geometry, deposition cross section, and the speed of print head movement by the equation $\frac{t_l}{d_r c} = k$. Such a constant is useful for defining the individual parameters of a specific AM system. Simplifying and rearranging the relationship we obtain Equation 1.7 relating the time (T) to print an object of volume (V_0) and the size of the deposition path (r_x).

$$T = \frac{k V_0}{n r_x^3} \quad (1.7)$$

Rearranging and taking the logarithm, we obtain the following log-linear Equation 1.8.

$$\log V_s = \log \frac{V_0}{T} = 3 \log r_x + \log \frac{n}{k} \quad (1.8)$$

If we consider the minimum resolution discernable on a system as approximately equal to r_x for all systems (r_x for the x/y resolution and $d_r r_x$ for the z resolution). We can see that V_0/T is the same as the volumetric build rate (V_s), and that Equation 1.8 corresponds a relationship between volumetric build rate V_s and resolution r_x which

is linear with a slope of ~ 3 when plotted on a log-log scale). This corresponds to the relationship observed by many current AM systems (as shown in Figure 1.2).

It is important to note that Equation 1.8 applies to all layer-by-layer top-down AM systems, including 0D (point deposition, i.e. FDM, SLS, SLA), 1D (line deposition, i.e. polyjet, binder-jet), and 2D (DLP, CLIP, MSLA). For quasi-volumetric methods such as axial lithographic printing, equivalent parameters are shown in Table 2.

1.4.2 Limitations of Memory Retrieval (Bottleneck 1)

In Section 1.4 we specified a number of “bottlenecks” which limited the rate of information conversion to physical structures. The SPR metric can be thought of as a theoretical requirement for the first general manufacturing rate limitation: the rate at which structural information must be retrieved from memory and passed to the assembler’s tool heads must be greater than the SPR. Seeing as the maximal value of n rarely exceeds 2×10^4 in the case of inkjet systems (Tables 1.1), and deposition path speed rarely exceeds 1 m/s, this gives a practical maximum t_l value of 3×10^{-5} , and we arrive at a SPR of 6×10^9 , or roughly 6 GHz- well within the capabilities of modern computers.

However, if we desired higher volumetric deposition rate, or higher resolution, this information processing limitation would begin to rear its head. If a CLIP system were to be developed with a 200k X 200k pixel display ($50 \mu\text{m}$ per pixel) which could print with a layer height of $50 \mu\text{m}$ at 5 s per layer, this would yield a SPR of 8 GHz, but if the layer height was reduced to $1 \mu\text{m}$ and the layer time decreased to 0.1 s (to utilize the potentially micron-scale resolution of CLIP systems), this machine would require an information transfer rate of 400 GHz which would quickly require advanced computer systems or sophisticated parallel processing in order to operate it.

1.4.3 Limitations of Machine Response (Bottleneck 2)

Our second manufacturing rate limitation is the rate at which the assembler’s tool head(s) can respond to commands and impart information to the material. This is *geometrically* constrained by the following factors:

1. The deposited volume of the object (V_0)
2. The minimum feature size of the object (r_x)
3. The number of simultaneous deposition paths (n)

4. The velocity at which the deposition path is able to move (v_t)

Experimentally, the volume (V_0) only applies to the deposited material, not the outside bounding volume, so infill structures can be used which avoid depositing material which does not meaningfully contribute toward the function of the object, saving time and material. However, such infill structures represent a compromise. One can look at an infill pattern as adopting a larger average feature size (since the cell size of the infill is equal to the print head diameter for 100% infill, and twice the feature size of the print head diameter for 50% infill, etc.) This compromise is represented in the c term in the relation 1.5 and captured in the printer constant k .

The last of these factors, deposition path velocity (v_t) is perhaps the most complex because it is a function of not just the physical constants of the system but also on the material and the rate at which information can be passed from digital storage into physical structure.

1.4.4 Limitations of Material Response (Bottleneck 3)

Our third manufacturing rate limitation is the rate at which the material can accept structural information and undergo conformational change. For thermal-based approaches such as SLS or FDM, the velocity of the metamorphic area is constrained largely by the thermal mass of the material and power of the system’s heaters. For photopolymer based systems the relationship is a much more complex function of the reaction rates for the specific polymer resin formation (initiation, growth and termination rate constants), as well as light intensity, oxygen inhibition and the presence of dyes/colorants in the photopolymer resin. [16]

Hahn et al. chose to represent the AM landscape in terms of SPR (“peak printing rate”: voxels/s) which they plotted against the voxel size. [15] They make the argument that the SPR is a key figure of merit with regards to AM technologies. We concur with this sentiment in the same way that one could look at processor speed as a key figure of merit for the performance of a computer. However, it is not the only figure of merit; like the architecture of an information processing system which can be bottlenecked by several pieces of hardware, the architecture of a structural patterning system can also be bottlenecked by several factors (as described in this section).

1.4.5 Tradeoffs in Top-Down AM: Size, Resolution, and Speed

An ideal print geometry which maximizes strength to weight ratio would likely feature hierarchical structures (such as those found in wood or bamboo) with fractal-like varying feature size throughout the object, with the largest features providing overarching structural features to facilitate overall growth direction, and the smaller features providing additional strength and material transport as the structure grows. The smaller the minimum feature size, the higher the specific strength could be achieved.

However, such structures are currently impractical to print in a reasonable time using our existing top-down additive manufacturing systems – one would not wish to use 2-photon polymerization (2PP), a AM method with sub-micron resolution, to print a 2x4 wood-like polymeric board with the same hierarchical strength to weight properties as lumber. So we arrive at a core *trilemma of linear manufacturing*. As minimum feature size r_x decreases (i.e. resolution increases), the volumetric print speed tends to decay in a cubic fashion. This means that finely detailed objects will either take far longer to print, or their size must be reduced. Printing of hierarchal or finely detailed large objects is challenging for Top-Down systems due to inherent geometric limitations.

1.4.6 Towards a Bottom-Up Paradigm: Quasi-Volumetric Systems

Any manufacturing system which uses an approach of a macroscopic system producing objects from the top-down, even with advanced multi-deposition path systems (such as CLIP or CAL) one is still dealing with the creation of a 3D system with (at best) a 2D deposition plane (in real or Fourier space, respectively). Table 1.2 presents a comparison of parameters for 0D/1D/2D/TAM systems. However it is still important to consider the fact that resolution is still traded off for speed. CAL (aka. Tomographic AM) is volumetric in the material space but quasi-volumetric or 2D in the informational space. It is capable of very rapid printing of objects, but generally requires special photopolymers in order to function. It also features a non-constant voxel size with respect to radial position, and challenges the fundamental limits of a top-down assembly system. Nonetheless, it challenges existing assertions about what AM exists in a transitional space between top-down and bottom-up manufacturing. It features hierarchal resolution of voxels and a non-layer by layer approach. Due to the fact that CAL is not layer by layer allows the theoretical possibility of multiple resolutions to be incorporated into a single print. But the assembled structures are still limited by the build volume of the

assembler.

Another potential avenue may be to pursue AM from the Bottom-Up. Employment of self-assembling and self-replicating systems can effectively form a truly volumetric (3D) deposition plane, since the object's bulk is formed from many points simultaneously and the information is contained within the assemblers themselves, freeing Bottom-Up systems from Bottlenecks 1 and 2.

1.5 A Proposed Model for Bottom-Up AM systems

1.5.1 Self-replication of of Notional Bottom-Up Assembly System

Self-replication of reconfigurable organisms presents an alternate approach for the construction of physical structures from digital information. [17] In such a bottom-up paradigm, it may be possible to produce large, complex structures in a reasonable timeframe.



Figure 1.4: A system of self-replicating, self assembling volumetric assemblers can be parameterized similarly to the top-down assembly systems described in Section 1.4, such as a notional bottom-up assembly system comprised of genetically engineered *e. coli* bacteria growing through binary fission.

For binary fission of self-replicating systems, we can apply the well-known rela-

relationship commonly applied to the growth of bacterial colonies (Equation 1.9) to model the bottom-up construction rate in its early stages. [18] For such a self-assembling system, we can largely re-use the same parameters as developed to describe a top-down system (Figure 1.4), where the number of simultaneous deposition paths (i.e self-replicating assemblers), n , is a function of the current time (t), the initial number of assemblers (n_0) and the self-replication (doubling) time: t_d of the assembler.

$$n(t) = n_0 2^{\left(\frac{t}{t_d}\right)} \quad (1.9)$$

Multiplying by the volume of an individual assembler (assuming that the assemblers themselves become part of the physical structure they are creating), we obtain Equation 1.10 relating the object volume (V_0) to the assembler volume (kr_x^3 , where k is a geometric constant) with the notable addition that the object volume is now a function of time.

$$V_0(t) = kr_x^3 n_0 2^{\left(\frac{t}{t_d}\right)} \quad (1.10)$$

From Equation 1.10, it should be plain to see why such a bottom up approach is advantageous. In bottom-up systems, the time to print an object of volume V_0 increases at an exponential rate with respect to time, rather than a proportional rate as in the relationship 1.7 for top-down systems. Rearranging for clarity and setting the current time (t) at the completion time (T) we obtain Equation 1.11:

$$T = t_d \log_2 \left(\frac{V_0}{kr_x^3 n_0} \right) \quad (1.11)$$

We can see that the time to produce an object of volume V_0 is linearly related only to the self-replication time, and to a far lesser extent (\log_2 relationship) with the actual volume of the object and the minimum feature size.

1.5.2 Comparison Between Top-Down and Bottom-Up Assembly Systems

Using Equation 1.10 we can evaluate V_0 as a function of time t to get a better understanding of the theoretical size of a self-replicating system over time. Using the size, doubling time and initial cell count of a notional e. coli colony: $r_x = 5 \mu m$, $t_d = 30 \text{ min}$, and $n_0 = 100$ cells, we obtain the following logarithmic growth curve shown

in Figure 1.5 which suggests that a structure volume of 1 m^3 could be constructed in approximately 24 hrs of logarithmic growth. It is important to note that this exponential growth is not the practical speed of a self-replicating bottom-up assembler, but rather a theoretical maximum rate. A real bottom-up manufacturing system would exhibit a finite lifespan, necessitate the acquisition of resources via diffusion, and therefore would need to exhibit more complex growth patterns (i.e. vascularization, division, senescence, and deposition of non-living structural materials) versus a theoretical bacterial colony with infinite proximal resources for unconstrained living material growth.

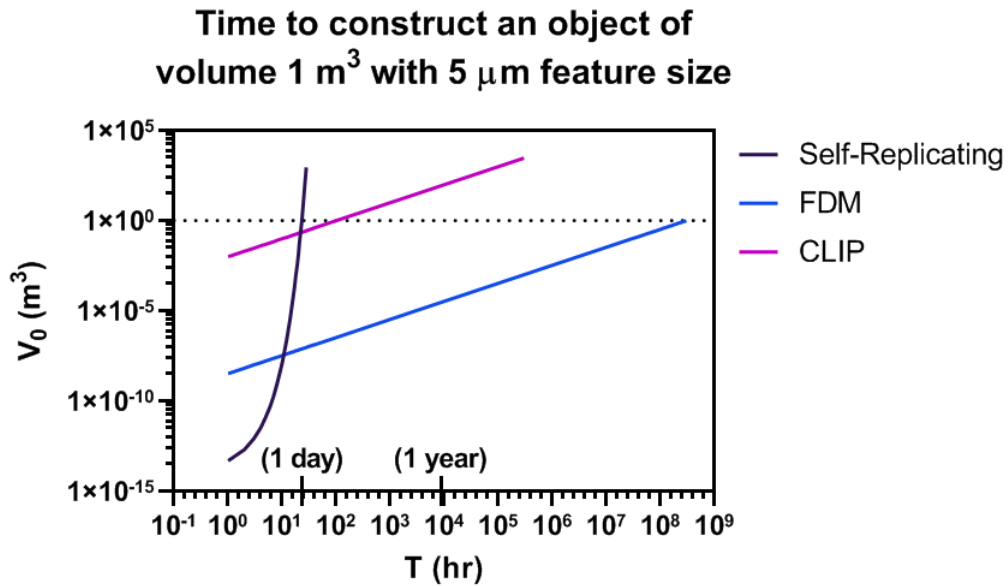


Figure 1.5: Volume of self-replicating system with respect to time. Using the model in Equations 1.7 and 1.11 we obtain a volume of 1 m^3 at approximately 10 hrs with a self replicating system with parameters $r_x = 5 \mu\text{m}$

We can contrast the self-assembling colony with a hypothetical CLIP system with a 1 m^2 display surface and a $200\text{K} \times 200\text{K}$ display ($5 \mu\text{m}$ pixel width) printing at 10 mm/hr , which would require 100 hours to print such a structure, assuming the display could be cooled adequately. A similarly capable FDM system operating with a single independent print head of $5 \mu\text{m}$ diameter at the highest recorded FDM print speed would require 34,000 years of operation to print such a structure.

While the barriers associated with CLIP systems are technical and economical in nature (construction of the extremely large, high pixel density display, cooling, UV

light source, etc.), and the barrier associated with FDM systems is print time, the upfront investment in self-replicating systems has far-reaching applications beyond that of additive manufacturing.

A practical self-replicating assembler therefore would need to incorporate vascularization (i.e. xylem and phloem) into the assembled structure to enable structural growth past the natural diffusion length of gases and minerals, as well as providing structural rigidity to the self-assembling system.

If we take into account the fact that all practical structures will have some porosity (i.e. they will not be a solid 1 meter cube of material), we can see that while the FDM print time will decrease, and the CLIP print time will remain roughly constant regardless of infill density.

The presence or absence of porosity in self-replicating systems of course makes little difference in terms of growth time, but may be necessary for sustainment of nutrient sources, gas diffusion, etc. which this simplistic model yields obviously neglects.

Exponential Growth is an Insufficient Model for Bottom-Up Assembly Systems

A simple bacteria-like replicating unit cannot sustain logarithmic growth indefinitely as it would quickly deplete its nutrient sources, even if perfect gas diffusion could be accomplished. A practical self-replicating assembler therefore would need to incorporate vascularization (i.e. xylem and phloem) into the assembled structure to enable structural growth past the natural diffusion length of gases and minerals, as well as providing structural rigidity to the self-assembling system.

As more complex differentiated systems are eventually designed, our simplistic growth rate (Equation 1.11) may no longer be adequate to describe the rate of structure assembly. Mathematicians and biologists have begun to develop models for the limits and characteristics of this growth rate of biological systems; which mainly point to limitations in the diffusion of nutrients to actively dividing cells as the limiting factor of growth, but a full understanding of the requirements and limitations for engineered self-assembling living systems appears to be still elusive at this time. [19]

Differentiation and structurally directed replication mechanisms for the creation of such structures have been proposed via genetic engineering. [20,21] Even though such systems are still in their infancy, we can expect that as the cost of custom DNA syn-

thesis continues to fall, researchers will rapidly begin to engineer custom differentiation conditions and structural information into living systems, which will catalyze the next paradigm of bottom-up manufacturing. The biggest limitation to such a paradigm is the ability to direct the living system to recursively assemble a final desired structure. Machine learning and artificial intelligence have recently proved key in predicting once “unsolvable” folded protein structures from amino acid sequences [22], and may as well hold the key to achieving such similar predictive feats of bottom-up directed cellular assembly.

1.5.3 A Forward Look at Biological Self-Assembly as a Possible Manufacturing System

While the computational tools necessary to develop self-assembling, self-replicating assembled features from living systems are still forthcoming, one could envision that such systems may eventually come to replace or supplant existing manufacturing methods. In the same way that subtractive mechanical fabrication, mass production and automation eventually replaced artisan hand-shaping, chisel and hand tools; self-directed assembly may hold the potential to supplant top-down mechanical fabrication. Assembly of a biopolymer structure in the desired geometry might be as simple as planting a seed and allowing a self-assembling system to absorb nutrients from the soil and energy from the sun. Such a paradigm would allow for massively parallel “farming” of objects and independence from centralized production and tooling. This would be ideal for survival in austere environments or construction of large structures without the requirements to transport large tooling or assembly machinery to such locations (i.e. planetary colonization). While we do not yet possess the plethora of tools which evolution and biology have taken billions of years to develop, we can take a pragmatic approach to capitalize on the massive parallelization possible through bottom-up assembly. Intermediary approaches such as the use of phototaxis or magnetotaxis may be employed to pattern and direct the replication of cells in a similar fashion.

1.6 Conclusion

We have proposed three basic limitations on the speed of manufacturing, derived a generalized relationship (Equation 1.8) between volumetric deposition rate, structural

resolution and the physical properties of manufacturing systems which fits well with the empirical specifications of various commercial systems and which we anticipate will hold true for any top-down manufacturing system. This relationship describes the theoretical limits of volumes which additive manufacturing is capable of constructing within a reasonable timeframe. We posit that the three limitations (information retrieval rate, movement rate, rate of material change) apply to all forms of manufacturing: whether material is being removed or added, and via thermal, mechanical, chemical, or biological means.

In order to move beyond such limitations, we propose that a bottom-up self-replicating paradigm should be considered. A basic idealized theoretical model for which is presented here (Equation 1.11), however such a model is not adequately advanced to take into account the complex growth conditions, or the vast array of parameters and configurations which self-replicating bottom-up assemblers might adopt.

While top-down additive manufacturing systems traditionally require highly specialized feedstocks with high chemical or mechanical precision for their requisite printers, bottom-up approaches are more likely to maximize the functionality and utility of the material feedstock since decomposition and (re)construction can be integrated into a single assembler unit at the micro-scale.

While it is likely that top-down systems will remain valuable tools for many industrial processes, in order to build next generation, multi-scale structures with high resolution in a practical timescale, a bottom-up approach should be considered.

1.7 Supplemental Tables

Table 1.1: Systems plotted in Figure 1.2 and associated references.

Technology class	System description	Min feature size (μm)	Volumetric build rate (mm^3/hr)	Notes	Ref
3D Volumetric	LLNL/MIT prototype	100	252,000	Max volume / min exposure of current config $0.7 \text{ cm}^3/\text{s}$	[7]
	UC Berkeley Prototype	300	146149		[10]
	UC Berkeley micro-CAL	20	32311	trifurcated channel, silica, $20 \mu\text{m}$ resolution, 30 s print time, 3.5 mm diam x 7 mm height	[23]
CLIP	Carbon3D	400	250,000	Shoe $100 \times 25 \times 100 \text{ mm}/\text{hr}$	[8]
		100	288,000	Argyle $24 \times 25 \times 500 \text{ mm}/\text{hr}$	[8]
		50	14,400	Paddles $24 \times 24 \times 25 \text{ mm}/\text{hr}$	[8]
	Research prototype	370	13586418	Theoretical max	[8]
	HARP	300	16700000	High area rapid printing	[9]
2PP DLW	Nanoscribe	0.15	0.01	Using 63x objective	[7]
		0.5	0.02	Using 25x objective	[7]
		0.4	0.05746		[15]
		1.275	0.29	Using 25x objective	[24]
	Parallelized 2PP	0.7	6.31		[15]
		0.35	1.51	Using 9x beam-splitting	[15]
		20.0	0.6025	Using simultaneous spatiotemporal focusing of the femtosecond laser	[25]
		1.0	0.039916	Using a digital micromirror device (DMD)	[26]
		0.4	0.000011		[27]
		0.4	0.000763		[28]
0.4	0.009383		[29]		
1.56	0.005341		[30]		

†Specifications obtained from relevant company websites.

Table 1.1: Systems plotted in Figure 1.2 and associated references. (Cont)

Technology class	System description	Min feature size (μm)	Volumetric build rate (mm^3/hr)	Notes	Ref
2PP DLW	2PP	0.4	0.000189	Using parallel lasers	[31]
		2.3	53.0207		
	2PP NIL	0.4	0.00076	Fabrication of Nano-Imprint Lithography	[33]
Polyjet	Stratasys Objet 5000 Connex 1	30	129117	Vendor information release, 2014	†
	HP Jet-Fusion 3D 4210	50	4016845	Vendor information release, 2017	†
DIW	J. Lewis (UIUC)	1	0.000707	1 μm filaments at 250 $\mu m/s$	[34]
		2	0.0181	1 μm filaments at 250 $\mu m/s$	[35]
	LLNL DIW	610	21,041	20 mm/s	[36]
		250	1,767	10 mm/s	[7]
	DIW	490	8459		[36]
	MEMS DIW	1	0.00088	DIW assembly of Si-MEMS photonic crystals	[34]
SLA	Autodesk Ember	50	46,080	50 μm XY, 50 μm layer height, 64x40 mm area, 18 mm/hr	†
	FormLabs Form2	100	2,000	2 cm/hr , 10x10 mm area, rook example part	†
	3D Systems Projet 7000 HD	75	522	Vendor information release, 2012	†
SLS	3DS sPro 230 HD-HS	100	3,000,000	3.0 L/hr , 100 μm layer height and 100 μm XY res	†
	EOS P770	250	2,880,000	400 μm laser spot x 100 μm layer height x 20 m/s scan speed	†
	EOS P110	274	5,260,000	With PA 2200 “Top Quality”	†
FDM	Prusa	200	54,000	0.4 mm nozzle, 15 mm^3/s	†

†Specifications obtained from relevant company websites.

Table 1.1: Systems plotted in Figure 1.2 and associated references. (Cont)

Technology class	System description	Min feature size (μm)	Volumetric build rate (mm^3/hr)	Notes	Ref
FDM	Voron	200	432,000	0.4 <i>mm</i> nozzle, 120 mm^3/s	†
		400	1,728,000	0.8 <i>mm</i> nozzle, 480 mm^3/s	†
	Univ. Maine 3DP	5,000	31,500,000	2.268 $m^3/72hr$	†
	Stratasys Mojo	343	20,425		†
	Stratus Fortus 360MC	400	68,129		†
	Ultimaker 2	400	19,430		†
MSLA	Anycubic Mono	50	520,000		†
	Anycubic Mono X	50	1,382,400		†
	Anycubic Photon	50	149,500		†
	LED-based Projection SLA	120	13770	Early research prototype	[37]

†Specifications obtained from relevant company websites.

Table 1.2: Equivalent parameters for 0D, 1D, 2D, and tomographic volumetric AM processes. DMD = Digital Micromirror Device. †Tomographic volumetric AM represent a special case where scanning is conducted in spatial frequency space instead of real space. The number of tomographic projection required is proportional to the number of voxels in the lateral direction. [10, 38, 39]

	FDM, SLA, SLS (0D point scanning)	Inkjet (1D nozzle array)	DLP, CLIP (2D)	Tomographic VAM †
Information to be patterned	Total of voxels in object: $N_{total} = \frac{V_0}{v_0} = N_x N_y N_z$			
Structural patterning rate (SPR) and the limits of characteristic time t_l	$SPR = \frac{n}{t_l}$ where $\frac{1}{t_l} < \min(f_{extru}, f_{motion})$	$SPR = \frac{n}{t_l}$ where $\frac{1}{t_l} < \min(f_{jetting}, f_{motion})$	$SPR = \frac{n}{t_l}$ where $\frac{1}{t_l} < \min(f_{DMDfps}, f_{motion})$	Total voxels in frequency domain†: $\frac{\pi}{2} N_{pixels} N_{lateral} = \frac{\pi}{2} N_x \max(N_x, N_y)^2$ where $\frac{1}{t_l} < \min(f_{DMDfps}, f_{motion})$
Parallelism applied (physical meaning of n)	$n = n_{nozzle}$ (number of nozzles)	$n = n_{nozzle} = N_x$ (number of jetting nozzles in the 1D array)	$n = n_{pixels} = N_x N_y$ (number of pixels on 2D DMD)	$n = N_z \max(N_x, N_y)$ (number of pixels on 2D DMD)
Minimum print time $T = \frac{N}{SPR}$	$\frac{N_x N_y N_z t_l}{n}$	$N_y N_z t_l$	$N_z t_l$	$\frac{\pi}{2} \max(N_x, N_y) t_l$

1.8 Acknowledgements

Chapter 1, in part, is currently being prepared for submission for publication of the material. Wirth, David M.; Li, Chi C.; Pokorski, Jonathan K.; Taylor, Hayden K.; Shusteff, Maxim. The dissertation author was the primary investigator and author of this material.

Chapter 2

Self-Expansion of Additively Manufactured Polymeric Structures

2.1 Introduction

The objective of this chapter is to discuss one potential avenue for the circumvention of current limitations of additive manufacturing, specifically the reliance on top-down hardware with a build volume sufficient in size to encompass the bounding volume of the object to be constructed. In modern manufacturing it is a widely accepted limitation that the parts patterned by an additive or subtractive manufacturing process (i.e. a lathe, mill or 3D printer) must be smaller than the machine itself which produced them. Once such parts are manufactured they can be post-processed, fastened together, welded or adhesively bonded to form larger structures. We have developed a foaming pre-polymer resin for lithographic additive manufacturing which can be expanded after printing to produce parts up to 40x larger than their original volume. This allows for the fabrication of structures significantly larger than the build volume of the 3D printer which produced them. Complex geometries comprised of porous foams have implications in technologically demanding fields such as architecture, aerospace, energy, and biomedicine. This chapter presents a comprehensive screening process for resin formulations, detailed analysis of printing parameters, and observed mechanical properties of these novel 3D-printed foam structures.

2.2 Background

Current methods of 3D printing (3DP) have enabled the fabrication of a wide variety of complex structures and geometries not possible through other forms of manufacturing. While Additive Manufacturing (AM) of polymers unlocks countless doors in terms of design and geometric freedom, these methods are generally limited by the repertoire of materials available to the specific processes. These limitations become especially apparent when contrasted with mature polymer processing techniques such as extrusion or injection molding, which can be carried out using essentially any thermoplastic polymer. Lab-scale 3DP of polymers is typically enabled by two-technologies: fused deposition modeling (FDM) and stereolithography (SLA). FDM produces objects by extruding melted thermoplastics through a heated nozzle and is largely amenable to the melt processing techniques commonly employed by the polymer processing community. In contrast, SLA forms parts by selectively exposing light sensitive resins to patterns of light. The materials selection of SLA is significantly limited compared with FDM due to the chemistry needed to rapidly cure polymers with light. Thus, SLA has been traditionally restricted to materials that undergo photo-induced radical crosslinking of acrylates and acrylamides. [40, 41] Parts made with SLA are generally capable of much higher detail than FDM with minimal gradation between layers. However, the properties of SLA-produced parts are limited since commercial resins generally produce stiff, brittle, highly-crosslinked parts. Efforts have been made to expand this selection of materials by incorporating novel resin chemistries, composites, or advanced methods of additive manufacturing but such advances have traditionally relied on expensive equipment or specialized reagents. [42–44] In short, there is a great need to expand the collection of materials available to SLA printing and currently there are no examples of highly expandable foams produced using this technique.

While 3DP offers a high degree of flexibility in the geometry of finished parts, the time required to print an object is proportional to its volume. Consequently, many commercial printers have small build volumes, forcing larger objects to be assembled from multiple separate prints. However, these limitations can be mitigated by developing resins that cure to form expanding polymeric foams, thus allowing one to print an object quickly at small scale and then expand it after printing to reach a larger finished scale. Perhaps the most famous example of a polymeric foam is expanded polystyrene [45] or Styrofoam. It has a broad range of applications due to its low cost,

excellent insulating properties, ease of fabrication, and high expansion ratio (20-90x). [46] However, polystyrene foam is not amenable to SLA printing due to its low cure rate and volatile blowing agents (such as pentane) which would evaporate from the resin bath during long prints. Researchers have attempted to solve this problem by creating 3D printable foam materials using direct ink writing [47, 48] or FDM. [49–51] but the resultant parts generally have low expansion ratios or poor resolution in comparison to SLA parts. Many of these methods rely on the patterning of cured polymer with a dissolvable component (such as salt [48] or sugar [52]) and submerging the structure in water after the print is complete; leaving a porous, open celled sponge. While these methods are promising for a variety of applications, particularly in biomedicine, many are ill suited to a broad range of applications due to their open cell nature, negligible expansion [49] and/or low mechanical strength (typically under 0.1 MPa modulus). [48, 52] Recently, an inkjet 3DP formulation using a hydrazine-based blowing agent, 4,4'-oxybis(N'-benzoylbenzenesulfonohydrazide) demonstrated up to 44% volumetric expansion using a modified PolyJet system. [40] While this initial work is promising, it relies on a specialized system and requires a pre-expansion prior to fully curing the part, making the process unsuitable for SLA systems.

In our work we aimed to use a widely-available Mask Stereolithography (MSLA) system, the Anycubic Photon, which costs under \$300 and does not rely on sensitive optics. While this printer is highly accessible to researchers, it is only able to produce a light intensity less than 1 mW/cm^2 . Based on the available literature and the nature of the MSLA process, we propose the following conditions are necessary to create a foam-able resin for MSLA printers:

1. The prepolymer resin must cure quickly at light intensities under 1 mW/cm^2 to allow for practical print times.
2. The decomposition point of the blowing agent must be above the glass transition (T_g) and below the melting (T_m) or decomposition temperature (T_d) of the cured polymer to allow for deformation and gas trapping, but not melting or decomposition of the printed object during expansion.
3. The blowing agent must be soluble in the neat monomer to prevent precipitation during the print in order to ensure homogenous expansion of the printed part.
4. The prepolymer resin must contain a low concentration of crosslinking species.

Crosslinks increase the glass transition temperature of the printed object as well as reduce the free volume of the polymer, leading to reduced expansion of foams.

Herein, we describe a resin formulation which can be printed in an unexpanded state and controllably expanded to create structures significantly larger than their printed size. We present a systematic evaluation of resin components including: monomers, blowing agents (BA), and photoinitiators (PI). Finally, we present an evaluation of 3D print parameters to enable controllable foaming, analysis of the mechanical properties of several foam variants, and demonstrations for potential applications of the technology (available in the supplemental videos).

2.3 Results and Discussion

2.3.1 Optimization of Monomer

In order to develop a resin suitable for 3D printing, our first endeavor was to determine a monomer which was suitable for 3D printing and characterize its layer curing time. Three potential monomers were explored for a foaming resin: methyl methacrylate (MMA), hydroxyethyl acrylate (HEA), and hydroxyethyl methacrylate (HEMA) (Table 2.2). Rather than doing full-scale prints for each composition; the cure time for each formulation was evaluated by placing a 20 μL droplet of each resin compositions on a glass slide, and exposing them to a 340 $\mu\text{W}/\text{cm}^2$, 405 nm light source while periodically inserting a metal probe into the liquid resin until the probe was no longer wetted by the polymer sample. This provided a reliable indication of the minimum exposure time for viable 3D printing layers of new resin formulations and accelerated our ability to test compositions (Figure 2.1A, 2.1E).

Despite MMAs widespread use in commercial resins, it is commonly augmented by a large proportion of crosslinker (CL) and oligomer species, without which MMA would be impractical due to its slow cure rate. [53] Our results further verify this, and even at high densities of ethylene glycol dimethacrylate (EGDMA), cure time was in excess of 100 seconds (Entry A8, Table 2.2). Furthermore, the thermal window between T_g (85-102 $^{\circ}\text{C}$) [54,55] and T_m (160 $^{\circ}\text{C}$) [54] was fairly narrow, making appropriate pairing with a blowing agent difficult. Other widely used monomers that are cured by radical polymerization, such as urethane acrylate oligomers, tripropylene glycol diacrylate, bisphenol A-glycidyl methacrylate, and tetraacrylates [53] were not explored in this work

because they would form a tightly crosslinked network in a finished part. Crosslinked polymers tend to decompose rather than soften or melt, thus they are less amenable to foam expansion. Consequently, we aimed to minimize the use of crosslinking species in our resin formulations and discarded MMA for future development.

Of the monomers tested, HEMA, and HEA were promising candidates due to their rapid cure times and current use in 3DP scientific literature. [56,57] It is known that these monomers contain small amounts of cross-linking species when unpurified which helped to accelerate curing but were present in sufficiently low concentrations to enable expansion (1.72 mol% in HEA vs 0.18 mol% in HEMA), (Figure 2.14). The cure rate of HEA was roughly one order of magnitude faster than HEMA. We tested additional cross-linking components to improve cure time, however cure rate was negligibly enhanced (Entries: A18,19,28,29, Table 2.2). HEA compositions cured quickly, but the mechanical and gas retention properties of the final pHEA polymer were poor in comparison to pHEMA (see section on blowing agent selection). While pHEMA is mechanically rigid even without the use of additional crosslinkers, pHEA is mechanically pliable and allows gas to escape during expansion (Table 2.4). The very low glass transition temperature ($T_g < 0$ °C) of HEA is poorly suited for its use in expanding foams which must hold their shape during expansion. HEMA was chosen as the most promising monomer in initial screenings due to its stability in ambient conditions, reasonable cure time, favorable mechanical properties, glass transition temperature above room temperature ($T_g = 70$ - 82 °C) [55,58], and a high decomposition temperature ($T_d = 230$ - 293 °C). [55]

In order to correlate these empirical findings to theoretical models in the literature [59], FT-IR analysis was carried out on our most promising resin, HEMA by determining disappearance of the band at 1636 cm^{-1} , when compared to an internal control at 1718 cm^{-1} , using equation (2.1) to correlate degree of conversion (α) with light dosage at a given time (Figure 2.1B, 2.1C, and 2.1D).

$$\alpha = \left\{ 1 - \frac{[A_{1636\text{cm}^{-1}}/A_{1718\text{cm}^{-1}}]_t}{[A_{1636\text{cm}^{-1}}/A_{1718\text{cm}^{-1}}]_{t=0}} \right\} \quad (2.1)$$

FT-IR spectra were taken of HEMA with 5 wt% photoinitiator with samples taken at 10 s time points (Sample A26, Table 2.2). The absorbance values in Equation 1 correspond to absorption peaks of C=O and C=C bonds at 1718 and 1636 cm^{-1} , respectively. While the FT-IR analysis is not strictly necessary for evaluating the potential resins for 3D printing, it was conducted to verify that our results correspond well

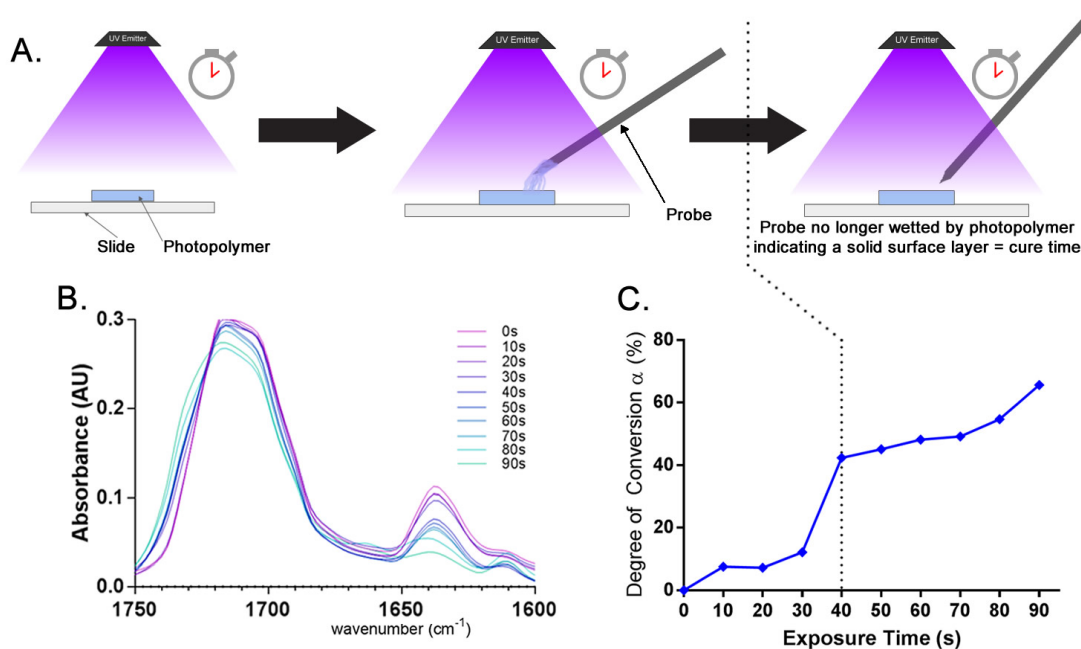


Figure 2.1: A) Procedure used for experimentally determining cure time after calibration via FTIR of a variety of photopolymer resins. B) Selected region of FTIR absorbance spectra corresponding with equation 1 for a HEMA photopolymer with 5 wt% BAPO/TPO (in a 1:1 molar ratio), C) calculated degree of conversion of (B) as a function of exposure time (s) under a 0.34 mW/cm^2 light source at 405 nm, D) raw FTIR transmittance spectra for (B) and (C), E) photograph of HEA (left) and (HEMA) samples after curing and cure time determination (scale bar 10 mm). Raw FTIR data and photographs of cured polymers can be found in Figure 2.16.

to theoretical models. Our experimental data agrees with the theoretical predictions in the literature that once a “threshold” dose of light is delivered to a volume of resin, its degree of conversion undergoes a sharp transition. [59] This threshold also corresponds to the point at which the resin turned from a sticky gel into a solid. The time required to achieve this threshold dose at a given light intensity we define as the “cure time”, which is the minimum layer exposure time for which 3D printing of the material is viable.

2.3.2 Optimization of Photoinitiator

Following identification of suitable monomers, a more comprehensive screen took place which considered photoinitiator species and concentration and pairing with an appropriate blowing agent (Table 2.2). Two PIs and combinations thereof were tested for

their amenability for curing in a traditional 405 nm SLA systems (Table 2.2). Phenylbis(2,4,6-trimethylbenzoyl)phosphine oxide (BAPO) and diphenyl(2,4,6-trimethylbenzoyl)phosphine oxide (TPO) both produced a rapid cure at 405 nm. BAPO/TPO in a 1:1 molar ratio was especially versatile and produced the best cure performance for many of the monomers tested, including HEMA. Formulations containing HEMA cured fastest when using high concentrations of PI around 5 wt% whereas 2-hydroxyethyl acrylate (HEA) formulations provided the most rapid curing at low concentrations of PI between 1-2 wt%.

2.3.3 Optimization of Blowing Agent and Foaming Resin Composition

Determining a synergistic combination of blowing agent (BA) and monomer was perhaps the most challenging aspect of resin development. After selecting HEMA as a monomer, it was necessary to select a blowing agent with a decomposition point below that of HEMA's decomposition point ($T_m = 230$ °C), but above that of HEMA's glass transition ($T_g = 70-82$ °C), while maintaining low volatility to avoid evaporation over the course of a multi-hour print. Table 2.1 summarizes a number of common blowing agents employed in industry or in literature including di-tert-butyl dicarbonate (BOC_2O), azodicarbonamide (ADC), p-toluenesulfonhydrazide (TSH), sodium bicarbonate (NaHCO_3), water (H_2O), and ethyl acetate (EA). [41, 60–62]

Many of these blowing agents are largely insoluble or difficult to stabilize as emulsions in HEMA (see results in Table 2.3). Slow precipitation of undissolved blowing agent led to inhomogeneity of prints and uneven expansion of the finished parts. While ADC and NaHCO_3 both produce copious amounts of gas, especially in the presence of activators (such as urea, citric acid and zinc oxide), they were the least soluble in all monomers found suitable for printing. TSH had better solubility but also produced the lowest volume of gas and proved unreliable as a blowing agent. Solvent-based blowing agents such as hexane, toluene, ethyl acetate or pentane exhibited high volatility and would evaporate from the resin bath prints, rendering them ill-suited for application in SLA 3D printing. Water was explored as a blowing agent, but due to its activity as a plasticizer in pHEMA, [63] it resulted in foams with very large cell sizes and/or foams which were unable to contain the expansion of resultant steam. Lowering the concentration of water resulted in insufficient and uneven expansion of the final foams.

Due to our dissatisfaction with traditional blowing agents, we sought to use a non-

Table 2.1: Composition of blowing agents explored in the current study. *When used with urea and ZnO as activators † Boils rather than decomposes.

Blowing Agent	Thermolysis temperature (°C)	Benefits	Drawbacks
BOC ₂ O	196-220 [55]	Solubility, high gas production	Toxicity
ADC	150-190* (205-215) [60]	High gas production	Insoluble in all monomers
TSH	120-130 [60]	Low decomposition temperature	Low gas production, poor solubility
NaHCO ₃	160 [61]	Non-toxic, inexpensive, high gas production	Insoluble, low gas production
H ₂ O	100†	Safe, miscible with monomers, high gas production	Plasticizer for HEMA and HEA, uneven expansion, large cell size of foams
EA	77†	Safe, miscible with monomers, high gas production	Uneven expansion, large cell size, volatility

traditional agent which is soluble in organic solvents, decomposes at low temperatures, and yields a high molar volume of gas upon decomposition. BOC₂O is soluble in many organic compounds (including neat HEMA, HEA, and MMA), thermolyzes at a low temperature (into 4 mols of gaseous products), and has recently been the subject of study both as an epoxy blowing agent [64] and also as a conjugated moiety on both poly(4-(tert-butoxycarbonyloxy)-styrene) and poly(2-(tert-butoxy-carbonyloxy)ethyl methacrylate) [55,65], but to our knowledge such polymers have yet to be employed in a 3D printing capacity. BOC₂O is not commonly employed as a polymer blowing agents due to its reactivity and reports of its toxicity in gaseous form. Because of these concerns, we evaluated the chemical compatibility for use in this application.

NMR analysis (Figures 2.7 and 2.8) revealed that BOC₂O is unreactive towards the HEMA monomer and that the solution is chemically stable when mixed for up to 1 week. Thermogravimetric Analysis (TGA) (Figure 2.12) demonstrated a two-step decomposition of the pHEMA/BOC₂O polymer with a first phase of weight loss occurring between 100-150 °C and the second phase above 160 °C consistent with the decomposition temperature of BOC₂O. [55,65,66] We attempted to assess the risks of thermolyzing

large quantities of BOC₂O by characterizing the gaseous effluents of the resultant foams to determine if any potentially toxic compounds were generated. Based on the results of the TGA, thermal expansion was conducted at a temperature of 200 °C to ensure complete decomposition of BOC₂O. GC-MS headspace analysis (Figure 2.13) found no detectable BOC₂O residue in samples of BOC₂O in pHEMA after heating to 200 °C for 10 minutes. The effluents consisted of only gaseous thermolysis products (t-butanol, CO₂, and isobutylene) and no appreciable vaporized BOC₂O was released during expansion. Nevertheless, due to the reported toxicity of BOC₂O, we erred on the side of caution and conducted all large-scale tests of this material in a vacuum oven connected to a gas scrubbing system which was repeatedly flushed before opening. An alternate approach would be to conduct expansion in a vacuum oven vented through an in-line filter of NaOH pellets or to conduct expansion in a fume hood.

We attempted to optimize and quantify the expansion ratio of small samples of foaming polymer mixtures using the test setup of Figure 2.2A: 20 μ L droplets of liquid resin with blowing agent were placed between two glass slides, one of which was coated with a non-stick polyethylene film and separated by two 120 μ m thick glass cover slips (Figure 2.2B). After exposure to light, the samples cured and were transferred to an oven preheated to 200 °C, (Figure 2.2C and 2.2D), removed from the slide, and measured to determine their expansion ratio. Samples of HEMA and HEA were also imaged under SEM (Figures 2.2E, 2.2F, and 2.2G) to demonstrate foam morphology. Tests with BOC₂O as a blowing agent are documented in Tables 2.4 and 2.1 and regularly demonstrated expansion ratios between 50-750%. Approximate foam cell size (measured via SEM using a random selection of 5 cells) appeared to correlate inversely with BOC₂O content. A subset of tests conducted with alternate blowing agents are documented in Table 2.3 and generally achieved expansion ratios between 0-200% with one formulation containing ADC achieving up to 400%, however poor mechanical properties or inhomogeneity of the materials led us to proceed with BOC₂O as a blowing agent. Figure 2.11 demonstrates the difference in expansion ratio and uniformity between selected compositions containing BOC₂O and other blowing agents.

Foams using HEA as a monomer (Figure 2.2D) cured quickly but had low stiffness and could not trap gases as well as HEMA-based foams (Figure 2.2C), thereby resulting in a lower expansion ratio. Mixtures of pHEMA using BOC₂O as a blowing agent yielded the best performance out of all combinations tested and were thus selected as the

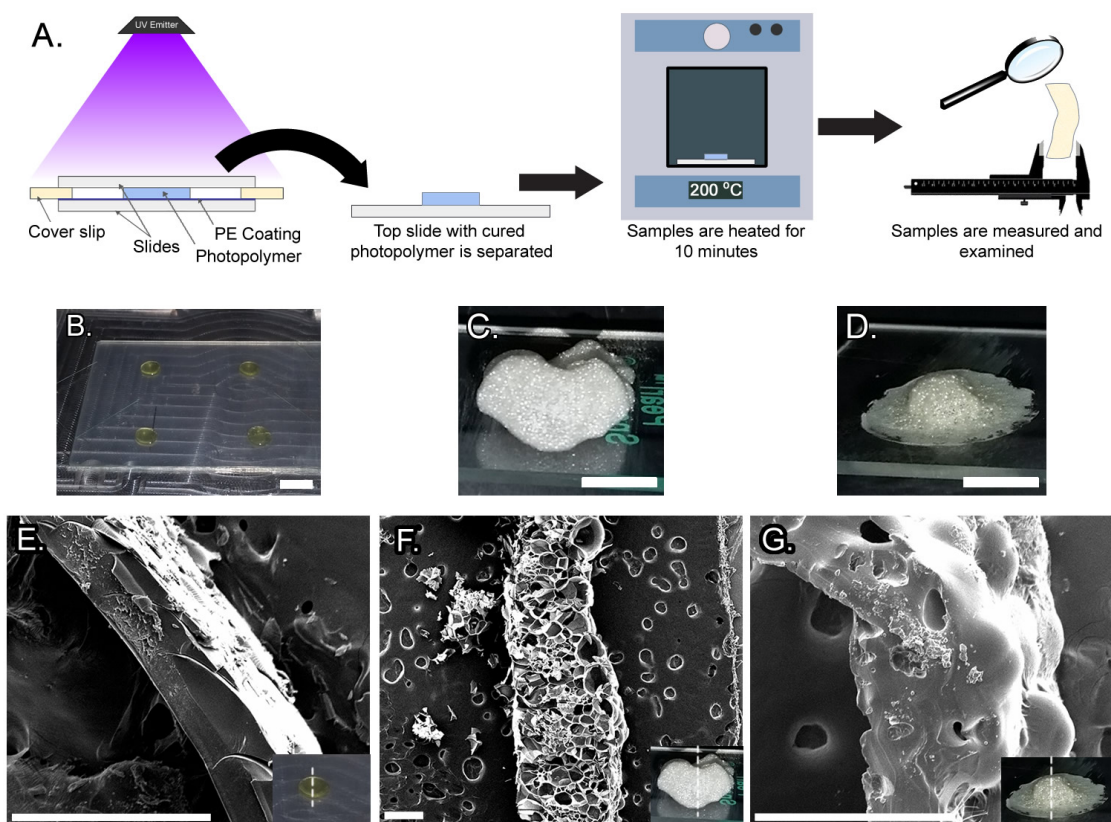


Figure 2.2: A) Procedure used for experimentally determining the expansion ratio of small samples of foaming polymer, B) photograph of unexpanded polymer samples prior to heating, C) photograph of pHEMA polymer sample containing 10 wt% BOC_2O after heating, D) photograph of pHEA polymer sample containing 10 wt% BOC_2O after heating, E) cross-sectional micrograph of unexpanded polyHEMA, 10 wt% BOC_2O under SEM, F) cross-sectional micrograph of C under SEM, G) cross-sectional micrograph of D under SEM (B, C, D: scale bars 5 mm, E, F, G: scale bars $500 \mu\text{m}$). Note: the circular pores in the backgrounds of F and G are artifacts in the conductive carbon tape adhesive rather than the foamed polymer.

baseline resins for full scale prints.

2.3.4 Characterization of the Presence and Impact of Added Crosslinkers

In order to create a polymeric foam upon heating an unconfined blend of polymer and blowing agent, we found it necessary to select a blowing agent with a decomposition temperature above that of the glass transition temperature of the polymer. It is well

documented that the addition of a crosslinker dramatically increases, and eventually altogether eliminates the glass transition temperature of a polymer. [67] Crosslinkers such as EGDMA or poly(ethylene glycol) diacrylate $M_n=575$ (PEGDA575) cured rapidly and increased the cure rate of formulations to which they were added, but reduced the expansion of resulting foams. This may be beneficial as for some applications as it offers another variable to control the expansion ratio of foams.

When crosslinkers were added to formulations consisting of 10 wt% BOC₂O in a solution of HEMA (Table 2.4, Entry C3), the addition of 0.5 wt% crosslinker decreased foam expansion by roughly a factor of 2, and the addition of 1.0 wt% crosslinker decreased foam expansion by a factor of 4-12. Addition of EGDMA resulted in a more dramatic reduction of foam expansion than addition of PEGDA575. We hypothesize that the increased glass transition temperature and rigidity of crosslinked polymers increases the viscosity of the polymer when heated to the blowing agent's decomposition temperature, thereby resulting in less deformation of the polymer as gas is released, causing higher pressure gas to build up within the softened polymer rather than expanding. Therefore, the best expansion relied on neat monomers with minimal crosslinking activity and little to no added crosslinking species. HEA has been shown in the literature to contain up to 10 wt% of intrinsic crosslinking species [57], the concentration was less than 2 wt% in our tests via GC-MS (Figure 2.14). Furthermore, we found such intrinsic crosslinking species to comprise 0.18 wt% in HEMA samples.

2.3.5 3D Printing of Expandable HEMA/BOC₂O Resin

The general process flow for the SLA 3D printing of highly expandable polymeric foams consists of modeling an object in Computer Aided Drafting software (CAD), which is then sliced into layers using software tools (Figure 2.3A). These digital slices are saved on a storage card or stick (SD) and the 3D printer projects patterns of light in the shape of the digital slices sequentially to produce a finished object at 1x scale. The part is then cleaned and supports removed, and heated at 200 °C for 10 minutes, causing the BOC₂O to thermolyze into 4 mols of gaseous products (Figure 2.3B), this expands the printed part to its final size by creating gas bubbles within the thermoplastic printed polymer part. The size of these gas bubbles and thus the ratio of expansion can be controlled digitally (by varying the height of printed layers) or chemically (by varying the BOC₂O content of the resin). Figure 2.3C shows the expansion process at a series of time points

over the course of 4 minutes.

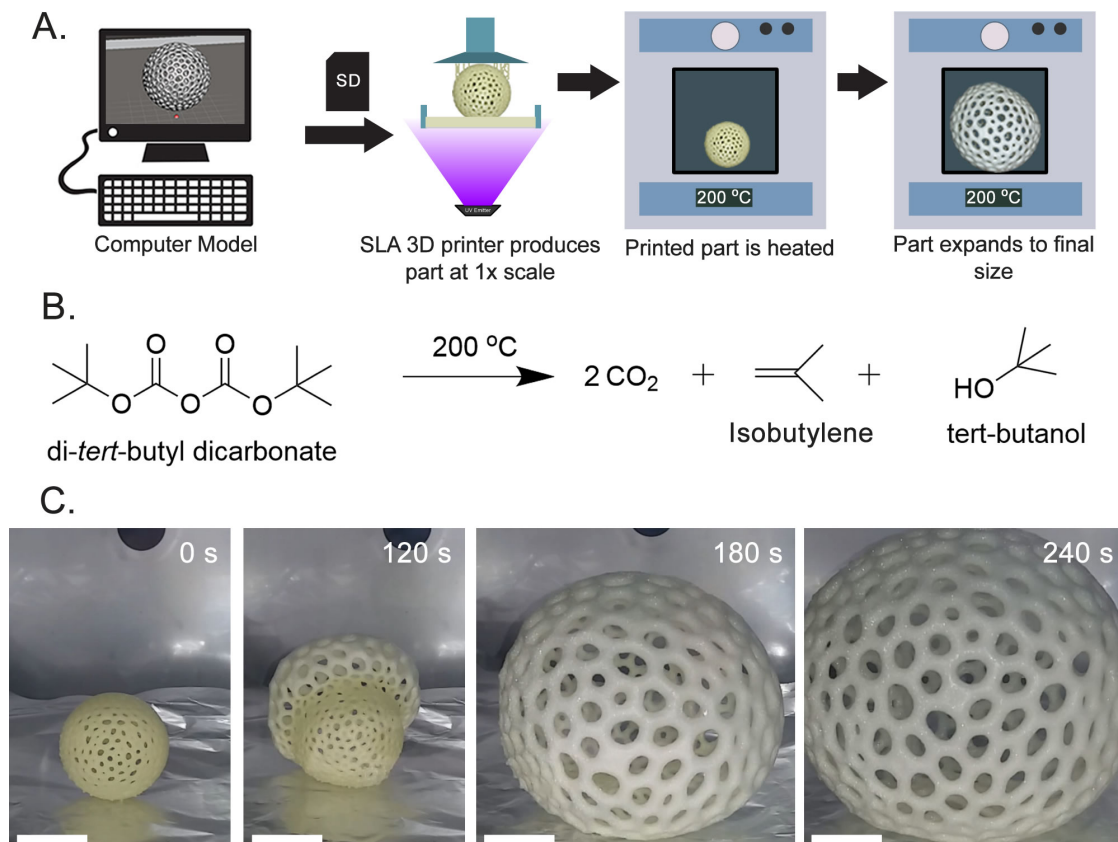


Figure 2.3: Overview of high expansion 3D printable foaming polymer A) process flow: structure is designed on CAD and exported to STL. Structure is printed at reduced scale, then heated at 200 °C and expanded to final size. B) Decomposition of BOC₂O which serves as the blowing agent for expansion. 4 mols of gas are produced per mol of solid. C) photographic time-frame images taken of a Voronoi sphere showing high expansion ratio of printed parts over the course of a 4-minute expansion (scale bars 25 mm).

This process is extremely versatile allowing a user to produce a wide variety of sample geometries including simple shapes such as cylinders (Figure 4A and 4B) and disks (Figure 4C and 4D) as well as more complex shapes such as Voronoi (Figure 4E, 4F) structures or cubic lattices (Figure 2.10). Importantly, this method demonstrates the capacity to produce objects larger than the build plate of the printer (Figure 4G). All samples in Figure 4 were produced with resin consisting of 10 wt% BOC₂O and 5 wt% of a 1:1 molar ratio of BAPO/TPO in HEMA. It was observed that objects with solid infill tended to split open or expand unevenly, and the most promising results were had with lattices, Voronoi meshes or hollow structures. It was also found that thin

structures or thin portions of structures with one or more dimensions less than 2 mm tended to expand unevenly. We hypothesize that this behavior is due to the inability of such thin segments to effectively trap gases when the polymer is heated above its T_g . Conversely, structures with thickness exceeding 10 mm in all dimensions tended to over-expand, showing splitting behavior and uneven expansion. We hypothesize that this behavior is due to gas buildup within the center of the structure leading to a high rate of expansion, this high rate of expansion causes the outer layers to undergo a ductile to brittle transition due to the non-Newtonian nature of polymers under tensile loading. [68] Thin parts (such as disks or flat plates) tended to contort and flex during expansion but most eventually righted themselves to roughly their original shape once all portions of the polymer had fully expanded. Examples of this behavior can be observed in the supplemental videos.

We found that 3D printed structures with 10 wt% BOC₂O tended to expand to a final size between 1-40x their original volume (1-3.5x original width) as shown in Figure 2.4 and 2.5. For the remainder of this work we defined a volumetric expansion ratio parameter as the following equation (2.2) where ρ_i is the initial density of the unexpanded polymer, and ρ_f is the final density of the foam after expansion.

$$\text{expansion ratio} = 100 \left(\frac{\rho_i}{\rho_f} - 1 \right) \quad (2.2)$$

Expansion of most printed parts occurred after 3-5 minutes of heating and parts expanded to their full size within 10 minutes, nucleating at a single or a few points simultaneously and conversion followed an expansion front until the entire part had been converted to foam. The reproducibility of expansion ratios of 3D printed parts was remarkably consistent, with triplicate samples usually falling within $\pm 15\%$ of the mean value (by average normalized standard deviation). To date, the largest volumetric expansion ratio of layer-by-layer structures was demonstrated by Wagner et al. (74% by density/bounding volume) [40], the current work demonstrates expansions of roughly 4000% by density, comparable with the expansion of commercial Styrofoam. [69]

2.3.6 Digital Control of Expansion Ratio and Cellular Structure

In order to examine the effect of print parameters, such as layer height and layer exposure time, on the expansion of foaming structures, cylinders (10 mm x 10 mm) were printed in triplicate from a single bath of resin (Figure 2.5A, also see Figure 2.17 for print

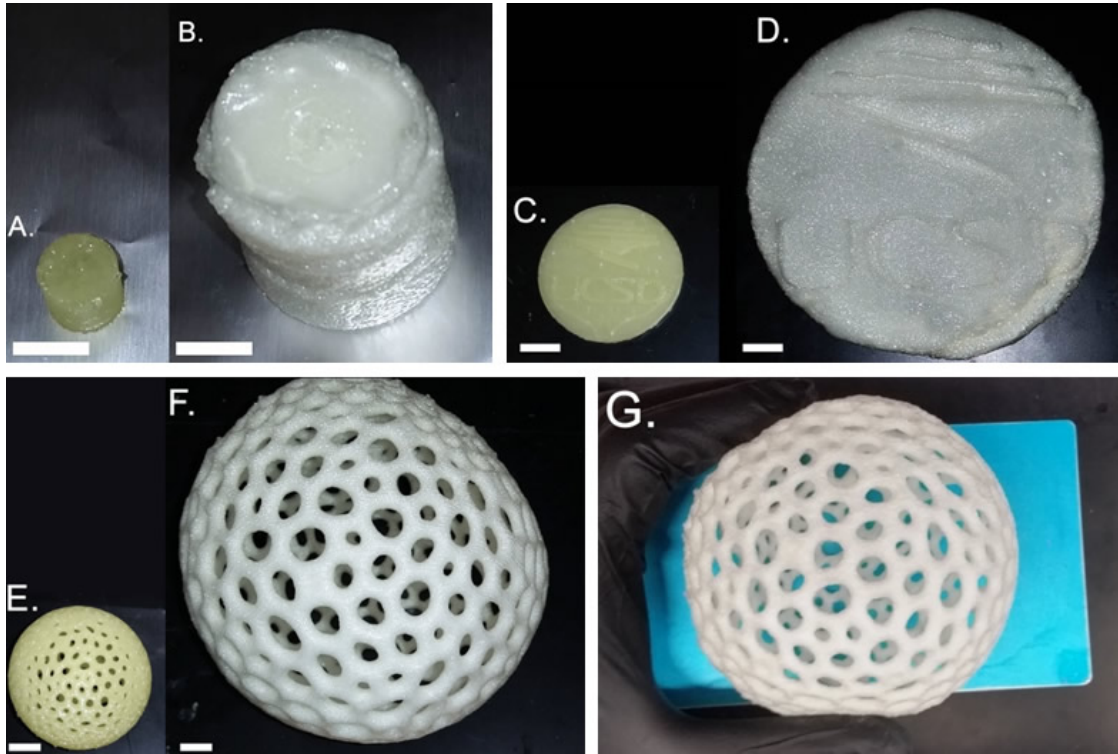


Figure 2.4: Samples shown before and after expansion at 200 °C for 10 minutes. Both samples were 3D printed with 65 s exposure at 0.18 mm layer height from the same bath of resin composed of 10 wt% BOC₂O, 2.5 wt% TPO, and 2.5 wt% BAPO in HEMA. A) 10 x10 mm cylinder before and B) after expansion, C) 35 mm diameter “puck” before and D) after expansion, E) 43 mm Voronoi sphere before and F) after expansion. G) Demonstration of the size of the voronoi sphere relative to the Anycubic build plate, demonstrating production of objects larger than the printer’s build volume. All scale bars 10 mm.

images and model design). We found that both layer thickness and light exposure time effected not only the expansion of foams after printing, but also the cellular structure of foams (open cell vs closed cell). Print parameters were studied to quantitatively determine the effect on expandable pHEMA/BOC₂O foams (Figure 2.5, 2.16).

Cylinders (10 mm x 10 mm) were printed in triplicate from a single bath of resin (Figure 2.5A). When print parameters were varied between tests it was found that the expansion ratio was most heavily dependent on layer thickness (Figure 2.5B and 2.5C) and there was no correlation between volumetric light dosage and expansion ratio (Figure 2.5D). Several samples were printed with 150 μm layer thickness and 80 s exposure time in HEMA resin with varying concentrations of BOC₂O to determine

the effect of BOC_2O concentration on expansion ratio (Figure 2.5E). The results were surprising: as expected, increasing the concentration of BOC_2O up to 10 wt% increased the expansion ratio, but increasing the concentration over 10 wt% resulted in a dramatic drop in expansion ratio and a change in structure to open cell foams (Figure 2.5F). Interestingly, a similar effect was observed when foams were printed with layer thickness below 100 μm , where the resultant foams adopted an open cell structure and showed negligible expansion (Figure 2.5B and 2.5G). These results contrasted with the closed-cell structure of all other highly expanded samples (Figure 2.5H). The open and closed cell foams were compared qualitatively by cutting them open and adding a drop of red food dye to the surface (Figure 2.5I). Due to the hydrophilic nature of pHEMA, the water-based food dye penetrated into the pores of the open cell foam; in contrast, the dye only stained the surface of the closed cell samples. Figure 2.5J summarizes our results from over 50 samples printed from a resin bath containing 10 wt% BOC_2O and printed at varying layer thicknesses and exposure times. It was necessary to maintain the layer exposure time within a window for a given layer thickness to prevent over or under-exposure of the print (both cases leading to print failure as shown in Figure 2.9), but within this window, exposure time had a negligible correlation with expansion ratio (Figure 5B). Below 100 μm layer thickness the foams formed open cell structures, and above 100 μm layer thickness, the foams formed closed cell structures and trapped gases effectively, expanding up to 40x (4000%) by volume at layer thicknesses of 150-180 μm . A general trend was observed that longer exposure times at higher layer thicknesses produced higher expansion ratios; but in making the layers thicker, one sacrifices print resolution and in making exposure times longer one greatly extends the print time.

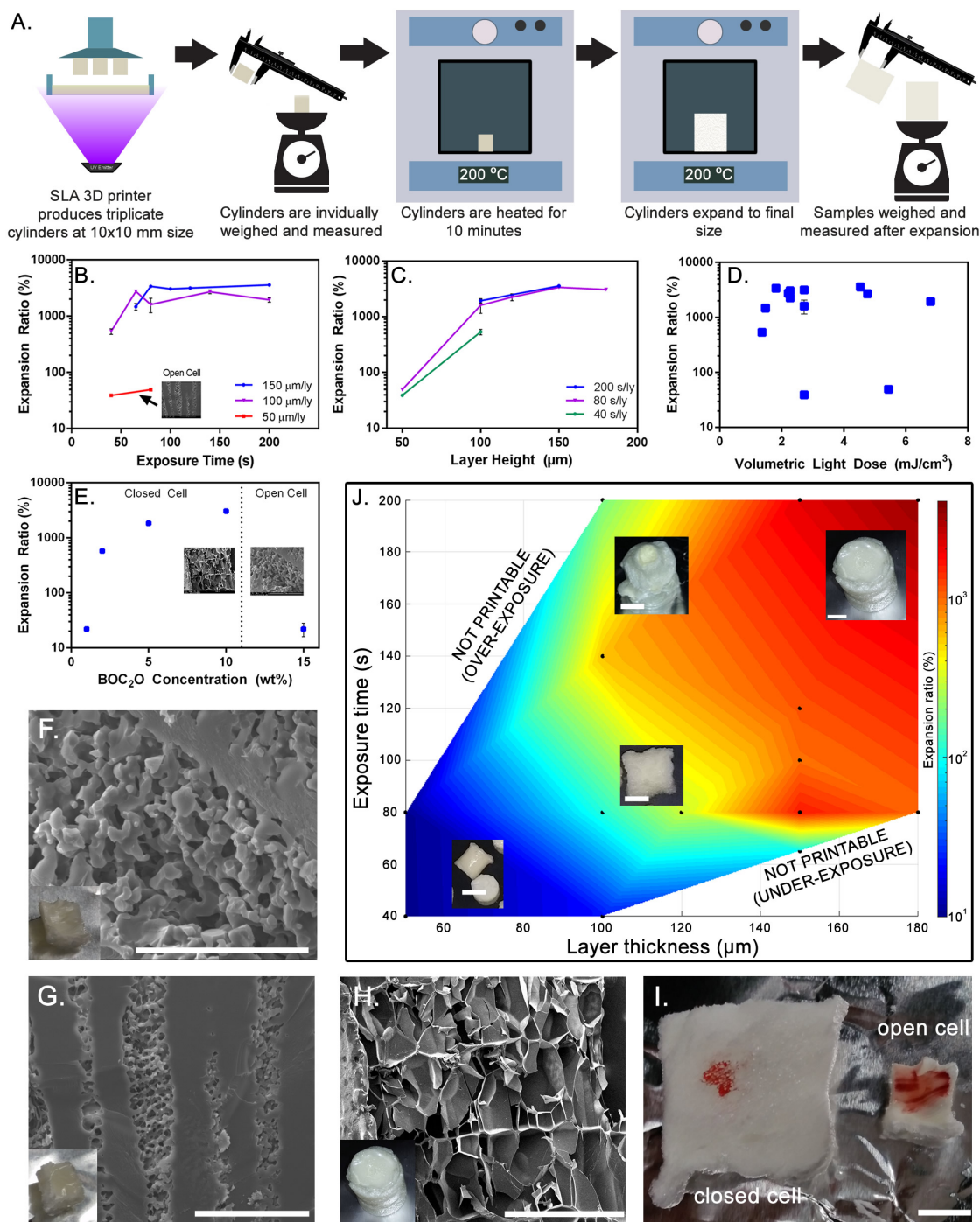


Figure 2.5: A) Diagram of the process used to evaluate the expansion ratio of various print parameters, the results of which are shown below: B) expansion ratio vs. exposure time, C) expansion ratio vs layer height, D) expansion ratio vs volumetric light dose, E) expansion ratio vs blowing agent concentration, as well as SEM micrographs of selected samples, F) 15 wt% BOC_2O open cell foam, G) 10 wt% BOC_2O open cell foam, H) 10 wt% BOC_2O closed cell foam, I) effect of red food dye on open and closed cell foams, J) 2D contour plot of exposure time and layer thickness vs expansion ratio. Scale bars: F-G) 0.1 mm, H) 1 mm, I) 10 mm, J) 10 mm

2.3.7 Mechanical Testing of 3D Printed Foams

Compression testing was conducted on samples of foamed polymer as well as the virgin polymer. All samples were triplicates of printed cylinders with diameter 10 mm, length 10 mm and printed at 80 s/layer exposure with varying concentrations of BOC₂O, and varying layer heights (Figure 2.6). Compressive loading was performed at constant strain rate of 3 mm/min and load cell sampling frequency of 5 Hz. While all tests were performed with similar strain rate and sampling frequency, we anticipate similar resultant properties at low strain rate due to the relatively low change in relaxation modulus of pHEMA with respect to time (5-10% ΔE with a time constant of roughly 500 s for unconfined compression). [70] We anticipate similar values of viscoelastic creep as a percentage difference in modulus in the expanded and unexpanded state so long as the absorption of water is negligible. However, if the pHEMA polymer does absorb water we expect this value to increase dramatically.

After heating, samples which did not appreciably expand (50 μm layer height and 0 wt% BOC₂O samples) increased in mechanical stiffness. We hypothesize that this is due to thermal curing, initiating any unreacted monomer and driving the degree of conversion close to 100% (Figure 2.6A and 2.6B). Samples which did expand experienced a drastic shift in mechanical properties, with both stiffness and density decreasing dramatically (Figure 2.6A, 2.6B, and 2.6C). In the case of 150 μm / 10 wt% BOC₂O samples, the density became comparable with that of commercial Styrofoam [69] (shown in red dotted lines, Figure 2.6D). Open cell foams which did not expand only decreased in density slightly. Overall, while the expanded pHEMA resin is not as stiff or as strong as Styrofoam, it may be advantageous for some applications where destructibility is desired, such as in a cushioning foam. During compressive testing, we found that samples exhibited a short range of elastic deformation followed by a large region of plastic deformation. Due to the limits of our apparatus we were unable to determine the ultimate compressive stress, but we suspect it to be on the order of the unexpanded foams (~ 50 MPa) due to the eventual complete compression of the foam's cellular structure. We anticipate the effect of residual stresses to be negligible after expansion due to the low glass transition temperature of pHEMA (~ 100 °C) and the length of time the pieces are held above their glass transition temperature, after which we expect all residual stresses from expansion to normalize.

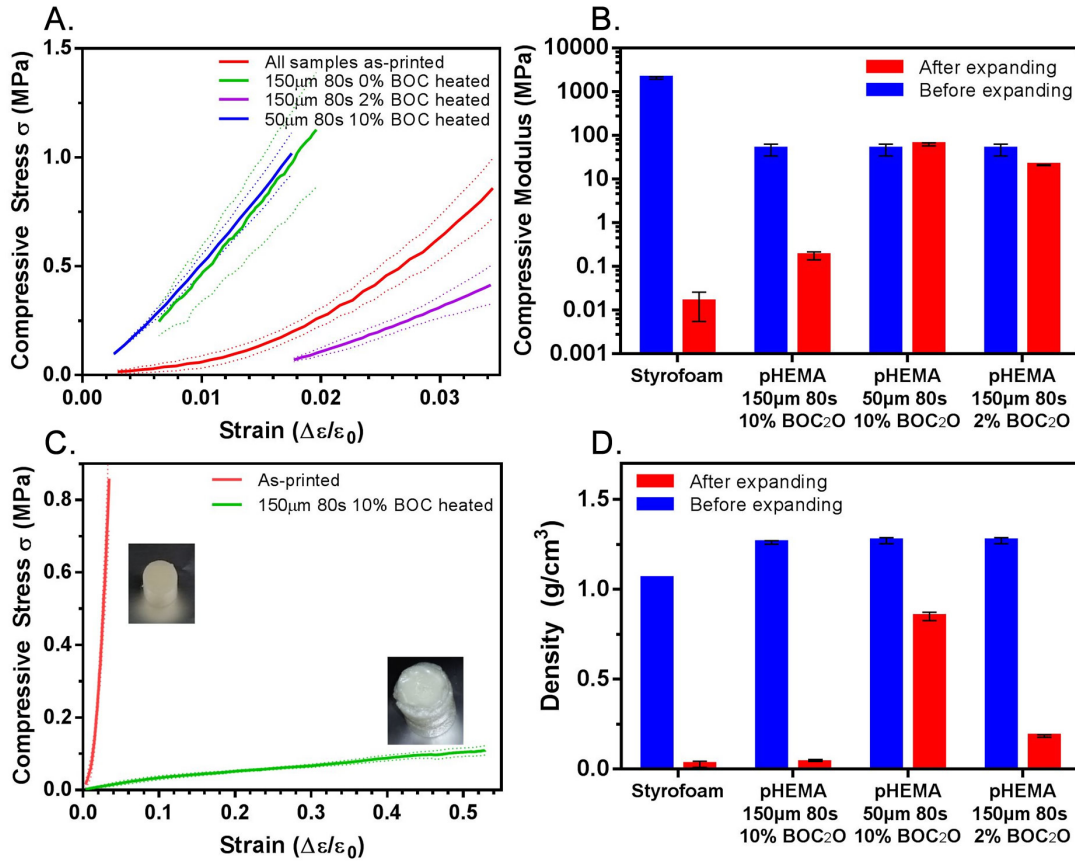


Figure 2.6: A-D) Mechanical compressive analysis and summary of physical properties of foam polymer samples prepared from a solution of 2.5 wt% TPO, and 2.5 wt% BAPO in HEMA with varying concentrations of BOC₂O and varying layer heights comparing mechanical properties before and after heating compared with that of commercial Styrofoam (shown as dotted lines on B and D). A) Mechanical stress/strain behavior of samples with low expansion ratios before and after expansion and B) summary of compressive moduli of samples before and after expansion C) mechanical behavior of a 150 μm /80s (high expansion ratio) sample before and after expansion, highlighting the large change in modulus. Data sets are shown on different axes for sake of clarity. D) Summary of changes in density before and after expansion. Studies were carried out in triplicate, dotted lines show standard error margin between sample runs.

2.3.8 Applied Technology Demonstration

Two applications for the foaming resin were explored: an expanding raft for cargo transport and an expanding airfoil for electricity generation. In the former, a structural boat hull was printed from a resin composition consisting of HEMA containing 10 wt% BOC₂O at 1x scale (8.6 cm in length) and was floated in a tank of water. Weights were

added to the floating boat until 12.7 g of mass was added, at which point it sank. The boat hull was then placed in an oven at 200 °C for 10 minutes to initiate expansion and the test was repeated with the boat hull now 28.6 cm in length. In the second test, the boat could carry over 250 g of mass, and returned to the surface (due to the trapped gasses within the foam structure) even when forcefully submerged. In the second application, a helical air turbine was designed and printed at 1x scale (3.6 cm in diameter) and was placed in front of a small fan blowing cold air at a distance of 15 cm. The helical turbine was mechanically connected via a pulley to a small DC electric generator, and the fan was turned on. The small turbine was not able to generate sufficient torque to spin the generator in the air stream. The helical turbine was then placed in an oven at 200 °C for 10 minutes and allowed to expand and the test was repeated with the turbine now 10.9 cm in diameter. In the second test, when exposed to the same conditions, the turbine generated sufficient torque to spin the generator and generate a small voltage (roughly 100 mV with no load).

2.4 Conclusion

We have demonstrated the facile formulation, chemical stability, printability, controllable expansion, controllable cell structure and selected applications for a novel, highly expandable foam material made from 2-hydroxyethyl methacrylate (HEMA) and a blowing agent, Di-tert-butyl dicarbonate (BOC₂O). We have demonstrated volumetric expansion ratios up to 4000% by volume, surpassing the state of the art by 2 orders of magnitude. The highly expandable foam developed in this work allows for the production of large objects using small amounts of precursor resin, allowing for the fabrication of structures which are significantly larger than the build volume of the printer which produced them, and which are light enough to serve as airfoils or buoyancy aids. We believe that the capability to produce such large objects from a small printer with reasonable fidelity represents a significant advancement in the design space for 3D printing, and a versatile tool for the future of manufacturing.

2.5 Experimental Section

2.5.1 Materials

Diphenyl(2,4,6-trimethylbenzoyl)phosphine oxide (TPO), 2-hydroxyethyl methacrylate (HEMA), methyl methacrylate (MMA), azodicarbonamide (ADC), di-tert-butyl dicarbonate (BOC₂O), Tween 20, poly(ethylene glycol) diacrylate, $M_n=575$ (PEGDA575), acrylic acid (AA), citric acid, and sodium dodecyl sulfate (SDS) were purchased from Sigma-Aldrich. Urea, agarose, mineral oil, ethylene glycol dimethacrylate (EGDMA), tetraethylene glycol dimethacrylate (TGDMA), poly(ethylene glycol) diacrylate $M_n=575$ (PEGDA575), sodium bicarbonate (NaHCO₃) and dimethyl sulfoxide (DMSO) were purchased from Fisher Scientific. Phenylbis(2,4,6-trimethylbenzoyl)phosphine oxide (BAPO) and 2-hydroxyethyl acrylate (HEA) were purchased from VWR Scientific. Zinc oxide (ZnO) and sodium bicarbonate (NaHCO₃) were purchased from Amazon. All liquid monomers, oligomers and crosslinkers were passed through a column of silica and basic alumina to remove inhibitors prior to use.

2.5.2 Equipment

DLP experiments were carried out in an Anycubic Photon UV LCD 3D Printer (Amazon part B07TVW9HGH). Testing of resin compositions A1-C12 employed a 3W 405 nm UV lamp mounted on a Cellink Inkredible+ bioplotter (Obtained from Cellink AB) with samples placed at a distance of 12 cm, providing an equivalent light intensity to the Anycubic Photon build chamber. The measured intensity of both sources was 340 $\mu W/cm^2$. Due to the hydroscopic nature of the HEMA monomer and effect of water as a plasticizer on HEMA which contributed to print failures, the print chamber was packed with vials of sodium hydroxide and calcium chloride to keep the ambient moisture in the print chamber to a minimum. Computer aided drafting (CAD) was performed on Rhinoceros 3D version 3 (Educational edition). Autodesk Meshmixer 11 was used to adjust and optimize STL files for DLP printing and to develop lattice and Voronoi structures from CAD files. Computer aided manufacturing (CAM) was performed via the Anycubic Photon Slicer. Foams were expanded using a Thermo Scientific Lindberg/Blue M VO914A vacuum oven (750 W heating power).

2.5.3 Instrumentation

Electron microscopy was carried out using a FEI Quanta 600 SEM and mechanical analysis was conducted on a CellScale Univert mechanical testing apparatus with 100 N load cell. Proton nuclear magnetic resonance (^1H NMR) measurements were carried out using a 600 MHz Bruker Avance III spectrometer with DMSO-d_6 and CDCl_3 solvents procured from Sigma Aldrich. Fourier Transform Infrared (FT-IR) measurements were taken using a PerkinElmer Spectrum Two FT-IR Spectrometer. Thermo-Gravimetric Analysis (TGA) was performed on a Perkin Elmer Pyris 1 TGA system with 20 L/min N_2 flow rate and 5 $^\circ\text{C}/\text{min}$ thermal ramp for polymer samples and 30 $^\circ\text{C}/\text{min}$ for BOC_2O reference sample. Gas Chromatography/Mass Spectrometry (GC-MS) was performed on a Thermo Fisher Scientific Trace 1310/TSQ 8000 Evo Triple Quadrupole Mass Spectrometer at the UCSD Environmental and Complex Analysis Laboratory. Analysis of BOC_2O decomposition products (Figure 2.13) was conducted via headspace techniques on an HP-PLOT/Q column 30 m in length 0.320 mm in diameter with 20 μm film. GC ramp consisted of a 12 minute soak at 90 $^\circ\text{C}$, 5 minute ramp to 220 $^\circ\text{C}$, and 7 minute hold at 220 $^\circ\text{C}$. Analysis of diacrylates and HEMA stability (Figures 2.14, and 2.15) was conducted on a TR-5MS liquid column 30 m in length, 0.25 mm in diameter and 250 μm film. GC ramp consisted of a 5 minute soak at 102 $^\circ\text{C}$, followed by a 10 minute ramp to 330 $^\circ\text{C}$ and 0.1 minute hold at final temperature. Liquid samples conducted on the TR-5MS column were dissolved in dichloromethane at a volumetric concentration of 0.01% which was obtained via serial dilution. A calibration curve fitting was carried out to obtain quantitative wt% values for diacrylate species. The calibration curve was derived by mixing three samples of EGDMA in a sample of HEMA at 1 wt%, 30 wt% and 60 wt%, dissolving the samples in dichloromethane at a volumetric concentration of 0.01% and correlating the integrated area of the total ion concentration peaks corresponding to EGDMA divided by the overall integrated area with the known concentration added.

2.5.4 NMR Analysis

Nuclear Magnetic Resonance (NMR) was performed on pure BOC_2O , pure HEMA, freshly prepared and 1 week old monomer/photoinitiator/ BOC_2O solutions as well as un-expanded polymer and expanded polymer samples as shown in Figures 2.7 and 2.8. Polymerized samples were cured using the Anycubic Photon at a 65 s cure time and 0.18 mm layer height and the post-expanded sample was expanded for 10 min at 205 $^\circ\text{C}$. It

is evident from the disappearance of the peak at roughly 1.45 ppm that the thermolysis of the BOC_2O during heating is complete and the presence of toxic BOC_2O in the final expanded polymer is negligible. Further analysis shows that the monomer solution is chemically stable and there is no reaction between the HEMA and BOC_2O upon mixing, although the monomer appears to be quite hygroscopic and readily absorbs water from the air.

2.6 Supplemental Figures

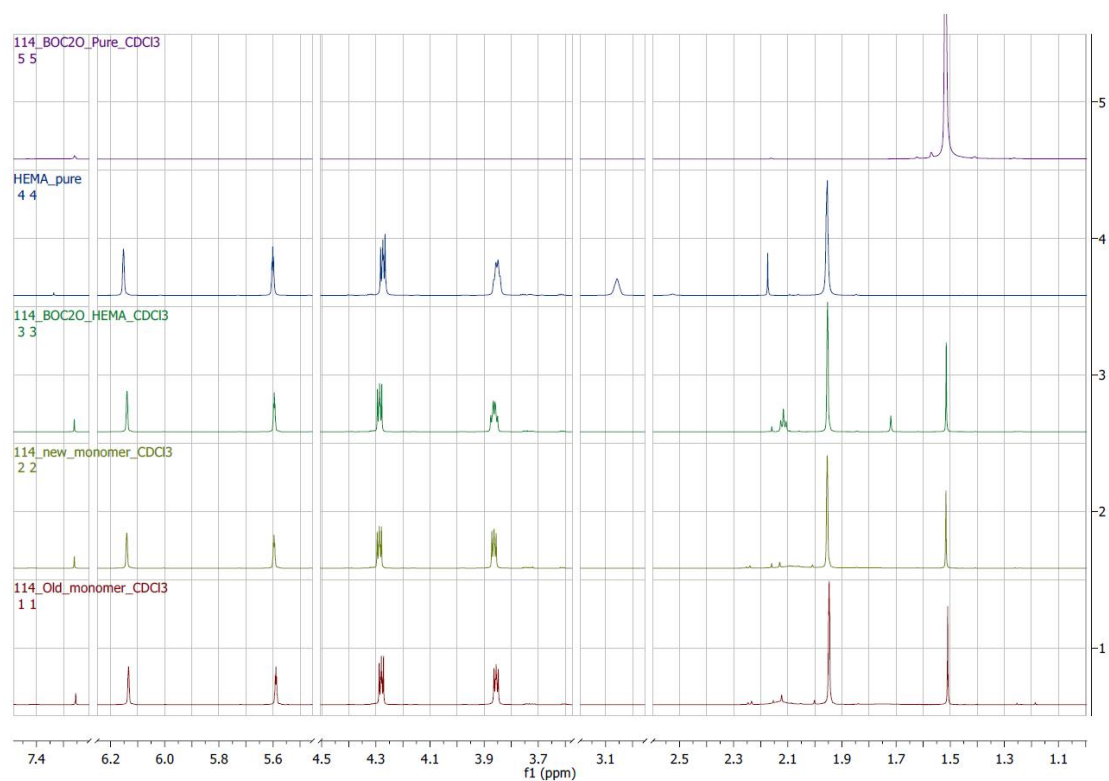


Figure 2.7: Nuclear Magnetic Resonance of samples in CDCl_3 . From top to bottom; 5) pure BOC_2O in CDCl_3 , 4) pure HEMA monomer, 3) a mixture of 10 wt% BOC_2O in HEMA, 2) a freshly prepared mixture of resin C3, 1) resin C3 after sitting in ambient air for 1 week at 25 °C.

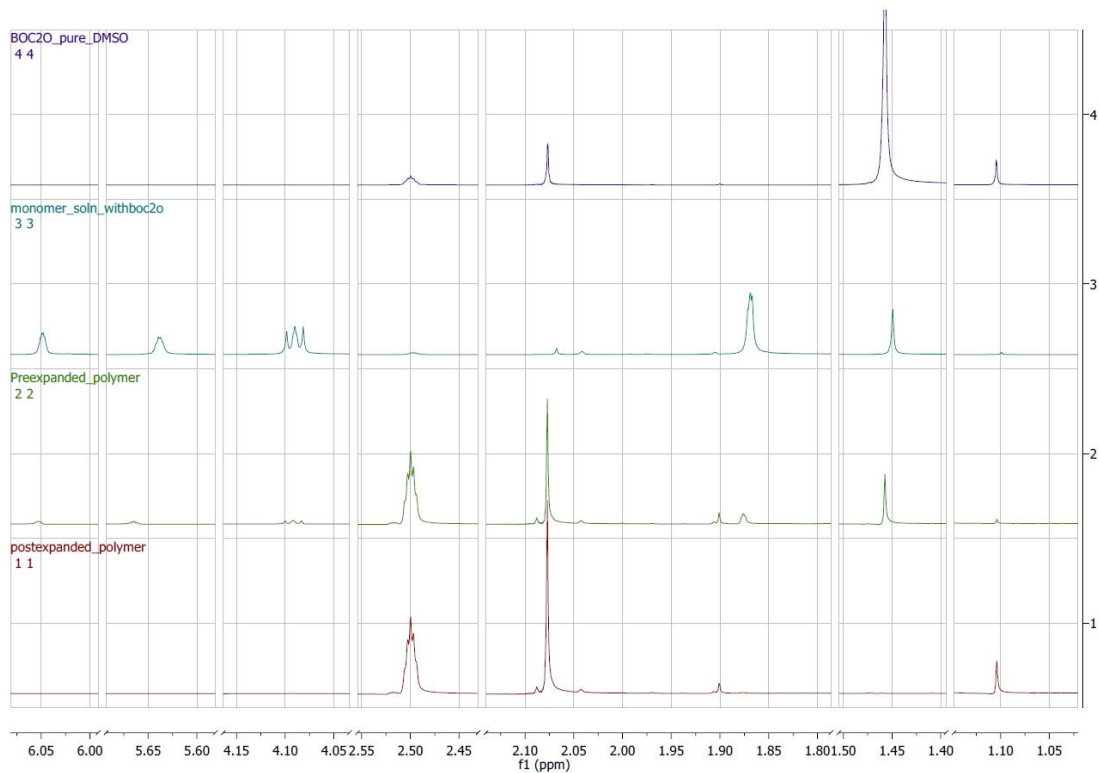


Figure 2.8: Nuclear Magnetic Resonance of monomer samples in DMSO-d₆. From top to bottom; 4) pure BOC₂O, 3) freshly prepared resin C3, 2) resin C3 after curing with 405 nm light for 65 s per layer in printer, 1) resin C3 after curing with 405 nm light for 65 s per layer in printer and expansion into a foam via heating at 200 °C for 10 min.

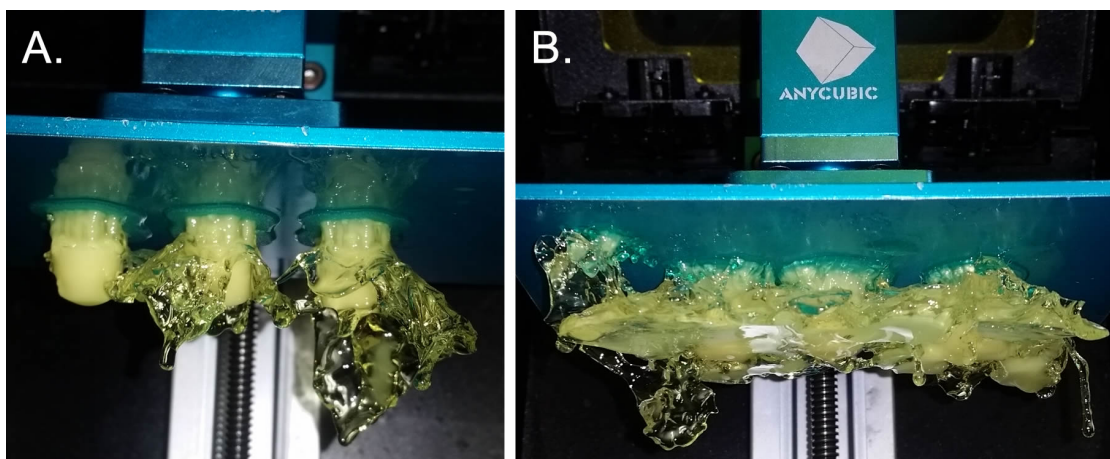


Figure 2.9: Photographs of the effect of long print times and high light doses on undesirable extraneous polymerization of the resin bath. A) The result of the same geometry printed at 5.44 mJ/cm^2 light dosage ($50 \mu\text{m}$ at 80 s/ly), and B) 8.16 mJ/cm^2 light dosage ($50 \mu\text{m}$ at 120 s/ly).

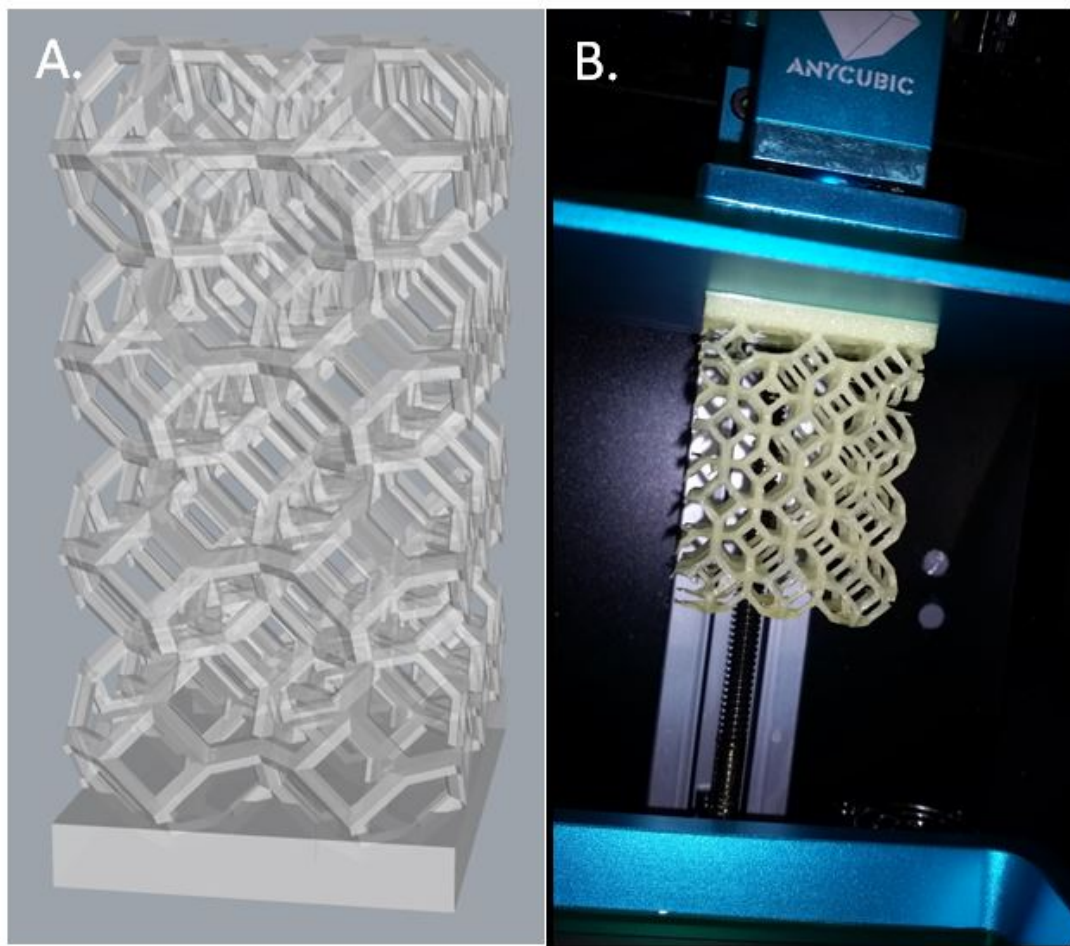


Figure 2.10: A) Computer Aided Drafting model of the ProFab Lattice shown in Rhinoceros 3D, and B) as-printed lattice shown immediately after printing in the Anycubic Photon with 0.18 mm layer height and 65 s layer exposure time. Resin composition C3.

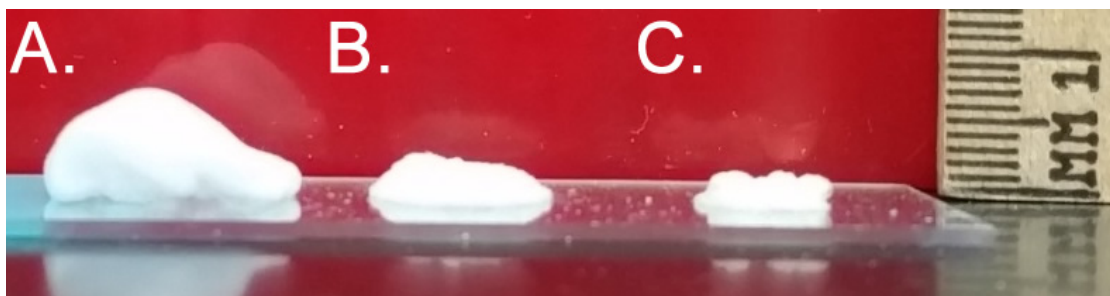


Figure 2.11: Photograph showing a comparison of selected foam samples: A) resin sample C3, B) resin sample B31, and C) resin sample B22.

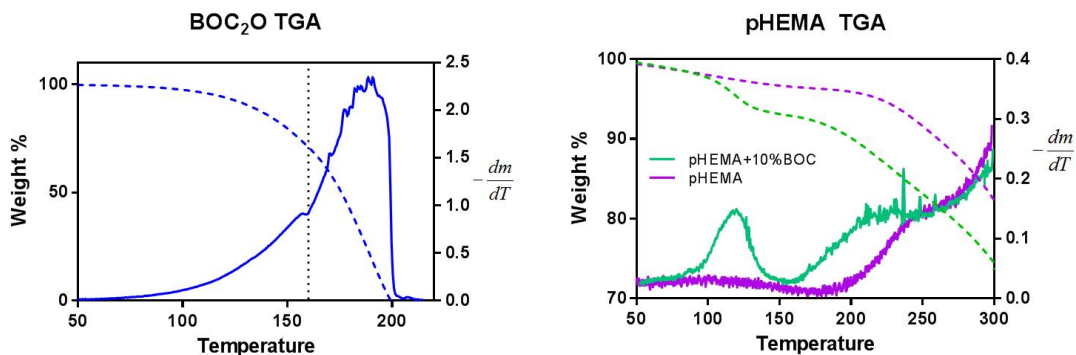


Figure 2.12: Thermo-gravimetric Analysis (TGA) of A) BOC_2O and B) polymerized HEMA samples. Dashed lines show weight% of sample, solid lines show the absolute value of the 1st derivative (change in mass) with respect to temperature. Results suggest a two-phase decomposition of BOC_2O with a first phase beginning at $\sim 100^\circ\text{C}$ where blowing agent near the outer edges of the sample vaporizes without decomposing, and a second phase at $\sim 155^\circ\text{C}$ where thermolysis of the blowing agent occurs, leading to expansion of the foam followed by a slow diffusion of t-butanol and other side products out of the thin-walled foam at high temperature.

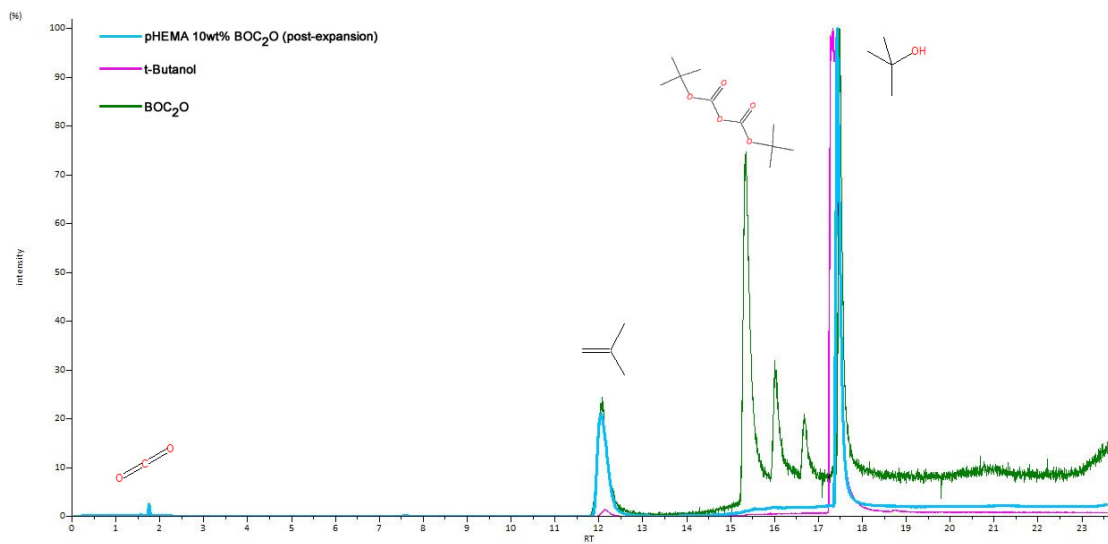


Figure 2.13: GC-MS processed chromatogram of m/z 55-57 showing retention times of BOC_2O , t-Butanol and foam sample expanded immediately prior to gas sampling via headspace.

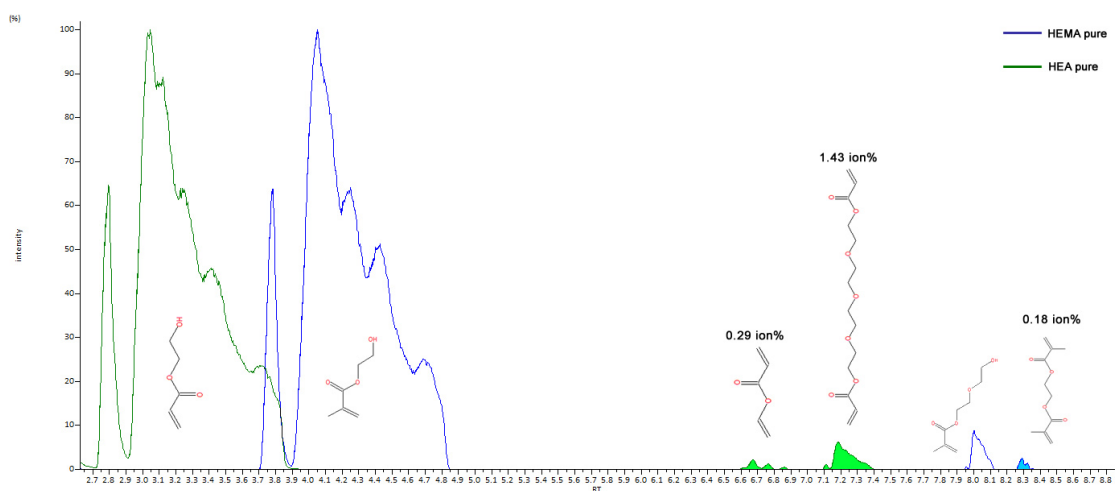


Figure 2.14: Total ion concentration vs retention time graph showing GC-MS chromatograms of as-purchased HEMA and HEA monomers. Integration was performed on diacrylate peaks of both samples to determine ion%. It is interesting to note that HEA has two peaks which were identified as diacrylate and HEMA only a single, much smaller peak.

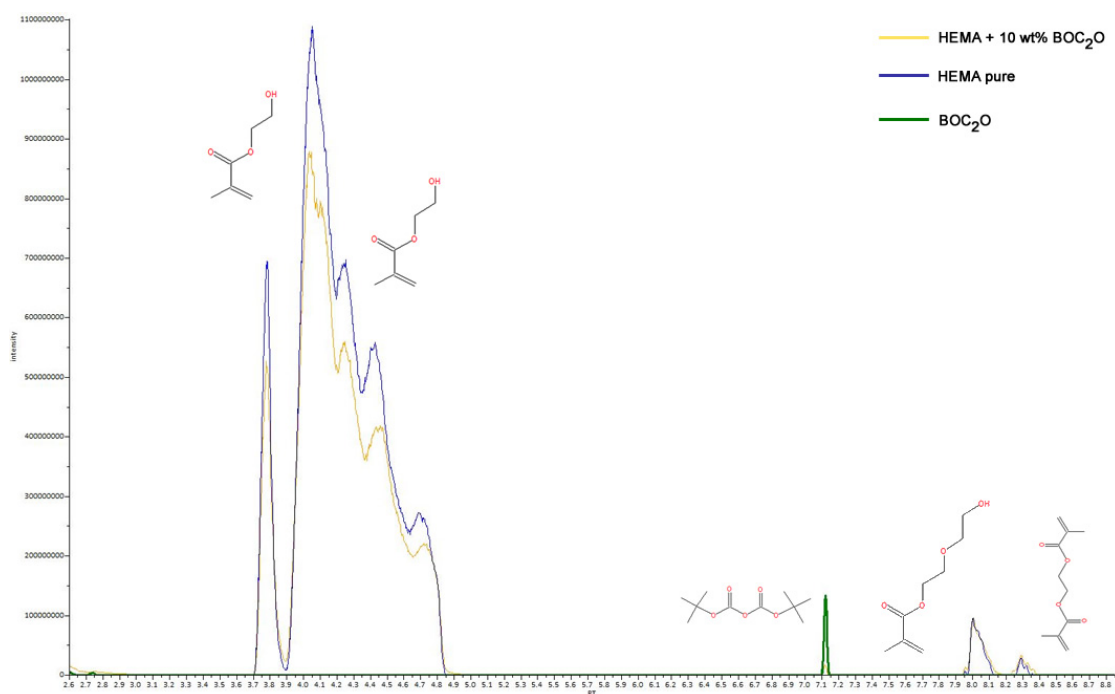


Figure 2.15: Total ion concentration vs retention time graph showing GC-MS chromatograms of HEMA + 10 wt% BOC₂O, pure HEMA and pure BOC₂O. The chromatogram backs up NMR results showing no appreciable chemical reaction between BOC₂O and HEMA at room temperature.

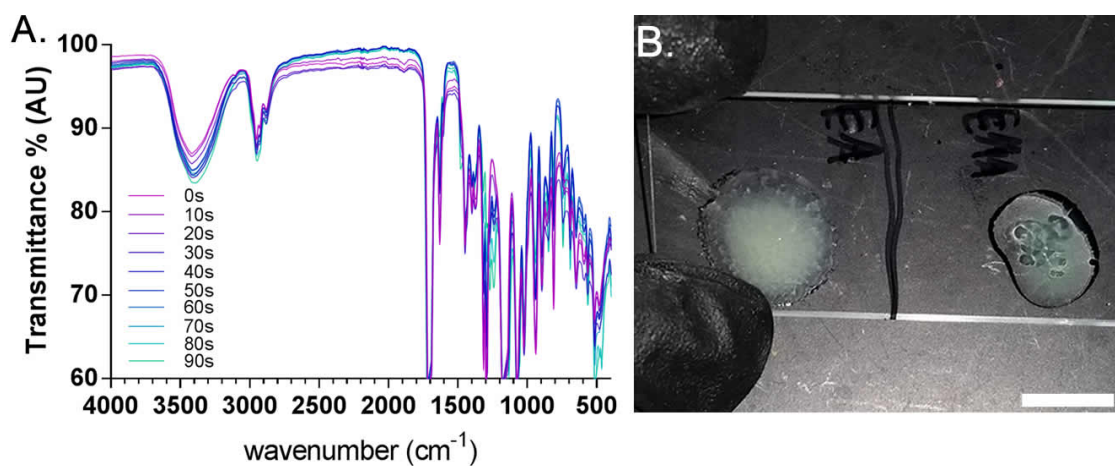


Figure 2.16: A) Raw FTIR data used in determination of cure time and B) representative photograph of HEA (left) and HEMA (right) samples after curing.

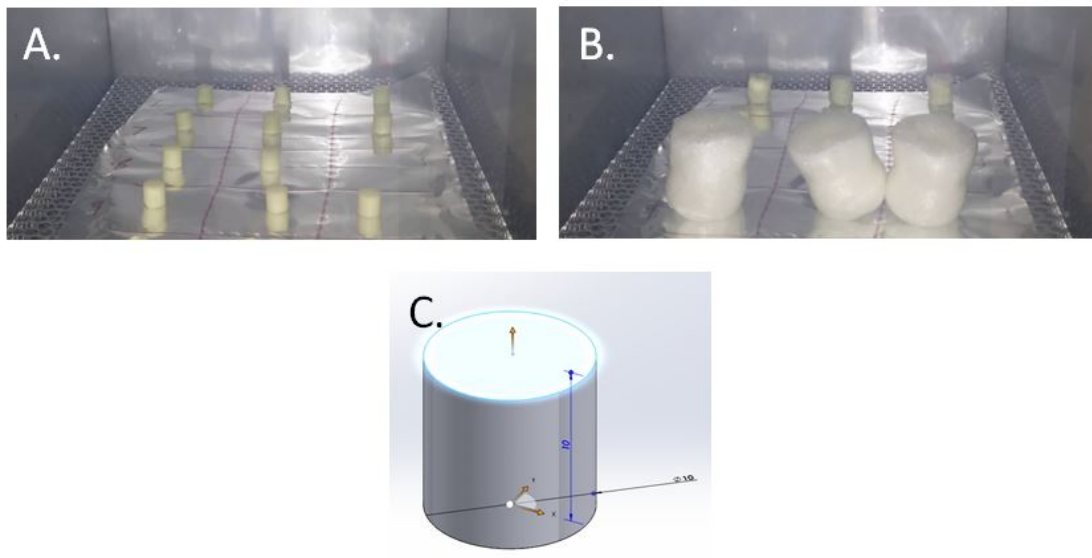


Figure 2.17: A) Examples of 10x10 mm cylindrical test samples with identical resin chemical composition (10 wt% BOC₂O, 2.5 wt% TPO, and 2.5 wt% BAPO in HEMA) printed with various parameters (i.e. layer thickness and layer exposure time) placed in an oven at 200 °C, B) the same samples after exposure to 200 °C for 240 s, and C) a computer model of the cylinder from which the parts were printed.

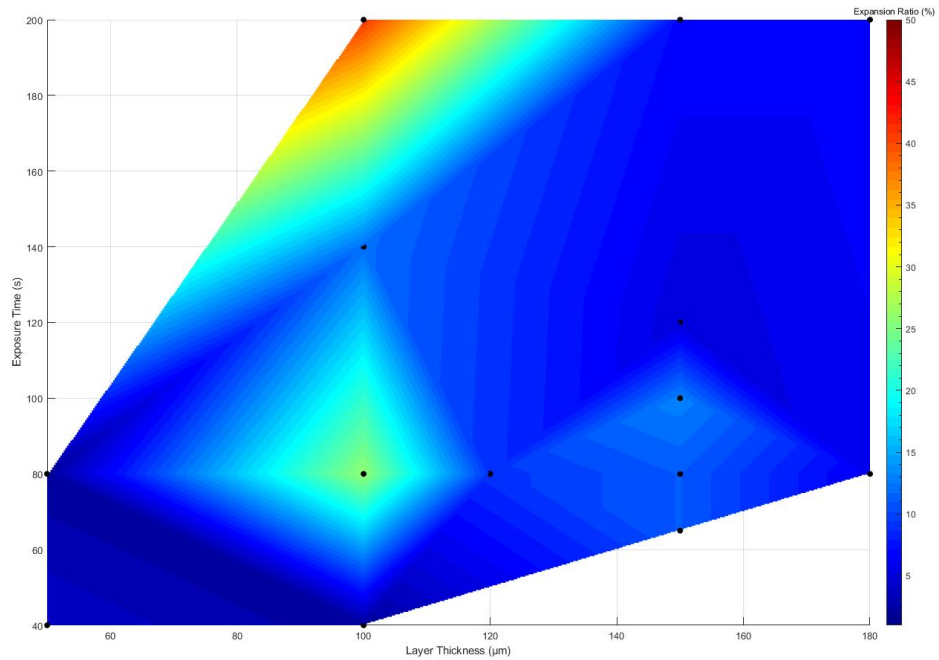


Figure 2.18: Contour surface plot of mean anisotropy of 10x10 mm cylindrical test samples after expansion. Anisotropy was computed from the following formula: $\text{abs}(\left(\frac{\text{final length}}{\text{final diameter}}\right) - \left(\frac{\text{initial length}}{\text{initial diameter}}\right))$. In the vast majority of test samples the initial l/d ratio was close to unity. We found no meaningful correlation between expansion anisotropy and printing parameters, but the results were repeatable between samples with a standard deviation between replicates less than 15%.

2.7 Supplemental Tables

Table 2.2: Composition of various samples tested for cure time in the current study

Sample #	Monomer	wt%	CL	wt%	Photoinitiator	wt%	Cure time (s)
A1	MMA	95	-	-	BAPO	5	720
A2	MMA	90	-	-	BAPO	10	540
A3	-	-	EGDMA	95	BAPO	5	20
A4	-	-	EGDMA	90	BAPO/TPO 1:1	10	30
A5	MMA	95	-	-	BAPO/TPO 1:1	5	660
A6	MMA	90	-	-	BAPO/TPO 1:1	10	205
A7	MMA	87.5	EGDMA	7.5	BAPO/TPO 1:1	5	520
A8	MMA	67.5	EGDMA	27.5	BAPO/TPO 1:1	5	110
A9	MMA	47.5	EGDMA	47.5	BAPO/TPO 1:1	5	70
A10	MMA	27.5	EGDMA	67.5	BAPO/TPO 1:1	5	35
A11	HEA	99	-	-	BAPO	1	10
A12	HEA	98	-	-	BAPO	2	5
A13	HEA	97	-	-	BAPO	3	10
A14	HEA	95	-	-	BAPO	5	15
A15	HEA	90	-	-	BAPO	10	20
A16	HEA	95	-	-	BAPO/TPO 1:1	5	10
A17	HEA	90	-	-	BAPO/TPO 1:1	10	15
A18	HEA	87.5	EGDMA	7.5	BAPO/TPO 1:1	5	15
A19	HEA	67.5	EGDMA	27.5	BAPO/TPO 1:1	5	20
A20	HEA	47.5	EGDMA	47.5	BAPO/TPO 1:1	5	25
A21	HEA	27.5	EGDMA	67.5	BAPO/TPO 1:1	5	25
A22	HEMA	98	-	-	BAPO	2	60
A23	HEMA	97	-	-	BAPO	3	50
A24	HEMA	95	-	-	BAPO	5	45
A25	HEMA	90	-	-	BAPO	10	60
A26	HEMA	95	-	-	BAPO/TPO 1:1	5	40
A27	HEMA	90	-	-	BAPO/TPO 1:1	10	55
A28	HEMA	87.5	EGDMA	7.5	BAPO/TPO 1:1	5	30
A29	HEMA	67.5	EGDMA	27.5	BAPO/TPO 1:1	5	20
A30	HEMA	47.5	EGDMA	47.5	BAPO/TPO 1:1	5	25
A31	HEMA	27.5	EGDMA	67.5	BAPO/TPO 1:1	5	25

Table 2.3: Composition of non-BOC₂O samples tested for curing time and expansion ratio in the current study. All samples use BAPO/TPO in a 1:1 ratio by weight as a photoinitiator at a 5wt% concentration unless otherwise specified. The expansion ratio of compositions is defined as the final thickness (t_f) of the foam after heating to 200 °C for 2 minutes divided by the initial thickness (t_i) of the cured polymer, expressed as a normalized percentage.

Sample #	Monomer	Blowing agent	wt%	Other components	Cure time (s)	Exp. ratio $(\frac{t_f}{t_i} - 1) * 100\%$	Notes
B1	HEMA	-	-	-	40	0	Baseline
B2	HEMA	H ₂ O	5	-	90	0	
B3	HEMA	H ₂ O	10	-	100	0	Gas escaped
B4	HEMA	H ₂ O	12.5	-	110	0	Gas escaped
B5	HEMA	H ₂ O	5	2.5% agarose	80	5	
B6	HEMA	H ₂ O	10	2.5% agarose	80	20	Good gas trapping
B7	HEMA	H ₂ O	12.5	2.5% agarose	80	40	Some gas escaped
B8	HEMA	H ₂ O	17.5	2.5% agarose	90	10	Gas escaped
B9	HEMA	H ₂ O	20	2.5% agarose	100	10	Gas escaped
B10	HEMA	H ₂ O	25	5% agarose	120	100	Good gas trapping
B11	HEMA	H ₂ O	17.5	10% Tween 20	100	0	Gas escaped
B12	HEMA	H ₂ O	17.5	10% Tween 20 + 5% agarose	100	10	Gas escaped
B13	HEMA	H ₂ O	15	5% agarose	100	100	Good gas trapping
B14	HEMA	-	-	5% agarose	80	0	
B15	HEMA	NaHCO ₃	10	5% agarose	60	75	Excellent small cell foam - NaHCO ₃ is suspended, not dissolved
B16	HEMA	NaHCO ₃	20	-	60	50	Small cell foam
B17	HEMA	H ₂ O	15	5% agarose + 3% EGDMA	60	0	No expansion
B18	HEMA	H ₂ O	15	5% agarose + 1% EGDMA	80	0	No expansion
B19	HEMA	H ₂ O	15	5% agarose + 1% EGDMA + 10% ADC	60	400	Very brittle, non-uniform foam

Table 2.3: Composition of non-BOC₂O samples tested for curing time and expansion ratio in the current study. (Cont.)

Sample #	Monomer	Blowing agent	wt%	Other components	Cure time (s)	Exp. ratio $(\frac{t_f}{t_c} - 1) * 100\%$	Notes
B20	HEMA	H ₂ O	15	5% agarose + 10% ADC	60	100	Very brittle foam
B21	HEMA	ADC	10	-	40	150	Very brittle
B22	HEMA	ADC	10	2.5% agarose	60	150	Very brittle
B23	HEMA	Ethyl Acetate	10	-	100	100	Ethyl acetate evaporates out of resin quickly
B24	HEMA	ADC	5	5% ZnO, 5% mineral oil, 5% H ₂ O	120	100	ADC/ZnO dispersed in mineral oil before adding to HEMA
B25	HEMA	ADC	5	5% ZnO, 5% mineral oil, 5% Ethyl acetate	120	100	ADC/ZnO dispersed in mineral oil before adding to HEMA
B26	HEMA	ADC	5	5% ZnO, 5% mineral oil	120	100	ADC/ZnO dispersed in mineral oil before adding to HEMA
B27	HEMA	ADC	5	5% ZnO	150	50	
B28	HEMA	NaHCO ₃	10	5% agarose, 1% EGDMA	50	0	
B29	HEMA	NaHCO ₃	20	2% H ₂ O, 10% citric acid, 1.8% Urea, 0.2% ZnO	45	50	Poor dispersion of solid species, medium cell size foam
B30	HEMA	NaHCO ₃	20	2% H ₂ O, 10% citric acid, 1.8% Urea, 0.2% ZnO, 5% agarose	35	75	Poor dispersion of solid species
B31	HEMA	ADC	10	7.5% DMSO, 2.5% Urea, 0.5% ZnO, 0.5% SDS	60	200	Good expansion of foam

Table 2.4: Comparison of formulations containing BOC₂O as a blowing agent exploring the effect of BOC₂O concentration and monomer on expansion ratio in thin films. The expansion ratio of compositions is defined as the final thickness (t_f) of the foam after heating to 200 °C for 2 minutes divided by the initial thickness (t_i) of the cured polymer, expressed as a normalized percentage. A number of compositions were prepared and tested. All compositions contain 5 wt% of BAPO:TPO in a 1:1 molar ratio as photoinitiator in a neat solution of HEMA.

Sample #	Monomer	Cross-linker	wt%	Blowing Agent	wt%	Exp. ratio $(\frac{t_f}{t_i} - 1) * 100\%$	Avg. cell size (μm)
C1	HEMA	-	-	BOC ₂ O	2	50%	1200
C2	HEMA	-	-	BOC ₂ O	5	250%	650
C3	HEMA	-	-	BOC ₂ O	10	750%	400
C4	HEA	-	-	BOC ₂ O	10	100%	200
C5	HEMA	-	-	BOC ₂ O	20	150%	75

Table 2.5: Comparison of formulations containing BOC₂O as a blowing agent exploring the effect of exploring the effect of crosslinker on expansion ratio in thin films. The expansion ratio of compositions is defined as the final thickness (t_f) of the foam after heating to 200 °C for 2 minutes divided by the initial thickness (t_i) of the cured polymer, expressed as a normalized percentage. A number of compositions were prepared and tested. All compositions contain 5 wt% of BAPO:TPO in a 1:1 molar ratio as photoinitiator in a neat solution of HEMA.

Sample #	Monomer	Cross-linker	wt%	Blowing Agent	wt%	Exp. ratio $(\frac{t_f}{t_i} - 1) * 100\%$	Avg. cell size (μm)
C6	HEMA	EGDMA	0.25	BOC ₂ O	10	600%	300
C7	HEMA	EGDMA	0.5	BOC ₂ O	10	400%	125
C8	HEMA	EGDMA	1	BOC ₂ O	10	60%	90
C9	HEMA	PEGDA575	0.25	BOC ₂ O	10	750%	450
C10	HEMA	PEGDA575	0.5	BOC ₂ O	10	350%	150
C11	HEMA	PEGDA575	1	BOC ₂ O	10	200%	75

2.8 Acknowledgements

Chapter 2, in full, is a reprint of the material as it appears in “Highly Expandable Foam for Lithographic 3D Printing”, Wirth, David M.; Jacquez, Anna; Gandarilla, Sofia; Hochberg, Justin D.; Church, Derek C.; Pokorski, Jonathan K. ACS Appl. Mater. Interfaces 2020, 12, 16, 19033–19043. The dissertation author was the primary investigator and author of this paper. This work was supported by the National Science Foundation (OISE 1844463) and the ENLACE program at UCSD which provided research support.

Chapter 3

Development and Applications of High Strength Photo-curable Polymers

3.1 Introduction

The objective of this chapter is to expand the capabilities and explore the application space of the novel technology presented in Chapter 2 by improving the mechanical properties of such foams. This chapter presents one method for strengthening these lightweight polymeric structures via aerosol spray application of a high strength, low viscosity photocurable coating. This method is free from the reliance on often complex, large, or bulky on-site equipment ordinarily required by conventional high strength spray coatings. The newly formulated photocurable resin can be applied using an ordinary cordless paint sprayer and cured using sunlight in less than a minute, enabling the rapid production of large, load-bearing structures from a small volume of feedstock and low cost portable equipment. A comprehensive screening process for resin formulations, detailed mechanical compression and tensile analysis of coated polymer structures, and an applied technical demonstration of the technology is described. In sum, the photocurable coating described herein greatly strengthens porous polymeric structures using a method which can be easily implemented.

3.2 Background

The mechanical properties of a material largely determine its application space, making the selection of the appropriate material for a task a fundamental tenant of engineering. The library of materials known or available to contemporary engineers guides the design process and defines the scale and function of the structures, tools and products we are able to construct. Another critical tenant of engineering is the ability to shape, fasten, and bond materials together. Additive manufacturing (AM) has enabled a wealth of new capabilities for modern engineers. In recent years, the advancement of 3D printing technology has gone hand-in-hand with the development of new and better AM materials. These have seen intense interest due to the relatively low cost of polymer AM systems, as well as their simplicity, scale, and the wide range of applications for parts produced via these methods.

Lab-scale 3D printing of polymers is typically enabled by two deposition technologies; thermal processing and photochemical curing. Thermal based processes are primarily centered on fused deposition modeling (FDM), which produces objects by extruding melted polymer through a heated nozzle, offering a simple and robust solution, and offering the capability to pattern a wide materials portfolio consisting of most engineering thermoplastics. Photochemical methods such as stereolithography (SLA), masked stereolithography (MSLA) and digital light processing (DLP) form parts by selectively exposing light sensitive resins to patterns of light. The materials selection of these photochemistry based printers has been historically limited compared with FDM due to the necessity of developing novel resin chemistries which rapidly cure in response to light. Thus, SLA/MSLA/DLP has been traditionally restricted to materials that undergo photo-induced radical crosslinking, primarily with olefin-based monomers. [71, 72] Parts made with SLA/MSLA/DLP are generally capable of much higher detail than FDM with minimal gradation between layers. However, perfecting the photopolymer resins for this mode of printing has proven to be more challenging than the development of filament materials for FDM printers. In recent years a number of high toughness urethane-acrylate based photocurable polymers [73] such as Siraya Tech's Blu have been developed, allowing MSLA printers to produce structures with material properties and toughness comparable to that of FDM materials.

Using high strength resins, a MSLA system such as the Anycubic Photon, costing less than \$300, can be used to produce fully dense structures with tensile strength

rivaling that of some metals (up to 60 MPa). [74] However, a glaring limitation of such MSLA systems is their limited build volume. The masking optics used in these systems generally consists of an LCD display (rather than projection optics as used in DLP or SLA printers), and is therefore rather difficult to scale past a certain point due to the challenges of producing large, high resolution LCD monitors. Furthermore, the vat photopolymerization process as a whole faces challenges due to the localized heating of the projection window as high intensity light is projected through it leading to an exothermic polymerization reaction. While such challenges have been partially addressed for DLP printing through the use of fluorinated cooling oil between the polymer and window [9], or the use of oxygen permeable windows [8] – challenges associated with scaling MSLA printers, and the structures which they can produce may still remain.

One potential avenue to create large objects quickly from a small hardware footprint is by utilizing expanding foams. [75] In chapter 2 and our prior work [76], we employed a 2-hydroxyethyl methacrylate (HEMA) / di-tert-butyl dicarbonate (BOC₂O) expanding foam resin in order to produce parts larger than the printer’s build volume. Large objects may be printed quickly at small scale, using small print hardware, and then isotropically expanded (up to 40x by volume) after printing. The resultant objects retained their expanded size indefinitely and could be used as lightweight structural forms, molds, or airfoils. The printing method developed also allows for the rapid printing of desired geometric structures much faster than similar commercial off the shelf methods such as FDM or SLA.

However, the applications for these foams are limited due to their relatively weak mechanical properties, even lower than that of expanded polystyrene foam (despite their similar densities). Comparatively, polystyrene foam has a broad range of applications due to its low cost, excellent insulating properties, ease of fabrication, low density (21-70 kg/m³), moderate compressive yield stress (0.125-1.07 MPa) [77], and high expansion ratio (20-90x). [46, 78] Expanded polystyrene foam has commonly been chosen as a material for radio controlled airplanes/drone wing airfoils due to its high strength to weight ratio. [79] However, polystyrene foam is not amenable to SLA printing due to its low cure rate and volatile blowing agents (such as pentane) which would evaporate from the resin bath during long prints. If a method could be devised to bring the strength of our HEMA/BOC₂O foaming resin up to the level of Styrofoam, it would greatly enhance its usefulness in engineering applications.

Other research groups have explored 3D printable foams using direct ink writing [47, 48], and FDM. [49–51] While foam extrusion-based systems are largely similar to existing processing methods scaled down to AM technology, the development of two-step chemical vat-polymerized expanding foams presents additional challenges. Nevertheless; isotropically expanding foams for Polyjet [40], SLA [52], and recently with DLP systems [80] have also been demonstrated. Despite the comparatively low mechanical strength of such foams, a number of research groups and commercial venture [81] have explored the applications and made improvements upon the initial formulation. However, few efforts have been made to specifically improve the mechanical strength of these printed structures and instead many groups have focused on improving the stability, biocompatibility, isotropy or a specific use case of the technology. Nonetheless, we assert that improving the mechanical properties of 3D printed expandable foams is critical in order for this technology to capitalize on its full potential as an engineering material.

Therefore, we sought to modify and iterate on our original HEMA/BOC₂O resin in order to improve its final resultant mechanical properties. We describe a high strength, low viscosity, photo-curable tris-isocyanyl acrylate (TICA)-based spray coating, and a demonstration of a potential aerospace application of the technology.

3.3 Results and Discussion

3.3.1 Advantages of Isotropically Expanded Foams

In evaluating our expanding foam, we first wanted to consider the print speed advantages of the expandable foam when compared to traditional methods such as solid or infilled objects made by MSLA and FDM respectively (Figure 3.1). A sample cube which would take 42 minutes per object on a MSLA printer (Anycubic Photon, 150 μm layers, 3 objects in 1.7 hrs print time) or 102 minutes on a FDM printer (Prusa i3 Mk3, 150 μm layers, 15% gyroid infill, 3 objects in 5 hrs print time) at 100% scale, would comparatively only take **5 minutes per sample** if printed at 29% scale (1/40th scale by volume) from expandable HEMA foam resin (Anycubic Photon, 150 μm layers, 35 objects in 3 hrs print time). This advantage is further utilized by a larger printer such as the Anycubic Mono X, which with its larger build plate and more powerful UV emitter would be capable of printing 120 simultaneous samples in approximately 2.5 hours print time, for an **effective per-sample print time of 48 seconds**.

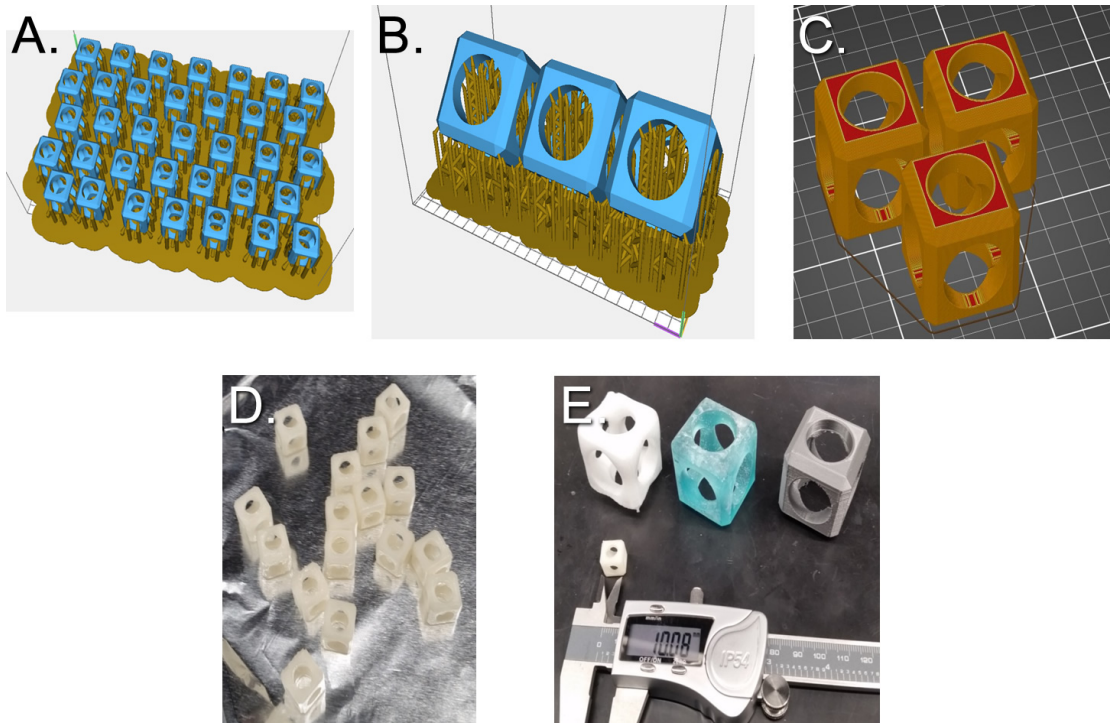


Figure 3.1: Test samples printed to assess compression strength of foam coatings. A) 29% scale compression cubes printed from baseline HEMA foam, B) pure Siraya Blu compression cubes printed at 100% scale on MSLA, C) PETG compression cubes printed at 100% scale on FDM, D) photograph of compression cubes (A) after printing and cleaning - prior to expansion, E) photograph of cubes from (A), (B), and (C) after printing and after expansion showing equivalent size of post-expanded material. Unexpanded cube shown for scale.

The advantages of an isotropically expanded foam as a method of structure production is that with this novel manufacturing method we are able to trade effective print resolution for final object volume, thus enabling the production of large objects or large quantities of objects in comparatively miniscule print times compared with traditional print methods. However, while the use of isotropically expanding foam offers engineers a great deal of flexibility in trading resolution for effective print speed, such objects are still several orders of magnitude mechanically weaker than their conventionally produced counterparts. In the current work, we attempt to remedy this disadvantage.

3.3.2 Initial Exploration of Alternate Foam Resin Compositions

Our initial explorations into improving the strength of our highly expandable HEMA/BOC₂O foams began with modification of the base monomer composition. A number of alternate monomers were explored in order to investigate their ability to trap gas and/or dissolve bismaleimide-containing crosslinker elements to improve mechanical properties. From our previous work we determined that crosslinking moieties in the initial photocuring step inhibited expansion of the resultant foam, but did not explore alternate monomers with BOC₂O anhydride as the blowing agent. In the current work we explore the incorporation of thermally crosslinking elements such as bismaleimides [82,83], blocked diisocyanates [84,85], or boc-protected amines with isocyanyl-conjugated acrylates into the foam resin in hopes that only the acrylate moieties would participate in radical polymerization during photocuring, and the stronger crosslinking moieties would not participate in crosslinking until after the foam had expanded and reached a steady state temperature of ~ 200 °C.

We also explore the use of polyurethane [86], polyurea [87–89], aramid nanofiber [90,91], and finally a bisphenol A/isocyanyl acid-based high strength acrylate coating which could be dip or spray coated onto the resultant foam after expansion.

However, many of these alternate monomers we found had either significant hydrophilicity or poor gas trapping. A summary of the various monomers is provided in Table 3.1. The results of this initial exploration concluded that HEMA remained the most promising monomer candidate for a 3D printable self-expanding foam. 4-Acryloylmorpholine (4ACM) showed promise as well, chiefly due to its rapid cure rate, but ultimately showed high anisotropy in its expansion and its gas trapping was not as favorable as the baseline HEMA monomer.

We further sought to incorporate various bismaleimide crosslinking species into the resin, for instance N,N' - (4,4' - Diphenylmethane) bismaleimide (4MBMI), but we found that the commercially procured 4MBMI had poor solubility in both HEMA and 4ACM. Derivative compounds 1,6-Bis(maleimido)hexane and 1,3- Bis (maleimido) pentane were then synthesized [92] (Figure 3.8, 3.9) to assess their solubility, material strength and expansion properties, but were ultimately detrimental to expansion in any composition that resulted in an appreciable qualitative increase in mechanical strength. Blocked diisocyanates as cross-linkers also proved problematic for expansion as well. Therefore, attention was turned to the development of a coating of high strength material

Table 3.1: List of alternate monomers explored in the current study and their respective cure times, qualitative hydrophilicity, qualitative gas trapping properties and solubility with maleimide precursors. Cure time was evaluated with a $340 \mu\text{W}/\text{cm}^2$, 405 nm light source and the cure time listed as the point at which the sample resin no longer stuck to a probe. All compositions in the table below contained 2.5wt% Phenylbis(2,4,6-trimethylbenzoyl)phosphine oxide (BAPO), 2.5 wt% diphenyl(2,4,6-trimethylbenzoyl) phosphine oxide (TPO), and 10 wt% di-tert butyl dicarbonate (BOC2O), with the remaining 85 wt% consisting of the monomer and N,N'- (4,4'- Diphenylmethane) bis-maleimide (4MBMI) at the specified wt%. List of acronyms: dimethyl acrylamide (DMAC), vinyl pyrrolidone (VP), 4-Acryloylmorpholine (4ACM), methyl methacrylate (MMA), methyl acrylate (MA), butyl acrylate (BA), hydroxyethyl acrylate (HEA), and hydroxyethyl methacrylate (HEMA).

Monomer	Cure time	Solubility with 4MBMI	Hydrophilicity	Gas trapping
HEMA	40 s	1-3 wt%	Softens in air	Excellent
HEA	5 s	1-2 wt%	Softens in air	Poor
VP	120 s	5-10 wt%	Fully water soluble	Fair
DMAC	10 s	5-13 wt%	Partially water soluble	Poor
4ACM	5 s	1-4 wt%	Softens in air	Good
MMA	250 s	5-10 wt%	N/A	Very poor
MA	60 s	2-5 wt%	N/A	Poor
BA	250 s	0-2 wt%	N/A	Very poor

which could be applied onto a finished foam structure.

3.3.3 Exploration of High Strength Foam Coating Materials

After repeated unsuccessful attempts to improve the strength of the base foaming monomeric resin, attention was turned to the application of a high strength coating to the printed structures post-expansion. The procedure for which is depicted in Figure 3.2.

Initially, we pursued a polyurea-based spray coating due to the notably high strength/toughness of commercial polyurea coatings such as LINE-X. [93, 94] However, due to the proprietary nature of the system's components and the necessity of high pressure spray equipment to adequately mix and coat structures, we found that this particular polymeric approach was counter to the initial aims of the study, namely to reduce the reliance on large, heavy and cumbersome equipment in the production of

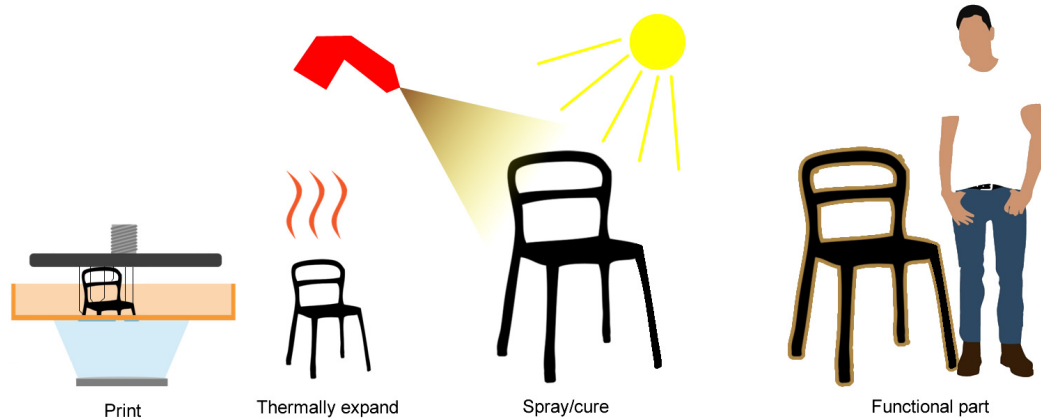


Figure 3.2: Diagram representation of our method to produce high strength 3D printable foam-based structures.

large structures on site.

Therefore, attention was turned to dip coating of photo-curable urethane-acrylate oligomers, and oligomer composites containing aramid nanofibers. Siraya Blu resin is a commercially available high strength (>50 MPa) urethane-acrylate oligomer resin which can be directly printed on commercial MSLA systems such as the Anycubic Photon. As such it possesses a rapid cure rate at room temperature under modest UV exposure. It also boasts low shrinkage, up to 32% Elongation At Break (EAB), and high toughness for a photocurable resin. However, due to its high molecular weight polyurethane oligomer content, it also possesses a relatively high viscosity (700 CPS). [74]

Initial tests explored the dip-coating of foam printed parts in Siraya Blu yielded impressive strength. However, due to the high viscosity, the material properties of such resultant composite foam structures tended to be uneven as the high viscosity coating formed a thick layer during dip coating, but then flowed and pooled at the bottom of the print during curing, leaving parts with excess coating around the bottom and insufficient coating on the top. Attempts to remedy this phenomenon by applying successive coatings (dipping and curing from alternate directions) improved the uniformity slightly, but would present serious drawbacks to the dip coating method at scale.

Nonetheless, the approach of coating parts with a high strength resin showed promising initial results and we aimed to develop a more suitable high strength coating. Figure 3.10 shows this approach: preliminary tests were conducted by casting various

compositions of photocurable resin in a nonstick-aluminum foil coated mold (Figure 3.11) in the shape of an ASTM D638-IV mini-tensile test bar with test length 20 mm, width 5 mm and thickness ~ 1.5 mm. The resin was then exposed to a UV light source of $340 \mu\text{W}/\text{cm}^2$ for 60 s, and the bars (Figure 3.12) were demolded and subjected to tensile analysis at an extension rate of 10 mm/min until failure. The results were tabulated (Table 3.2) and the promising compositions iterated upon until a suitable high toughness resin was found which exceeded the yield strength of the baseline Siraya Blu resin, at which point a larger batch of the resin was prepared and printed into a larger tensile test dogbone using the Anycubic Photon MSLA printer. This confirmatory test was then subjected to an additional tensile analysis at the same strain rate to quantitatively measure the resin's mechanical properties.

Overall we discovered that the most promising high toughness resins incorporated a mixture of stiff monomers such as 4ACM, N-isopropyl acrylamide (NIPAM), or 1-vinyl 2-pyrrolidone (VP), high strength crosslinkers such as Bisphenol A ethoxylate diacrylate (BAEDA), Tris(2-acryloyloxyethyl)isocyanurate (TICA), or bismaleimides, in addition to flexible monomers such as hydroxyethyl acrylate (HEA), or hydroxypropyl acrylate (HPA). Copolymers containing at least one component from each of these three general categories tended to produce the highest toughness resultant materials.

3.3.4 Mechanical Tensile Characterization of High Toughness S100 Resin

After preliminary tests were performed, additional confirmatory tests were carried out on high performing samples (78-84) to determine if a post-processing step could be included to augment the strength of the baseline resins. 4 sets of confirmatory samples were prepared for each formulation, each subjected to a different post-processing technique including: an overnight bake at $150 \text{ }^\circ\text{C}$, a 200 s UV post cure under $340 \mu\text{W}/\text{cm}^2$ flood illumination, and a UV post cure followed by the overnight bake at $150 \text{ }^\circ\text{C}$. The results from the follow-on study are shown in Figure 3A/B.

The results of these studies showed that the post processing method did not provide a consistent difference in mechanical performance vs. baseline cured samples. The effect of including high strength reinforcements at low concentrations was explored in Samples #19, 20, 23, 24, 25, 33, and 34. Low concentrations of reinforcements were added to a control resin (containing 33% 4ACM, 33% BAEDA, X% reinforcement, and balance HPA). The results of such tests are displayed in Figure 3.3C. Overall, the in-

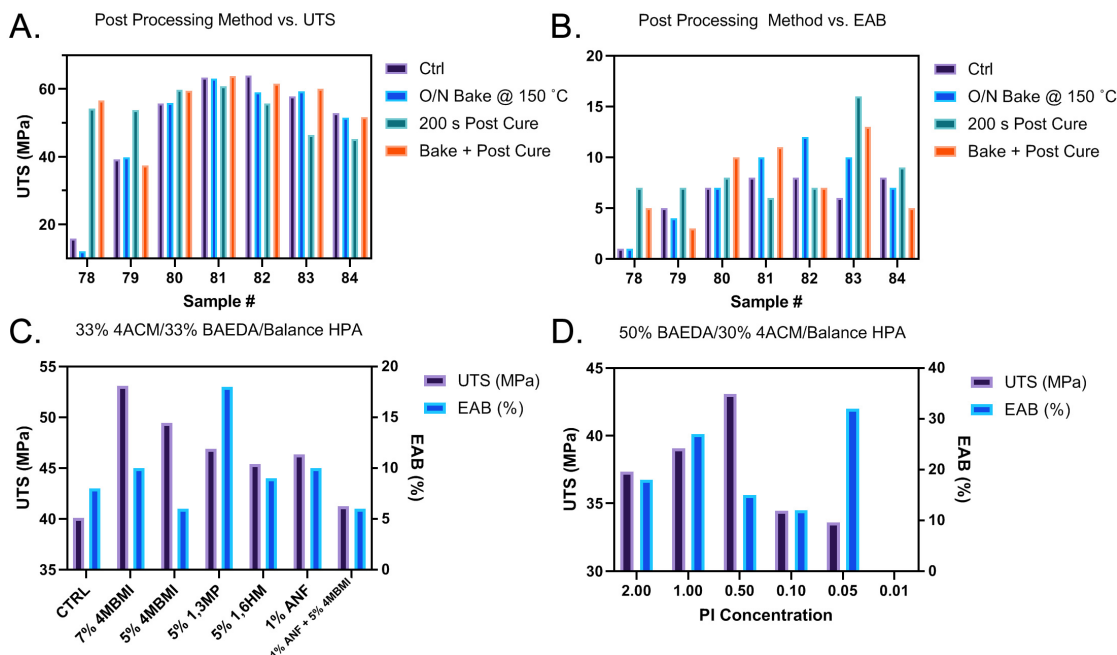


Figure 3.3: Summary of results from mechanical testing of preliminary resin samples: A) effect on post processing method vs ultimate tensile strength (UTS), and B) vs elongation at break (EAB), C) effect of the inclusion of high strength reinforcements on UTS/EAB, D) effect of PI concentration on UTS/EAB.

clusion of BMI-based crosslinkers at low concentrations showed a modest improvement in overall mechanical properties but the improvement was negated in many cases by an increase in brittleness. One exception was the inclusion of 1,3MP, which showed promise as a reinforcement, but later experiments with TICA demonstrated far higher strength improvement than the 1,3MP-based resins, while also exhibiting low viscosity (explained later) and high depth of cure (a quality which maleimide-based components tended to inhibit). Samples #50-54 (containing 30% 4ACM, 50% BAEDA, X% photoinitiator, and balance HPA) examine the effect of photoinitiator percentage on mechanical properties (Figure 3D) and our results showed that the best mechanical performance was found with the inclusion of between 1-0.5% photoinitiator. Samples with 0.01% photoinitiator failed to cure after 60 s of UV illumination. 0.5% was chosen for the majority of samples because it provided a consistent rapid cure with high strength relative to other PI concentrations. Sample 81/82 (containing 20% 4ACM, 35-40% BAEDA, 10-15% TICA, and balance HPA) showed good performance with and without post processing and overall

the most consistent performance out of all tested compositions. However both samples proved somewhat brittle and unreliable. After subsequent testing of various derivative compositions, our preliminary tests were completed after arriving at sample 100 (S100) which showed the highest strength, toughness, and most repeatable performance out of all samples.

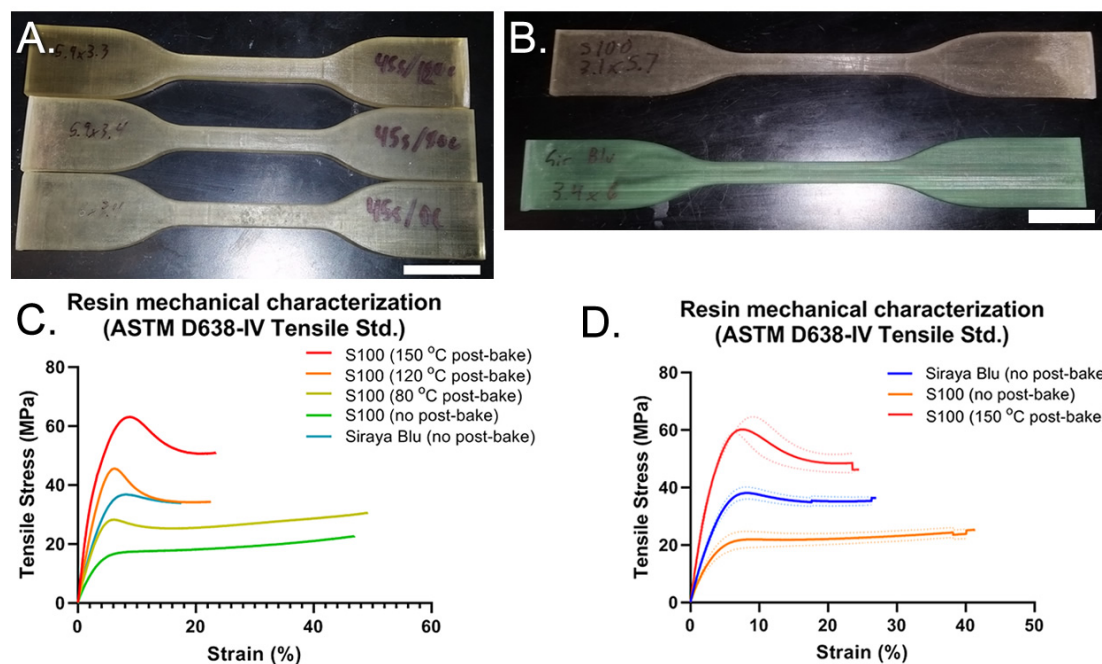


Figure 3.4: Confirmatory test samples of S100 resin printed on Anycubic photon with 50 μm layer height and A) 45s/ly with (top) 120 °C O/N post-bake, (middle) 80 °C O/N post-bake, (bottom) no post-bake, B) S100 resin printed test bar compared with Siraya Blu printed test bar, C) comparison of the mechanical performance of S100 resin with varying post-bake temperatures of samples (shown in A), D) comparison of the tensile curves of S100 resin with and without post-bake with baseline Siraya Blu Resin (shown in B). All scale bars: 20 mm.

After arriving at the S100 sample composition (Figure 3.13), confirmatory tests were performed by creating a larger batch of resin and printing test samples using an Anycubic Photon MSLA printer (Figures 3.14,3.15). Test samples were printed in the shape of an ASTM D638-IV sample test bar with test length 33 mm, width 6 mm, and thickness 3.4 mm, 50 μm layer height, and 45 s/ly exposure time. Samples were post-baked and compared with a commercial Siraya Blu resin test sample (Figure 3.4A/B). Our results showed that the ultimate tensile strength (UTS), modulus, and yield strength

of the S100 resin could be tailored via post-bake at different temperatures (Figure 3.4C). Post-bake at 120 °C or above yielded a stiffer, stronger, but slightly more brittle final resin than the commercial sample. We also demonstrated that the toughness of the S100 resin with and without post-bake (11.71 J/cm³ and 8.37 J/cm³, respectively) exceeded that of Siraya blu (7.66 J/cm³) when samples were tested in triplicate (Figure 3.4D).

3.3.5 Compression Testing of Foam/Resin Composite Samples

After arriving at a suitable resin composition that provided sufficient strength and toughness, the next task was to determine a method of application which could evenly coat large foam structures in order to maximize their strength to weight ratio and enable for the production of large functional parts with reasonable mechanical strength. Tensile testing was considered for these tests but due to the difficulty of clamping hollow tensile test dogbones and the propensity for microcracks in the material to give erroneous readings, we concluded that a compression-based study would provide more accurate data regarding the strength of high strength resin coated foams.

A compression test sample was modeled in the form of a cubic volume with chamfered sides and with a cylindrical hole cut in each face (Figure 5A). Using finite element analysis, we were able to model the surfaces of maximum load and estimate the mechanical stress on the load bearing elements from the force applied to two faces (Figure 5B) which allows for prediction of the points of failure, the stress at these points in proportion to the applied force on the top face, and to determine the effective cross sectional area at this failure point. Samples were printed from expanding HEMA foam at 29% scale ($\sqrt[3]{1/40}$), then expanded to their full size at 200 °C. The foam samples were then dip-coated with either Siraya Blu resin or S100 resin (Figure 3.5C) and were weighed, then characterized via mechanical compression to determine the total and specific strength (Figure 3.5E/F), and electron microscopy to determine the coating thickness (Figure 3.5D). Due to the difference in viscosity, a ~ 300 μm coating corresponded to 1 dip coat of Siraya Blu resin, and 3 coats of the S100 resin (each coat roughly 100 μm thick). This method of dip coating unfortunately resulted in unreliable thickness of coatings with poor reproducibility. While coating with either the S100 or Siraya Blu resin resulted in an increase in overall compressive yield strength compared with the baseline uncoated HEMA foam, the comparison of specific strength (strength per unit density) was less conclusive. We observed that a ~ 600 μm coating of either the S100 resin or Siraya Blu

resin on HEMA foam could nearly match the compressive strength of a 15% gyroid infill PETG cube printed via FDM (Figure 3.1C/E).

However, only the Siraya Blu coated foam cube could match the specific strength of the conventionally printed FDM sample. While coating with either S100 or Siraya Blu resulted in a large increase in compressive strength, only the additional coats of Siraya Blu resin resulted in a commensurate increase in specific strength. We hypothesize that this effect is due to the lack of a post-bake of the S100 resin samples. As we found in previous tests (Figure 3.4D), even though the post-baked S100 resin exhibited superior mechanical properties to the Siraya Blu, the unbaked samples were considerably weaker. When this effect is extrapolated to a thin film placed under axial loading, it is possible that the high flexibility of the unbaked S100 resin adds weight, but remains too flexible to provide a substantial increase in mechanical yield strength under compressive loading. From this we can conclude that the best way forward may be to apply a thin coat of S100 resin to achieve a lightweight structure, and if higher specific strength is required, the material may then be post-baked to increase overall strength while increasing brittleness.

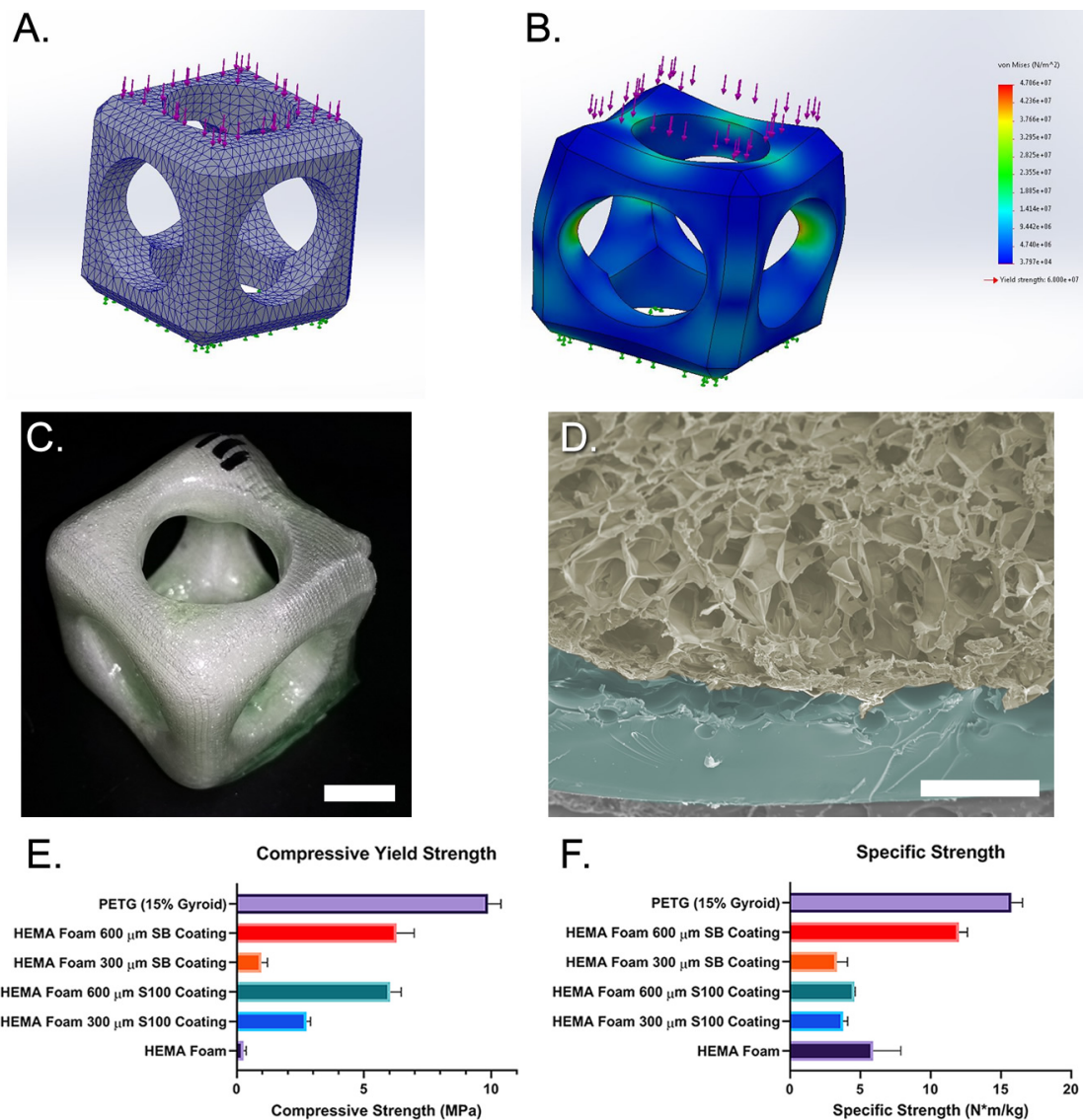


Figure 3.5: Compression test samples A) design, B) finite element simulation of stress loads, C) photograph of printed/expanded/dip coated sample cube with 2 coats ($\sim 600 \mu\text{m}$) Siraya Blu resin, D) colorized scanning electron micrograph of a section of (C) showing the underlying HEMA foam (yellow) and the dip-coated Siraya Blue resin layer (blue) which was analyzed via imageJ to confirm the coating thickness, E) comparison of compressive yield stress of sample cubes, F) comparison of specific compression strength of sample cubes. Scale bars: C) 10 mm, D) 500 μm .

3.3.6 Spray Coating of Foam/Resin Composite Samples

A spray coating method was preferred over dip coating due to the potential of sprayed coatings to cover sufficiently large surface areas of fabricated parts without the

necessity for large volumes/vats of resin to use in dip coating procedures. Modern high strength coatings (such as polyurea) already utilize a sprayed approach. However, modern high strength photo-curable resins (such as Siraya Blu) tend to be high in viscosity and would necessitate similarly high pressure equipment to polyurea sprayers in order to effectively apply such coatings to workpieces. Therefore, we pursued the creation of a coating (S100) which was low in viscosity and therefore could be applied using an ordinary venturi-based cordless paint sprayer. Moreover, we sought out to determine whether the S100 resin could be cured using sunlight as well an artificial UV source by creating 4 groups of triplicate expanded HEMA foam samples (Figure 3.6A).

- Group 1 was a control sample, expanded and uncoated.
- Group 2 consisted of cubes sprayed with a single coat of S100 resin using a commercial paint sprayer in a fume hood, then exposed to a high intensity UV light source emitting roughly $1460 \mu\text{W}/\text{cm}^2$ at a distance of 30 cm for 60 s.
- Group 3 consisted of cubes sprayed with a single coat of S100 resin outside in the shade, then once coated, the samples were moved into the sunlight to cure for 60 s.
- Group 4 consisted of cubes sprayed in the sunlight and once evenly coated left to cure in the sunlight for 60 s.

After coating and curing, the samples were subjected to mechanical compression analysis at a loading rate of 10 mm/min. A similar procedure was performed using strips of tissue paper coated with S100 resin and subjected to tensile analysis (Figure 3.16-3.18). The aim with both experiments was to determine whether sunlight could be used to effectively cure the resin coating on foam samples and to what extent sunlight as a UV light source changed the mechanical properties of the resultant composite samples.

Through these tests (Figure 3.6) we determined that the mechanical properties of S100 resin coated samples were largely indistinguishable between samples coated with resin prior to exposure to a UV source, whether that UV source was artificial or natural (Groups 2/3). Furthermore, applying a single coat of S100 resin to the expanded HEMA foam resulted in the improvement of compressive yield strength by 330-430%, surpassing the strength of Styrofoam (shown by the dotted line in Figure 3.6E/F/G). In sample groups 2 and 3, the specific strength was also improved by 19% and 16% respectively.

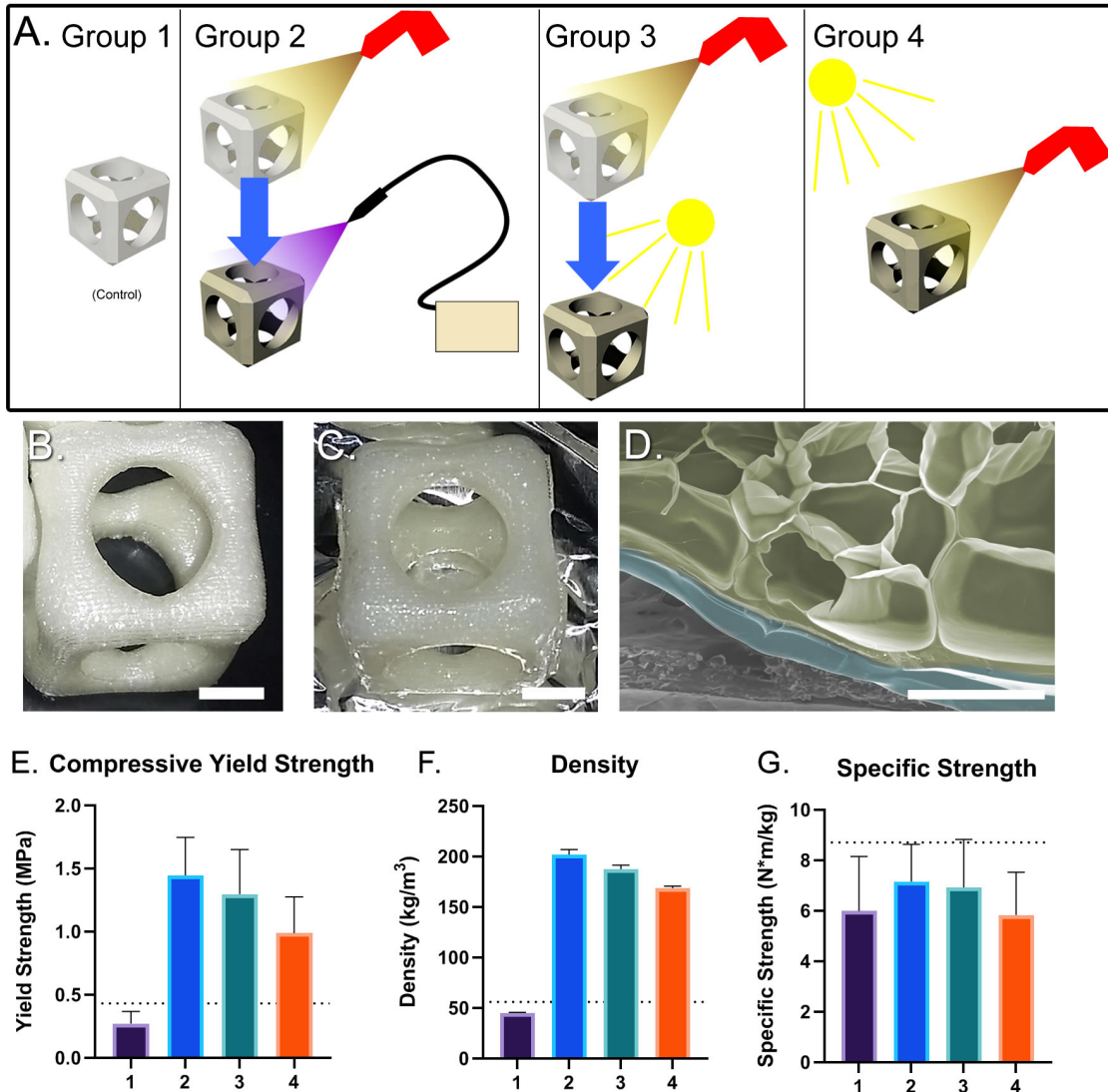


Figure 3.6: Compression testing of S100 resin. A) Sample groups used to determine the efficacy of sunlight as a UV curing light source, B) photograph of HEMA foam expanded sample cube prior to resin coating, C) photograph of group 2 S100 resin coated sample cube, D) scanning electron micrograph of the foam/coating interface of (C), E) comparison of compressive yield strength between sample groups, F) comparison of density between sample groups, G) comparison of specific strength between sample groups. Dotted line represents the literature values for expanded polystyrene foam. Scale bars: B,C) 10 mm, D) 400 μm .

There tended to be a small reduction in the strength and overall mechanical properties for samples sprayed while exposed to the sunlight (Group 4). We suspect that the diminished mechanical properties in group 4 were due to some of the sprayed S100 resin

curing in the air prior to bonding to the sample, resulting in microcracks in the coating and inconsistent bonding between partially cured droplets.

The thickness of this spray coating was relatively consistent between sample sets (Group 2: 116 ± 26 μm , Group 3: 102 ± 33 μm , Group 4: 111 ± 27 μm respectively) and no substantial qualitative differences could be observed in thickness, porosity, or surface morphology between sample groups (Figure 3.20). This increase in strength however was also accompanied by an increase in overall weight/density of the samples and therefore did not result in an appreciable increase in specific strength. It is hypothesized that subjecting the samples to a high temperature post-bake step may result in an overall increase in the specific strength. However, this post-bake step may not be necessary for applications that merely require added strength and not increase in strength to weight ratio. Furthermore, if additional strength is desired, additional coats of resin (Figure 3.21, 3.22) may simply be applied to the part until the desired coating thickness and strength is achieved.

3.3.7 Applied Technical Demonstration

A drone demonstration (conceptually based on the 3Drobotics Iris 3D printable drone) was constructed to showcase a potential application for this technology. The body of the drone was printed from expanding HEMA foam, motor mounts from Siraya Blu Clear V2 resin, and the structure coated with S100 resin.

The HEMA foam structural components were printed on a single build platform of the Anycubic Photon at 29% scale (Figure 3.7A). The parts were then cleaned and support removed (Figure 3.7B/C), and the internal surfaces of the drone body were carefully removed to leave an opening for inserting the electronics. The motor mounts required high dimensional precision and were printed conventionally from Siraya Blu Clear V2 resin at 100% scale (final configuration shown in Figure 3.7D), and were attached to the post-expanded drone body using S100 resin, then covered in masking tape prior to coating (Figure 3.7E). The parts were then coated with 6 layers of S100 resin via aerosol spray, followed by a post-bake at 120 °C for 24 hr (Figure 3.7F). Electrical components were assembled and inserted into the two halves of the drone body which was held together by nylon zip ties (Figure 3.7G/H).

While the flight test of the drone was largely unsuccessful due to poor load balancing resulting, it demonstrated that the S100 resin reinforced HEMA foam structural

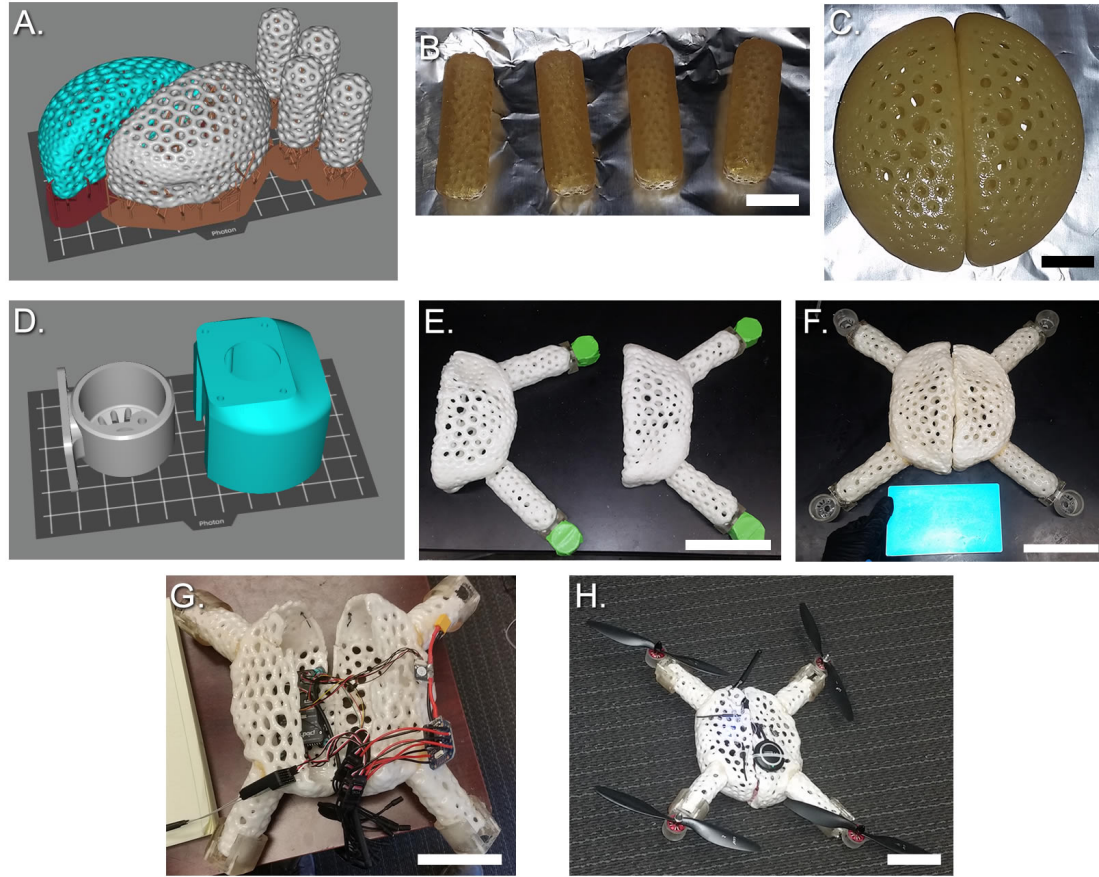


Figure 3.7: Applied technology demonstration of improved strength coating on expandable HEMA foams: A) Notional layout of HEMA foam structural components, printed on a single platform at 29% scale prior to expansion, B) photograph of pre-expanded HEMA drone legs prior to expansion, C) photograph of drone body prior to expansion, D) notional layout of conventionally printed motor mounts, E) photograph of post-expanded HEMA foam structural components prior to S100 resin coating and motor mounts masking taped to prevent undesired resin coating on those surfaces, F) photograph of full drone post-coating and after bake at 120 °C for 24 hr, original Anycubic build plate shown below for comparison, G) photograph of drone during component insertion, H) full drone secured together with electrical and flight control components attached prior to flight test. Scale bars: B-C) 15 mm, E-H) 100 mm.

members could indeed support aerodynamic loads and lift the drone body as well as its battery and control electronics (albeit briefly) off the ground. The applied technical demo also highlighted the dramatic print volume reduction capabilities of the HEMA foam (Figure 3.7A vs Figure 3.7F) to produce a self-supporting lightweight structure dramatically larger than the printer's build volume.

3.4 Conclusion

We have demonstrated a novel photocurable aerosol spray coating which may be applied to foam structural components which is capable of increasing the compressive strength of samples by up to 433% with a single layer application, or up to 2130% with 6 coating layers, as well as the UTS of composite paper samples by up to 767% with just a single layer. We have explored a wide range of alternate resin chemistries for high strength photocurable coating materials and arrived at a mixture with sufficiently low viscosity to be applied using an ordinary commercial venturi paint sprayer. Our increased strength foam samples were of sufficient strength to construct an applied technical demonstration of a functional quadcopter with a total printed volume 20x that of the printer's build volume.

The high strength coating explored in this work is able to be cured using sunlight alone with no substantial reduction in mechanical properties. Such properties can be tailored to a desired application through the use of post-baking of the coating at varying temperatures. The use of this coating and the associated technique of employing sunlight-curable resin reinforcement enables the construction of lightweight structures in resource constrained environments. Such structures retain sufficient mechanical properties to bear aerodynamic loads and may find applications in wind power generation or other applications where a lightweight expandable structure is needed. We believe that the capability to produce large objects from a small printer with improved mechanical properties will broaden the application space for isotropically expanded 3D printed foams, and provide another tool in the repertoire of future manufacturing engineers.

3.5 Experimental Section

3.5.1 Materials

Phenylbis (2,4,6 - trimethylbenzoyl) phosphine oxide (BAPO, # 511447), Diphenyl (2,4,6 - trimethylbenzoyl) phosphine oxide (TPO, # 415952), and di-tert-butyl dicarbonate (BOC_2O , # 34660), Hydroxypropyl acrylate (HPA, # 370932), Bisphenol A ethoxylate diacrylate $M_n=512$ (BAEDA, # 412090), dimethyl acrylamide (DMAC, # 274135), N-isopropyl acrylamide (NIPAM, # 415324), methyl methacrylate (MMA, # M55909), methyl acrylate (MA, # M27301), and butyl acrylate (BA, # 234923) were purchased from Sigma-Aldrich and used as received. 2-hydroxyethyl methacry-

late (HEMA, # 128635), was purchased from Sigma-Aldrich and was passed through a column of silica and basic alumina to remove inhibitors prior to use.

N,N'-(4,4'-Diphenylmethane) bismaleimide (# B110925G) and 4-Acryloylmorpholine (4ACM, # A0841500ML) were purchased from Fisher Scientific and used as received. 1-vinyl-2-pyrrolidone (# TCV0026), Tris(2-acryloyloxyethyl) isocyanurate (TICA, # TCT2325), and hydroxyethyl acrylate (# H11645) were purchased from VWR Scientific and used as received. High strength DLP printer resin (Siraya Blu Urethane blend, Siraya Fast Black, and Siraya Simple clear blend were purchased from Amazon (# B089SLXDFH, # B084JPQTRT, and # B084J71JL6 respectively) and used as received. Non-stick aluminum foil was purchased from Amazon (# B09F8PHR1L). A sample of bisguaiacol F diacrylate (BGFDA) was received as a powder from the Korley Research Group at the University of Delaware, and was dissolved in HPA in a 1:1 (by weight) stock solution prior to testing.

The electrical components for the drone: brushless motors 2212 size (# B075D-D16LK), brushless ESCs 30A (# B09MDYS235), Pixhawk flight controller (# B07NRM-FTXL), propellers (# B0823NNTKD), and a radio transmitter/receiver (# B07Z8VCB-45) were purchased from Amazon. Mission planner software version 1.3.76 was used to calibrate the Pixhawk firmware and provide remote telemetry and monitoring for the drone.

3.5.2 Equipment

MSLA printing experiments were carried out in an Anycubic Photon UV LCD 3D Printer (Amazon #B07TVW9HGH). Some samples were printed on a large format Anycubic Mono X 4K LCD 3D Printer (B08JGH83VS). Testing of resin compositions employed a 2W 395 nm UV lamp (Amazon #B07Q8Q2FQK) with samples placed at a distance of 12 cm, providing an equivalent light intensity to the Anycubic Photon build chamber of roughly $340 \mu\text{W}/\text{cm}^2$. High intensity UV illumination for large coatings was provided by an Omnicure Model S1500 standard filter 320 - 500 nm UV light source system, which provided roughly $1460 \mu\text{W}/\text{cm}^2$ at a distance of 30 cm. Sunlight was used as a UV source between the hours of noon to 3 pm in the months June-July in San Diego, CA.

An 800 mL, 18V Portable Cordless Spray Paint Gun (Amazon # B08VNWN19C) was used to coat foam structures with an even coating of photocurable resin. Computer

aided drafting (CAD) was performed on Rhinoceros 3D version 3 (Educational edition). Autodesk Meshmixer 11 was used to adjust and optimize STL files for DLP printing and to develop lattice and Voronoi structures from CAD files. Computer aided manufacturing (CAM) was performed via the Anycubic Photon Slicer and Photon Workshop 64. Foams were expanded using a Thermo Scientific Lindberg/Blue M VO914A vacuum oven (750 W heating power) set to 205 °C.

3.5.3 Instrumentation

Electron microscopy was carried out using a FEI Quanta 600 SEM and FEI Apreo LoVac FESEM. Mechanical analysis was conducted on an Instron 5982 test frame with 100 kN load cell. Proton nuclear magnetic resonance (^1H NMR) measurements were carried out using a 600 MHz Bruker Avance III spectrometer with DMSO- d_6 and CDCl_3 solvents procured from Sigma Aldrich.

3.5.4 Synthesis of 1,6-Bis(maleimido)hexane

Synthesis of 1,6-Bis(maleimido)hexane was carried out via the reaction of maleic acid anhydride with 1,6-diaminohexane via a procedure based on the scientific literature. [92] 29.05 g (0.25 mol) of 1,6-diaminohexane and 49.0 g (0.5 mol) of maleic acid anhydride were added to 150 mL of dry DMF under strong stirring which was continued for 30 minutes after the addition. 102.0 g (1 mol) of acetic anhydride, 10.0 g of triethylamine, and 0.5 g of nickel (II) acetate catalyst was added to the reaction mixture and over the next 5 minutes, the mixture turned dark brown. The mixture was kept at 90 °C for 30 min, after which the solution was cooled to 40 °C, and poured into 2 L of iced water and stirred to precipitate a brown powder which was filtered by suction, washed twice with cold water. The product was then dissolved in 700 mL of acetone, dried with magnesium sulfate and filtered once more. The acetone was removed by rotary evaporation to yield a beige powder which was analyzed with NMR to confirm intended product.

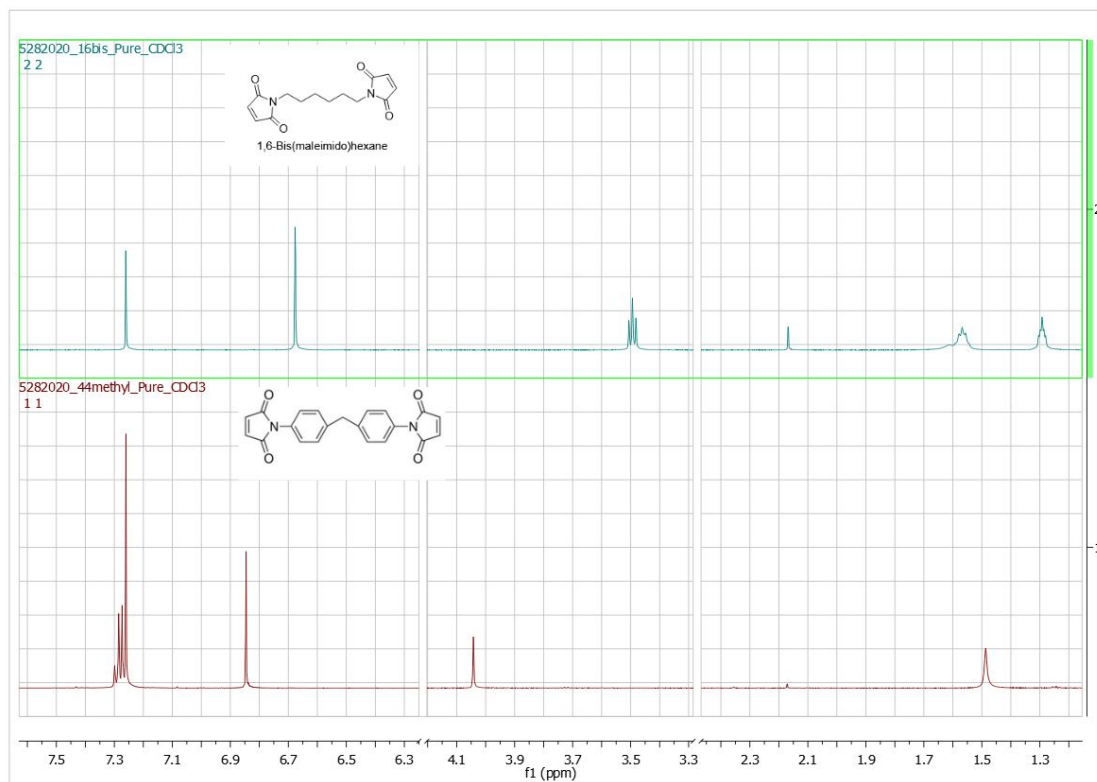


Figure 3.8: Nuclear Magnetic Resonance of synthesized (top) 1,6-Bis(maleimido) hexane and (bottom) commercial N,N' - (4,4'- Diphenylmethane) bismaleimide in CDCl₃.

3.5.5 Synthesis of 1,3-Bis(maleimido)pentane

Synthesis of 1,3-Bis(maleimido)pentane was carried out in a similar fashion as 1,6-Bis(maleimido)hexane. 25.5 g (0.25 mol) of 1,3-diaminopropane (Dytek EP diamine) and 49.0 g (0.5 mol) of maleic acid anhydride were added to 150 mL of dry DMF under strong stirring which was continued for 30 minutes after the addition. 102.0 g (1 mol) of acetic anhydride, 10.0 g of triethylamine, and 0.5 g of nickel (II) acetate catalyst was added to the reaction mixture and over the next 5 minutes, the mixture turned dark brown. The mixture was kept at 90 °C for 30 min, after which the solution was cooled to 40 °C, and poured into 2 L of iced water and stirred to precipitate a brown liquid which was extracted with DCM, then rotary evaporated to yield a brown oil. The brown oil was recrystallized in hexane and a beige crystalline solid was recovered which was analyzed with NMR to confirm intended product.

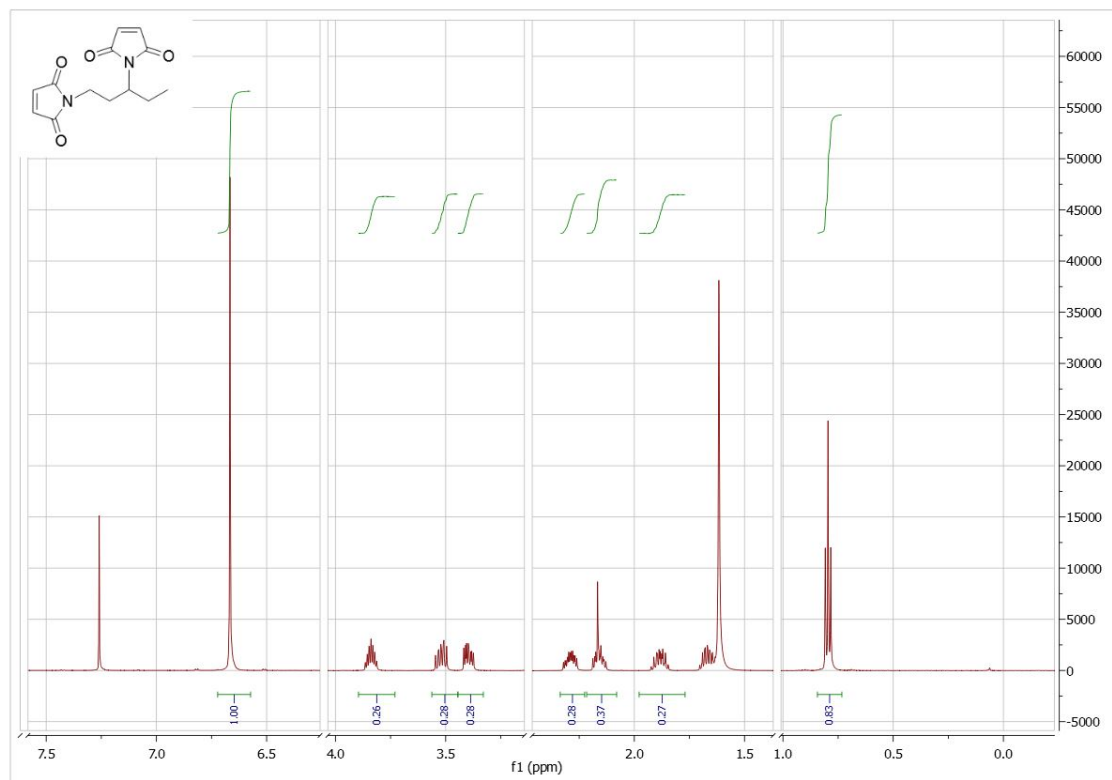


Figure 3.9: Nuclear Magnetic Resonance of synthesized 1,3-Bis(maleimido)hexane in CDCl₃.

3.6 Supplemental Figures

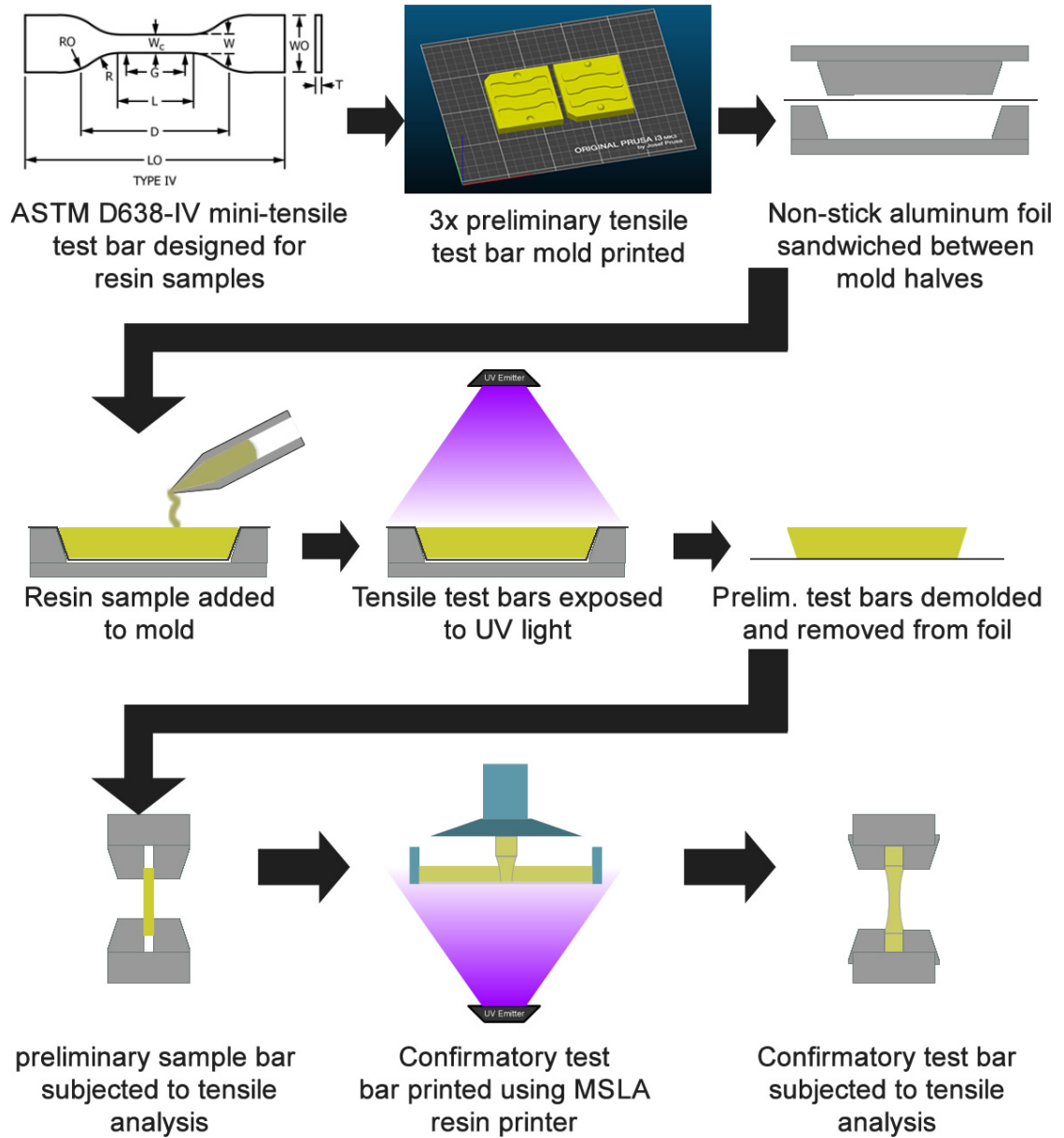


Figure 3.10: Method of testing and optimizing various coating chemical compositions for optimal mechanical properties.

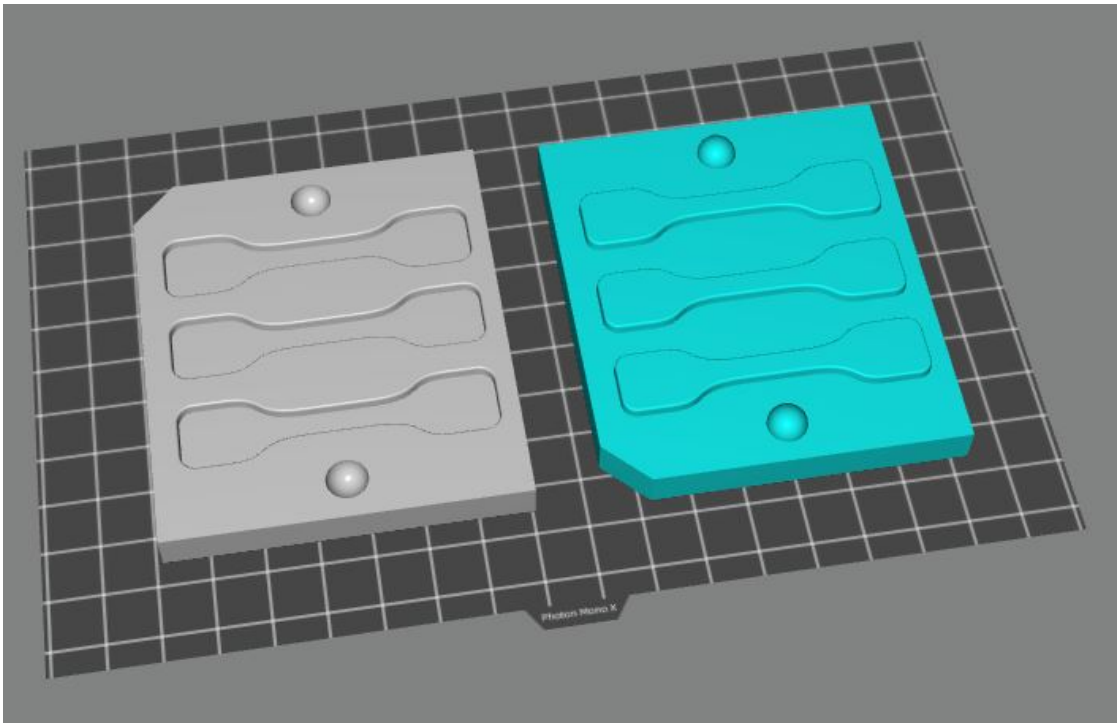


Figure 3.11: Preliminary test sample mold print layout printed on Anycubic Mono X.

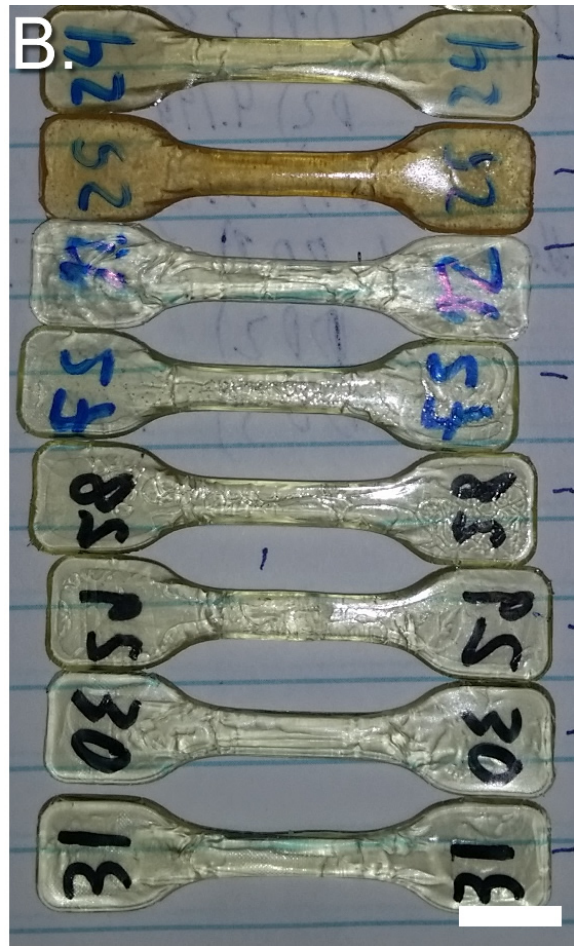


Figure 3.12: Photographs of preliminary resin test samples. A) Samples 1-21, B) Samples 24-31. Scale bars: 10mm.

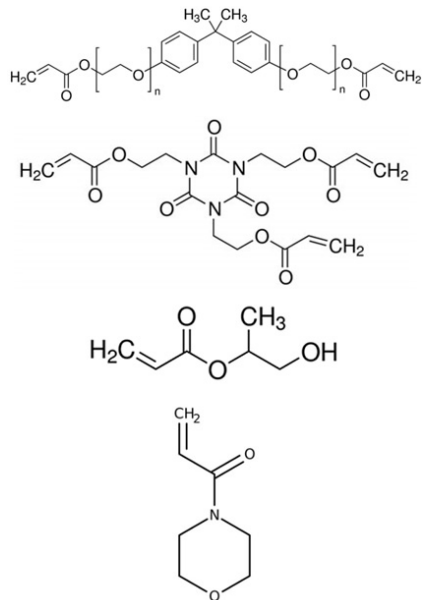


Figure 3.13: Components of S100 resin (from top to bottom): Bisphenol A ethoxylate diacrylate (BAEDA M=512), Tris(2-acryloyloxyethyl)isocyanurate (TICA), Hydroxypropyl acrylate (HPA), and 4-Acryloylmorpholine (4ACM).

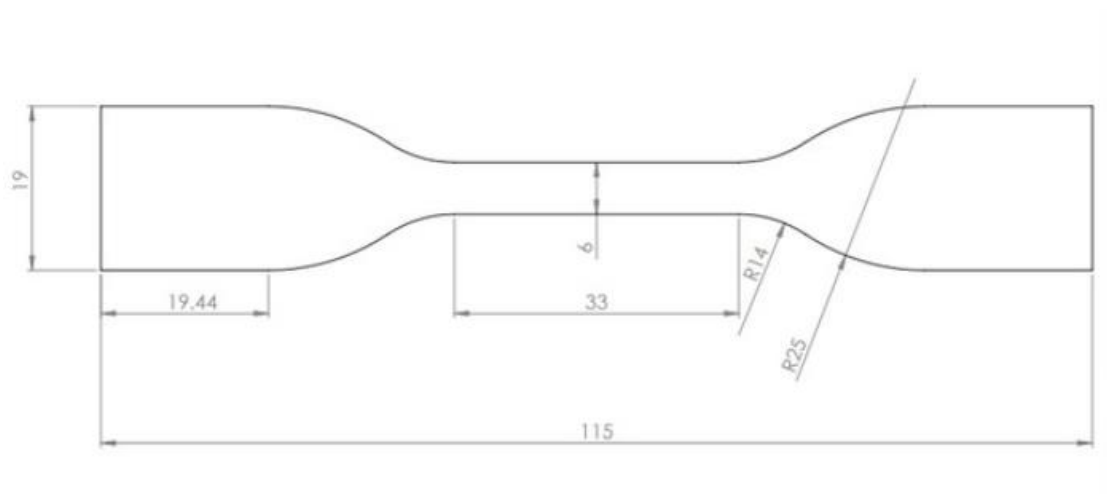


Figure 3.14: Confirmatory tensile test dogbone dimensions, created according to ASTM D638-IV.

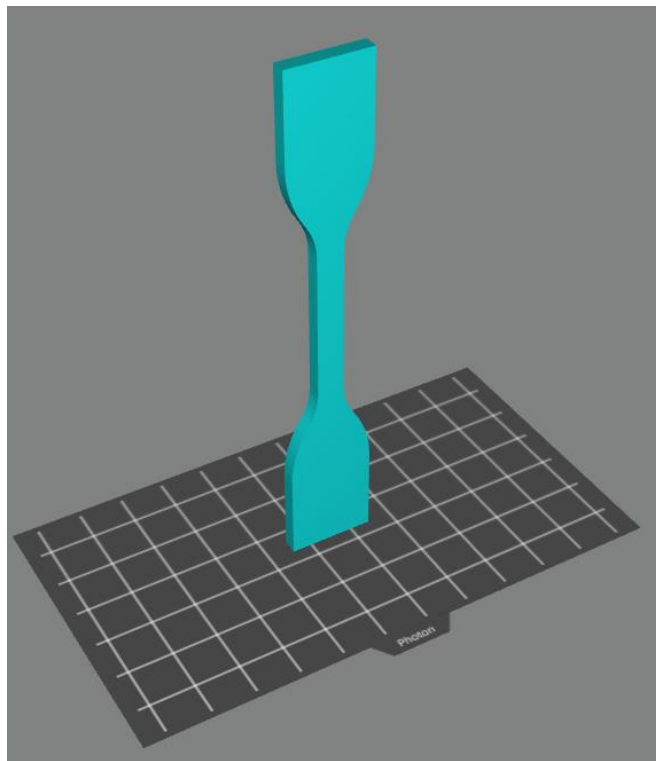


Figure 3.15: Confirmatory tensile test dogbone dimensions, created according to ASTM D638-IV.

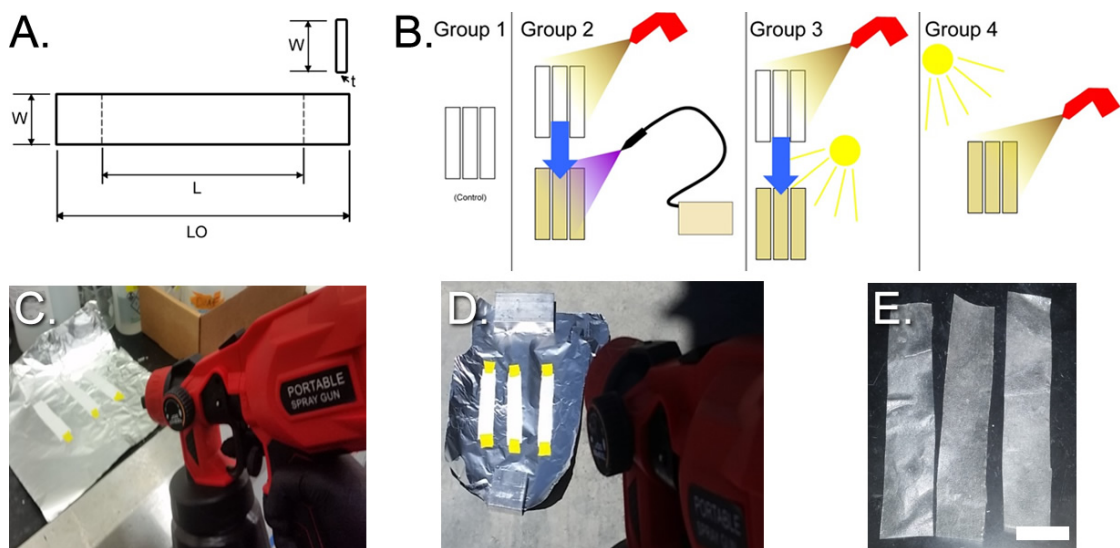


Figure 3.16: Testing procedure for S100 resin spray coated tissue paper strips A) diagram of tensile strips - $W = 23$ mm, $L = 38$ mm, $LO = 100$ mm, t was calculated for individual strips using SEM and imageJ analysis, B) diagram of the procedure for coating each group of samples, C) photograph of coating samples prior to UV exposure (group 2), D) photograph of coating samples under sunlight (group 4), E) photograph of coated test strips. Scale bar: 20 mm.

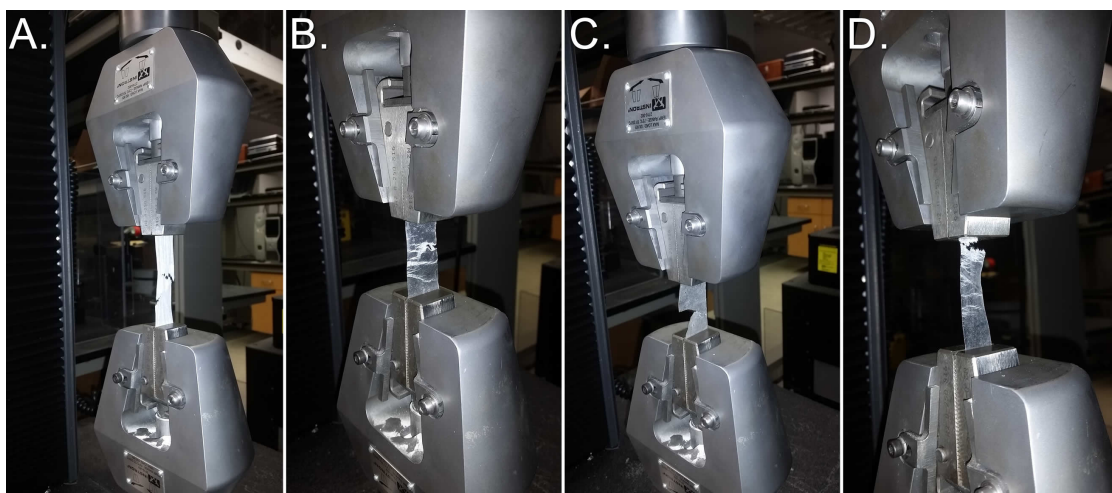


Figure 3.17: Photographs of the tensile failure mode of each group of samples: A) Group 1, B) Group 2, C) Group 3, D) Group 4.

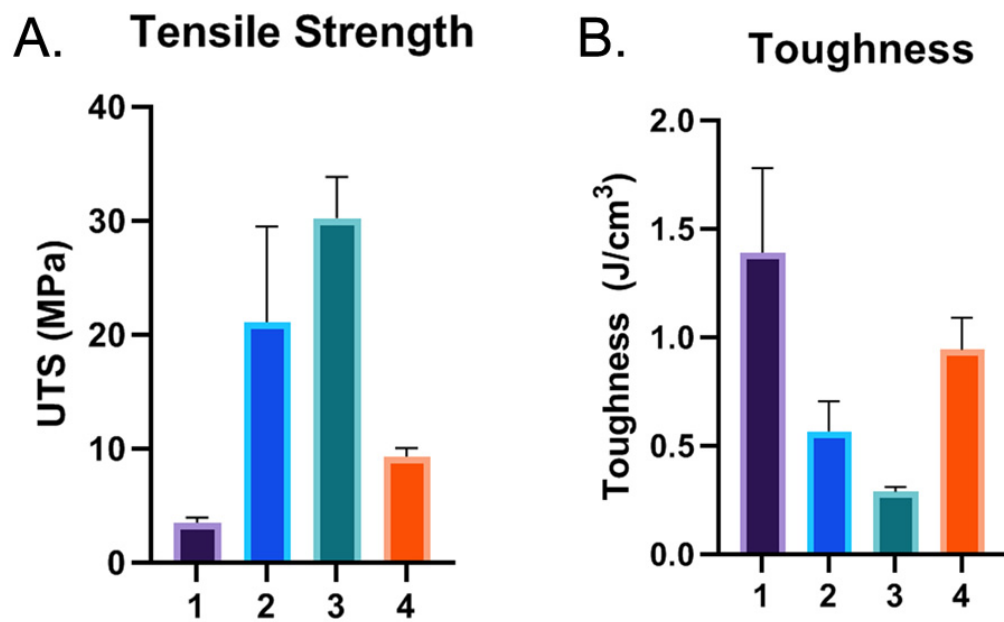


Figure 3.18: Results of tensile analysis performed on the S100 coated tissue paper strips (figure 3.16/3.17/3.19). It is important to note that the anomalously high toughness for the control (uncoated) sample is likely due to the comparatively lower thickness of the uncoated tissue paper relative to the other samples.

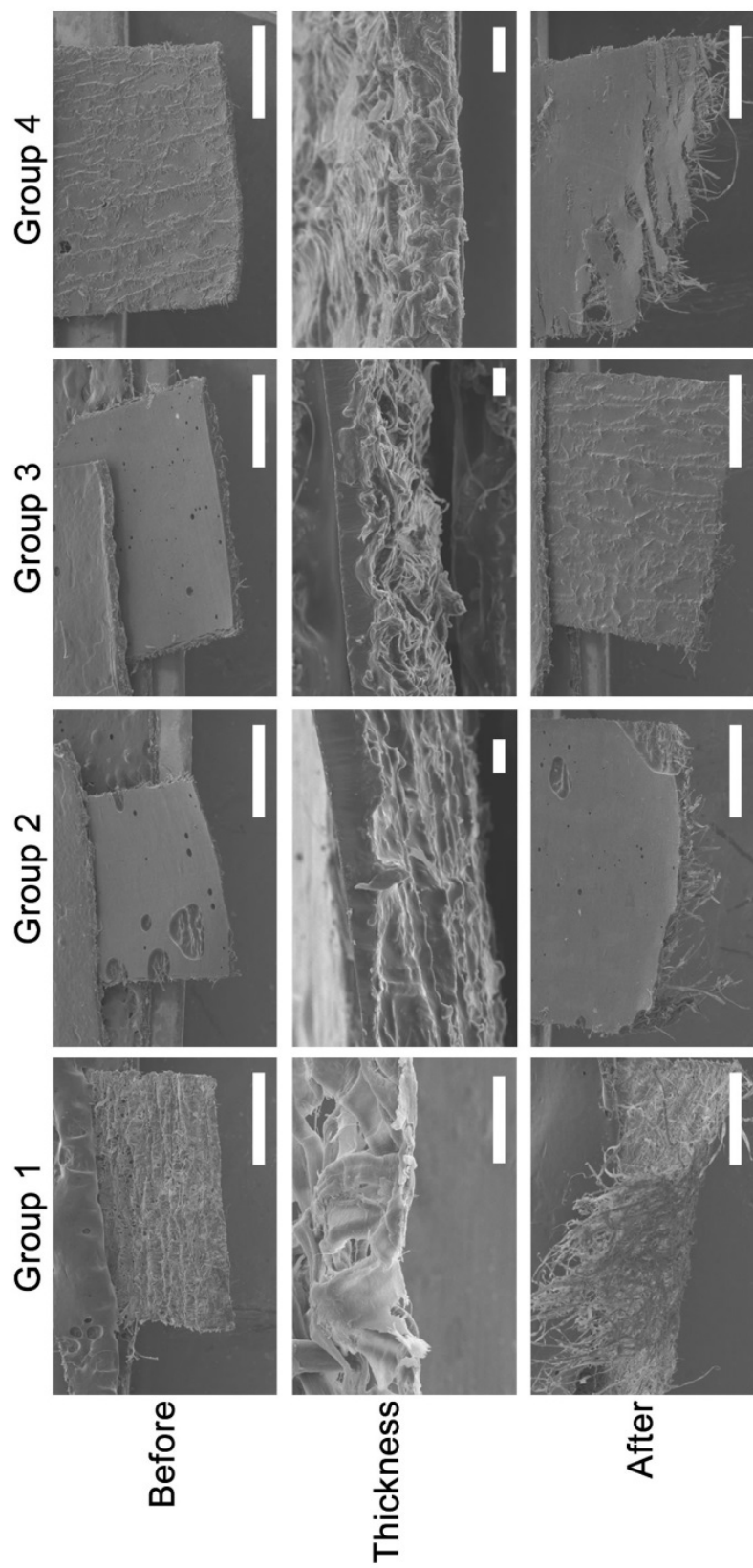


Figure 3.19: Scanning electron micrographs of sections of tissue paper test samples shown in figure 3.16/3.17 and their surface morphology before and after mechanical failure, as well as cross sectional images used to determine the thickness of each sample. Scale bars: middle row 50 μm , all other bars 1 mm.

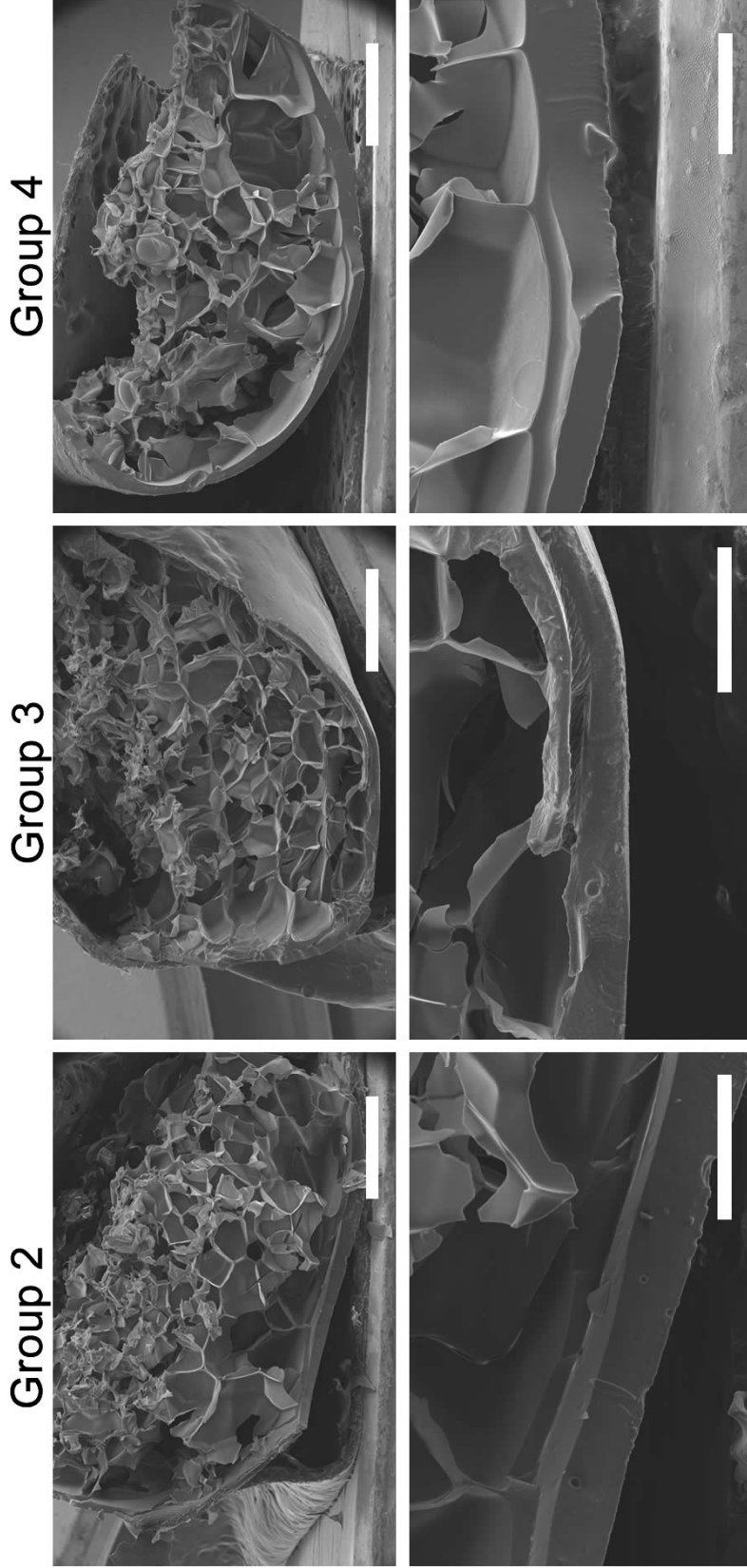


Figure 3-20: Scanning electron micrographs of S100 resin coated foam samples showing coating thickness and surface morphology. Both 25x (top row) and 100-125x (bottom row) magnifications are shown for comparison. Scale bars: Top row – 1 mm, bottom row – 300 μm .

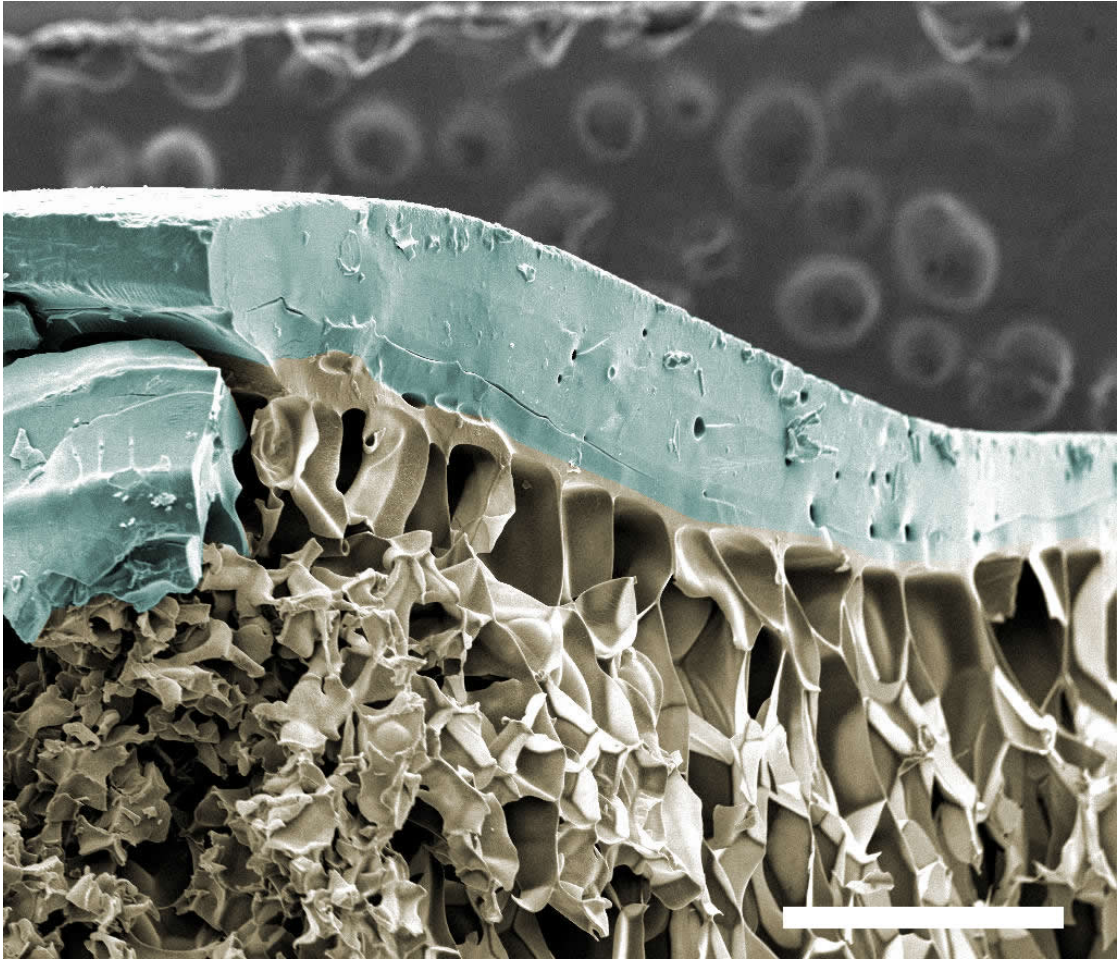


Figure 3.21: Colorized scanning electron micrograph of a S100 resin spray coated onto HEMA foam sample, 3 layers sequentially coated with 60 s UV cure for each layer. Scale bar: 500 μm

Compressive Yield Strength of HEMA Foam + S100 resin

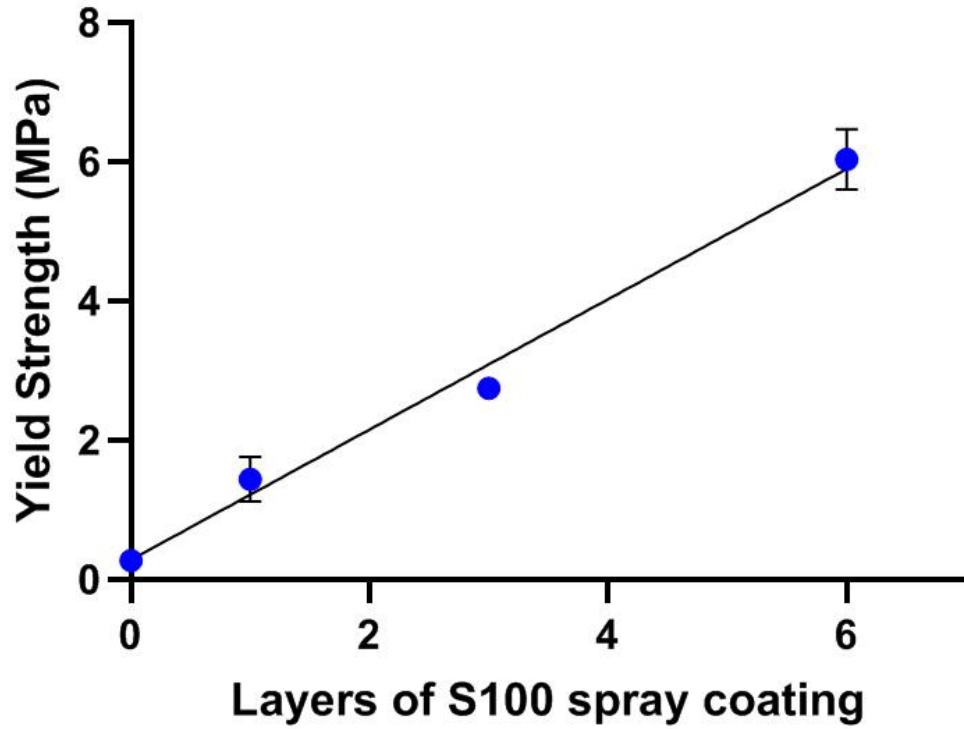


Figure 3.22: Plot of compressive yield strength vs layers of S100 spray coating

3.7 Supplemental Tables

Table 3.2: List of selected relevant resin formulations explored or discussed in the current study and their respective cure times. Cure time was evaluated with a $340 \mu\text{W}/\text{cm}^2$, 405 nm light source for 60 s via the method of Figure S3. All resins included the remaining wt% of hydroxypropyl acrylate (HPA) unless otherwise stated (i.e. control samples listing 100 or where all other components total 100). List of acronyms used in this table: N,N'-(4,4'-Diphenylmethane)bismaleimide (4MBMI), 4-Acryloylmorpholine (4ACM), N-isopropyl acrylamide (NIPAM), Tris (2- acryloyloxyethyl) isocyanurate (TICA), Bisphenol A ethoxylate diacrylate (BAEDA), 1,3- Bis(maleimido) pentane (1,3MP), 1,6- Bis(maleimido) hexane (1,6MH), dimethyl acrylamide (DMAC), aramid nanofibers (ANF), aramid nanofibers acrylated (ANFA), 1-vinyl 2-pyrrolidone (VP), hydroxyethyl acrylate (HEA). Photoinitiator consisted of a 50:50 (wt%) mixture of phenylbis (2,4,6- trimethylbenzoyl) phosphine oxide (BAPO), and diphenyl (2,4,6- trimethylbenzoyl) phosphine oxide (TPO) at a total loading of 0.5 wt% unless otherwise stated.

S#	Component 1 (wt%)	Component 2 (wt%)	Component 3 (wt%)	EAB (%)	UTS (MPa)	Notes
1	Siraya Blu – (100)			9	39.08	Control – commercial resin
2	Siraya Blu, Clear V2 – (100)			8	26.43	Control – commercial resin
3	2-hydroxyethyl methacrylate (100)			0	0.16	Very brittle, slow cure
7	BAEDA (20)	-	-	114	3.55	Very flexible but tough polymer
8	BAEDA (50)	-	-	56	12.18	Tougher but less flexible
11	BAEDA (40)	4ACM (10)	-	7	40.74	High strength, somewhat brittle
13	BAEDA (10)	4ACM (90)	-	5	31.74	Reasonably strong, good combination
16	4ACM (80)	4MBMI (10)	-	0	0.21	Brittle, BMI inhibits cure below surface
19	BAEDA (33)	4ACM (33)	4MBMI (7)	10	53.08	Quite tough, rigid polymer
20	BAEDA (33)	4ACM (33)	-	8	35.38	Reasonably strong
21	BAEDA (66)	-	-	4	25.94	Strong but uneven curing, high viscosity
23	BAEDA (33)	4ACM (33)	4MBMI (5)	6	49.44	Strong
24	BAEDA (33)	4ACM (33)	1,3MP (5)	18	46.90	Strong, similar to (23)
25	BAEDA (33)	4ACM (33)	1,6MH (5)	9	45.37	
28	BAEDA (40)	4ACM (40)	-	9	45.69	

Table 3.2: List of selected relevant resin formulations. (Cont.)

S#	Component 1 (wt%)	Component 2 (wt%)	Component 3 (wt%)	EAB (%)	UTS (MPa)	Notes
29	BAEDA (50)	4ACM (30)	-	16	55.13	
30	BAEDA (50)	4ACM (20)	-	14	45.40	
31	BAEDA (60)	4ACM (20)	-	12	49.26	
33	BAEDA (33)	4ACM (33)	ANF (1)	10	46.35	
34	BAEDA (33)	4ACM (33)	ANF (1)	6	41.23	Component 4: 4MBMI (5)
35	BAEDA (50)	4ACM (29)	ANF (1)	10	44.58	
36	BAEDA (50)	4ACM (24)	ANF (1)	5	44.69	Component 4: 4MBMI (5)
37	BAEDA (50)	4ACM (20)	HEA (20)	13	34.74	
38	BAEDA (50)	HEA (40)		18	17.97	
40	BAEDA (50)	VP (26)	ANF (4)	6	23.88	VP was used to better disperse ANF
41	BAEDA (50)	VP (26)	ANFA (4)	5	13.72	
42	BAEDA (50)	DMAC (26)	ANF (4)	6	32.95	
43	BAEDA (50)	DMAC (26)	ANF (2)	4	21.99	
44	BAEDA (50)	VP (26)	ANF (2)	4	31.62	
45	BAEDA (50)	VP (26)	ANFA (2)	6	21.59	
46	BAEDA (50)	DMAC (26)	ANFA (4)	3	21.27	
47	BAEDA (50)	DMAC (26)	ANFA (2)	4	32.29	
48	BAEDA (50)	DMAC (30)	-	16	39.30	
49	BAEDA (50)	VP (30)	-	17	35.43	
50	BAEDA (50)	4ACM (30)	-	27	39.06	Using 1% total PI – instant cure

Table 3.2: List of selected relevant resin formulations. (Cont.)

S#	Component 1 (wt%)	Component 2 (wt%)	Component 3 (wt%)	EAB (%)	UTS (MPa)	Notes
51	BAEDA (50)	4ACM (30)	-	15	43.09	Using 0.5% total PI – fast cure 5 s
52	BAEDA (50)	4ACM (30)	-	12	34.44	Using 0.1% total PI – cure time 15 s
53	BAEDA (50)	4ACM (30)	-	32	33.58	Using 0.05% total PI – cure time 30 s
54	BAEDA (50)	4ACM (30)	-	18	37.34	Using 2% total PI – instant cure w/excess bubbling
56	NIPAM (50)	-	-	0	6.15	Vapor released during cure
57	BAEDA (40)	4ACM (22)	NIPAM (18)	5	50.10	Small amount of vapor released
60	BAEDA (50)	4ACM (20)	NIPAM (10)	15	51.55	Tough but slightly brittle
61	BAEDA (60)	4ACM (30)	-	6	49.07	Quite brittle
62	BAEDA (50)	NIPAM (5)	4MBMI (2)	31	37.50	Component 4: 4ACM (13)
63	BAEDA (50)	NIPAM (5)	4MBMI (1)	13	31.61	Component 4: 4ACM (9)
64	BAEDA (55)	NIPAM (5)	4MBMI (1)	6	24.57	Component 4: 4ACM (4)
65	BAEDA (50)	NIPAM (10)	4MBMI (1)	6	33.79	Component 4: 4ACM (4)
66	BAEDA (55)	NIPAM (10)	4MBMI (1)	17	23.25	Component 4: 4ACM (4)
67	BAEDA (60)	NIPAM (5)	4MBMI (1)	0	21.62	Component 4: 4ACM (4)
71	BAEDA (30)	4ACM (10)	TICA (30)	3	36.75	Very fast cure, color changed from yellow to light brown after cure
72	BAEDA (30)	4ACM (20)	TICA (20)	19	49.15	
73	BAEDA (40)	4ACM (20)	TICA (20)	14	47.60	
74	BAEDA (50)	4ACM (29)	ANF (1)	11	33.69	

Table 3.2: List of selected relevant resin formulations. (Cont.)

S#	Component 1 (wt%)	Component 2 (wt%)	Component 3 (wt%)	EAB (%)	UTS (MPa)	Notes
75	BAEDA (50)	4ACM (29)	ANF (0.5)	7	42.08	
76	BAEDA (50)	4ACM (29)	ANF (0.25)	6	40.20	
77	TICA (50)	4ACM (20)	-	0	0	Too brittle for tensile analysis
78	BAEDA (30)	4ACM (20)	TICA (20)	1	15.86	
79	BAEDA (30)	4ACM (36)	TICA (20)	5	39.26	Component 4: 4MBMI (4)
81	BAEDA (35)	4ACM (20)	TICA (15)	8	63.37	
82	BAEDA (40)	4ACM (20)	TICA (10)	8	64.03	
83	BAEDA (45)	4ACM (20)	TICA (5)	6	57.90	
84	BAEDA (45)	4ACM (18)	TICA (5)	8	52.93	Component 4: 4MBMI (2)
87	BAEDA (30)	4ACM (20)	TICA (20)	4	28.40	Component 4: ANF (0.5)
92	BAEDA (50)	4ACM (30)	ANF (0.5)	2	29.55	
97	BAEDA (40)	4ACM (8)	TICA (10)	8	50.41	Component 4: 4MBMI (2)
98	BAEDA (40)	4ACM (10)	TICA (10)	10	46.18	
99	BAEDA (40)	4ACM (20)	TICA (10)	6	53.22	
100	BAEDA (35)	4ACM (20)	TICA (17)	11	56.75	

3.8 Acknowledgements

Chapter 3, in full, is currently being prepared for submission for publication of the material. Wirth, David M.; Hochberg, Justin, D.; Pokorski, Jonathan K. The dissertation author was the primary investigator and author of this material. This work was supported by the National Science Foundation (OISE 1844463).

Chapter 4

Design and Fabrication of a Pilot-Scale Melt Processing System

4.1 Introduction

The objective of this chapter is to explore new applications for an existing method of manufacturing. Injection molding (IM) and polymer melt processing are manufacturing processes which are largely free from the resolution/speed/size tradeoffs of programmable AM assemblers described in Chapter 1. Because there is no conversion of digital information to physical information, and the structural information is already present in the form of a physical mold or nozzle, they can achieve dramatically higher resolution, speed and size than programmable AM systems. The drawback of these systems in conventional applications is their large size and their comparative lack of design freedom. The extrusion nozzle can only produce 2D extruded structures through a nozzle, and IM can only produce objects for which a custom mold has already been designed and fabricated using an additive or subtractive manufacturing system, subject to the limitations described in Chapter 1. Nevertheless, IM and extrusion have served as mainstays of manufacturing and mass-production throughout the industrial age, enabling countless modern technologies and advancements. The current chapter will undertake the adaptation of an extrusion system toward a biopolymer processing application, reducing its size, cost, and dead volume to accommodate research on high

value-added polymers for drug delivery or implant applications. Described in this Chapter 4 and Chapter 5 are the design and fabrication of two iterative plunger-based melt processing systems for extrusion and injection molding on the milligram and gram scales of material respectively.

4.2 Background

Recently, studies have been carried out on lab-scale mini-injection molding of drug-delivery capsules, but the equipment needed for such studies remains large and expensive relative to the budget of most academic research labs, leading many in the field to forego the use of IM in favor of more economical alternatives. [95] In addition, due to the large scale and consequently large dead-volume of such traditional techniques, high value research articles may be impractical to process in such a manner. Even the smallest commercially available injection molding machine would require tens to hundreds of grams of material – an impractical amount for many academic labs which produce samples on the milligram to gram scale.

Our laboratory has used melt-processing techniques to manufacture protein-polymer composites, of which novel protein components are a precious and expensive resource. [96–98] Hence, the current work has sought to develop a simple instrument, accessible to the research community, which yields reproducible melt-processing results.

It may be here remarked that the system developed is not a full “melt processing machine” and is similar to a shaping machine since it has no mixing capability, nevertheless we have found that the machine developed in the current work fills capability gaps in the academic state of the art and its mixing capabilities are adequate for most applications. This bench-top system can process polymer and composite materials at scales below 0.2 cm^3 and can be fabricated at 2-3 orders of magnitude less expense than commercially available microinjection molders. Furthermore, a range of polymer composite materials are described along with a variety of self-made molds fabricated by CNC to dictate part geometry.

The machine shown in Figure 4.1 is best suited to the extrusion of small implantable medical devices for controlled release of drugs or vaccines.

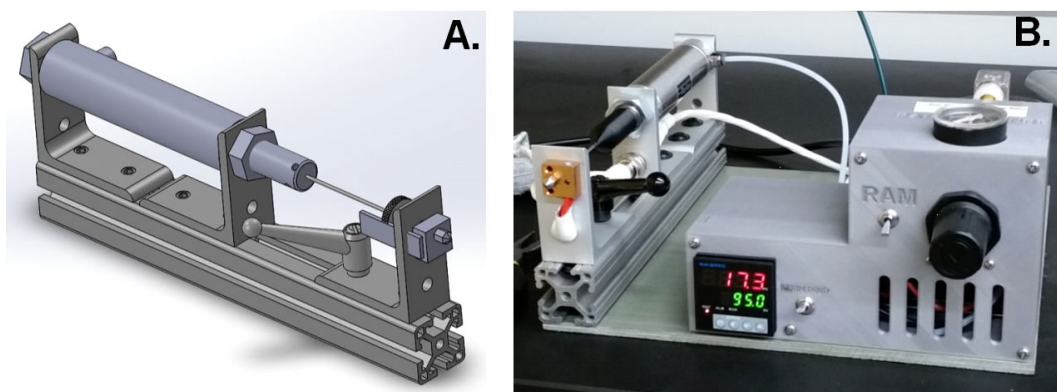


Figure 4.1: A) Mechanical design of pneumatic injection system, B) digital image of micro-injection molding instrument.

4.3 Results and discussion

4.3.1 Injection Molding of Polymer Composites

We aimed to investigate three different polymers and their composites: PLA, PCL, and PLGA due to their biocompatibility, low melting temperature and low melt viscosity. Using these three polymers and three dispersed species: Ferrocene, MWCNT and Doxorubicin, we aimed to demonstrate the capacity of the current system to process and shape devices from a variety of value-added materials in small batches with a uniform distribution of dispersed fillers. Mechanical testing was conducted to assess the homogenization of fillers and degradation of mechanical properties of injection molded parts as compared to literature values. We also conducted emphin-silico modeling of shear rate to determine safe extrusion and injection molding parameters for the efficacious loading of drug and nanoparticles without degradation in the final structure.

4.3.2 Characterization of Composite Samples

To assess the dispersion of additives in our polymer melt processed samples, Energy Dispersive X-Ray Spectroscopy (EDS) was chosen as a characterization technique due to its ability to examine the microscopic distribution of heavy elements throughout a sample. After injection molding and cleanup, PLA/PLGA samples (Figure 4.9) and PCL samples (Figure 4.10) were sliced into thin sections using a razor blade, carbon coated, and then imaged using EDS. Samples 1-4 are visualized in Figure 4.2 and samples 5-8

are seen in Figure 4.3.

PLA samples (Figure 4.2A-C) showed structural morphology consistent with the presence of microvoids – macroscopic voids can also be observed in the PLA samples in Figure 4.9. We suspect that PLA samples exhibited higher porosity due to trapping of air in the twisted extruded films and potentially also due to the presence of solvents trapped inside the polymers themselves which expand during high temperature molding and extrusion. Our PLGA sample Figure 4.2D, showed similar behavior and porosity to the PCL samples and was also processed without the use of solvents. We observe few voids in the PCL samples under electron microscopy Figure 4.3A-D, largely thanks to the solvent-free nature of the polymer processing. However, due to the low melting point of PCL, we had some difficulties imaging samples under high magnification electron microscopy as samples tended to heat, outgas and melt in the vacuum chamber as the electron beam scan area decreased at higher magnification.

The samples which were never exposed to solvents tended to show far lower porosity, likely because they were extruded as powders. This allowed for pre-compression of the blended materials eliminating unwanted air during the compounding process.

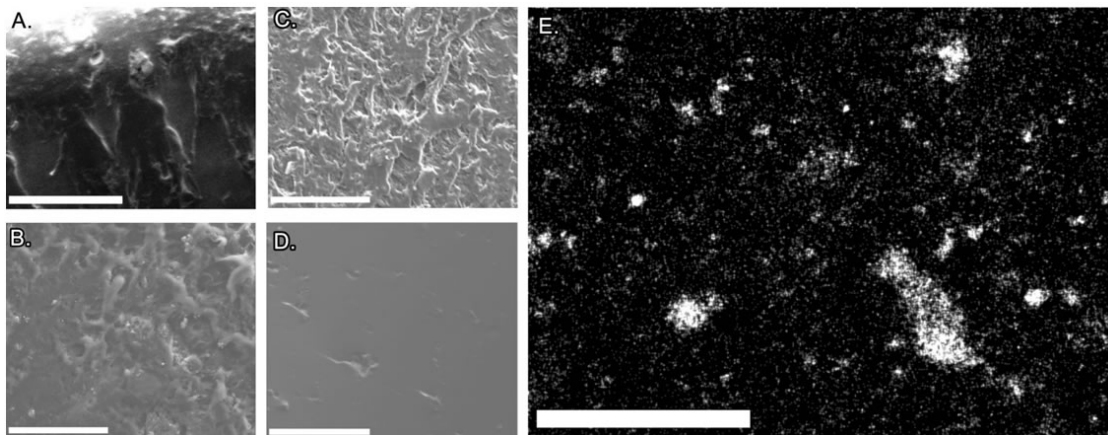


Figure 4.2: Electron micrographs of PLA-based samples: A) Sample 1 - PLA only, B) Sample 2 - PLA/MWCNT, C) Sample 3 - PLA/Doxorubicin, D) Sample 4 - PLGA/Doxorubicin, E) Ni $K\alpha$ EDS of sample 2. All scale bars 100 μm .

EDS results were taken via mapping of Ni and Fe $K\alpha$ signals of samples 2, 6 and 7 with respect to position. EDS of other samples were not acquired due to the lack of heavy metal atoms in such samples. Most telling were the EDS maps of samples 2 (PLA/MWCNT) and 6 (PCL/MWCNT), Figure 4.2E and 4.3E respectively. Figure 4.4

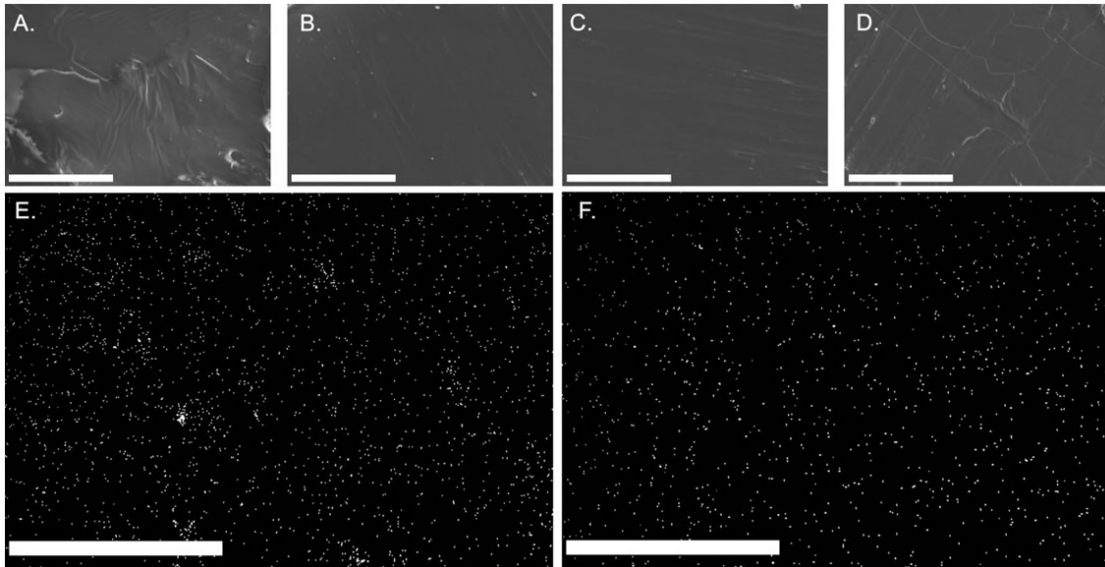


Figure 4.3: Electron micrographs of PCL samples: A) Sample 5 - PCL/Doxorubicin, B) Sample 6 - PCL/MWCNT, C) Sample 7 - PCL/ferrocene, D) Sample 8 - PCL control, E) Ni $K\alpha$ EDS of sample 6, F) Fe $K\alpha$ EDS of sample 7. All scale bars 100 μm .

shows a composite of both EDS Ni $K\alpha$ maps overlaid on SEM images of samples 2 and 6 and shown side-by-side to elucidate the difference in additive dispersion between solvent and melt-processed samples.

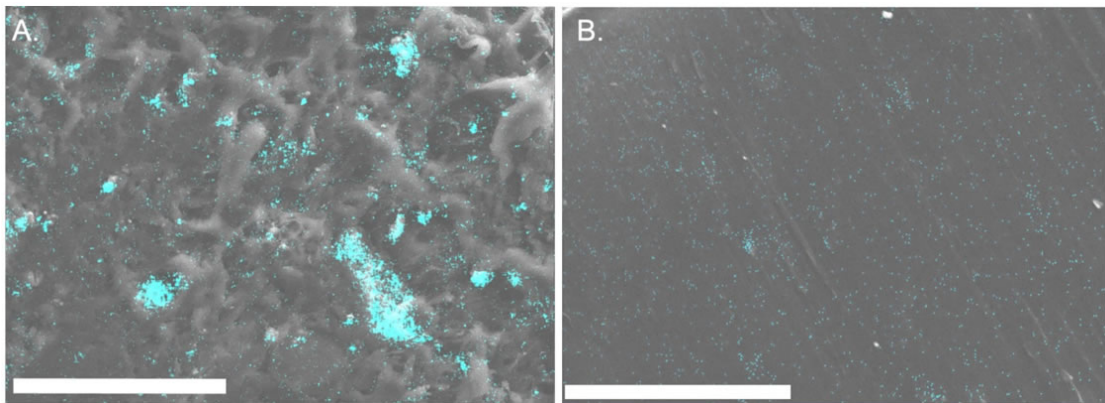


Figure 4.4: EDS/SEM composite micrographs of Ni $K\alpha$ EDS map overlaid on SEM images A) Sample 2: PLA/MWCNT, B) Sample 6: PCL/MWCNT. All scale bars 100 μm .

Due to the nickel content of the MWCNT and the iron content of Ferrocene,

aggregative behavior of filler species can easily be observed via EDS. Figure 4.4 shows low aggregation in the Ni $K\alpha$ EDS of Sample 6, and a fair amount of aggregation in the Ni $K\alpha$ EDS of Sample 2 where the Ni-coated MWCNT tended to cluster at various locations in the PLA samples processed using solvent-based techniques. Based on these micrographs, we observe a marked decrease in aggregation of nanoparticles in the PCL samples injection molded via a solvent-free process. Structural morphology also shows far fewer defects in samples prepared via solvent free-processes.

4.3.3 *In-silico* Simulation of Shear Forces Within a Polymer Extrusion Nozzle

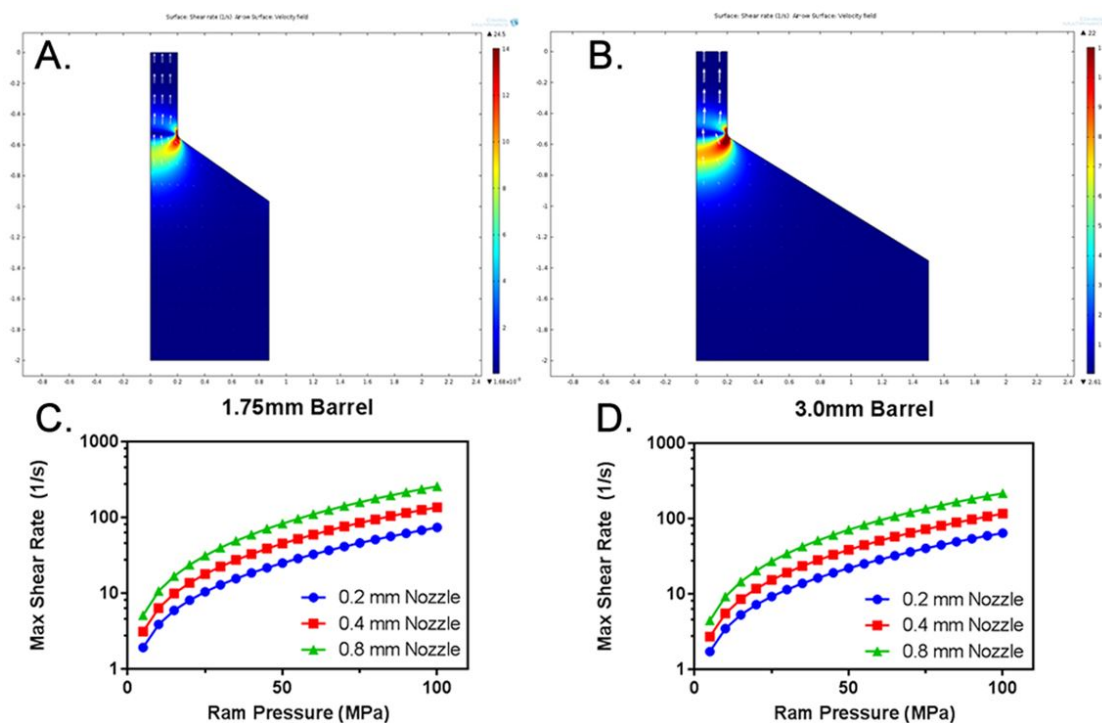


Figure 4.5: Theoretical max shear rate in nozzle as a function of barrel pressure, barrel diameter, and nozzle diameter. A-B, simulation of shear rate as a function of position at 36 MPa pressure for A) 1.75 mm diameter bore, B) 3.0 mm diameter. C-D, simulations of maximum shear rate as a function of pressure and nozzle exit diameter for C) 1.75 mm bore, D) 3.0 mm bore.

Since many of the applications for such a small-scale desktop injection molding system involve the preparation of sensitive biological samples, we simulated the forces exerted during extrusion, specifically shear rate. Many biomedical applications (such

as the delivery of proteins and pharmaceuticals) are heat or shear-rate sensitive. [99] Specifically, Lee et al. [97] examined the effect of shear rate on the stability of viral nanoparticles and found they were stable within a narrow window between 10-25 1/s shear rate. In order to precisely predict and control the shear rate inside our system, we developed a non-newtonian model using a Carreau-Yasuda dynamic viscosity approximation with boundary slip [100, 101] to estimate the shear rate for a given chamber pressure and nozzle size in order to produce more consistent results with biological samples. Because the ratio of pneumatic piston diameter to barrel bore diameter determines the nozzle pressure. This allows for the exertion of very high pressures in the barrel of the extruder, which might result in high shear rates at the nozzle. Since the area ratio is proportional to the square of the pressure ratio: 690 kPa (0.69 MPa) of air pressure driving the main 31.75 mm bore pneumatic cylinder will apply a force of up to 690 N to a small shaft which is mechanically coupled to the cylinder output, resulting in a barrel pressure which is $690 \text{ N}/(\text{shaft area in } m^2) \text{ Pa}$. In short: this results in a 257x multiplication of the applied pressure to the polymer inside the extruder barrel for a 1.75 mm shaft, or an 87.5x multiplication for a 3 mm shaft. It should be noted that the barrel and nozzle pressure is largely independent of any fluid properties of the polymer melt due to the largely incompressible nature of fluids (including polymers) [102] in laminar flow regimes. Warfield, et al. demonstrates that the compressibility of bulk polymers is negligible ($< 5\% \Delta V/V$) at pressures below 1000 atmospheres (100 MPa). Even in highly flow-restricted systems such as injection molding, incompressible flow can still safely be assumed due to the low flow rate, which allows the fluid pressure to equalize before compressibility effects occur. [103] Therefore: incompressible and laminar flow was assumed for the purpose of simulation and a theoretical model was created in COMSOL to predict shear rates of polymer mixtures for various nozzle and barrel diameters as shown in Figure 4.5.

From this model it can be observed that the shear rate is largely independent of the barrel diameter and depends only on the nozzle size and barrel pressure. Furthermore, it can be observed that the maximum shear rate increases with increasing nozzle size, due to the increased speed of polymer extrusion. Therefore, for future applications of this system, it is important for users to keep in mind that extruder shear rate is directly proportional to speed of extrusion. If higher barrel pressures are required for extrusion of a particularly viscous polymer, shear rates can be kept low by simply

reducing extrusion speed (by adjusting the regulator pressure) in a constant-pressure extrusion system.

4.3.4 Mechanical Characterization of Injection Molded Polymer Samples

Samples geometry was designed based on ASTM D638 “Standard Test Method for Tensile Properties of Plastics” and ASTM D1708 “Microtensile Testing of Plastics” was also considered in the experimental design. Since even the smallest test sample in ASTM D1708 required a larger sample than the mold, we used a scaled down version of the ASTM D638 Type I profile scaled down to the appropriate size (Figure 4.6A). ASTM D638 specifies that in specimens in samples thinner than 1 mm, ASTM D882 is the “preferred” test method, but D638 is still valid.

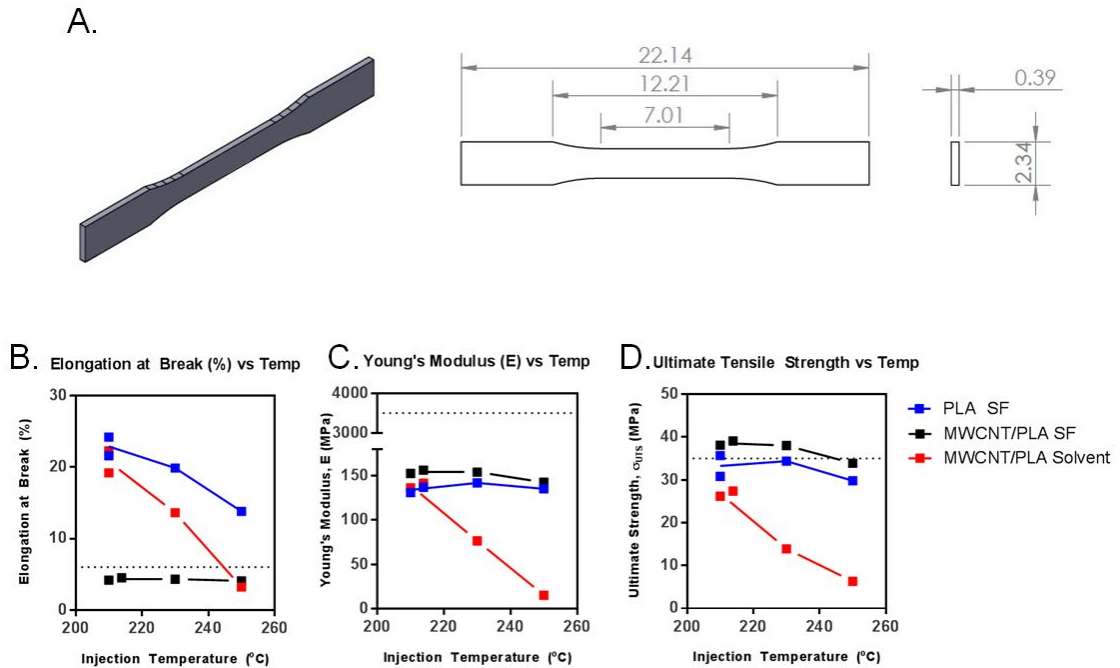


Figure 4.6: Mechanical properties as a function of processing temperature and use of solvent during pre-processing. SF indicates Solvent Free processing. A) Physical dimensions of test samples, B-D) mechanical properties as a function of injection molding temperature, the literature value for unfilled pristine PLA is shown as a dashed line on all graphs.

As noted by ASTM D1708, the elastic modulus obtained from this testing greatly

deviated from literature values, and this was to be expected. However; the tensile strength and elongation at break was in the neighborhood of reported literature values. Figure 4.6 shows the sample geometry and summary of mechanical properties; tensile strength was largely independent of extrusion parameters (i.e. temperature and pressure) for the solvent-free samples, but strength was greatly reduced in the solvent-processed samples and was strongly correlated to extrusion temperature.

Table 4.1: Average values of properties for tensile test samples prepared with and without solvent

	Literature Value	PLA (Solvent Free)	PLA (Solvent Processed)
Density (g/cm^3)	1.24	1.236	1.197
Elongation at Break (%)	2-9	4.3	15.3
Ultimate Tensile Strength (MPa)	36-77.1	37.3	18.7

The weight of samples was divided by the sample volume (since injection molds were CNC machined from a CAD model of known volume) and used to compute the average density for samples processed with solvent and without solvent. The results of the density study are listed below in Table 4.1. It is important to note that the density, ultimate tensile strength and elongation at break for solvent-free injection molded samples was remarkably close to that of the literature values (despite the addition of 2 wt% CNT, which may account for the slightly lower elongation and higher tensile strength)

4.4 Conclusion

A bench-top melt-processing system has been designed and developed. Such a device allows academic researchers access to melt processing technology which previously was cost and scale prohibitive. Such a system serves as a melt-processing test bed, allowing individual labs to run pilot studies on very small batches of material, accelerating development of devices made from a range of high value-added components. Its methods of fabrication and cost of acquisition (\$300) put it well within the reach of research labs across a wide variety of disciplines which may not have considered the use of melt-processing due to its large capital investment in injection molding equipment. The fabrication of molds was challenging; however, due to the rise in availability of distributed manufacturing services such as 3DHubs – the cost of fabrication of custom molds for this device (roughly \$200/mold) is far lower than the cost of traditional injec-

tion mold tooling for parts of a similar size (\$1000+). Furthermore, reducing the size and cost of IM to a desktop machine allows for individual research labs to tailor machine specifications and controls to individual laboratory needs (such as sterility, optimization for small quantities of material, etc.)

Samples of melt-process polymer were characterized via SEM and EDS for distribution of composite species and presence of gas inclusions. Our efforts to eliminate gas pockets were largely successful in PCL and PLGA due to the solvent-free nature of these polymer preparations. We suspect their lack of aggregation is due to the good wettability of additives with the polymer melt during processing, allowing the molten polymer itself to act as a solvent. Uniformity may be improved by incorporating a static mixer to the barrel, by increasing the pressure to allow for higher shear rate and thus more vigorous mixing in the nozzle throat, or by increasing the number of pre-extrusion cycles to allow for a more complete mixing of the additive with the polymer. It is unknown at this time the effect of additive miscibility with the polymer melt on aggregation – further experiments may be conducted on highly polar additives (such as salts) with highly non-polar polymers (such as PCL) to determine the aggregative behavior in these mixed polarity systems. In PCL the distribution of composite species was very uniform using a solvent-free approach, and little to no microscale or macro-scale aggregation was observed in samples processed without the use of solvents. In PLA, the distribution of composite species was largely dependent on shear rate; samples injected at higher pressure showed far lower aggregation than samples injected at lower pressure and higher temperature. Through our testing, we concluded that there was no clear correlation between mechanical strength of specimens and their injection molding properties in PLA for the temperature and pressures tested. There was, however, a statistically significant effect whereby the use of solvents in the processing of polymer samples resulted in a decrease in mechanical properties. Overall, we believe the current method is a beneficial tool for users across a wide variety of disciplines and may serve to facilitate discoveries and solutions which otherwise may not have been feasible .

4.5 Experimental section

4.5.1 Benchtop Injection Molding Instrument Fabrication

The design of the Desktop Injection Molding System (DIMS) began by leveraging existing 3D printer technology and commercially available 3D printer parts (Figure 4.7). The core of the system is an ordinary Fused Deposition Modeling (FDM) 3D Printer heater block. This extruder was mounted on a 1.5" T-slotted aluminum rail with removable gusset which facilitates easy removal of the extruder for loading of polymer material and cleaning. A pneumatic cylinder and 3D printed shaft collar were also mounted on the rail and secured into place with gussets. The shaft collar secures a 5/64 x 3" stainless steel rod into position with thumb screws which allow for ease of removal of the steel rod for cleaning.

We focused on a piston-based approach rather than a more conventional augur design due to its simplicity, cost effective construction and effectiveness at minimizing dead volume to allow for smaller batch sizes.

Lab air at 690 kPa was routed through an adjustable air regulator and 5-way valve to the two ports on the cylinder which allow for the piston to be extended and retracted at the touch of a button and the pressure to be independently adjusted by means of the regulator during extrusion.

The ceramic cartridge heater and thermocouple were connected to a commercial PID controller, which was powered by a 300 W 12 V power supply. The output of the PID controller was connected to the gate of an enhancement mode MOSFET which was used to switch the ground wire of the heater cartridge. Finally, electrical components were housed in a 3D printed PLA enclosure. The electrical and pneumatic connections are illustrated in Figure 4.7. Assembly instructions, pneumatic and electrical schematics, STL files and CAD diagrams can be found in supplemental information. It is important to note that the PID controller must be manually tuned to reduce overshoot – we found the following values worked well on the Inkbird ITC-106VL thermal controller: P=3, I=1, D=450-3000. In tuning the PID, we aimed to minimize overshoot, but the actual heater block temperature setting of the controller should be set according to the polymer being extruded. It is important to set the block temperature to a value between the melting point and decomposition point of the polymer being processed (i.e. between 160 and 300 °C for PLA).

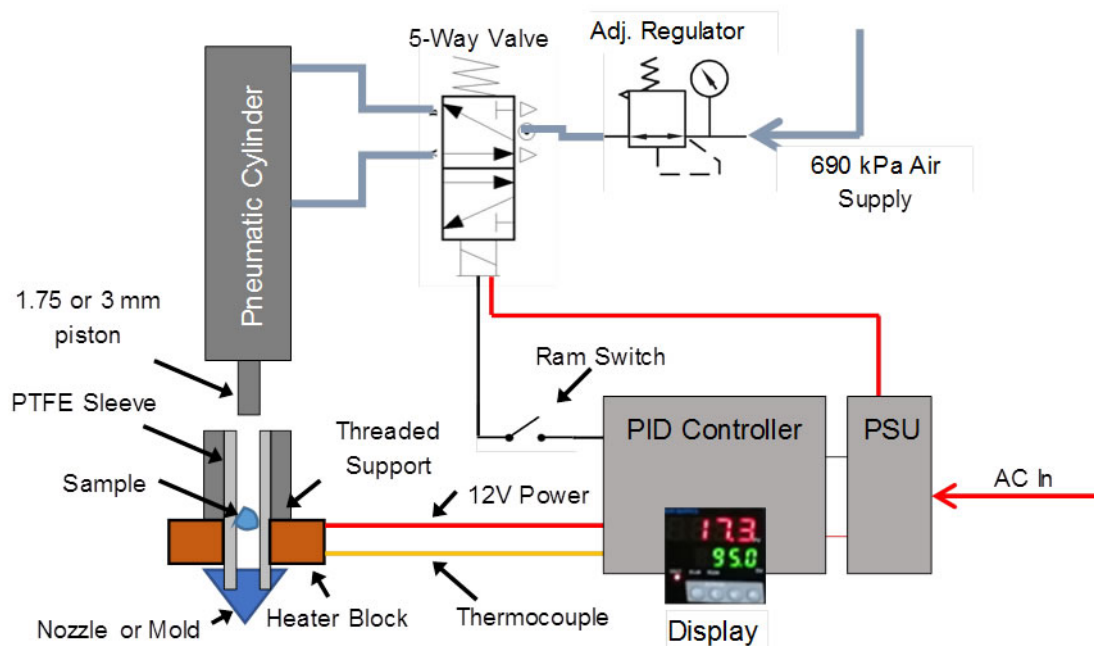


Figure 4.7: Design schematic of bench-top polymer melt processing system

4.5.2 Injection Mold Fabrication

Aluminum injection molds (Figure 4.8) were CNC machined on a Tormach PCNC1100. These molds consist of two halves, each 0.25" thick which are held together by M3 screws. The static mold half consists of a male M6 threaded port which screws into the extruder heater block. A M6 threaded barrel is loaded with a removable PTFE sleeve and sample of polymer to be extruded, then screwed into the heater block from the opposite end, creating a seal with the static mold half. The patterned mold is then screwed onto the threaded holes in the static mold. The heater block is brought to operating temperature (between 60 and 250 °C) and the pneumatic piston is activated to inject the molten polymer into the mold. After injection, the mold may be left to cool, unscrewed and separated to remove the polymer samples.

4.5.3 Polymer Composite Fabrication

The following polymer samples (Table 4.2) were prepared for co-extrusion with PLA, PLGA, and PCL powders. PLA samples were prepared by dissolving in 30 mL of THF and sonicated with the filler species at 30 W power for a pulse period of 5 s

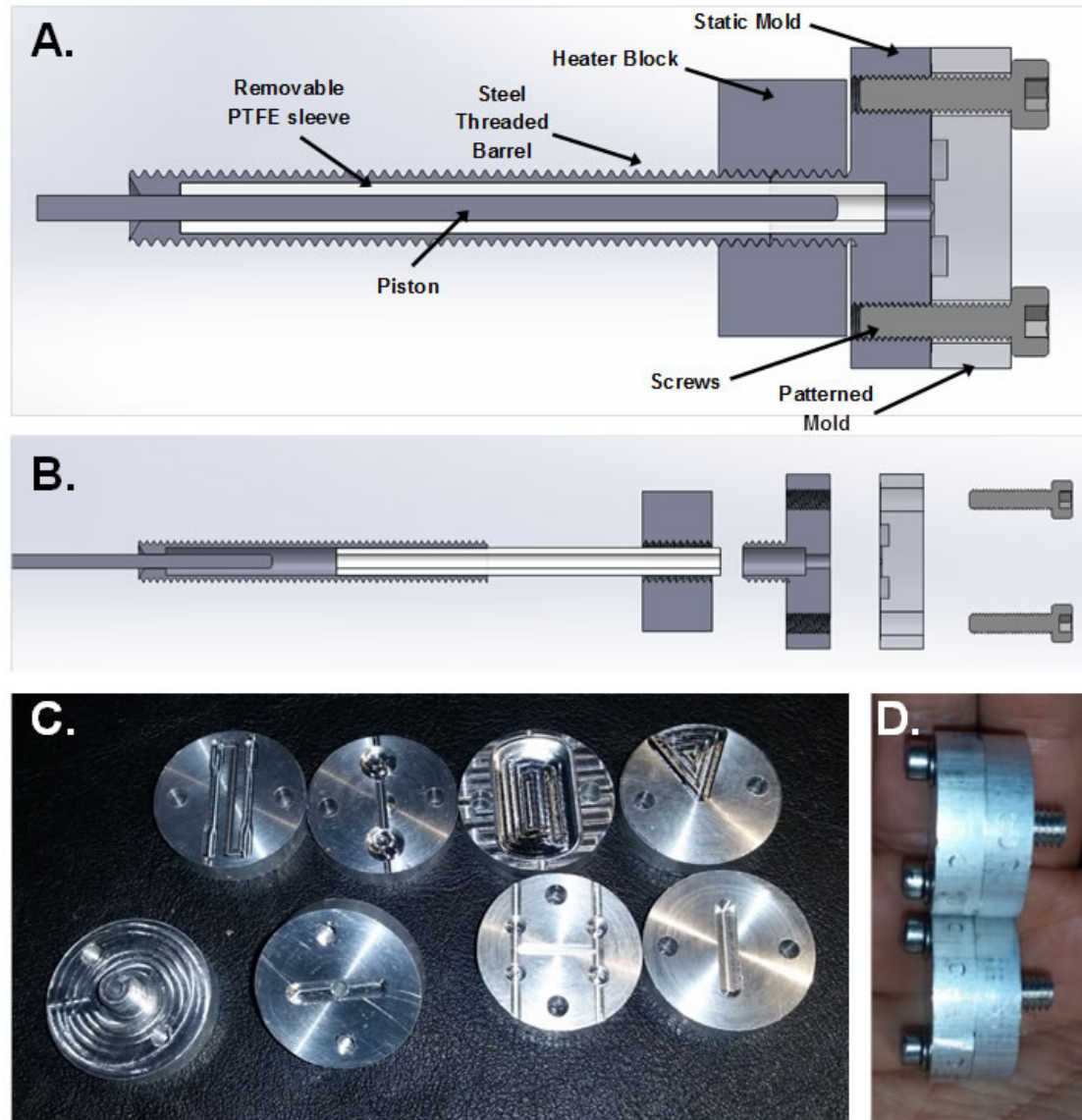


Figure 4.8: Injection molding component. A) Assembled model of injection molding system. B) Expanded model of injection molding system. C-D, Aluminum injection molds used throughout the current study, C) From top-left to right: dog bones, large disks, DLP mold, ribbon extruder. From bottom-left to right: standard nozzle, cylinder nozzle, small disks, cylinder mold. D) fully assembled molds

on and 10 s off for a total time of 5 minutes, then rotary evaporated at 25 °C/120 rpm and vacuum desiccated for 24 hours over sodium hydroxide. PLGA and PCL samples were prepared in Eppendorf tubes and mixed via vibratory shaking for 60 seconds before loading the powders directly into the extruder.

Table 4.2: Composition of samples prepared for injection molding

#	Poly- mer	Poly- mer mass (mg)	Filler	Filler mass (mg)	Ex- tru- sion Temp. (°C)	Ex- tru- sion Pres- sure (MPa)	Injec- tion Temp. (°C)	Injec- tion Pres- sure (Mpa)
1	PLA	500	None	N/A	210	10	210	50
2	PLA	500	Ni-coated MWCNT	50	210	10	210	50
3	PLA	500	Doxorubicin	1	190	10	190	70
4	PLGA	250	Doxorubicin	5	90	10	90	10
5	PCL	500	Doxorubicin	10	80	6	80	35
6	PCL	500	Ni-coated MWCNT	50	80	6	80	35
7	PCL	500	Ferrocene	10	80	6	80	35

The dried PLA films and the PCL and PLGA powdered samples were then placed into 3 mm PTFE sleeves and individually inserted into the extruder following the procedure below.

For each sample: the extruder was brought up to temperature and left to stabilize for 5 minutes after reaching its set point, then the regulator was brought up to its desired pressure, and the polymers were pre-extruded through a 0.8 mm stainless steel nozzle in the case of PLA, and a 0.6 mm nozzle in the case of PLGA and PCL as shown in Figure 4.9A. This first extrusion step was carried out in order to homogenize the polymer with the dispersed phase. The extrudate cylinders were then re-loaded into a fresh PTFE sleeve and inserted into the barrel, then an injection mold was screwed into the opposing side of the heat block in place of the nozzle. The extruder was then brought up to temperature and left to stabilize its temperature for 5 minutes after reaching its set point, the regulator pressure was brought to its set point, and the polymers were injected into molds. After each extrusion, the PTFE sleeve was replaced, and all parts were cleaned with appropriate organic solvents.

Composites were first extruded into thin cylinders to compound and homogenize the materials (Figure 4.9A) followed by IM into defined form factors as determined by the molds. Flashing (over-extrusion of material) was observed in all parts and was not detrimental to part geometry (Figure 4.9B). The flashing was very thin and was easily peeled away with a scalpel and flush cutters. Injection melt processed polymer samples

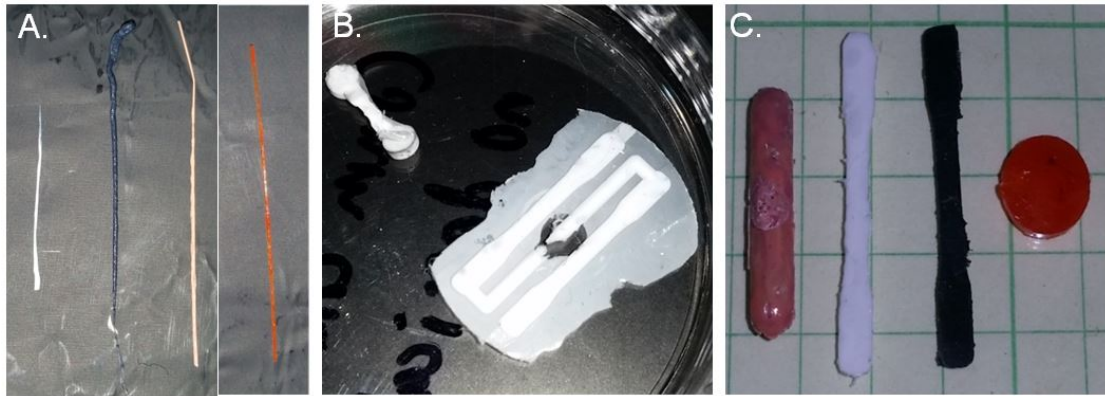


Figure 4.9: Melt processing of polymer samples; A) samples 1-4 (from left to right) showing extrudate cylinders after first extrusion, B) flashing of PLA directly after injection molding of sample 1, C) de-flashed PLA and PLGA injection mold samples 3,1,2,4 (grid squares 5x5 mm)

1-4 are shown in Figure 4.9C, and samples 5-8 are shown in Figure 4.10B with the flashing removed. MWCNT were chosen due to their nickel content (useful for EDS characterization of dispersion) and their tendency to aggregate in order to simulate a worst-case scenario to highlight the conclusions of this study. Ferrocene was chosen as a lipophilic small molecule additive with a heavy metal ion (again for EDS), and doxorubicin was chosen as a small molecule additive which was representative of the types of organic therapeutics used in medical implanted devices.



Figure 4.10: A) aluminum dog bone injection mold used during the current study, B) successfully injection molded PCL samples 5-8 (from left to right); Doxorubicin, MWCNT, Ferrocene, and pure PCL.

An additional set of samples were prepared from pure PLA powder (lot no. 7766) specifically for mechanical analysis, these samples were loaded with a much lower concentration of Ni-doped MWCNT (intended only for EDS contrast) as shown below in Table 4.3. SEM micrographs and EDS maps of the samples is provided in supplemental

figures.

Table 4.3: Composition of samples prepared for mechanical testing

#	Poly- mer	Poly- mer mass (mg)	Filler	Filler mass (mg)	Ex- tru- sion Temp. (°C)	Ex- tru- sion Pres- sure (MPa)	Injec- tion Temp. (°C)	Injection Pres- sure (Mpa)
9	PLA	500	Ni-coated MWCNT	10	210	10	210	30
10	PLA	500	Ni-coated MWCNT	10	210	10	210	12
11	PLA	500	Ni-coated MWCNT	10	210	10	230	12
12	PLA	500	Ni-coated MWCNT	10	210	10	250	6
13	PLA	500	Ni-coated MWCNT	10	210	10	210	30
14	PLA	500	Ni-coated MWCNT	10	210	10	210	12
15	PLA	500	Ni-coated MWCNT	10	210	10	230	12
16	PLA	500	Ni-coated MWCNT	10	210	10	250	6

Samples 9-12 were prepared in Eppendorf tubes and mixed via vibratory shaking for 60 seconds before loading the powders directly into the extruder. Samples 13-16 were prepared by dissolving PLA and MWCNT in 30 mL of THF and sonicated with the filler species at 30 W power for a pulse period of 5 s on and 10 s off for a total time of 5 minutes, then rotary evaporated at 25 °C/120 rpm and vacuum desiccated for 24 hours over sodium hydroxide. All samples were pre-extruded at 210 °C/10 MPa and only the temperature and pressure in the final injection molding step was varied between samples. Four additional control samples were also prepared in an identical fashion to samples 9-12 without the use of solvent and also without the addition of Ni-coated MWCNT to determine if the addition of MWCNT affected the overall mechanical properties of the composite parts.

4.5.4 Suggested Print Bed Layouts

A Prusa i3 Mk3 fused deposition modeling 3D printer was used to print the files from PLA filament purchased from Amazon. Shaft collars were printed from ABS filament also purchased from Amazon. STL files are included in the supplemental information. Suggested print bed layouts are below in Figures 4.11 and 4.12

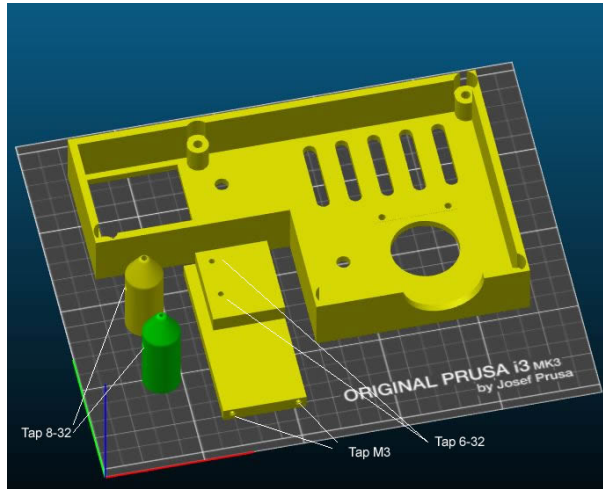


Figure 4.11: Recommended printbed layout #1

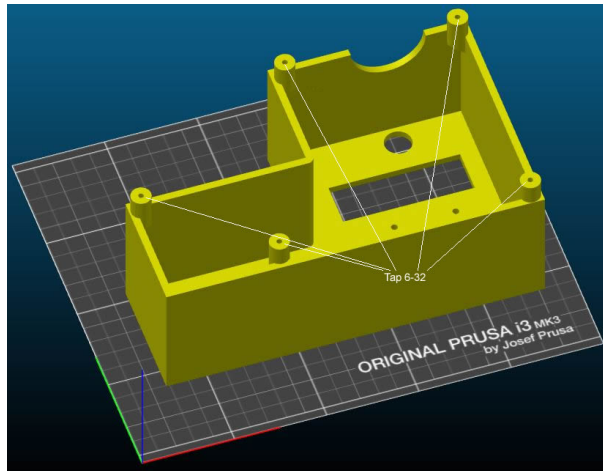


Figure 4.12: Recommended printbed layout #2

3D printing services (such as Shapeways and 3DHubs) offer custom 3D printed parts and can be employed to fabricate the parts if 3D printing is not available to the

individual user.

4.5.5 Mechanical Assembly

Numbers in the following section refer to the parts numbers in the Bill of Materials enumerated in Table 4.4.

Mark the 1'x1' green FRP sheet (9) using the 1.5" T-slotted aluminum bar (6) as a ruler roughly 0.75" from one edge. Drill two 5/16" diameter holes in FRP sheet along the line, each roughly 1" from opposing edges as shown in Figure 4.13.



Figure 4.13: Mark FRP base plate as shown above

Use step drills (19) or appropriate countersink drill to create countersinks for the 5/16" screws (7) on the bottom of the FRP sheet through the holes drilled previously as shown in Figure 4.14.

Insert fasteners (8) into T-slot rail (6) as shown in Figure 4.15 and secure to the FRP sheet (9) by tightening the countersunk screws (7) down on the rail fasteners through the FRP sheet (9). Insert washer (31) between rail and base plate. See Figure 4.16.

Insert dual bracket (2) into the top of the T-slot rail (6) now secured to the base plate (9). Remove both screws from the dual bracket. Place gusset (1) over the bracket holes and insert one of the bracket screws into one of the gusset holes and the handle (3) into the second hole. Discard the unused screw. The gusset should now be tightened down until it is loose enough to slide off of the ends of the rail, but can be clamped down tightly by turning the handle.

Remove heater block from assembly (16) and secure to the front gusset, screw



Figure 4.14: Deep countersunk holes in base plate using step drill or countersink drill



Figure 4.15: Insert rail fasteners into rail

M6 thumbscrew (5) onto M6 threaded tube with PTFE insert, securing the assembly to the gusset.

(optional) replace stock NTC thermistor with k-type thermocouple. Only attempt the replacement if you have the experience and proper tooling to weld the thermocouple together and attach it to the heater block.

Solder extensions onto the NTC (or thermocouple) wires as well as the heater block wires. Extensions should be at least 18" if you plan to wire directly into the main



Figure 4.16: Tighten screws to secure rail in place

box, and 4" if you plan to use a socket connector as shown below in Figures 4.17 and 4.18.

Take the second gusset (1) and widen the top hole to at least 3/4" in diameter using the step drills. Secure the gusset firmly to the rail using the attached screws and mounting plate.



Figure 4.17: Finished sliding gusset

Mount the pneumatic cylinder (18) to the second gusset with the large widened hole as shown in Figure 4.19. Secure it with the included nut as shown in Figure 4.20. Add NPT fittings (23) to both ports on the pneumatic cylinder.

Use the 7/16-20 tap (34) and 8-32 tap (33) to chase the 3D printed threads on the two shaft collars as shown in Figure 4.21. Attach the base of the shaft collar to the pneumatic cylinder, slide one of the gauge pins (4) through the shaft collar and secure it in place with the set screws as shown in Figure 4.22.

Connect the pneumatic switch (20), mufflers (21), regulator (22), and cylinder



Figure 4.18: Both gussets mounted to rail



Figure 4.19: Cylinder mounted in place



Figure 4.20: Cylinder secured using included nut

(18) using the NPT fittings (23-24) and 5/32" hose (25) as shown in the diagram in Figure 4.23. The switch can be mounted to the 3D printed bracket using 6-32 screws, and the regulator can be attached to the front panel using the included screw adapter



Figure 4.21: 7/16-20 threaded shaft collar



Figure 4.22: Gauge pin inserted into shaft collar with threaded 8-32 thumb screws securing it in place

as shown in Figure 4.24. The 3D printed frame has a cutout portion for the gauge

Use of Teflon tape on NPT threads is highly recommended to prevent leakage of high pressure air.

The remaining holes in the rear of the enclosure can pass the pneumatic inlet and outlet tubes.

Once all pneumatics and electronics have been connected and tested, the enclosure can be closed by securing both sides together with 6-32 screws.

4.5.6 Electrical Assembly

If using wall current: remove the insulation from your plug cord, and expose the green, blue and brown wires. Further strip the wires and connect to power supply as shown in Figure S13.

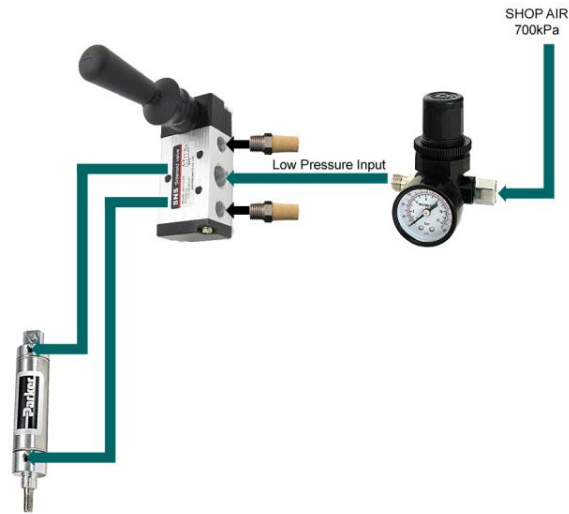


Figure 4.23: Diagram showing pneumatic connections between switch, regulator and cylinder

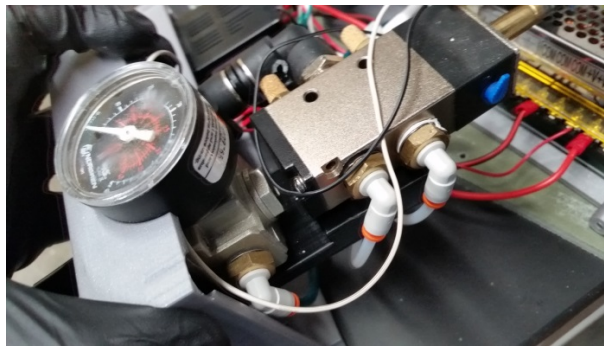


Figure 4.24: Photograph of pneumatic manifold and regulator

Connect the remainder of the wires using solder and/or crimp connectors. Be sure to use heat shrink tubing and/or electrical tape to insulate all exposed copper before powering on the system.

It is recommended to run long $>12''$ wires between the heater block and the other components of the system, preferably with a quick disconnect connector for easy removal of the heater block. Thread these $12''$ wires through one of the small holes on the back of the electronics enclosure.

Once powered on, the PID controller will need to be tuned and the thermometer measuring device set to the correct type. Follow the Inkbird ITC106-VL manual for

instructions.

It is important to note that the user will likely need to set the derivative setting of the PID controller manually to a very high value to prevent overshoots. P: 1-5, I: 1, D: 3,000 worked well for the system shown.

It is important to connect the 100k Ohm resistor between the gate and source of the MOSFET to serve as a pulldown on the gate.

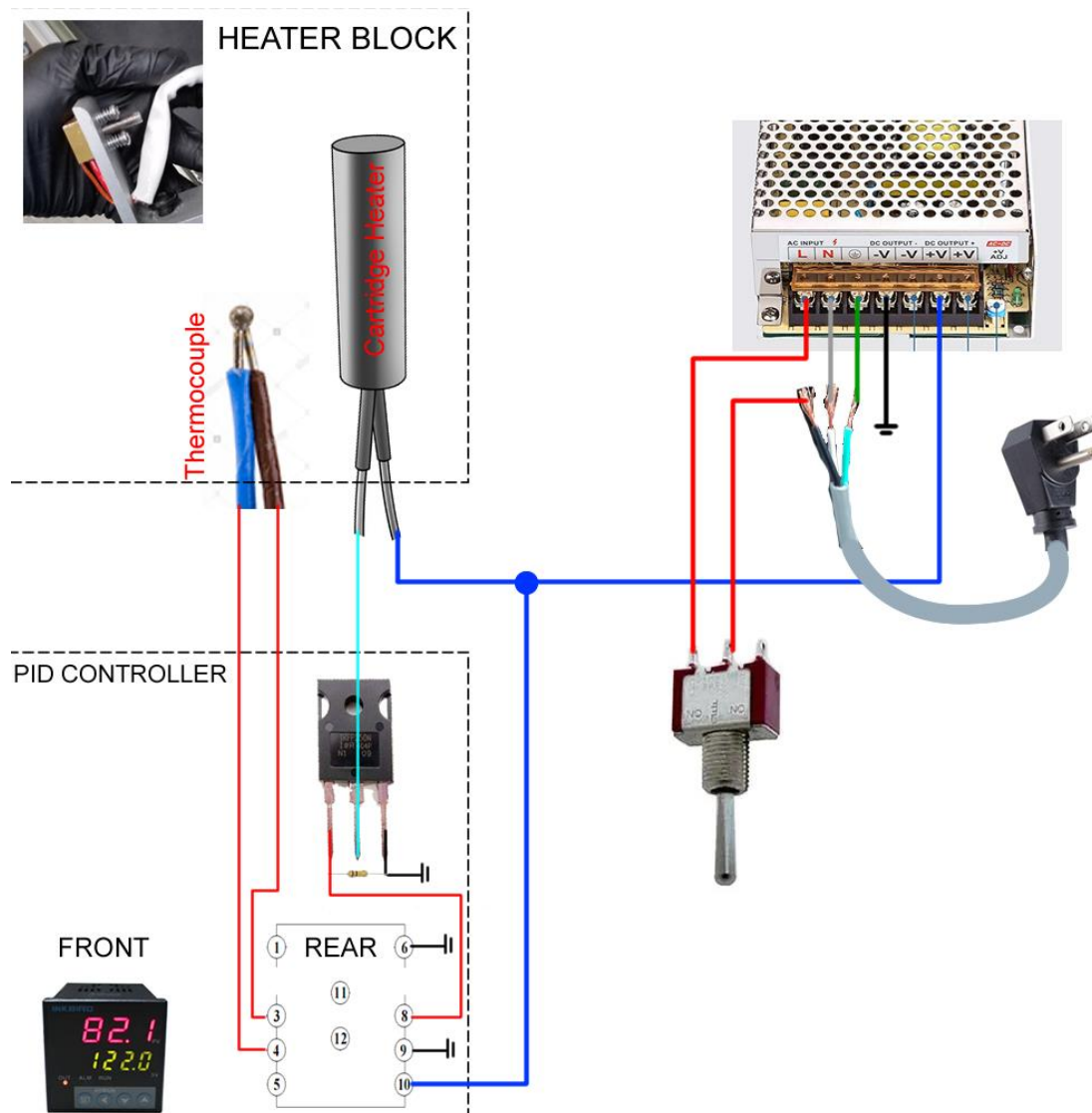


Figure 4.25: Wiring diagram of the electrical system

Once the electronics have been tested, all components can be fit into the electrical

enclosure.

It is recommended to secure the AC plug to the inside of the enclosure using a zip-tie to provide strain relief.

4.5.7 Materials

Polycaprolactone (PCL) powder (Cellink Part #TP60505001, MW 50 kDa), Poly lactic-co-glycolic acid (PLGA) powder (Polysciotech, AP041, MW 5-25 kDa) were extruded as received. Polylactic acid (PLA) filament was purchased from Amazon (B07D699XT5). Tetrahydrofuran (THF) was purchased from Fisher (ACS reagent). Each polymer composite was fabricated with varying amounts of Nickel coated Multi-Wall Carbon Nanotubes (MWCNT) (US Research nanomaterials, Inc., part number US4430), Ferrocene (Sigma), and Doxorubicin (TSZ Chemicals, RYG02), which were added according to Tables 4.2 and 4.3. Parts for melt-processing equipment fabrication are detailed in the supplementary information.

4.5.8 Instrumentation

SEM and EDS were carried out using a FEI Quanta 600 SEM and Bruker XFlash 6/60 Energy Dispersive X-Ray Spectroscopy.

Samples were weighed and tested on a CellScale Univert mechanical testing apparatus with 100N load cell.

4.6 Supplemental Figures

Stress vs. Strain for PLA IM Tensile Samples

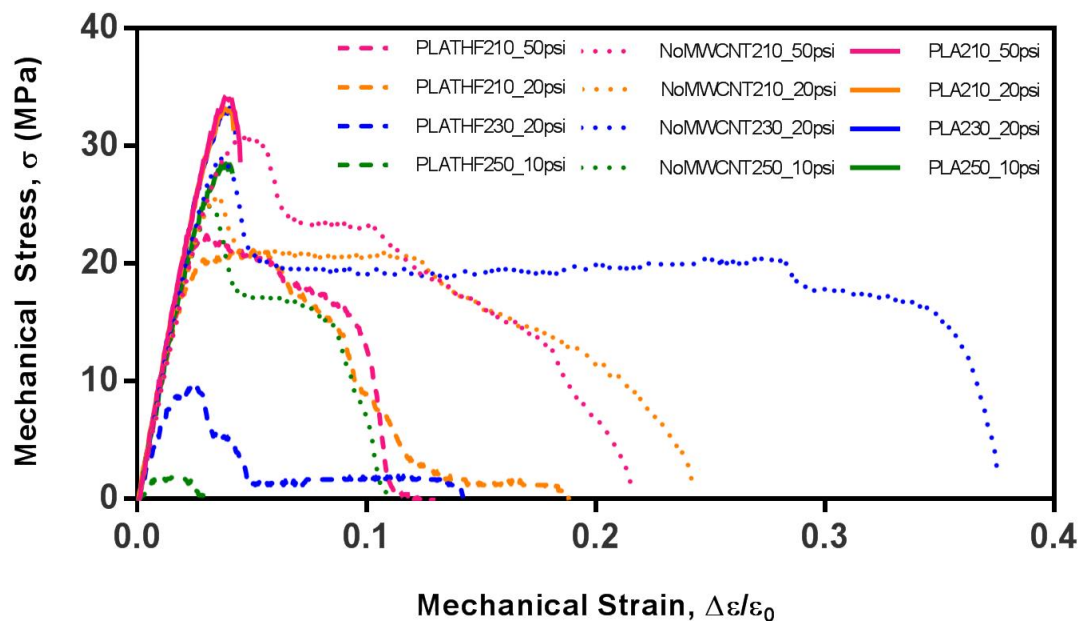


Figure 4.26: Raw stress-strain curves for samples. PLATHF samples were processed using the solvent THF and contained 2 wt% MWCNT. No MWCNT samples were processed using no solvent and also contained no MWCNT. PLA samples were processed using no solvent and contained 2 wt% MWCNT.

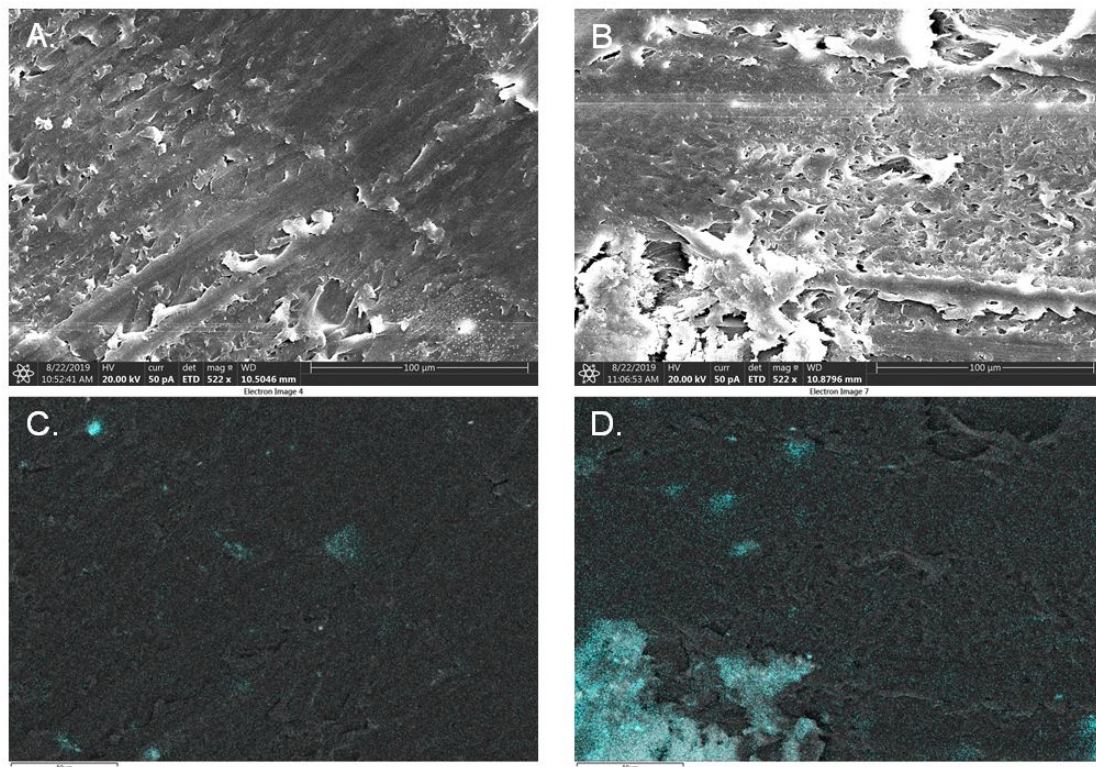


Figure 4.27: A) Sample 9 (solvent free, 210 °C, 50 MPa) secondary electron image, B) Sample 14 (solvent-sonicated, 210 °C, 20MPa) secondary electron image, C) Sample 9 EDS map showing Ni $K\alpha$ concentration in cyan, D) Sample 14 EDS map showing Ni $K\alpha$ concentration in cyan

4.7 Supplemental Tables

Table 4.4: Bill of Materials (BOM) for construction of benchtop melt-processing system

No.	Description	Part	Vendor	Qty
1	1.5" gusset	47065T241	McMaster Carr	2
2	Dual bracket	47065T149	McMaster Carr	1
3	Handle, zinc, 5/16-18 threaded stub	6271K210	McMaster Carr	1
4	5/64 x 3" Gauge pin	1263K113	McMaster Carr	10
5	Thumb screw, SS M6	90368A300	McMaster Carr	1
6	T-slot, 1.5" rail, hollow, 1ft length	47065T102	McMaster Carr	1
7	5/16-18 x 0.5 SS countersunk screws	92210A578	McMaster Carr	1
8	SS end feed fastener T-slot 5/16-18	47065T145	McMaster Carr	2
9	Structural FRP 1'x1'x1/4"	8537K25	McMaster Carr	1
10	PTFE Tube, 4x2mm, 5ft length	52335K32	McMaster Carr	1
11	Inkbird ITC-106VL PID temperature controller 12V	B01L8BD8H6	Amazon.com	1
12	120W 12V PSU	B01E6RMASC	Amazon.com	1
13	BIQU Aluminum Heater Block Specialized for MK7 MK8 3D Printer Extruder(Pack of 5pcs)	B01G1JWKQK	Amazon.com	1
14	3D printer nozzles, M6 thread 0.2, 0.3, 0.4 mm extruder	B07G2GFHC2	Amazon.com	1
15	CHPOWER 12V 40W 620 Ceramic Cartridge Heater and NTC Thermistor 100K 3950	B079K299MM	Amazon.com	1
16	CHPOWER CR-10 Hot End Assembled MK10 Extruder Kit	B07B6HSYR8	Amazon.com	1

Table 4.4: Bill of Materials (BOM) for construction of benchtop melt-processing system (Cont.)

No.	Description	Part	Vendor	Qty
17	ZRM&E 6pcs Makerbot MK8 Nozzle Throat Teflon Feed Tube PTFE Tube for 3D Printer Extruder HotEnd Barrel M6x30mm	B07HG1QGD1	Amazon.com	2
18	Parker Double acting cylinder 1/8" NPT 1.25" bore	1.25DSR02.0	PARKER	1
19	Step drill set	B001OEPYWK	Amazon.com	1
20	2 Position 5 Way Pneumatic Air Inlet Manual Hand Pull Lever Valve 4H210-08	B07DVXQRWC	Amazon.com	1
21	uxcell 1/8PT Male Thread Brass Air Exhaust Silencer Muffler Gold Tone 10 Pcs	B00OK97QCW	Amazon.com	1
22	Primefit R1401G Mini Air Regulator with steel-Protected Gauge, 60-Scfm At 100-Psi, 1/4" Npt	B00IDCYKEY	Amazon.com	1
23	5/32 Tube to 1/8" NPT push to connect	B019W973C2	Amazon.com	1
24	5/32 Tube to 1/4" NPT push to connect	B00B5NZ8BM	Amazon.com	1
25	Flexible nylon tubing 5/32" OD – per ft.	5548K72	McMaster Carr	5
26	Power MOSFET	IRFP250N	Mouser	1
27	1" Aluminum rod stock	8974K13	McMaster Carr	1
28	M3x12 socket head cap screws	91292A114	McMaster Carr	1
29	8-32x1/2 SS thumb screws	99607A135	McMaster Carr	1
30	6-32 x 1.5" screw	92196A157	McMaster Carr	1
31	5/16 washers	92141A030	McMaster Carr	1
32	Metric drill and tap set	B074D3V5QN	Amazon.com	1
33	Imperial drill/tap set	B077JDZF28	Amazon.com	1
34	7/16-20 tap	2521A724	McMaster Carr	1
35	100k Ohm Resistor	MF1/4LCT52R104G	Mouser	1
36	AC Rated power switch	612-100-A1111	Mouser	1

4.8 Acknowledgements

Chapter 4, in part, is a reprint of the material as it appears in “Design and fabrication of a low-cost pilot-scale melt-processing system”, Wirth, David M.; Pokorski, Jonathan K. *Polymer*, 181, 121802, 2019. The dissertation author was the primary investigator and author of this paper. This work was supported by the National Science Foundation (OISE 1844463) and UCSD.

Chapter 5

Design and Fabrication of a Pilot-Scale Injection Molding Instrument for Rapid Prototyping of High Precision Parts

5.1 Introduction

The objective of this chapter aims to address shortcomings in the availability of polymer injection molding equipment for small batch scale research use, and to enable a wider audience to leverage this powerful solvent-free polymer processing technique. Polymeric drug delivery devices are among the most promising avenues to improve equitable distribution of life saving medications throughout the world. At present, most research into manufacturing of these devices relies heavily on solvent-based methods, limiting scalability, reproducible manufacture, and leading to potential cytotoxicity of the resultant devices. Solvent-free polymeric biomedical implants manufactured through traditional thermal processing methods eliminate the bulk of these concerns, however they are difficult to manufacture in a laboratory setting. Investigation of techniques, such as injection molding, have been limited in the past due to the high upfront cost of polymer equipment and the large scale necessary to conduct pilot experiments. This study describes a low cost bench-top milliliter-volume vacuum injection-molding system, capable of pilot-scale injection molding of small shapes of arbitrary geometry. The plans presented herein open

this convenient and scalable manufacturing technique to academic research laboratories interested in pilot-scale experiments with polymeric devices specifically aimed at polymers relevant for polymeric drug or vaccine delivery. Demonstration of the fabrication of simple geometric parts and solvent-free polymeric microneedle patches is described. In particular, microneedle patches demonstrate the capabilities and limitations to produce fine feature sizes for biomedically relevant products in large quantities.

5.2 Background

Research into the injection molding (IM) of high value polymeric materials is a promising avenue which has been historically limited due to the high cost of traditional IM equipment. Barriers to the field are created by the difficulty of constructing a high pressure, high temperature durable mechanical apparatus, liquid cooling, hydraulic systems and/or mechanical augurs [104, 105] Historically, IM as a technique was first developed in the late 1800's and matured quickly after the discovery of Bakelite in the early 1900's. [106] IM is carried out by forcing molten polymer through an orifice into a mold cavity where it expands and solidifies. An augur, metering screw or piston is used to exert driving force on the polymer to move it through the barrel where it melts, and once liquefied is forced through the nozzle and into the mold consisting of a desired shape. [107] The augur or piston then retracts and spring loaded ejector pins assist in removing the solid part from the mold, clearing the cavity for the next injection. This cycle is very simple and may be highly automated, allowing industrial users to manufacture large volumes of identical parts automatically with little supervision. Industrial injection mold pressures are normally between 70-112 MPa. [108] Small scale systems intended for testing, analysis and demonstration may be as low as 10-60 MPa. [109] The power of IM lends itself well to industrial manufacturing in order to mass-produce parts continuously at very high production rates. [107] The rapid solidification of polymer in the mold is usually assisted by water cooling channels drilled throughout the mold block, but such water cooling is mainly required to achieve fast cycle times and is not essential for the operation of a small scale pilot IM system.

In recent years, a number of microinjection molding systems have sought to offer simpler, cheaper and/or smaller scale alternatives to mass production IM system for bench-top or laboratory scale applications, allowing for R&D and pilot scale studies to take place with injection volumes as low as 1 cm^3 , with some specialty systems offering

volumes as low as 82 mm³. [110] However, such systems are generally high in cost and difficult to adapt to research settings, making IM a seldom-explored technique in academic biomaterial research despite its high scalability and unique advantages over other techniques. [95]

In Chapter 4 and our recent work [111], we demonstrated a polymer melt processing system which was cost-reduced and scaled down to fill this capability gap with the hope of expanding research into IM as a manufacturing technique for high-value materials such as therapeutic drugs and nanomaterials. [96,97] However, despite our success at cost-reduction and decreasing the dead volume to ensure minimal waste, its maximum capacity was limited by the size of a commercial 3D printer hot-end. In this manuscript our design has been iterated to include custom metal parts to increase the melt volume and produce larger part geometries. The newly designed instrumentation affords far greater flexibility to design a modular system which can create custom and arbitrary geometries as well as solvent-free microneedle patches and biomaterial implants.

Polymer drug delivery devices are an active area of research and have been used to treat various diseases and infections. [112–117] Despite inherent difficulties in scaling and storage, these devices are ordinarily fabricated with solvent-based centrifugal or drop-casting due to the flexible material requirements and low waste of these processing methods. However, residual solvent in such devices may limit their shelf life. Similar to solvent casting, IM is commonly used to produce objects with various shapes and functions. [118–120] Unlike solvent casting, IM production can be extremely rapid and devices produced via IM do not need excessive drying to remove potentially trapped solvents. Despite the advantages of IM over traditional solvent casting, IM as a manufacturing technique is typically overlooked by many laboratories due to the high budget and/or feedstock production capabilities required for its use. [121]

The melt-processing of polymers is commonly used in cosmetic and pharmaceutical packaging, but more recently has been the subject of research for the production of biomedical devices including controlled release drug delivery methods including biopolymer implants and microneedle patches. [122–126] Melt processing techniques can allow researchers to tailor the shape, dimensions, or release properties of implantable devices within the body to deliver drugs where and when they are needed for maximum therapeutic effect. [127–129] Furthermore, the IM process applies both heat and high pressure to the formed polymer, sterilizing the molded components, reducing microbial contamina-

tion, and potentially improving the bioavailability of poorly soluble drugs administered via this method. [130–132] Recently, the need for versatile and highly scalable drug delivery platforms has been highlighted by the COVID-19 pandemic. [133] The rapid manufacturing and worldwide distribution of delivery devices made possible by IM production could provide substantial advantages in terms of addressing future pandemics in terms of easing the burden on HCP, and reducing the need for cold-chain storage of vaccines. [97, 111, 134–136]

In this work we have designed an instrument which can IM many polymers into arbitrary geometries. We chose microneedles as a test-bed for the system due to their fine feature size and high aspect ratio, thus allowing us to quantify the performance of our high-resolution vacuum-assisted injection molding system and assess the potential utility of IM-produced biopolymer devices.

5.3 Results and discussion

5.3.1 Design and Construction of a Pilot-Scale Injection Molding System

The system was designed to be capable of injecting up to 1.5 cm^3 of polymer per injection, since a larger volume of polymer would likely be required for most applications of drug delivery devices.

We intended our system to serve as a pilot-scale device which could be easily replicated and modified by others in the field. The system was constructed to investigate the feasibility of fabricating parts of arbitrary geometry via IM- for which we would need to test many different polymers and blend/composite formulations before arriving at one which was suitable. In keeping with these goals: we designed the system to accommodate ease of disassembly, and the barrel to ensure ease of cleaning so that various polymers could be tested and various mold designs swapped out with minimal work. It was chiefly for this reason we chose to construct our pilot-scale system with a piston-based constant-pressure design rather than a more conventional augur-based constant-volume design. Such a design also allows for easy cleaning of all components and minimal dead volume for rapid prototyping of molds and materials.

The design of the Pilot-Scale Injection Molding System (Figure 5.1) iterated upon the design of the Desktop Injection Molding System in our earlier work and is

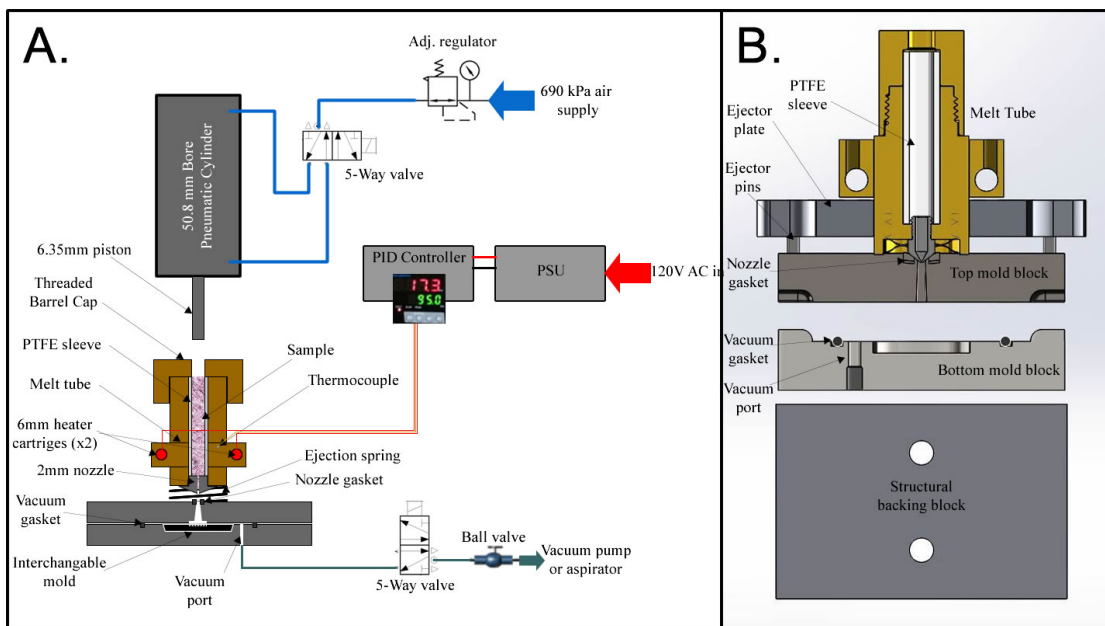


Figure 5.1: Injection molding system design - A) Schematic representation of injection molding system, B) computer aided drafting cross sectional model of critical design elements in the injection molding system

briefly described below. [111] Exact specification, as well as assembly instructions are available in the experimental section 5.5.2 as well as subsections 5.5.3, 5.5.4, and 5.5.5, supplemental figures (Figure 5.10, 5.11, 5.12, 5.13, and 5.14) and supplemental tables (Table 5.2, and 5.3). The system was constructed around a 0.25" (6.35 mm) diameter piston. Due to lab air pressure of 690 kPa, we used a 2" (50.8 mm) bore actuator to exert the necessary force on our larger diameter piston. The larger 2" bore actuator was permanently bolted onto a 3x1" T-slotted aluminum frame where the mold block also slides using a handle to manually increase the friction between the mold block assembly and the rails. Clamping force from the handle creates friction between the backing block and 3" T-slot, which alone was sufficient to hold the mold block in place even at maximum actuator pressure. Two ceramic cartridge heaters and a thermocouple were connected to a commercial PID controller, which was powered by a 300 W 12 V power supply.

Due to the larger barrel diameter of our new system, a larger piston was needed and in order to maintain similar injection pressure on the molten plastic (~ 50 MPa) with the larger piston, a larger pneumatic actuator or a higher pressure would consequently

be required. We opted to use a larger actuator because it would eliminate the need for a costly high pressure pump. Furthermore, keeping the pressure low would increase overall system safety, and allow for others to reproduce our system as 690 kPa is a common supply pressure for in-house compressed air.

The system was originally designed for the mold block to slide along 9/16" shafts but such reinforcement was found to be unnecessary and friction between the backing block and 3" T-slot alone was sufficient to hold the mold block in place even at maximum actuator pressure.

Two ceramic cartridge heaters and a thermocouple were used for heating of the barrel, however after testing this setup, it is recommended to use the highest wattage 6 mm cartridge heaters available - using standard 30 W cartridge heaters will result in excessively long warm-up times and may require external insulation of the melt tube.

5.3.2 Polymer Blend Formulation

Several polymer samples (Table 1) were successfully prepared for injection molding.

Table 5.1: Composition of samples prepared for injection molding.

[†] PLGA is an amorphous polymer and exhibits no clear T_m

#	Polymer(s)	Ratio (wt%:wt%)	Polymer T_m ($^{\circ}\text{C}$)	Polymer T_g ($^{\circ}\text{C}$)	Injection Temp. ($^{\circ}\text{C}$)	Injection Pres- sure (MPa)
1	PCL	N/A	60 [137]	-60 [137]	55-90	9-50
2	PEG 100kDa	N/A	65 [138]	-40 [138]	60-100	35-42
3	PEG 100kDa/ PVP K15	90:10	\sim 65	-35	80-100	35-42
4	PEG 100kDa/ 8kDa/ PVP K15	80:10:10	\sim 65	-35	80-100	35-42
5	PLGA [†]	N/A	N/A	\sim 42.6 [139]	80-120	35-42

Pure polymers were obtained from commercial vendors (Chemicals and Sources are detailed in the Materials section 5.5.1). The blends were fabricated by mixing the bulk powders at their respective ratios and placing them in an aluminum foil pouch on a hydraulic press heated to 100 $^{\circ}\text{C}$. The mixture was heated, pressed, and then folded

on itself three or more times to ensure proper homogenization. Characterization of the melting point of polymer blends along with the as-purchased Poly(lactic co-glycolic acid), (PLGA) was conducted via DSC (Figure 5.15).

5.3.3 Injection Mold Insert Fabrication

A stainless steel mold holder (Table 5.3, “M3/Bottom Mold”) was CNC machined, into which an approx. 1” diameter mold “mold insert” can be placed. A variety of 3D printed insert molds for notional geometries were fashioned without the need to re-machine expensive metal components. The method to create such mold inserts in a laboratory setting is summarized in Figure 5.2.

The fabrication of such 3D printed insert molds was accomplished by first drafting the geometry to be fabricated on a suitable CAD program, and using a boolean subtraction tool to remove the desired geometry from two sides of a mold insert blank. This was then exported as an STL and sliced using a suitable SLA/MSLA/DLP slicing utility (such as Photon Workshop). The mold was then printed in resin (Siraya Blu or Siraya Fast Black), cleaned, washed and sprayed with mold release (CRC Silicone Mold Release #03302), placed in the Pilot-Scale IM System and injected with polymer.

Detailed description of the fabrication instructions for the formation of microneedle array mold inserts is detailed in (Figures 5.16, 5.17, and 5.3).

Because of the reinforcement provided by the steel mold holder, these mold inserts can be made from inexpensive polymeric materials which are easily replaceable. One sample layout for printable inserts is provided for a cylindrical implant shape (Figure 5.2C/5.2F/5.2G, and 5.3). Two other insert molds (“smiley” face, and spherical implants) are shown in Figure 5.2D and 5.2E, respectively. The molded inserts for which are shown in Figure 5.2H and 5.2I, respectively. These 3D printed insert molds are easily designed and adapted to any desired geometry. It was important to design insert molds from a rigid, heat resistant 3D print resin. We used primarily Siraya Tech resins for their high toughness, Siraya Blu was particularly robust and we employed it for the majority of our parts. Siraya Fast Smokey Black was also found to be suitable for 3D printed insert molds.

In designing the 3D printed insert molds, we focused on reducing dead volume between the injection port and the vacuum ring by extending the upper mold insert into the cavity of the upper steel mold tool. Vent ports can be added to one or both sides of

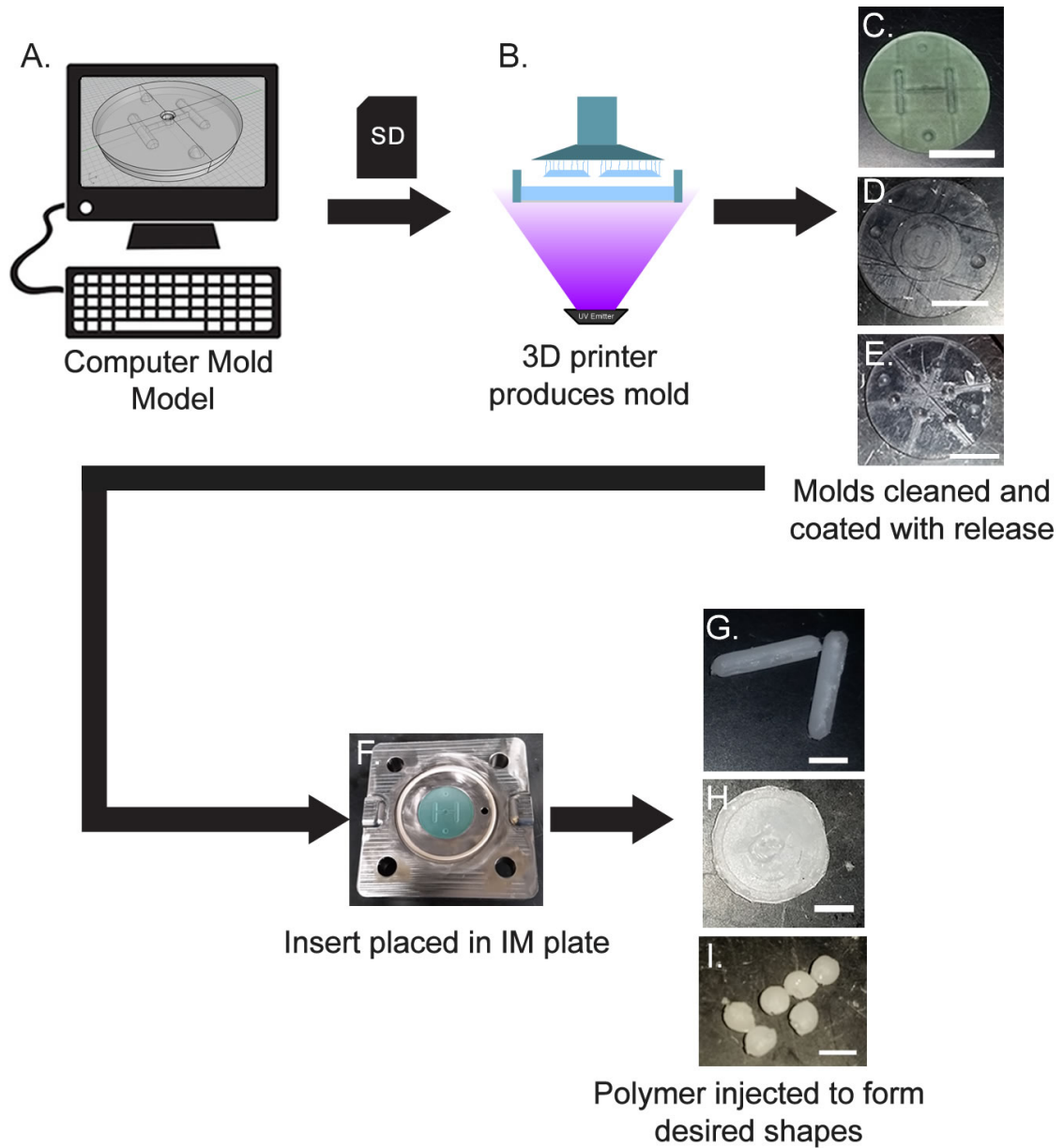


Figure 5.2: Procedure for forming insert injection molds for implants, scaffolds and other arbitrary shapes with millimeter-scale features. A) Mold is drawn on CAD and exported to as STL, B) resin 3D printer produces insert molds, C/D/E) molds are removed from printer, cleaned and coated with silicone mold release, F) placed in the machined IM plate, then G/H/I) injected with molten polymer and the resultant structures demolded. Scale bars: C,D,E: 10 mm, G,H,I: 3 mm.

the insert to facilitate evacuation of the excess polymer after the mold insert cavity has been filled.

5.3.4 Injection Molding Procedure

Injection molding was carried out by first coating all mold surfaces with silicone mold release, placing the mold insert in the steel bottom mold, then assembling the stack and connecting the vacuum line. Finely pulverized polymer (20 mesh or smaller) was then loaded into the melt tube. The melt tube was then heated electrically to the desired temperature and left to equilibrate for 2 minutes once the temperature was reached. The vacuum was then turned on and the setup was inspected to ensure the vacuum seal was good (no hissing noise). The desired injection pressure was dialed in on the regulator (see Table 5.1 for injection pressures and temperatures), and the injection was carried out using the lever-actuated 5-way valve. After injection was complete, the pressure regulator was dialed to 0, and the line pressure allowed to vent. Then the vacuum was broken using the button valve on the vacuum line, and the heating was stopped. The vacuum line was disconnected and the top and bottom mold halves were left to cool for 5-10 minutes. The melt tube was also removed from the piston while the polymer was molten and left to cool separately. After the mold halves cooled, the injection molded structures could be extracted and flashing removed with a pair of scissors or flush cutters (Figure 5.2). The setup could then be re-assembled and the process repeated for additional samples.

5.3.5 Method of Fabrication of Microneedle Insert Molds

While it is possible to simply 3D print many of the insert molds for arbitrary geometries, there are some which require very fine negative (concave) features far below the minimum resolution of traditional MSLA printers, microneedles being one example of such a structure. The goal of fabricating self-administrable microneedle patch based therapeutic devices via IM could yield great advantages in terms of rapid vaccine distribution to developing nations. Effective vaccination ordinarily requires health care professionals (HCP) to administer doses, which is challenging in poor or densely populated areas. Nearly 20 million children were under-vaccinated or un-vaccinated in 2019 and 2.8 million vaccines were lost in five countries due to cold chain failures, with less than 10% of countries meeting WHO recommendations for effective vaccine management practices. [140, 141] A single-dose slow-release implant or microneedle patch based vaccine fabricated using high-throughput IM techniques could accelerate production, distribution and reduce reliance on the cold chain.

To begin our fabrication process we started with a polydimethylsiloxane (PDMS)

negative microneedle mold (which was commercially obtained). One could also choose to fabricate such a positive mold to the desired dimensions and needle sharpness using a variety of silicon etching/processing techniques which are beyond the scope of this work. These are traditionally used as a template to create single-use drop cast microneedle patches from water-soluble polymers such as Poly(vinyl pyrrolidone) (PVP). [142]

However, such silicone molds cannot be used directly in injection molding. PDMS is far too soft and in our initial tests showed that the jet of molten polymer at 50 MPa punctured the center of the PDMS mold without forming any cavities. In order to fabricate a stronger microneedle cavity insert mold, a photocurable HEMA resin was used as a transfer material to cast an insert from high temperature epoxy without sacrificing geometric details or concave needle sharpness.

poly-hydroxyethyl methacrylate (pHEMA) was chosen as the material of choice for this procedure because it could be cured in a reasonable timeframe without the use of additional crosslinkers, using an ordinary photoinitiator, while still forming a rigid resultant polymer which could retain its shape and small geometric features after demolding from the silicone. It could then be dissolved in solvents such as DMSO/HNO₃ to remove all traces from the fine features of the resultant mold.

Fabrication of insert molds (Figure 5.3) was accomplished by first adding a photocurable 2-hydroxyethylmethacrylate (HEMA) resin (2.5 wt% BAPO and 2.5 wt% TPO photoinitiators added to a solution of neat HEMA previously passed through basic alumina to remove inhibitors)- to the PDMS mold and centrifugally casting at 3000 rcf in a bucket-wheel centrifuge for 5 minutes to remove air bubbles. The molds were then cured under UV light (0.34 mW/cm² for 4 minutes) and the HEMA mold positives (transfer molds) were carefully removed from the PDMS. A mold tooling jig (Figure 5.17D) was then printed, along with a negative casting mold (Figure 5.16A). The casting mold was then incubated in a vacuum oven set to 65 °C o/n with full vacuum, then sputtered with gold, coated with aliphatic mold release (1 part light mineral oil in 20 parts hexane v/v) and PDMS resin (Sylguard 184 1:10 initiator w/w) was poured into the mold and cast to form an outer insert mold which was placed in the jig from Figure S1 (Figure 5.16D). The positive pHEMA microneedles were then sputtered with gold and attached using double-stick tape to the adjustable placement mount (Figure 5.17C), which was screwed into the top tooling mount and attached to the bottom mold jig. The PDMS insert in the jig was coated with aliphatic mold release then filled with high temperature epoxy

which was previously degassed under vacuum and heated to 50 °C to facilitate ease of flow into the small features. After filling the jig with epoxy, the entire assembly was placed into an oven set at 65 °C o/n at atmospheric pressure.

The epoxy was demolded from the PDMS jig, the printed parts were broken off from the double stick tape, and the top of the epoxy was sanded flat to expose the pHEMA. The mold insert was then submerged in neat DMSO at 37 °C for 1 hr under gentle agitation to swell the pHEMA. The mold was then removed from the DMSO and the majority of the softened pHEMA was removed with tweezers. The insert was then washed twice with deionized water and submerged in a glass beaker containing a mixture of 1M HCl and 5M HNO₃ at room temperature for 2 min in an ultrasonic bath to clear the remaining pHEMA from the small microneedle cavities. The mold was then washed again with DI water to remove any residual acid.

Of note about the procedure: it is important to NOT to wash the mold with bicarbonate or basic solution to neutralize the acid - this may cause pitting and deformation of the epoxy mold. It is also important to note that these times and concentrations for the DMSO and acid steps were painstakingly engineered and while we do not claim our values to be perfectly optimized, we found detrimental results were obtained with longer DMSO or acid soak times, higher concentrations of HNO₃, or higher DMSO soak temperatures – all of which resulted in destruction of the microneedle molds. Unsatisfactory results were also obtained when shorter soak times or lower concentrations were used, resulting in blunted needle tips as a result of the incomplete removal of pHEMA.

A combination of HCl and HNO₃ was required to fully remove the pHEMA from the microneedle tips. We hypothesize that the HNO₃ is required to dissolve the pHEMA, and the HCl (in combination with HNO₃) is required to dissolve the thin coating of sputter-coated gold, allowing the remaining pHEMA to lift-off from the epoxy with the assistance of sonication.

We found that microneedle transfer blanks could also be produced from PVP rather than pHEMA, and the DMSO/HNO₃ washings replaced with warm water. While this greatly simplified the procedure and eliminates the need for a tricky and potentially dangerous aqua regia sonication step, it introduced defects in the mold which are discussed and characterized in greater detail in the supplemental information.

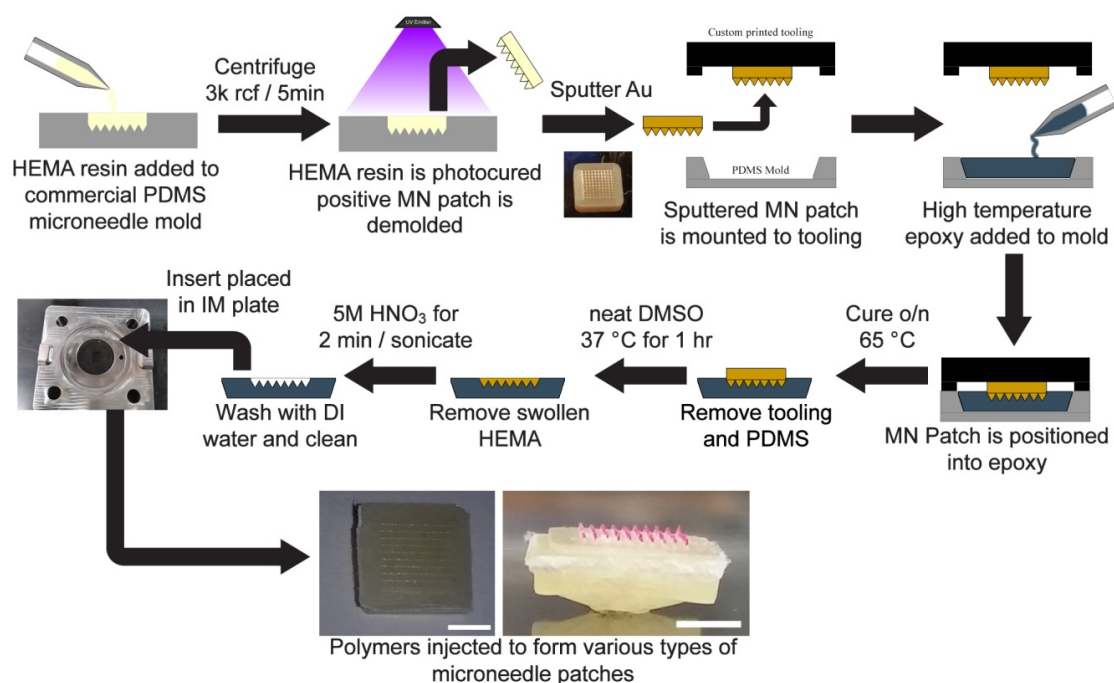


Figure 5.3: Procedure for forming injection molded microneedle patches with micro-scale features. All scale bars: 3 mm.

5.3.6 Polymer Blend Characterization and Testing

Using these newly formed MN insert molds we were then able to fabricate microneedle patches from a variety of materials. We initially struggled to obtain highly sharp microneedles from our insert molds, regardless of mold geometry. We suspect that this was due to the comparatively high viscosity of the injected polymer and the comparatively low injection pressure of our pneumatic piston injector system. We experimented with a vast array of polymers, blends, and plasticizers with the hope of finding a suitable mechanically robust polymer which could be injected into the finely detailed cavities of a microneedle mold and extracted without breaking the sharp tips. The blends which showed promise are listed in Table 5.1 and a summary of our other findings can be found in the Table 5.4, along with rheometry of several polymer blends in Figure 5.4.

Using PCL as a starting point (due to its high flexibility, low melting point and low melt viscosity), we determined that a temperature between 70-90 °C with pre-vacuum was optimal for the formation of sharp tips in this material (Figure 5.18). However, we also sought to fabricate an injection moldable dissolvable microneedle patch.

Polyethylene glycol, (PEG) possessed similar melt characteristics to PCL as well as high solubility in water.

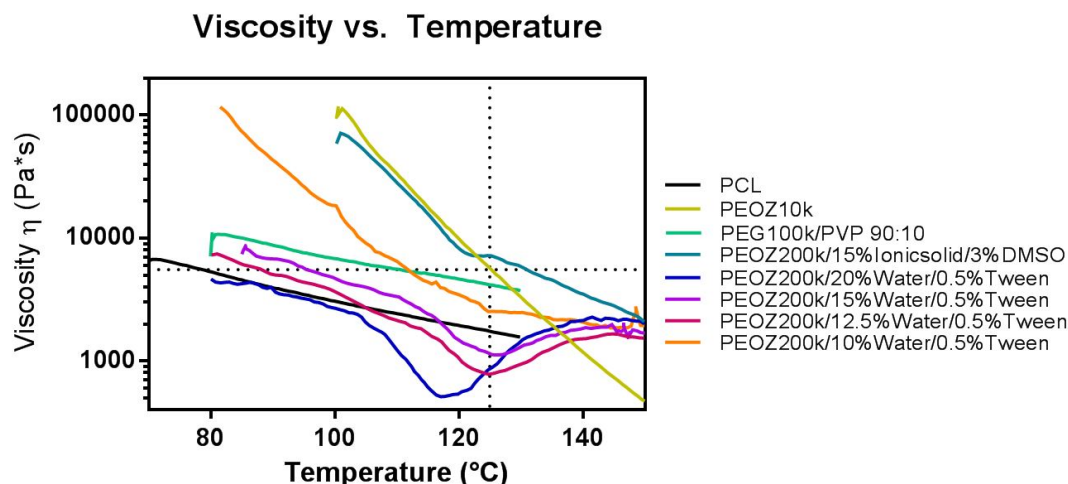


Figure 5.4: Rheometer viscosity profiles of various polymer compositions with respect to temperature. The horizontal line at 5500 Pa*s represents the empirically determined maximum viscosity for which molten polymer tends to adequately flow into microneedle tip cavities. The vertical line represents the maximum safe processing temperature for our rapid prototyped polymeric mold inserts and also the maximum temperature where it is preferable to process biologically relevant adjuvants.

We found that pure PEG 100k offered good mechanical strength, while also possessing a low enough melting temperature (65 °C) to avoid damage to sensitive components during injection. However, PEG 100k by itself dissolved rather slowly and we felt it was necessary to augment it with another polymer: in this case a low molecular weight PVP “K15” in order to allow for faster dissolution in the skin. We created two polymer blends which seemed to offer a best-of-both-worlds solution and our efforts resulted in a microneedle base which could be injected at a temperature under 100 °C, along with good mechanical strength [143], and fast dissolution in moist skin: PEG 100k/PVP 90:10, and PEG 100k/8k/PVP 80:10:10.

5.3.7 Characterization of Microneedle Arrays

IM microneedles were mechanically tested to investigate their needle breaking strength compared to conventional solvent cast microneedles. The mechanical testing

of a PEG 100k/PVP 90:10 polymeric IM MN patch as well as a solvent-cast PVP MN patch is demonstrated in Figure 5.19 and the results from such testing in Figure 5.20. It can be seen that while solvent cast microneedles tended to exhibit uniform stress loading, leading to a surprisingly ductile failure of the PVP tips, the PEG/PVP MN patches had uneven strain response, likely due to their uneven needle lengths. The IM patches required nearly 0.4 mm to settle into uniform strain response, and exhibited a similar ductile failure mode to the PVP cast MN patches. This suggests that even though the PEG/PVP IM MN patches have non-uniform tip lengths, their bending load and consequently their ability to penetrate skin may be similar to that of the solvent cast PVP MN patches. The applicability of such tests to real world conditions, however, is limited due to the fact that real skin is significantly more compliant and would allow the microneedles to penetrate straight rather than bending over on a non-compliant metal plate.

For injection molding of PLGA MN patches, we were able to achieve somewhat sharper tips with higher temperatures (Figure 5.5A), but still not as sharp as those molded from PCL. PCL failed to mold at temperatures below 60 °C, but once above its T_m , we found that further increases in temperature had little correlation with tip sharpness (Figure 5.5B). We also found no correlation between tip sharpness and injection pressure for PCL (Figure 5.5C).

The use of pre-vacuum was found to be critical to achieving high sharpness injection molded microneedle arrays. Arrays molded without pre-vacuum were not as sharp as those with mild or moderate vacuum applied during the injection process (Figure 5.5D, 5.18). We suspect that when injection molding very small features with high aspect ratios, the presence of trapped air plays a large part in determining the sharpness and fidelity of the resultant structures which ordinarily is not seen in macro-scale injection molded parts with comparatively small aspect ratios. The application of even mild vacuum showed a significant improvement in feature resolution over no vacuum. However, the application of a deeper pre-vacuum showed no significant improvement.

When injection molding parameters are adjusted correctly, the needles formed from PCL were nearly as sharp as their pHEMA analogues made from commercial solvent-casting molds (Figure 5.6A, 5.6B). However, we found it was more difficult to make sharp microneedles from high molecular weight PEG100k, PLGA, or blends of such due we suspect to their lower mechanical toughness and tendency for small needle tips to

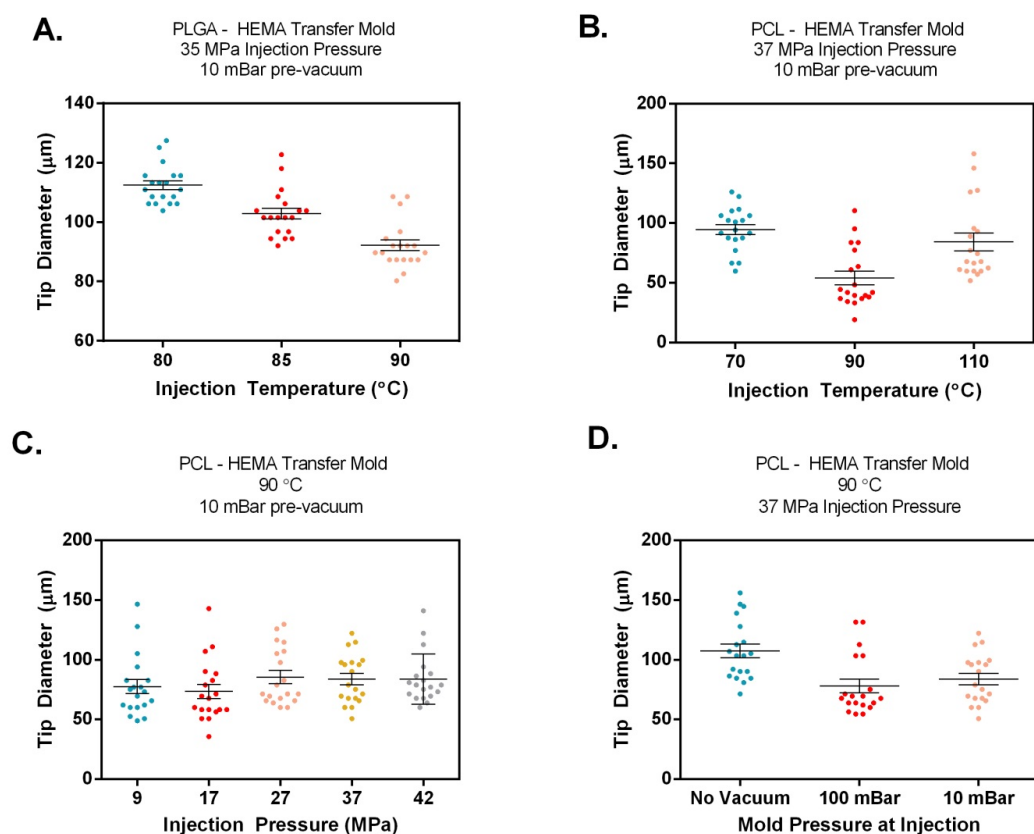


Figure 5.5: Summary of data taken from electron micrographs of many microneedle patches injection molded with a variety of settings showing effect of changes in pressure, temperature, polymer material and use of pre-vacuum: A) effect of varying injection temperature on PLGA, B) effect of injection temperature on PCL, C) effect of varying injection pressure on PCL, and D) effect of pre-vacuum on tip diameter of PCL. Tip diameter was measured directly by image analysis of MN patch samples via SEM.

break off in the mold rather than pulling out with the base material like those molded in PCL (Figure 5.6C). Patches fabricated from PLGA presented additional difficulties due to PLGA's amorphous nature and high melt viscosity coupled with its comparatively low molecular weight (resulting in poor/brittle mechanical properties), with many patches breaking upon attempts to remove them from the mold.

Microneedles containing embedded microparticles (Figure 5.6D, and 5.8) are especially promising due to the potential to embed active delivery systems or controlled release devices within the microneedle tips allowing for self-administration of prime-boost vaccines to be accomplished in seconds by the end user with controlled drug or vaccine

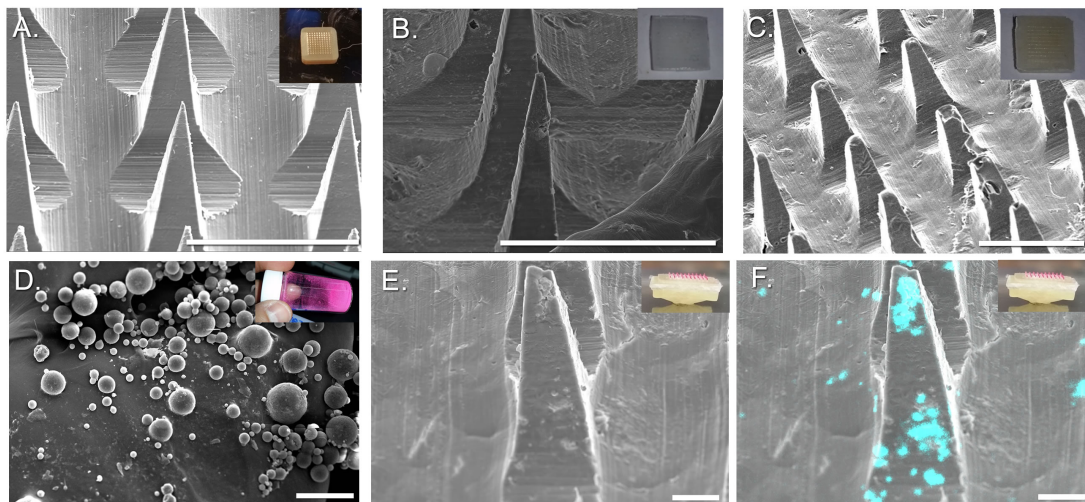


Figure 5.6: Injection molded microneedles - A) poly 2-Hydroxyethylmethacrylate (pHEMA) positive cast used to form negative microneedle cavity mold, B) injection molded microneedle patch in poly(ϵ -caprolactam) (PCL), C) injection molded microneedle patch in poly(ethylene glycol) $M_w=100,000$ (PEG100k), D) PLGA microparticles doped with rhodamine B (for fluorescence microscopy – Pd/C was the dopant for EDS), E) SEM micrograph of PEG100k/poly-Vinyl Pyrrolidone (PVP) dissolvable microneedle patch with PLGA microparticles, and F) EDS Pd $L - \alpha$ composite map showing microparticles concentrated at the tips of needles. Scale bars: A, B, and C: $500 \mu\text{m}$, D, E and F: $100 \mu\text{m}$.

nanoparticle release which could last for weeks or months. [144,145] Microparticles were loaded into the IM insert mold by manually loading dry microparticle powder onto the cavities of the insert mold prior to injection. We found that during injection molding, microparticles consistently remained in the needles as the molten polymer flowed around them. This phenomenon is evident from photography (the red color in the needle tips is due to the presence of RhB-doped PLGA microparticles) and was verified by EDS using Pd/C doped PLGA microparticles (Figure 5.6E and 5.6F).

We found that the sharpness of the microneedle tips (indicating the quality of the injection molded parts by demonstrating a quantitative measure of minimum feature size/aspect ratio) was limited by melt viscosity, mechanical strength of the polymeric material (to retain tips during demolding), and also by an unknown factor which seemed to limit tip diameter to $50\text{-}100 \mu\text{m}$ even in the best-case materials with low melt viscosity (PCL). Exploration of this limitation was pursued, but ultimately left unsolved. We suspect that the thermal mass of the molds may play a pivotal role in this edge case. As the

polymer flows and the needle cavity narrows and the polymer's thermal mass decreases in proportion to the reduction in cross sectional area, the temperature of the polymer approaches the temperature of the cold mold, resulting in early solidification prior to full penetration of the needle cavity. This would explain why the epoxy needle molds showed high fidelity at the base of needles, but the tips were blunted. We attempted tests with molds made from other materials such as stainless steel, which showed poorer fidelity and needle cavity filling (likely due to their increased thermal mass). However our studies on such molds are ongoing and conclusive results have yet to be obtained.

In future iterations we suspect that sharp tips may be obtained by through-drilling the mold insert and applying vacuum through a fritted stainless steel disk to ensure the polymer does not contact the sides of the mold past a certain aspect ratio (roughly 1:8). Pre-heating of the mold insert may also accomplish a similar function, but the current iteration of the prototype is not set up to conduct such tests.

5.3.8 Delivery of Microneedle Payload

To demonstrate needle penetration and in vitro delivery across porcine skin we fabricated fluorescently labeled microneedles embedded with PLGA microparticles containing an orthogonal fluorophore. Dissolvable PEG microneedles with embedded PLGA particles (Figure 5.7A) can be fabricated with high throughput at low temperature (90 °C), and with sharp enough tips to penetrate porcine skin (Figure 5.7B, 5.7C shown after 40 N pressure applied for 120 s).

For our porcine skin experiments, PVP was mixed with FITC in a solution of methanol (250 mg/mL PVP with 10 mg/mL FITC), then the methanol was removed using a vacuum oven and drying under vacuum for 24 h at 100 °C to yield a brittle powder which was incorporated with PEG 100k in a 10:90 ratio by weight, via the method stated in Table 5.1, composition 3 to produce a FITC-doped composite polymer.

Such microneedles not only release their prime payload (shown in green FITC fluorescence in Figure 5.7C, 5.7D, and 5.7E), but also deposit PLGA microparticles (shown in red RhB fluorescence) up to 440 μm into porcine skin.

A GIF video showing fluorescence microscopy of the partial dissolution of a similar patch dissolving in a pH 5.5 20% acrylamide gel. [146] The microneedle patch was pushed into the gel, left to dissolve for 2 minutes, then the patch backing removed and images were taken at 2 minute intervals using a digital fluorescence microscope - show-

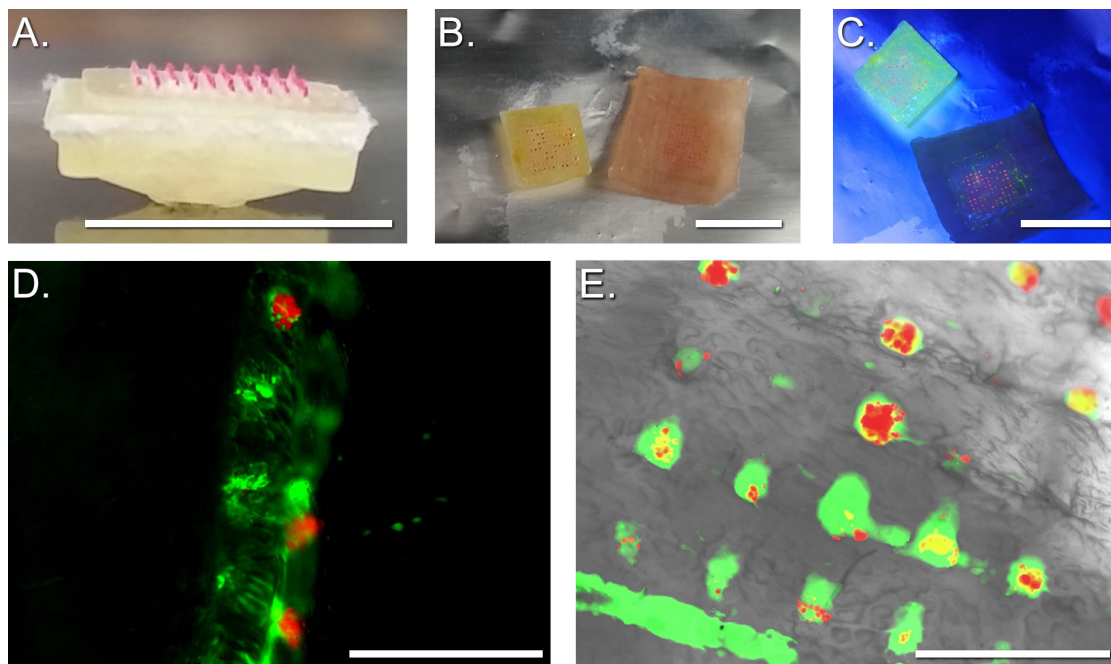


Figure 5.7: Demonstration of dissolvable microparticle-laden microneedles fabricated via an injection molding approach. A) FITC-containing MN patch with Rhodamine-containing MP after de-molding, B) MN patch after pressing into porcine skin using 40 N force for 120 s under white light, C) under 395 nm UV light, D) composite cross sectional fluorescence micrograph of porcine skin after MN injection, E) composite transmission fluorescence micrograph of porcine skin after MN injection. Scale bars: A-C) 10 mm, D-E) 1 mm.

ing diffusion of the FITC (green) into the acrylamide gel on the right hand side but the microparticles containing RhB (red) remain in place in their cavities. SEM images of the microparticles (after injection molding with PEG 100k/PVP 90:10, and dissolution of needles in pH 5.5 buffer) show some agglomeration of the PLGA microparticles (Figure 5.9) which could serve to slow release kinetics but remains to be determined definitively.

5.3.9 Characterization of Microparticles

PLGA microparticles were prepared using both a solvent-based and solvent free method.

In the solvent-based method, 100 mg of PLGA powder along with 1 mg of dye (rhodamine B, RhB) or 10 mg of EDS contrast agent (Pd/C) was dissolved in 1 mL of ethyl acetate. The solvated PLGA was then injected into a bath of water containing

1g/L poly(vinyl alcohol) under strong stirring to form small microparticles, which were then filtered and dried in a vacuum desiccator over calcium chloride for 24 hr before use (Figure 5.8A). [147]

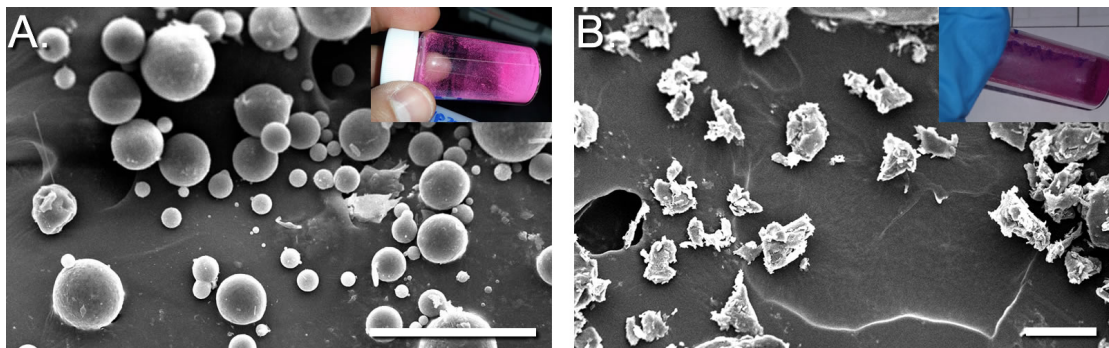


Figure 5.8: Microparticles used in various microneedle tests - electron micrograph and photograph of rhodamine B- doped microparticles: A) made using ethyl acetate/water method, B) made using solvent free cryo-ball milling process. All scale bars: 100 μm .

In the solvent-free method, 100 mg of PLGA powder along with 1 mg of dye (or 10 mg contrast agent) was mixed thoroughly and then passed through a polymer melt processing system to homogenize the mixture. Such homogenization can also be carried out using a heated press or vacuum oven via melting and refolding. The solid mass of PLGA with embedded dye was then placed in a ball mill, submerged in liquid nitrogen, then milled for 5 minutes at 50 Hz oscillation frequency (Figure 5.8B).

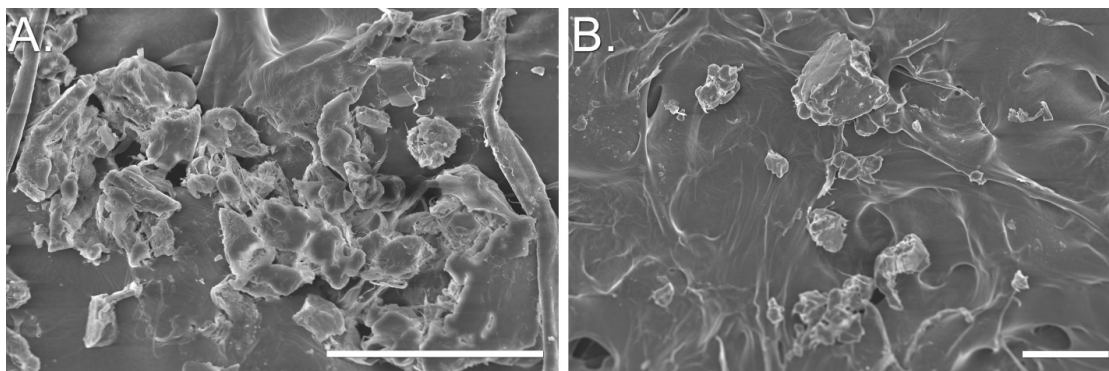


Figure 5.9: SEM micrographs of PLGA microparticles A) made using ethyl acetate/water method, B) made using solvent free cryo-ball milling process. After injection molding into patch needles and dissolution in 0.15M pH 5.5 citrate buffer following by drying in a desiccator. All scale bars: 200 μm .

5.4 Conclusion

We have constructed a pilot scale injection molding (IM) machine to demonstrate the production of arbitrary geometries which can be created via pHEMA/epoxy transfer casting or resin 3D printing of interchangeable insert molds on an inexpensive MSLA 3D printer (Anycubic Photon <\$300 MSRP). These epoxy or 3D printed insert molds greatly simplify the system's design and reduce prototyping cost dramatically, allowing greater flexibility in research and development of new geometries and materials for injection molded medical devices. The system has a small bench footprint (1x1 sq ft.) and can be constructed for under \$3,000 which puts it well within the reach of academic and industrial labs who may not have the space or budget for more expensive conventional injection molding systems. Our work includes a full set of plans, CAD drawings, machining documents, bill of materials, STL files, assembly instructions, and injection molding parameters along with an optimization of molding parameters has been provided so that others may replicate and improve upon our system design.

We have also successfully demonstrated a scalable system for the production of dissolvable IM microneedle patches from well-studied polymers (PEG/PLGA/PVP). The sharpness and strength of these microneedles produced has been characterized. Such MN patches could one day hold the key to the delivery of therapeutic doses at scale without the need for low temperature cryopreservation, HCP administration or cold-chain infrastructure. These microneedle patches could be adapted to not only deliver small molecules and therapeutic nanoparticles but to do so with controlled release capability built-in. Samples of microneedles fabricated using our system were characterized via SEM and EDS. Furthermore, porcine skin penetration was conducted to validate the viability and release characteristics of microneedles produced using this method.

The scalable production technique we have demonstrated thus far represents a significant step forward in the manufacturing of self-administrable medical devices which may one day aid in the scale and distribution of therapeutics worldwide and help to curb the spread of future pandemics.

5.5 Experimental Section

5.5.1 Materials

Polycaprolactone (PCL) powder (Cellink Part #TP60505001, MW 50 kDa), Poly(ethylene oxide) (PEG-100k) powder (Alfa Aesar, 042236.14, MW 100 kDa), Poly(vinyl pyrrolidone) (PVP-K15) powder (TCI, P0471, MW 10 kDa), Polyvinyl Alcohol (PVA) powder (Sigma, 81381-50G) and Poly(2-ethyl-2-oxazoline) 200k MW, (PEOz) powder (VWR International, BT225725-100G), were injection molded as received. Rhodamine B, Diphenyl(2,4,6-trimethylbenzoyl) phosphine oxide (TPO), 2-hydroxyethyl methacrylate (HEMA), and Phenylbis(2,4,6-trimethylbenzoyl) phosphine oxide (BAPO, also known as Irgacure 819) were purchased from Sigma and used as received. N-vinyl 2-pyrrolidone (NVP) was purchased from VWR Scientific and used as received. Fluorescein isothiocyanate (FITC) (Chem-Impex, 00860), High Temperature Epoxy (MG Chemicals 832HT, Amazon B005T8PQFC), Sylguard 184 PDMS (Amazon #B004IJENBG), and high strength DLP printer resin (Siraya Blu Urethane blend, Siraya Fast Black, and Siraya Simple clear blend - Amazon #B089SLXDFH, #B084JPQTRT, and #B084J71JL6 respectively) were used as received. PLGA (Akina, AP041, 50:50 LG Ratio, MW 10-15 kDa) was ground in a mechanical blender (Magic BulletTM, Amazon #B012T634SM) and passed through a 45 mesh screen (Sigma, Z675415) prior to injection and/or processing.

Acrylamide (Acryl 40) and Tetramethylethylenediamine (TEMED) were purchased from VWR Scientific and prepared into a 20% gel by combining 5 mL Acryl 40, 2.2 mL DI water, 2.6 mL pH 5.5 1.5 M citrate buffer, 100 μ L 10% SDS solution, 100 μ L 10% APS solution, and 10 μ L TEMED – the gel was left to polymerize for 12 hr before insertion studies were carried out.

Many commercial epoxies were tested and only the MG Chemicals High Temperature epoxy exhibited resistance to warm DMSO, high mechanical strength and good dimensional stability at elevated temperatures.

5.5.2 Equipment/Instrumentation

A heated press (Dulytek Model DHP7) was used to mix polymer blends (such as VP:PEG) prior to injection. Solvent-casting PDMS microneedle molds were obtained from Micropoint Technologies (MPatchTMSilicone Template ST-24, 8x8 mm, 10x10 nee-

dle, 675 μm height, 200 μm base, 500 μm pitch). 3D printed parts were produced on an Anycubic Photon MSLA printer (Amazon #B07TVW9HGH). Rhinoceros 3D version 3 (Robert McNeel & Associates) and Solidworks (Dassault Systems) Computer Aided Drafting (CAD) software was used for design and drafting of the pilot scale injection molding system. Anycubic Workshop V2.1.2 (Anycubic Corporation) was used to prepare STL files for printing. A Thermo Scientific Lindberg/Blue M VO914A vacuum oven was used for vacuum degassing of PDMS and epoxy. Precision loading and mechanical testing of microneedle patches was carried out using CellScale Univert mechanical testing apparatus with 100 N load cell, which was adjusted to apply a constant 40 N compressive force on a patch into porcine skin for the penetration assays, and 1 mm/min constant speed ramp applied for the compressive failure studies with 15 Hz sample rate. Optical fluorescence microscopy was carried out on a Life Technologies EVOS FL 4300 imaging system. Electron microscopy was carried out using a FEI Quanta 600 SEM. Gold sputter coatings were applied using a Pelco SC-7 Auto Sputter Coating system. Ball milling of microparticles and powdered polymers was conducted using a Fritsch Pulverisette 23 ball milling system using a 10 mm stainless steel ball in a Teflon sample holder. Differential Scanning Calorimetry was carried out using a Perkin Elmer Pyris Diamond Low Temperature DSC. Rheometry was carried out on a TA InstrumentsTMDiscoveryTMHR-30 Hybrid Rheometer.

A Prusa i3 Mk3 fused deposition modeling 3D printer was used to print the files from ABS filament purchased from Amazon. 3D printing services (such as Shapeways and 3DHubs) offer custom 3D printed parts and can be employed to fabricate the parts if 3D printing is not available to the individual user.

Other equipment recommended:

- Flush cutters
- Wire strippers
- Soldering iron/solder/flux
- Heat shrink tubing/ electrical tape
- Various wire gauges
- Crimp or solder connectors for quick assembly/disconnection

- K-type thermocouple (Amazon B074DL428K recommended, more accurate and durable than NTC thermistor)
- Allen key set
- Teflon tape
- A variac, 12v/8A+ laptop adapter or AC wall plug
- Nylon zip ties

5.5.3 Mechanical Assembly

All numbers in (parentheses) refer to the items enumerated in the bills of materials: Table 5.2, and 5.3.

The first and perhaps most tricky step in assembling the mechanical structure of the pilot scale desktop injection molding system is the assembly of the heated barrel. The barrel consists of 6 core components. Three machined from brass, one replaceable reamed Teflon tube, one replaceable 3D printer M6-threaded nozzle, and a wave spring (Figure 5.10A).

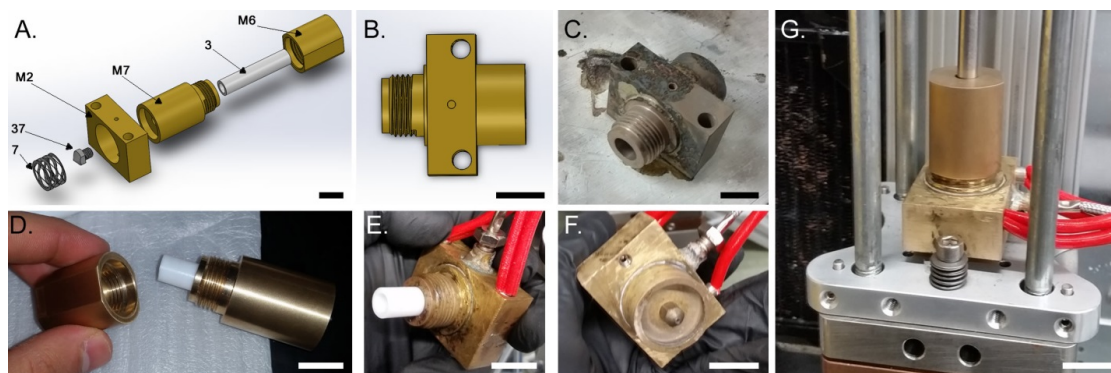


Figure 5.10: Photographs and computer aided drafting models of the heated barrel and assembly procedure. All scale bars: 15 mm.

The machined parts (M2) and (M7) are positioned as shown in Figure 5.10B, the internal mating surfaces coated with flux (42) and then they are held in place with metal clamps and heated to soldering or brazing temperature. If soft (tin/lead) solder is used, the maximum service temperature of the system will be limited to the solder's melting point (typically 200-180 °C). If higher temperature is desired, the joints may be brazed

using silver solder (41) and higher temperature (Figure 5.10C), allowing for service at temperatures up to the decomposition point of Teflon (260 °C).

The Teflon barrel (3) must fit snugly into the melt tube. After the parts have been brazed and cooled, it is recommended to ream the inside of the brass melt tube with a 0.3850" reamer (1), and the inside of the Teflon melt tube with a 0.2550" reamer (2) to ensure a close fit (Figure 5.10D). The full assembly complete with thermocouple (included in (35), or any suitable K-type) and heater cartridges (38) can be held in place with set-screws (25) and the barrel can then be assembled (Figure 5.10E).

It is important to insert the Teflon tube first through the top and ensure it is properly seated before screwing on the M6 3D printer nozzle from the bottom (37) (Figure 5.10F). We found that it was beneficial to drill out the 3D printer nozzle to a diameter of between 1.5-2mm for good flow. The system can then be attached to the main injection molding assembly (Figure 5.10G).

The main assembly consists of a support truss made from T-slot framing (9,17), gussets (8, 16) and a structural FRP base plate (18) into which all components are screwed using counter-sunk bolts (22). The adapter standoff (47) is attached to the cylinder (15), and the piston (13) mounted to the adapter (47).

The cylinder (15) is then bolted onto the vertical T-slot frame (17) through the cylinder spacer (M4), and secured using gussets (16) (Figure 5.11). The backing block (M1) is then attached to the vertical frame using specialized T-slot nuts (10), ball detents (24), knurled knob (11), and handle (12), using the threaded rod (26) attached to the handle and knurled knob using Loctite 603 retaining compound (34).

The ejector plate (M5) is then attached to the top mold (M8) through the use of set screws (25), dowel pins (4), Belleville washers (5), and connecting screws (6). It is important to not over-tighten the Belleville washers down as this will prevent the pre-vacuum from forming a tight seal between the bottom mold vacuum chuck and the top mold plate.

Consumable pre-vacuum seals are prepared for the injection port on the top mold made from high temperature chemical resistant Aflas (32). We recommend using a 9 or 10 mm hole punch (43) to punch them out of the sheet and then using an awl to pre-punch a center hole in them to allow the molten polymer to flow smoothly into the mold.

The bottom mold is then prepared with its O-ring (31), and the bottom pre-

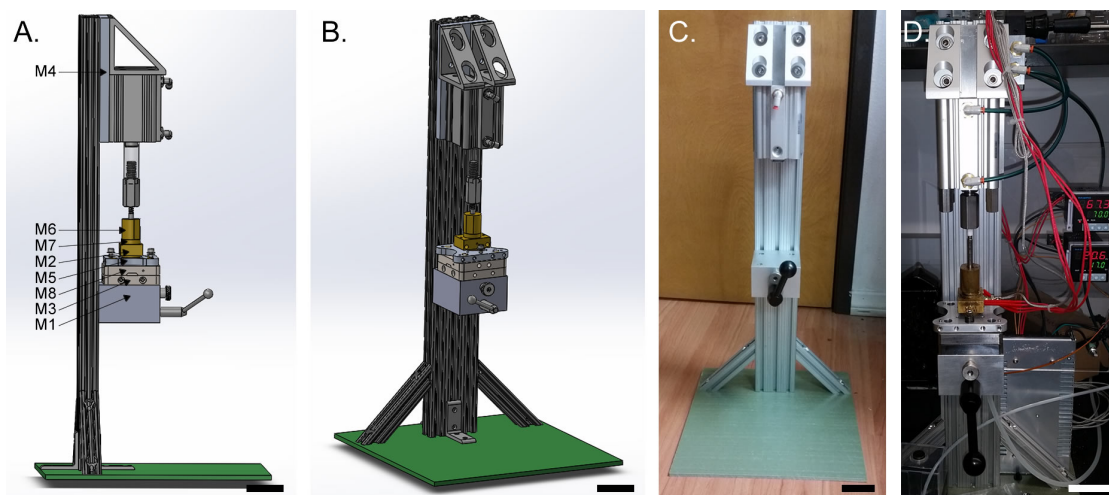


Figure 5.11: Photographs and computer aided drafting models of the assembled mechanical structure of the injection molding system. All scale bars: 50 mm.

vacuum port attached (33).

5.5.4 Electrical Assembly

If using wall current: remove the insulation from your plug cord, and expose the green, blue and brown wires. Further strip the wires and connect to power supply as shown in Figure 5.12. Connect the remainder of the wires using solder and/or crimp connectors. Be sure to use heat shrink tubing and/or electrical tape to insulate all exposed copper before powering on the system. Run long 12" wires between the heater block and the other components of the system, preferably with a quick disconnect connector for easy removal of the heater block. Thread these 12" wires through one of the small holes on the back of the electronics enclosure. Once powered on, the PID controller will need to be tuned and the thermometer measuring device set to the correct type. Follow the Inkbird ITC106-VL manual for instructions.

It is important to note that the user will likely need to set the integral setting of the PID controller manually to a high value to allow the block to heat in a reasonable time. P: 30, I: 500, D: 100 worked fairly well for the system using two 30 W cartridges, but we advise the user to purchase the highest wattage 6mm heater cartridges to allow the block to heat in a reasonable time. Connect the 100k Ohm resistor between the gate and source of the MOSFET to serve as a pulldown on the gate.

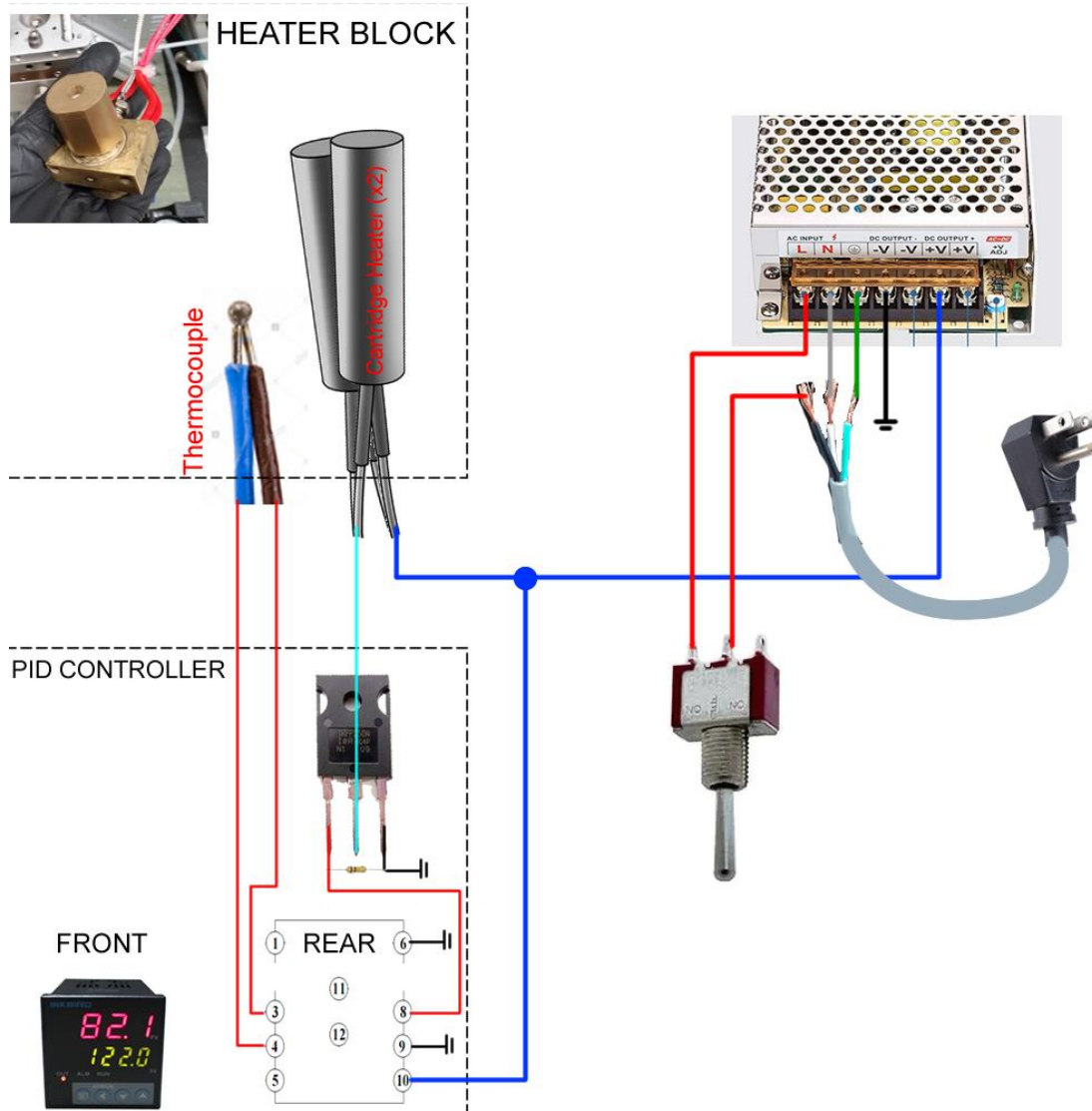


Figure 5.12: Wiring diagram of the electrical system

Once the electronics have been tested, all components can be fit into the electrical enclosure. Secure the AC plug to the inside of the enclosure using a zip-tie to provide strain relief.

5.5.5 Pneumatic Assembly

Connect the pneumatic switch (40), mufflers (39), regulator (20), and cylinder (15) using the NPT fittings (14) and 5/32" hose (19) as shown in the diagram in Figure

5.13. The switch can be mounted to any desirable location, and the regulator can be attached to the base plate using a 3D printed mounting bracket available in the supplemental information of this work. The 3D printed frame has a cutout portion for the gauge. Use of Teflon tape on NPT threads is highly recommended to prevent leakage of high pressure air.

The remaining holes in the rear of the enclosure can pass the pneumatic inlet and outlet tubes. The pre-vacuum system should be connected as shown in Figure 5.14. 1/8" ID soft silicone tubing may be used to connect the bottom mold to the secondary 5 way valve (30) which may be connected through the valve plenum to a pump, ball valve or aspirator depending on the end user's specific vacuum system configuration.

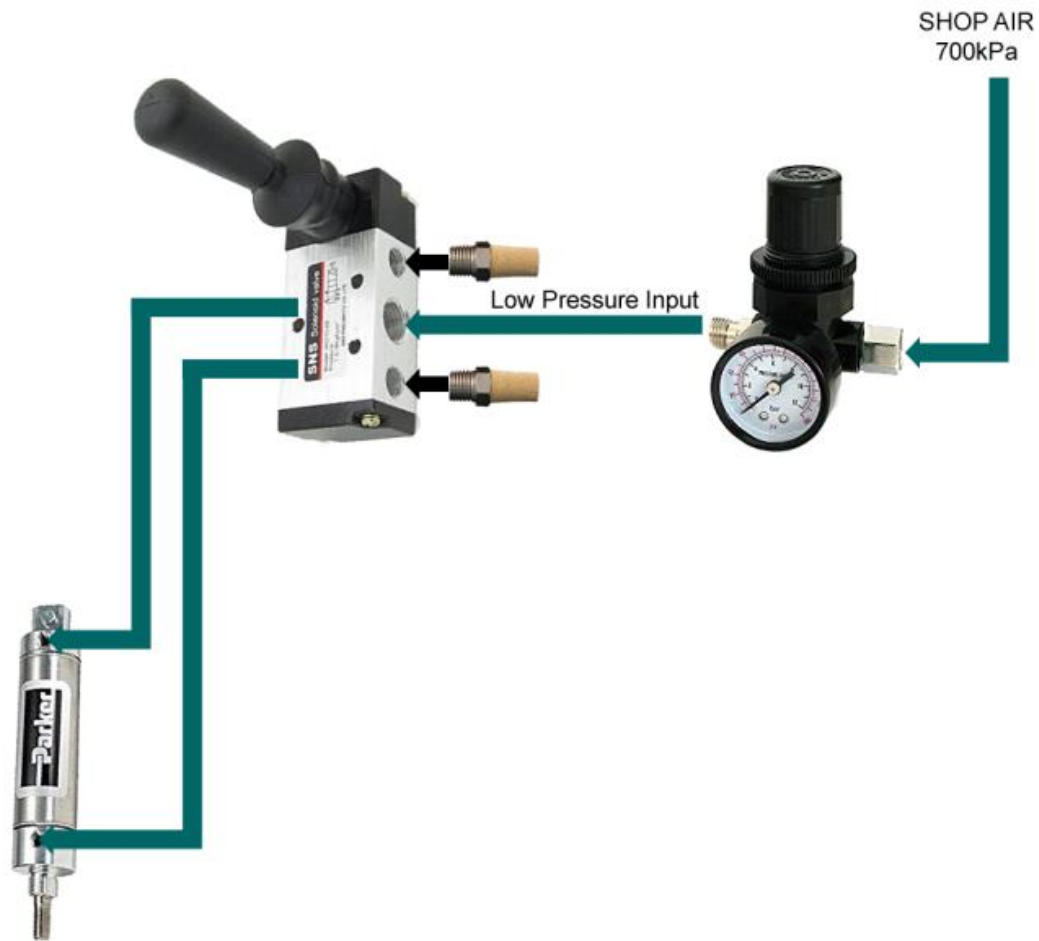


Figure 5.13: Diagram showing pneumatic connections between switch, regulator and cylinder

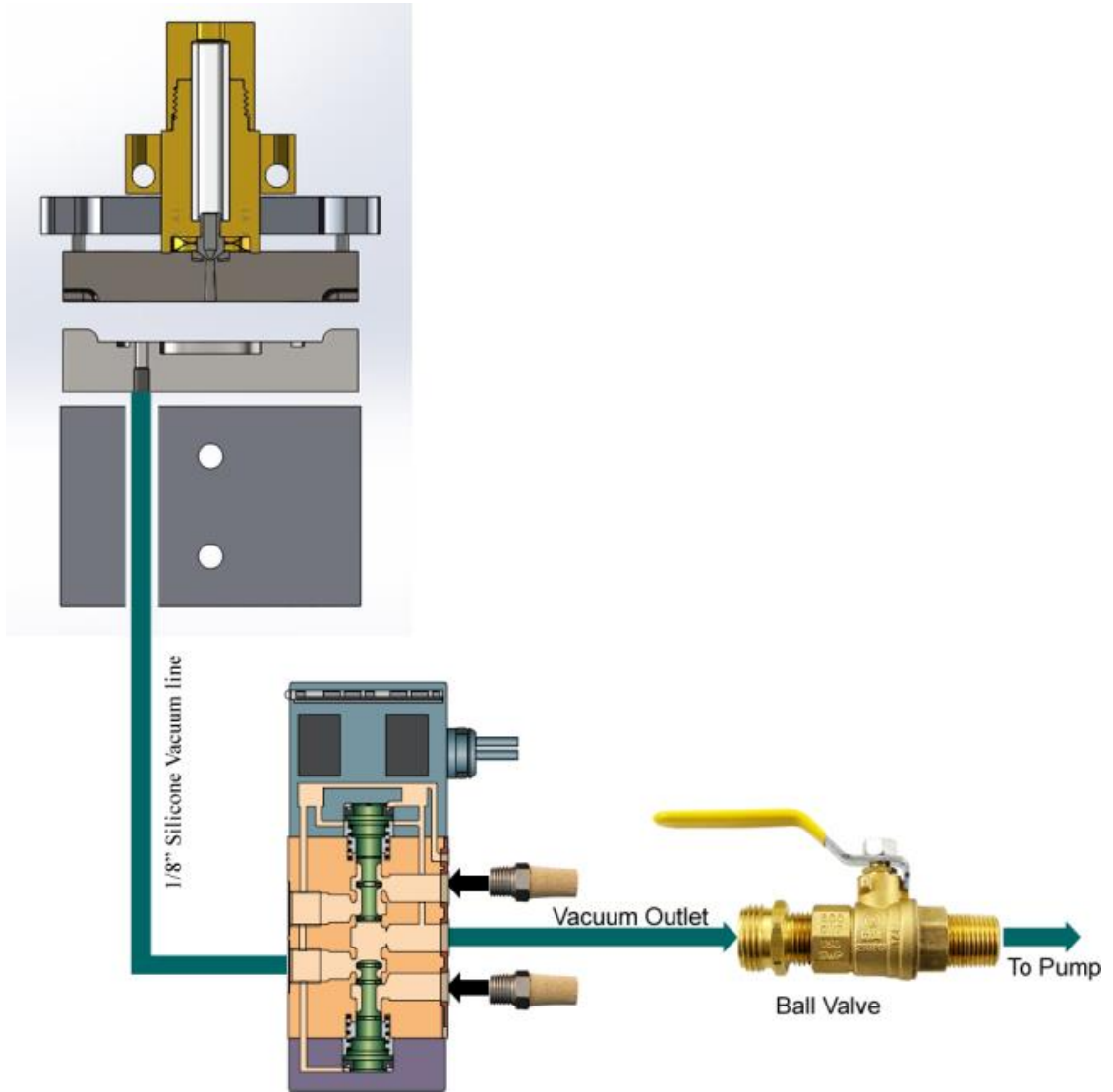


Figure 5.14: Diagram showing mold pre-vacuum system

5.6 Supplemental Figures

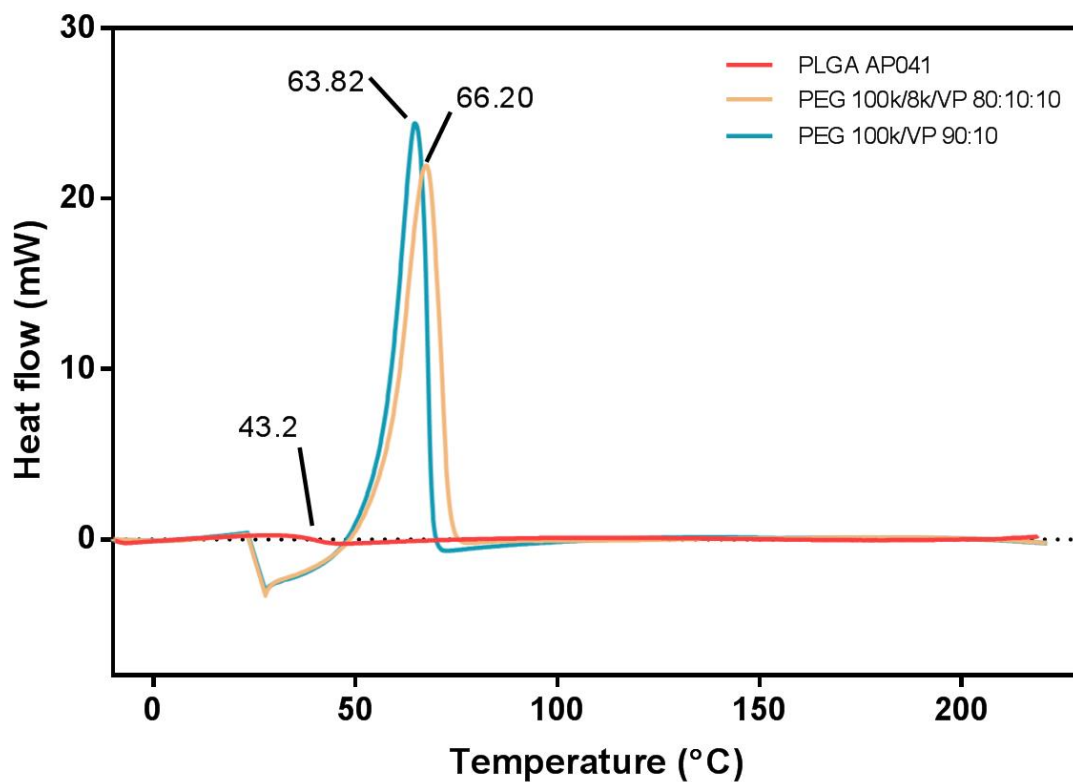


Figure 5.15: Differential scanning calorimetric results showing amorphous character of PLGA AP041 polymer with no apparent T_m and a possible T_g around 43 °C which is consistent with the literature. PEG composites showed distinct crystalline melting behavior with T_m for both approximately 65 °C, the literature value for high molecular weight PEG polymer.

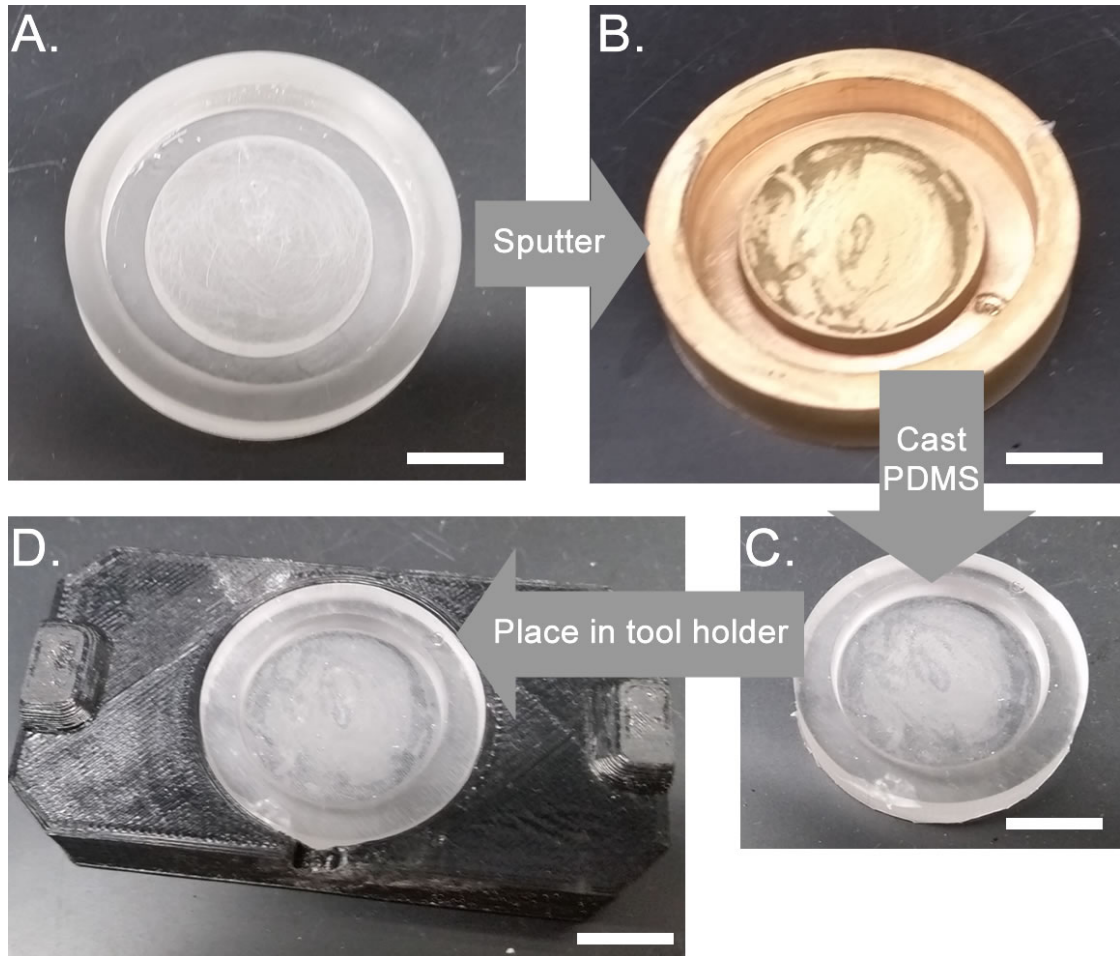


Figure 5.16: Photographs of the preparation of PDMS mold tooling for epoxy casting: A) S2.STL as printed after 12h vacuum bake-out at 100 °C, B) after sputter coating, C) after coating with aliphatic mold release and casting Sylguard 184 PDMS for 12h at 65 °C, D) final placement of the PDMS mold tooling in tooling holder S1.STL. All scale bars 10 mm.

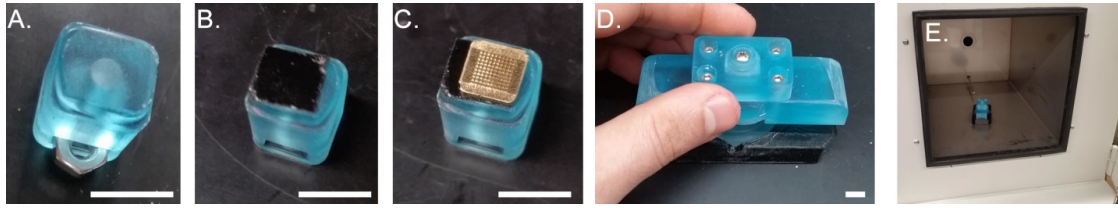


Figure 5.17: Photographs of the preparation of High Temperature epoxy mold tooling: A) S5.STL as printed showing the insertion of 4-40 hex nut, B) S5.STL after adding double stick tape, C) S5.STL after attachment of HEMA positive MN patch, D) photograph of assembled mold tooling (S5, S6 and S7) placed on PDMS mold (from Figure 5.16, coated in release agent) and high temp epoxy added to the PDMS mold, E) assembly of mold tooling placed in oven at 65 °C for 12 hr. All scale bars 10 mm.

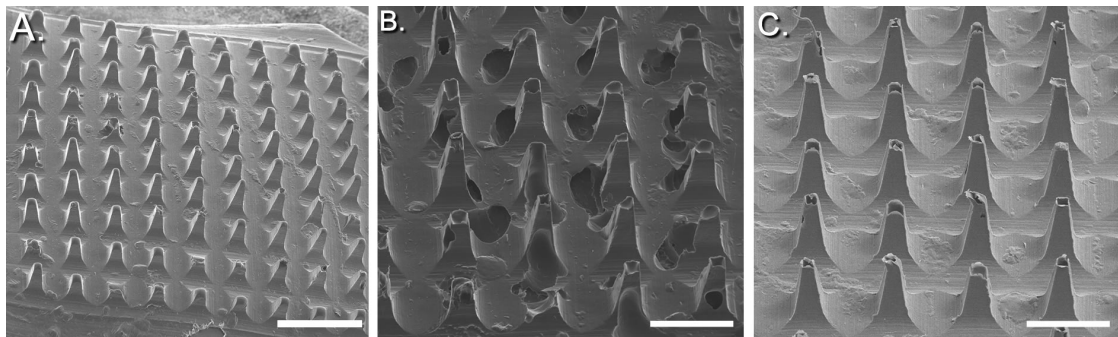


Figure 5.18: Electron micrographs of microneedles fabricated using different processing parameters, all patches were PCL at 37 MPa using: A) 70 °C/10 mBar pre-vac, B C) 90 °C/no pre-vac, C) 90 °C/10 mBar pre-vac. It is important to note the presence of voids and reduced sharpness of tips in (B) is also noted and contrasted with (C) where the needles are well-formed with fewer voids. Scale bars: A: 1000 μm , B,C: 500 μm .

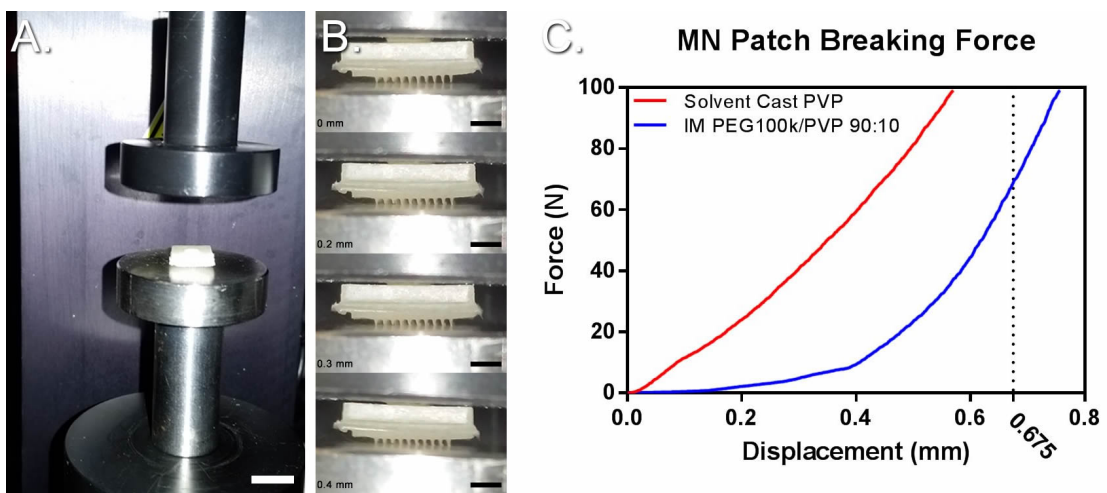


Figure 5.19: Mechanical testing of microneedle patches. A) Photograph of test system, B) time sequence of images showing PEG100k/PVP MN patch at displacements 0, 0.2, 0.3, and 0.5 mm demonstrating bending of MN tips, C) load cell force vs. displacement graph of conventional solvent cast PVP MN vs IM microneedles. 0.675 mm is the theoretical height of the microneedles in both samples. Scale bars: A: 10 mm, B: 2 mm.

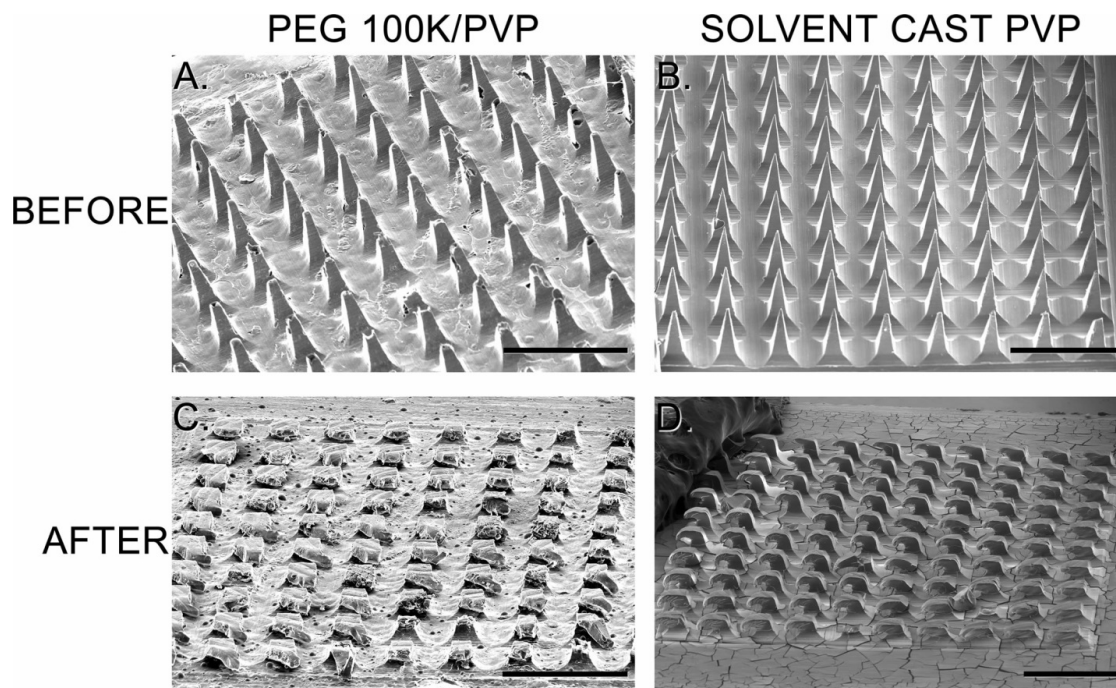


Figure 5.20: SEM images of IM and solvent cast MN patches before and after mechanical testing, showing failure mode on a hard surface: A) PEG 100k/PVP 90:10 patch (shown in Fig 5.19) before testing, B) solvent cast PVP patch (red line on Figure 5.19C graph) before testing, C and D) IM and solvent cast PEG/PVP and PVP patches respectively after mechanical testing. All scale bars: 1 mm.

5.7 Supplemental Tables

Table 5.2: Bill of materials for construction of pilot-scale injection molding system.

No.	Description	Part	Vendor	Qty
1	Reamer, 0.3850"	8803A739	McMaster Carr	1
2	Reamer, 0.2550"	8803A488	McMaster Carr	1
3	Chemical-Resistant Slippery PTFE Tube 3/8" OD X 1/4" ID, 1 ft. Length	8547K11	McMaster Carr	3
4	Dowel Pin, pack, 1/8" Diameter, 1" Long	90145A475	McMaster Carr	1
5	Belleville Disc Spring for 0.216" Shaft Di- ameter, 0.220" ID, 0.437" OD, 0.0160" Thick, pack	9712K17	McMaster Carr	2
6	18-8 Stainless Steel Socket Head Screw, 10-32 Thread Size, 1" Long, pack	92196A274	McMaster Carr	1
7	Stacked Wave Disc Spring for 15 mm Shaft Diameter, 0.20 mm Thick, 10.54 mm High, pack	1561T747	McMaster Carr	1
8	Silver Corner Bracket, 2" Long for 1" High Rail T-Slotted Framing	47065T239	McMaster Carr	2
9	T-Slotted Framing, Silver Diagonal Brace for 1" High Single Rail, 6" Long	47065T186	McMaster Carr	2
10	T-Slotted Framing, End-Feed Triple Nut, 1/4"-20 Thread Size, Packs of 4	47065T991	McMaster Carr	1
11	303 Stainless Steel Knurled Knob with 1/4"-20 Threaded Through Hole, 3/4" Di- ameter Head	60205K221	McMaster Carr	1
12	Steel Adjustable-Position Handle with 1/4"-20 Threaded Hole, 3" Projection	6272K12	McMaster Carr	1
13	18-8 Stainless Steel Partially Threaded Stud, 1/4"-20 Thread, 3" Long	97042A240	McMaster Carr	1
14	Push-to-Connect Tube Fitting for Air and Water, 90 Degree Elbow, 5/32" Tube OD x 1/4 NPT, Brass Threads	5111K194	McMaster Carr	4
15	Flexible-Mount Air Cylinder, Double Act- ing, 2" Bore Size, 2.5" Wide, 2" Stroke Length	62245K253	McMaster Carr	1
16	Silver Gusset Bracket, 3" Long for 1-1/2" High Rail T-Slotted Framing	47065T762	McMaster Carr	2
17	T-Slotted Framing, Triple Rail, Silver, 3" High x 1" Wide, Solid, 2 Feet Long	47065T512	McMaster Carr	1
18	Structural FRP Fiberglass Sheet, 12" Wide x 12" Long, 1/4" Thick	8537K25	McMaster Carr	1
19	Hard Nylon Plastic Tubing for Air and Water Semi-Clear White, 7/64" ID, 5/32" OD, 25 ft. Length	5548K72	McMaster Carr	1

Table 5.2: Bill of materials for construction of pilot-scale injection molding system.

(Cont.)				
No.	Description	Part	Vendor	Qty
20	Easy-Set Precision Compressed Air Regulator, 1/4 NPT Female, 0-160 PSI	4963K31	McMaster Carr	1
21	Single Scale Pressure Gauge with Plastic Case, 1/8 NPT Male Center Back Connection, 1-1/2" Dial, 0-160 PSI	3847K72	McMaster Carr	1
22	18-8 Stainless Steel Hex Drive Flat Head Screw, 1/4"-20 Thread Size, 3/8" Long, Packs of 50	92210A535	McMaster Carr	1
23	T-Slotted Framing, End-Feed Single Nut with Button Head 1/4"-20 Thread Size, Packs of 4	47065T139	McMaster Carr	2
24	Slotted Spring Plunger with 440C Stainless Steel Ball-Nose, Steel Body, 1/4"-20 Thread, 2-4 lb. Force, without Thread Lock	3408A73	McMaster Carr	2
25	18-8 Stainless Steel Cup-Point Set Screw, 8-32 Thread, 1/4" Long	92311A190	McMaster Carr	1
26	1/4-20 stainless steel threaded rod, 4"	95412A558	McMaster Carr	2
27	4-40x1/2" screws	92196A110	McMaster Carr	1
28	4-40 bottoming tap	2522A735	McMaster Carr	1
29	4-40 hex nut	91841A005	McMaster Carr	1
30	5 way valve spring return actuation	62475K38	McMaster Carr	1
31	Soft Viton Fluoroelastomer O-Ring, Chemical-Resistant, 1/16 Fractional Width, Dash Number 030	1284N131	McMaster Carr	1
32	Chemical- and Steam-Resistant Aflas Rubber Sheet, 6" x 6", 1/8" Thick	5499T14	McMaster Carr	1
33	10-32 x 1/8" tube ID Barb tube fitting	4406T12	McMaster Carr	1
34	Loctite 603 Retaining compound	B0074NALBO	Amazon	1
35	Inkbird ITC-106VL PID Temperature controller	B01L8BD8H6	Amazon	1
36	240W 12V PSU	B01E6S0JS4	Amazon	1
37	M6 3D printer nozzles	B07XYW6FL5	Amazon	1
38	2V 50W Upgraded Ceramic Cartridge Heater	B07RGDR87M	Amazon	1

Table 5.2: Bill of materials for construction of pilot-scale injection molding system.

(Cont.)

No.	Description	Part	Vendor	Qty
39	uxcell 1/8PT Male Thread Brass Air Exhaust Silencer Muffler Gold Tone 10 Pcs	B00OK97QCW	Amazon	1
40	5 way valve lever acting 1/4" manual	B07L3F7CSX	Amazon	1
41	Harris Safety-Silv 56% 1/16 Sil- ver Solder Brazing Alloy 1 Troy Ounce, 75310 5631	B0713Y6V2F	Amazon	1
42	Harris SSBF1 Stay Silv Brazing Flux, 1 lb. Jar, Black	B00EDMM4KU	Amazon	1
43	Hole punches	B01L9CTMWE	Amazon	1
44	Power MOSFET	IRFP250N	Mouser	1
45	100k Ohm Resistor	MF1/4LCT52R104G	Mouser	1
46	AC Rated power switch	612-100-A1111	Mouser	1
47	18-8 Stainless Steel Male-Female Hex Thread Adapter, 1/2"-20 to 1/4"-20 Thread Size	92499A233	McMaster Carr	1

Table 5.3: Bill of machined parts for construction of pilot-scale injection molding system.

No.	Description	Material	Dwg. #	Qty
M1	Backing Block	Aluminum 6061	007	1
M2	Barrel Heaterblock	Brass	002	1
M3	Bottom Mold	Aluminum 6061	004	1
M4	Cylinder Spacer	Aluminum 6061	006	1
M5	Ejector Plate	Aluminum 6061	003	1
M6	Melt Tube Cap	Brass	009	1
M7	Melt Tube	Brass	001	1
M8	Top Mold	SS 17-4 PH	005	1

Table 5.4: Selected unsuccessful polymer formulations used for microneedle injection molds.

Composition	Processing Temp (°C)	Drying	Observations
PVA/10% Water	105	Vacuum Dessicator 60 °C	Minimal needle formation. Melt viscosity likely too high
PVA/20% Tween 20	Water/1% 105	Vacuum Dessicator 60 °C	Minimal needle formation, but better than 10 W. Melt viscosity likely too high
PVA/30% Water	105	Vacuum Dessicator 60 °C	Moderate but insufficient needle formation. Melt viscosity could be too high.
PEOz 200k/20% Ter/0.5% Tween 20	Wa- 90	No	Too sticky and pliable. Deformed when removing from mold. However, needles seemed to form needles nicely.
PEOz 200k /10% Ter/1% Tween 20	wa- 95	Dessicator 60C	Needles melted
PEOz 200k /10% Glycerol	100	No	Sticky gunk w large crystals. Glycerol is not promising.
PEOz 200k /10% Xylitol	120	No	Did not melt well. Crystals. Xylitol is not promising.
45% PVA/ 10% water	45% PEG/ 115	No	Suggestion from literature. PVA did not fully melt, crumbly.
PEOz 200k /10% DMSO/1% Tween 20	Xyli- 115	No	Failure to form desired geometry
PEOz 200k /10% DMSO	water/ 100	Vacuum Dessicator 60 °C	Severe bubbling in dessicator
PEOz 50k	137	No	Removed from mold, but still quite brittle. Did not form good needles at 137 °C.
PEOz 200k	167		Good test, indicated it was a good idea to try 50k
PEOz 67.5%/27.5% Water	200k/10k w/5%	Metal Dessicator Worked	Poor needle formation.

5.8 Acknowledgements

Chapter 5, in part, has been submitted for publication of the material as it may appear in “Fabrication of an Inexpensive Injection Molding Instrument for Rapid Prototyping of High Precision Parts”, Wirth, David M.; McCline, Leonard G.; Pokorski, Jonathan K., *Polymer*, 2022. The dissertation author was the primary investigator and author of this paper. This work was sponsored in part by the UC San Diego Materials Research Science and Engineering Center (UCSD MRSEC), supported by the National Science Foundation (Grant DMR-2011924), as well as NSF awards OISE 184463 and CMMI 2027668.

Chapter 6

Directed Biological Polymerization of Aniline

6.1 Introduction

The objective of this chapter is to discuss a novel method for additive manufacturing by delving into the field of engineered living materials. This novel method focuses on the manufacturing of conductive structures using genetically engineered cyanobacteria in order to catalyze the enzymatic synthesis of polyaniline with minimal top-down direction. Such a process is pursued in order to offer a different approach to the manufacturing of electronics. While there are clear applications for a method of producing structural objects that can break free of the constraints of a traditional manufacturing system's build envelope (as described by Chapter 2 and 3), the advantages of constructing electronics via a living materials approach cannot be overstated. As discussed in Chapter 1, structures produced via a bottom-up process may expand exponentially rather than polynomially, and thus can reach far larger areas or volumes than with existing manufacturing techniques. The largest man-made structure currently in existence (at the time of publication) is the Tesla Giga-Factory in Austin Texas with a floor area of roughly 1 square kilometer. [148] However, bottom-up fabrication of electronics via the self-assembly of living systems (such as cyanobacteria) could enable the rapid creation of a biochemical battery or solar cell with a surface area equivalent to that of a small lake ($>10 \text{ km}^2$), potentially surpassing the energy storage and generation capacity of man-made structures, without incurring the costs of traditional construction.

The current chapter will discuss efforts to construct this cyanobacterial bioelectronic assembly system, a general method proposed, and progress thus far, with the hope that such documentation of results will enable others to build upon the work that has been done to enable bottom-up manufacturing via similar processes in the years to come.

6.2 Background

Since the Paleolithic era, humans have adapted biological materials and the material products of once-living organisms to serve useful functions in our daily lives. Sticks, bones, foliage, and animal pelts were adapted and engineered into including rudimentary tools, weapons, shelter, and clothing. Similarly, the utilization of nonliving materials (stones and metal-bearing ores, etc.) into engineered functions (stone, copper, bronze, and iron) have served as milemarkers through the progress of mankind's technological advancement. While advances in the utilization and harvesting of living materials have gone hand-in-hand with advances in the engineering of inorganic materials, for the vast majority of human history, a conceptual wall existed between these two fields. This wall, which was called the *theory of Vitalism* proposed that living organisms (and the materials of which they comprise) were fundamentally different than the materials that comprised non-living materials. While the physical contradictions of such an assertion are readily apparent in the modern understanding of chemistry and physics; it was not until the mid-1800's that Friedrich Wohler disproved this theory by synthesizing Urea (a product solely of living organisms) entirely from inorganic starting materials. [149] This discovery was fundamental to the field of modern organic chemistry, and one could assert, the origination of the concept of engineered living materials.

In recent years- advancements in computer-aided manufacturing technology along with the emergence of low-cost gene sequencing, synthetic biology and genetic engineering have further blurred the lines between living organisms and engineered systems, and scientists are beginning to craft them both with the aid of digital information processing tools.

For years, biologists have asked the question: can 3D printers and/or optical patterning be used to direct the growth of cells into living structures [150–153]- in other words, can we use engineered machines to facilitate the growth of living things? However, in this chapter we attempt to answer the converse: can we use living things to create engineered machines? [154, 155]

6.2.1 Engineered Living Materials

The field of engineered living materials involves the genetic modification, digital control, biotemplating and biomanufacturing of materials for structural applications [156], biohybrid devices, responsive materials [157], self-assembly or self-assembling of engineered structures. [158, 159] It is distinct from, but related to, the engineering of simple organisms to produce usable feedstocks such as chemical precursors [160], and it leverages bio-organic techniques such as radical polymerization to enable the construction of polymeric structures. [161]

Additive manufacturing has also played a major role in the field, AM systems have been utilized to pattern hydrogels and inorganic structures which can support, sustain and direct the growth of living organisms. [155]

6.2.2 Biosynthetic Conductive Materials

In order to realize the goals of this chapter, namely the directed biosynthetic production of circuitry, an investigation into various conductive materials which can be deposited by biological means should first be carried out.

The first logical choice for conductive materials easily producible by simple biological systems is the class of entirely organic conductive polymers. Melanin is a naturally occurring biological polymer with known conductivity, and can be produced on demand in *E. coli*, however its conductivity in aqueous solution is low (generally $< 10^{-7}$ S/cm) and extensive processing is required to convert it to a form with higher electrical conductivity. [162, 163]

Aniline is a simple monomeric primary amine not readily produced in natural organisms, but a metabolic pathway for its biosynthesis has been proposed. [164] Polyaniline (PANI), the conductive polymerized form, is produced as a result of oxidative polymerization, and was among the first conductive polymers discovered. It was the first documented in the scientific literature. The discovery of the polymerization of monomeric aniline into "aniline-black" dates to the mid 19th century and its properties as a conductive polymer were discovered in the 1960s. [165, 166] Its conductivity is sufficient for many engineering applications (typically 0.1 to 20 S/cm) [167, 168], and it can be polymerized by a wide array of chemical, electrochemical and biochemical processes including enzymatic oxidation by bacterial peroxidases. [169]

Pyrrrole is also a simple monomeric amine, polymerizable into the conductive

polypyrrole (PPy) via chemical, electrochemical and enzymatic means. [170] It also possesses high electrical conductivity of 10^2 to 7.5×10^3 S/cm. [167] Biological processes do produce pyrrole derivatives naturally (including vitamin B₁₂, porphyrins, heme, and chlorophyll), however monomeric pyrrole itself presents significant toxicity and is not naturally occurring, so its biosynthesis in significant quantities may pose a challenge. [171] Nonetheless, groups have demonstrated chemical polymerization of PPy onto the surface of bacterial cells by functionalizing their outer cell membranes with Fe³⁺ cations, allowing the biocompatible PPy to graft-from the cell surface without significant penetration of pyrrole into the cells. Furthermore, photodirected polymerization of PPy has recently been demonstrated in additive manufacturing systems. [172]

Moving away from the amines and looking into the thiophene class of conductive polymers immediately leads to a wealth of studies on poly(3,4-ethylenedioxythiophene) poly(styrene sulfonate) (PEDOT:PSS), a conductive polymer which is easily prepared in aqueous solution with relatively high conductivity (35 to >1100 S/cm) and excellent biocompatibility in its polymerized form. [167, 173–175] Enzymatic polymerization of 3,4-ethylenedioxythiophene (EDOT) to PEDOT is possible in aqueous solution, but the high toxicity of the monomer to bacterial cells is likely to prove problematic for a full biosynthetic pathway. [176] Despite this, there is evidence of naturally occurring thiophenes and thiophene derivatives produced by plants, specifically the *Tagetes* species. [177, 178] Furthermore, Stavrinidou et al. have demonstrated the in-vivo polymerization of an EDOT-derivative, bis(3,4-ethylenedioxythiophene) 3-thiophene butyric acid (ETE-S) via profusion in living plant xylem, lending further credence to the potential future applications of such conductive polymers in biological energy storage applications. [179]

Lastly, the biocatalytic reduction of metals presents a fascinating alternative method for the fabrication of very high conductivity structures and potentially energy storage technologies via dramatically different mechanisms than the conductive polymers. Generally these are formed as nanoparticles reduced from trace metal salt-bearing aqueous environments by bacteria and fungi, of particular interest are gold, silver, copper, platinum, and palladium nanoparticles which can be biosynthesized by a variety of microorganisms. [180] Also of note is research into the genetic engineering of *E. coli* curli fibers which can be secreted with active sites which can reduce metallic gold from a chloroauric acid soln into fiber-like formations. [181] Finally, certain cyanobacteria have also shown the capacity to precipitate gold, silver and palladium nanoparticles out of

various aqueous solutions [180,182]

In summary, a wide variety of biological organisms have demonstrated the capacity to create conductive structures through natural, genetically engineered, or enzymatic means. However, the presence of carbon is abundant in nearly all environments on Earth, and autotrophic organisms have the capacity to capture this carbon from the air itself to form living structures. Therefore, if the goal of this study is to fabricate living structures with minimal top-down feedstock requirements or intervention, an organic conductive element should be pursued. Trace metal salts are rare in the natural environment and present significant toxicity to both microorganisms and people. Thiophene and pyrrole-based conductive polymers, while biocompatible in their polymerized form are not naturally occurring in their monomeric form and many present significant toxicity as well. Thus, polyaniline was chosen for further investigation due to its relatively high conductivity, potential biosynthetic pathway, organic character, and relatively high biocompatibility in its monomer form.

6.2.3 Polymerization of Aniline

The polymerization of aniline is easily demonstrated through the oxidation of aniline to polyaniline with hydrochloric acid and ammonium persulfate (APS); this reaction proceeds to completion within 5-10 minutes after APS (0.135 M) is added to a solution of aniline (10 mM) in 1 N HCl. This reaction can also include crosslinkers such as triphenylamine in order to enhance conductivity. [183] Like many conductive polymers, the conductivity and morphology of the resulting PANI is highly influenced by the presence of dopant species during the oxidative polymerization reaction. In the traditional APS/HCl method this dopant is the Cl^- ion, but many other dopants may be used including: sulphuric acid, acetic acid, camphorsulfonic acid (CSA), poly(styrene sulfonate) (PSS), p-toluene sulfonic acid (PTSA), dodecylbenzenesulfonic acid (DBSA), or polyacrylonitrile. [184,185] The pH of the polymerization strongly affects the conductivity of the resultant PANI. In an oxidizing acidic environment, the aniline forms the conductive “emeraldine” salt form of PANI (thus named for its vibrant green, emerald-like color). In a basic environment, the aniline forms the blue “emeraldine base” form, which is dramatically less conductive, or the violet pernigraniline base in a strongly oxidizing environment. Reducing the PANI from the emeraldine form yields the yellow-clear leucoemeraldine morphology. Of the various forms of PANI, only the green emeraldine

salt is electrically conductive.

Silver nitrate can also be used as an oxidizer in place of APS, which allows the reaction to be accelerated in the presence of light. [186] UV light catalyzes the decomposition of the nitrate ion into a nitrite radical and a singlet oxygen radical which combines with water to form a hydroxide ion and an OH radical. The OH radical attacks the lone pair electrons on the aniline primary amine group, producing a radical aniline ion which propagates the polymerization reaction. This reaction proceeds much quicker than the APS oxidation, with a color change observed in under a minute of UV irradiation (Figure 6.1).

Through this mechanism, the photo-patterning of polyaniline onto various substrates is easily demonstrated. Figure 6.1A shows a photomask through which UV light was irradiated on a filter paper coated in a solution of aniline and AgNO_3 , Figure 6.1B demonstrates the rapid color change associated with UV exposure, and Figure 6.1C shows the remaining conductive traces after washing. Other studies have investigated the acceleration and enhanced conductivity of this reaction in the presence of aniline crosslinkers such as p-phenylenediamine (PPD) or triphenylamine (TPA), with the most conductive PANI generally forming from solutions of a 97:2:1 molar ratio of aniline:PPD:TPA monomers. [187–190] However, silver nitrate is not a readily biosynthesized compound, being dependent on trace metal salts and toxic to many organisms, a more biocompatible alternative oxidizer should be considered.

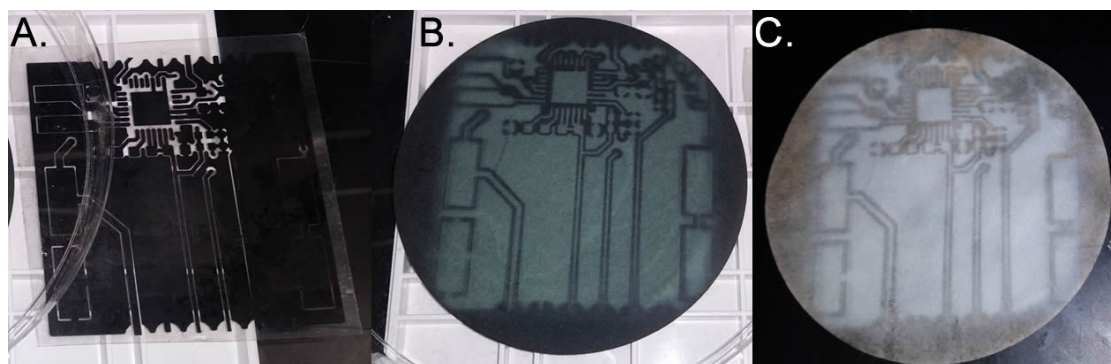


Figure 6.1: The photopatterning of polyaniline via UV exposure and oxidation with silver nitrate. A) Inkjet printer transparency photomask with printed pattern for photolithography, B) 75 mm diameter filter paper after soaking in an aqueous solution of aniline and silver nitrate and exposure to UV light through the photomask (A) for approximately 60 s, C) the exposed filter paper (B) after washing with water.

The polymerization of aniline can also be accomplished via an enzymatic route via the oxidation of aniline in the presence of hydrogen peroxide and horseradish peroxidase (HRP). [169] Zou et al. describe this process within a sodium bis-(2-ethylhexyl) sulfosuccinate (AOT) micellar solution by mixing 1.0 mM aniline and 2.5×10^{-7} M HRP within 10 mL of 200 mM, pH 4.2 buffered AOT micellar solution, then adding 0.6 mM H_2O_2 to trigger the enzymatic reaction.

The use of hydrogen peroxide as an oxidizer is a promising avenue, since it is a commonly encountered molecule in biological systems, readily biosynthesized, and the vast majority of living cells are chemically tolerant of its presence or have naturally evolved protections against its reactivity. Thus, in pursuit of a purely biological route toward the polymerization of aniline, an investigation into both the biosynthesis of hydrogen peroxide and the requisite peroxidase enzymes is required.

It is important to note that the enzymatic catalysis of HRP on the H_2O_2 oxidation of PANI does not necessarily translate to the polymerization of other conductive polymers. This is suspected to be a result of the difficulties associated with the higher oxidation potentials (E_p) of pyrrole ($E_p = 1.2$ V) (Ag/AgCl) or EDOT ($E_p = 1.305$ V) (Ag/AgCl) versus aniline ($E_p = 0.9$ V) (Ag/AgCl), with respect to the potential of the HRP enzyme in the presence of H_2O_2 substrate ($E_p = 1.09$ V) (Ag/AgCl). [170] This oxidation potential difference may be overcome with the aid of a redox mediator (such as 1-hydroxybenzotriazol (HBT) [191]) or the oxidation potential of the pre-conductive monomer may be lowered by using a dimerized derivative. [192] However, without the presence of a mediating species or dimerized reactant it is unlikely that HRP could catalyze the polymerization of pyrrole or EDOT in a similar fashion to aniline.

Table 6.1 summarizes the properties of a few relevant pre-conductive monomers, their respective E_p values and conductivity values.

Table 6.1: List of pre-conductive monomers suitable for enzymatic oxidative polymerization, oxidation potentials and conductivities of resultant polymers

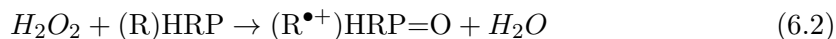
Monomer	E_p(Ag/AgCl)	Polymerized Conductivity (S/cm)
Aniline	0.9V [170]	0.1 - 20 [167, 168]
Pyrrole	1.2V [170]	10^2 - 7.5×10^3 [167]
EDOT	1.305V [193]	35 - 1100 [167, 173-175]

6.2.4 Biological Peroxidase Enzymes

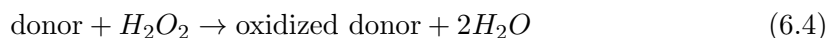
There are a wide variety of biological peroxidase enzymes which have evolved to allow organisms to adapt to many harsh environments. The most well studied of such is the peroxidase of horseradish, its oxidative properties were known since the early 20th century, and today enables a core biochemical assay, the enzyme-linked immunosorbent assay (ELISA). [194] These naturally occurring enzymes are hypothesized to have evolved in organisms in response to harmful biomolecules in their environment such as hydrogen peroxide, reactive radicals, and other toxins. These peroxidase enzymes act upon hydrogen peroxide as a substrate to produce reactive radicals which in turn are used to neutralize the harmful molecule species. The mechanism for this reaction is complex but can best be summarized by the simplified mechanism in Equation 6.1. [195]



In contrast to a peroxidase enzyme, a catalase enzyme dismutates H_2O_2 (a harmful toxin in excess quantities) by converting it into water and oxygen gas in a two step process:



Finally, some organisms, such as cyanobacteria possess a gene for a catalase-peroxidase which is generally used to both eliminate harmful H_2O_2 and also to oxidize other harmful species in the environment (albeit at a lower oxidation potential than the more specialized peroxidase enzymes). [196] The catalase-peroxidase enzyme operates by one of two proposed mechanisms depending on the donor.



From an engineering perspective, the E_p of a peroxidase enzyme in the presence of H_2O_2 determines the scope of reactions it can initiate. Peroxidase enzymes also have an associated activity which is measured in units of U/mg and describes their *rate of reaction*, measured by the amount of 2,2'-azino -bis(3- ethylbenzothiazoline- 6

-sulfonic acid) (ABTS) substrate which can be oxidized in an amount of time with a known concentration of peroxidase in the presence of an excess of H_2O_2 . [197] Table 6.2 describes a few important peroxidase enzymes and their respective oxidation potentials and activities.

Table 6.2: List of peroxidase enzymes, oxidation potentials, and activities

Peroxidase	$E_p(\text{Ag}/\text{AgCl})$	Activity (U/mg)
SBP	1.2V [170]	~ 15 [198]
HRP	1.09V [170]	10-250 [199]
Laccase	1.0V [170]	~ 0.05 [200]
LSPOX	Unknown	0.6-3.4 [201]
APEX2	$\sim 1.0\text{V}$	> 10

Beginning with the most promising: soybean peroxidase (SBP) is an enzyme easily extracted from soybean seed hulls which possesses both reasonable enzymatic activity (8-17 U/mg) and high oxidation potential (1.2V). [170, 202, 203] Its genetic sequence has recently been isolated and its synthetic expression in *E. coli* has also been demonstrated. [204] Due to its high E_p it is able to oxidize many pre-conductive monomers including pyrrole and EDOT. [205] However its biosynthesis and properties are not quite as well studied as HRP.

HRP is the most well-studied peroxidase and thus its production and activity have been heavily optimized owing to its commercial usefulness. Commercial samples regularly attain activities of 150-250 U/mg [199] and its oxidation potential is sufficient to catalyze the oxidation of aniline and even EDOT [176] under some circumstances. It has been sequenced, and its activity as an expressed protein has been optimized via directed evolution. [206] Several groups have demonstrated full biosynthetic expression in *E. coli* and it appears to be by far the most attainable peroxidase for expression in bacteria and controlled oxidation of aniline. [207, 208] However, close examination of the literature suggests that extracellular heme or hemin may be required for proper expression and activity of the expressed HRP protein.

Laccase has also been investigated as a peroxidase-like enzyme capable of oxidation of a variety of substrates, but its oxidation potential is fairly close to that of aniline (within 0.1V) so the reaction may be very slow. Some isolated literature suggests that the laccase-induced enzymatic direct oxidative polymerization of aniline may be

possible. [209] However, because laccase operates by a different mechanism than that of peroxidases, carrying out enzymatic oxidation in the presence of *atmospheric oxygen* (O_2) rather than requiring the presence of soluble H_2O_2 . This is advantageous for many applications including wastewater remediation where O_2 is abundantly available and fine spatial control of the reaction is not needed. However, for the application of directed growth of conductive polymers with fine spatial control required, it may not be an ideal enzyme for the method.

Other peroxidases such as Anabaena 7120 peroxidase or Lyngbya peroxidase (LsPOX) have been studied and may allow for higher expression in cyanobacteria, but ultimately could require more work to optimize for activity and expression in a proposed bacterial conductive polymer generation system. [210,211]

Recently, ascorbate pea coat peroxidase (APEX2) has been sequenced and has emerged as a highly active, easily expressible protein in both mammalian and bacterial cells which does not require the presence of extracellular heme for proper expression and activity. [212] While the activity of this peroxidase is high, its oxidation potential is likely to be similar to that of laccase and lower than that of horseradish peroxidase, due to the fact that it cannot directly oxidize aniline to PANI. Nonetheless, APEX2 has enabled some remarkable applied demonstrations such as that by Liu et al. where a dimerized aniline solution and a low concentration of hydrogen peroxide was exposed, *in-vivo* to mouse and *C. elegans* neurons which had been genetically targeted to express APEX2. [213] These neurons exhibited dramatically different firing patterns than the non-PANI induced samples. However, despite its promising applications in biology, the low oxidation potential of APEX2 and necessity of the use of dimerized aniline monomer limits its application in a purely biosynthetic method for the production of conductive structures. Dimerized aniline is difficult to biosynthesize and is also not shelf stable as it spontaneously polymerizes to PANI in the presence of oxygen.

6.2.5 Cyanobacteria Photo-Induced Production of Reactive Oxygen Species

We have established that the biosynthetic production of conductive wires, specifically conductive PANI wires requires 3 components: aniline, an oxidizer, and a catalyst. Ideally, all three of these components should be organic in nature and easily produced by a bacterial or cyanobacterial organism. Metabolic engineering of aniline has been

discussed, as well as pathways for the expression of peroxidase enzymes in the previous sections. In this section, the biological production of oxidizing species will be investigated.

Some chemical catalysts have been engineered which directly produce H_2O_2 and molecular oxygen from sunlight, but such catalysts are either inorganic (TiO_2) or difficult to biosynthesize (C_3N_4 or other pyromellitic diimides). [214]

Many cyanobacteria species are also known to produce H_2O_2 when exposed to high levels of light. [215] Stevens et al. classify cyanobacteria into four types according to their production of H_2O_2 in response to light (Figure 6.2).

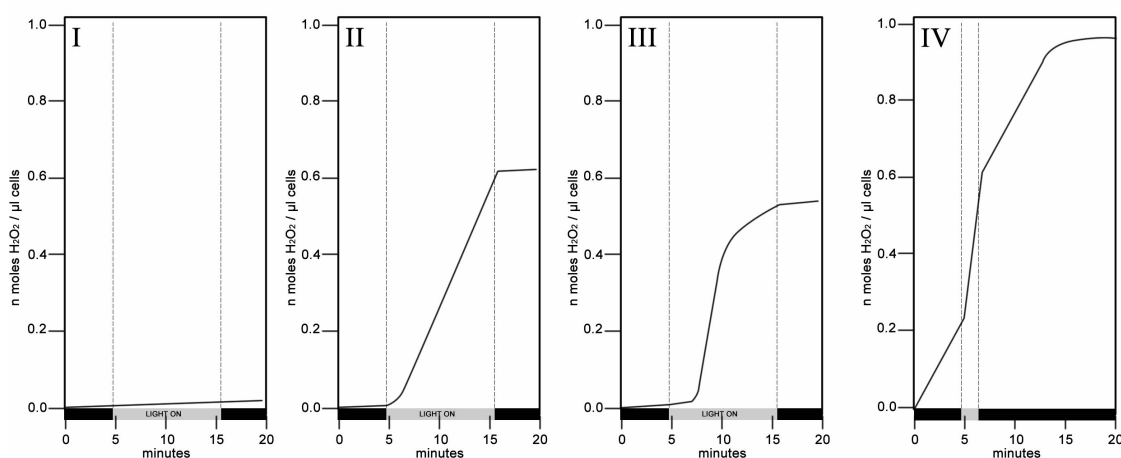


Figure 6.2: H_2O_2 production by cyanobacteria in response to light. Type I shows no response to light in terms of H_2O_2 production, Type II demonstrates a roughly linear production of H_2O_2 in response to light and ceases production when light is turned off, Type III demonstrates linear production of H_2O_2 up until a threshold where production ceases, and Type IV demonstrates production of H_2O_2 even in the absence of light, and demonstrates acceleration of production in response to light, up until a threshold where production ceases regardless of illumination status. (Based in part on a figure contained in: S. E. Stevens Jr., C. O. Pat Patterson, and Jack Myers. The Production of Hydrogen Peroxide by Blue-Green Algae: A Survey. *Journal of Phycology*, 9(4):427-430,1973.) [215]

Of these categories, Type I would be unsuitable. Type IV would similarly be unsuitable if our objective is to control the production of PANI in response to light via controlling the production of H_2O_2 in response to light. Therefore, a Type II or Type III cyanobacteria species would be preferable for the photodirected patterning of conductive structures. *Synechococcus sp. (7942)* is categorized as a Type III producer of H_2O_2 and also exhibits a rapid growth rate in aqueous media. *Synechococcus sp.*

(7942), a unicellular cyanobacteria, has dramatically lower reactive oxygen species (ROS) production than eukaryotic photoplankton. [216] However, its genome has also been fully sequenced and a library of knockout genes has been made available through the CYANOVECTOR tool courtesy of the Golden Lab, making it an ideal platform for genome engineering to harness its H₂O₂ production (and potentially enzymatic expression). [217]

It is important to note that the amount of H₂O₂ produced by most cyanobacteria is relatively low in comparison to the amount necessary to facilitate the enzymatic polymerization of aniline. Where the polymerization of aniline may require 0.2-1 mM of H₂O₂ in solution, cyanobacteria do not naturally produce H₂O₂ in concentrations excess of a few μ M. [218] This is due to the toxicity of peroxide species to the living cells and the presence of two layers of protective enzymes within the cyanobacteria: catalase-peroxidase (katG) and superoxide dismutase (SOD). [219] In order to increase the concentration of H₂O₂ generated by the cells to a usable level, one or both of these protective mechanisms must be either chemically or genetically disabled, or the amount of reactive oxidants generated must be so great as to overwhelm the mechanisms.

One chemical approach to increasing the photo-induced production of reactive species is the use of electron transport chain (ETC) inhibitors such as those shown in Figure 6.3.

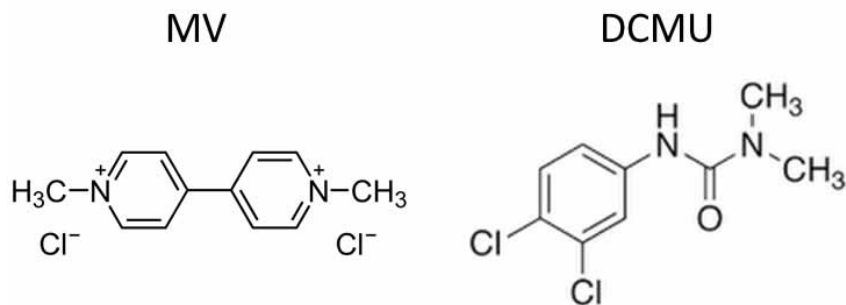


Figure 6.3: The molecular structures of N,N'- dimethyl- 4,4'- bipyridinium dichloride (aka. Methyl Viologen, MV) and 3- (3,4- dichlorophenyl)- 1,1- dimethylurea (DCMU)

Methyl viologen (MV, also known as paraquat) can be used as an ETC inhibitor which in low concentrations blocks the excitation of the P₇₀₀ reaction center of photosystem I, leading to the generation of superoxide radicals (O₂^{•-}) which are converted by SOD into O₂ and H₂O₂. [220] This mechanism has been employed to facilitate the continuous photogeneration of H₂O₂ from water in *Anacystis nidulans R2*. [221] Unfortu-

nately, many species of cyanobacteria (such as *PCC 7942*) possess a catalase-peroxidase enzyme, which further reduces the H_2O_2 into water and oxygen with a limited electrochemical potential for the oxidation of other substrates. Increasing the concentration of MV leads to the rapid generation of superoxide radicals which overwhelms SOD, leading to cell death.

3-(3,4-dichlorophenyl)-1,1-dimethylurea (DCMU) can also be used as an ETC inhibitor which preferentially binds to the reducing side of photosystem II. This action blocks the binding of plastoquinones, leading to a buildup of electrons within PSII which are passed off to nearby water molecules in the form of ROS, these ROS are then reduced by SOD into H_2O_2 . [222, 223] Because DCMU acts on photosystem II rather than photosystem I and the inhibition is not as complete as with MV, it should theoretically be less toxic to the cells and allow the buildup of higher concentrations of H_2O_2 without excessive damage to the photosystems. However, as stated earlier, even if an ETC inhibitor can be employed to stimulate the production of additional H_2O_2 , the action of catalase-peroxidase within *PCC 7942* may reduce it to H_2O before it is able to diffuse out of the cells and into the media, thereby limiting this technique's usefulness.

Using double homologous recombination, it is possible to knock out the gene responsible for the formation of catalase-peroxidase. These knockout cyanobacterial mutants (referred to in the literature as (ΔkatG)) are significantly more sensitive to the presence of H_2O_2 and are also unable to remove it from solution once it forms. [218, 222] Combining this knockout recombinant technique with ETC inhibitors may enable the rapid production of H_2O_2 by cyanobacteria in response to light.

6.2.6 Bottom-Up Manufacture of Polyaniline Conductive Structures

Considering the prior sections, a schema for the formation of conductive PANI structures via an entirely biosynthetic pathway is proposed in Figure 6.4.

In the proposed method, a solution containing genetically engineered cyanobacteria is prepared (Figure 6.4A) which contains either aniline or a metabolically engineered organism capable of secreting aniline. [164] A low concentration of ETC inhibitor may also be required in the initial solution. The cyanobacteria present have been genetically modified to produce a sufficient concentration of H_2O_2 in response to light, and also to secrete HRP continuously into the media (Figure 6.4B). Because extracellular HRP degrades relatively quickly, especially in high temperatures or under intense illu-

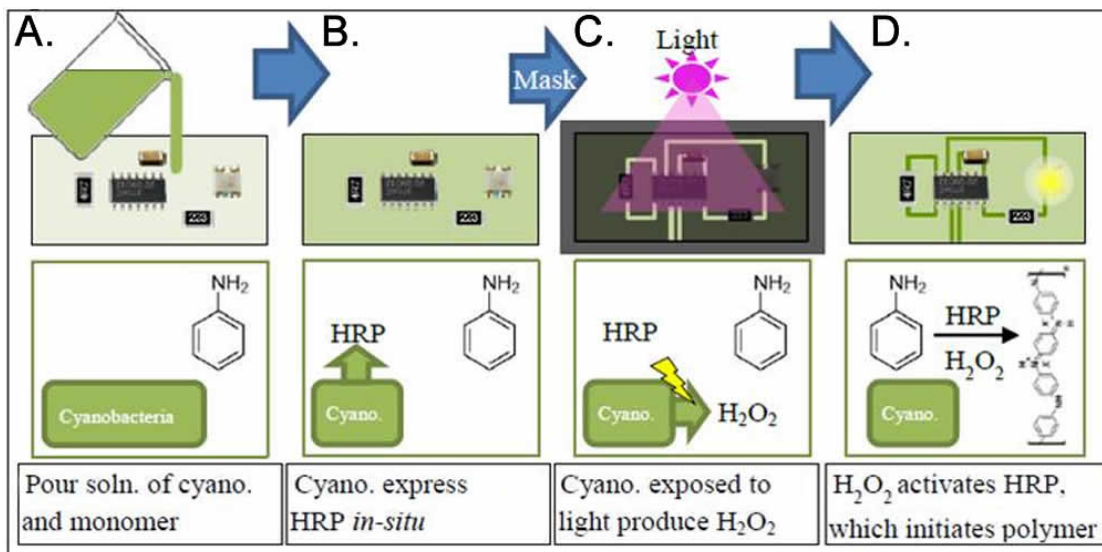


Figure 6.4: Proposed method for the photodirected biosynthetic fabrication of polyaniline wires via HRP-catalyzed oxidation of aniline with H_2O_2 produced *in-situ* by *Synechococcus sp.* 7942. A) Formulation of an solution containing buffer, polyaniline, dopants and cyanobacteria which is poured onto the desired substrate, B) induction of the cyanobacteria to produce HRP *in-situ*, C) photopatterning of cyanobacteria which produce hydrogen peroxide (H_2O_2) in response to light, and D) the substrate with polyaniline in a directed pattern.

mination, its secretion by the cyanobacteria is essential to continued catalyzation of the aniline oxidation reaction. Once a sufficient concentration of HRP has been secreted and (ideally) the cyanobacteria have reached their stationary phase of growth, the media is exposed to a masked or projected light source with a desired pattern (Figure 6.4C) and the cyanobacteria begin producing H_2O_2 in response to light in the desired areas. The areas which contain peroxide, peroxidase and aniline undergo localized polymerization to PANI which is conducting, and conductive pathways form in the desired patterns (Figure 6.4D).

Applied engineering applications of such a system, if fully realized, could enable electrical pathways to connect electrical grids to wide area self-assembled bioelectronic systems such as self-replicating solar cells [224, 225], or self-replicating energy storage devices [226], enabling the production of functional electronic devices far exceeding the scale of traditionally manufactured structures. The rapid production of hydrogen peroxide in proximity to such electrical interconnects could enable energy generation from the production of hydrogen peroxide in such engineered cyanobacteria [227–229], or the

ability to produce hydrogen peroxide as a fuel for aerospace applications on a large scale in resource-constrained environments. [230]

6.3 Results and Discussion

The following sections will detail the attempts and progress made towards the ultimate goal of a self-replicating directed biological system for the creation of conductive structures.

6.3.1 Investigation of Polyaniline Precursor Solution

An initial investigation was conducted into the chemical tolerance of the cyanobacteria *Synechococcus sp.* 7942 (hereafter referred to as simply "7942") in hopes of determining the maximum concentration of precursors which could be added to a solution to demonstrate the oxidation of aniline to PANI without causing immediate cell death. Literature sources [215,222] suggested that it would be necessary for the 7942 to survive at least 20-60 minutes in order to generate sufficient quantities of H₂O₂ under illumination, so for these initial tests, we sought to investigate 1) the optimal concentrations of precursors to quickly and effectively form PANI in solution via enzymatic oxidative polymerization, and 2) what concentrations of precursors would result in an environment too toxic for the 7942 to survive? With regards to the former, it was hypothesized that a successful demonstration of the production of PANI with reasonable concentration (and thus conductivity) to accomplish engineering demonstrations would result in a visible color change of the solution. With regards to the latter, when cyanobacteria are overwhelmed by ROS, they tend to die and/or photobleach. After which, they cease to absorb light energy and therefore no longer produce H₂O₂ in solution. Thus, it is preferable to create a precursor solution in which the cells could survive for at least 20 minutes, preferably for 60-120 minutes, and ideally for an indefinite period.

Figure 6.5 details the process undertaken to answer these two questions. First, a solution comprising: 0.1 M aniline, 0.1 M pH 3.5 citrate buffer, 0.12 M CSA (dopant), 45 U/mL HRP, and 1.176 mM (0.001%) H₂O₂ was noted as a "baseline" starting point for the optimization process. A polypropylene well plate was prepared (Figure 6.5A) with the following rows.

A: Each well charged with 100 μ L of: 0.1 M pH 3.5 citrate buffer, 0.12 M CSA

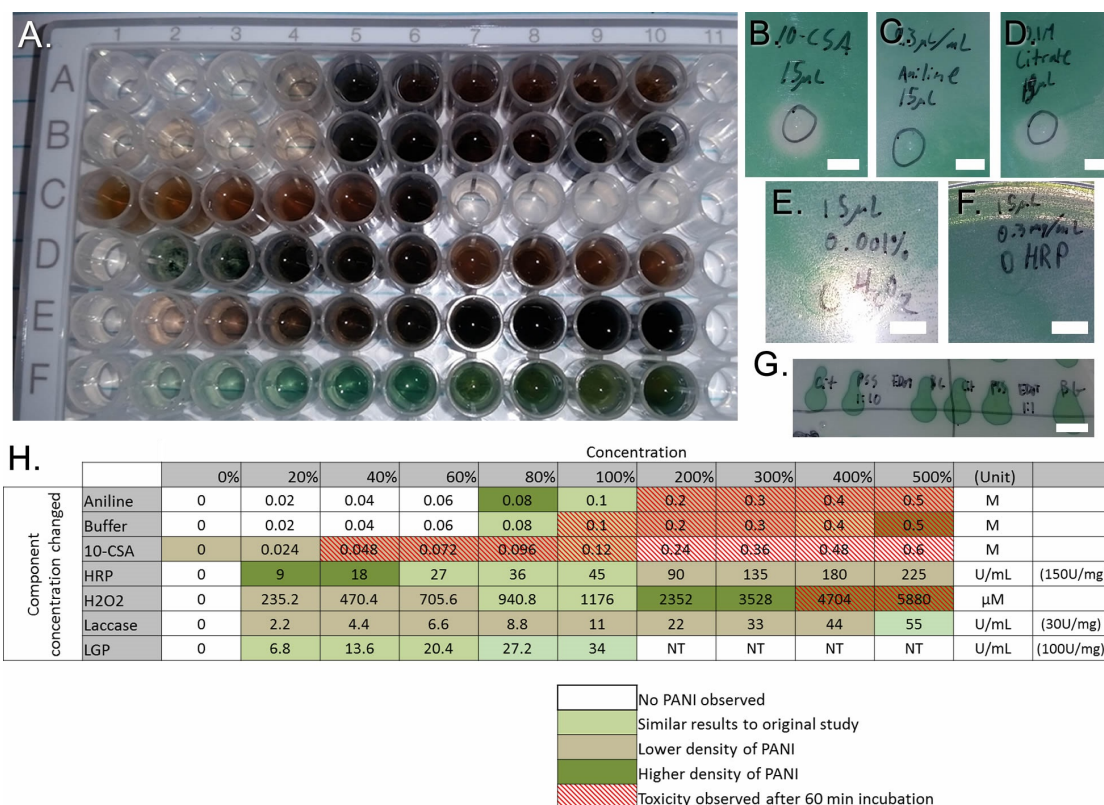


Figure 6.5: Optimization of the enzymatic pre-conductive polymer solution component concentrations. A) well plate prepared with test samples showing variations in color as concentrations of the components were changed with respect to the baseline, B) 7942 agar plate toxicity study showing the photobleaching of 7942 after 60 minutes exposure to a drop of 15 μ L 0.12 M CSA, C) toxicity study showing the results of 60 minutes exposure to 0.1 M aniline, D) toxicity study results for 60 minutes exposure to 0.1 M pH 3.5 citrate, E) toxicity study results for 60 minutes exposure to 1.176 mM (0.001%) H_2O_2 , F) toxicity study showing results for 60 minutes exposure to 45 U/mL HRP, G) alternate toxicity study showing results of 7942 growth after 10 minutes incubation in a solution of (left to right) 0.01 M citrate, 0.01 M PSS, 0.01 M EDOT, and 0.01 M BG-11 (control), 0.1 M citrate, 0.1 M PSS, 0.1 M EDOT, and 0.1 M BG-11 (control). Panel H) shows the summarized results from the toxicity and optimization studies. All scale bars: 5 mm.

(dopant), and 45 U/mL HRP. The concentration of aniline per well was varied from 0% of baseline to 500% of baseline over the course of the row.

B: Each well charged with 100 μ L of: 0.1 M aniline, 0.12 M CSA (dopant), and 45 U/mL HRP. The concentration of pH 3.5 citrate buffer per well was varied from 0% of baseline to 500% of baseline over the course of the row.

- C: Each well charged with 100 μL of: 0.1 M aniline, 0.1 M pH 3.5 citrate buffer, and 45 U/mL HRP. The concentration of CSA per well was varied from 0% of baseline to 500% of baseline over the course of the row.
- D: Each well charged with 100 μL of: 0.1 M aniline, 0.1 M pH 3.5 citrate buffer, and 0.12 M CSA (dopant). The concentration of HRP per well was varied from 0% of baseline to 500% of baseline over the course of the row.
- E: Each well charged with 100 μL of the baseline solution.
- F: Each well charged with 100 μL of: 0.1 M aniline, 0.1 M pH 3.5 citrate buffer, and 0.12 M CSA (dopant). The concentration of laccase (as an alternative enzyme) per well was varied from 0% of the activity of baseline to 500% of baseline over the course of the row.
- G: Each well charged with 100 μL of: 0.1 M aniline, 0.1 M pH 3.5 citrate buffer, and 0.12 M CSA (dopant). The concentration of lyngbya peroxidase (as an alternative enzyme) per well was varied from 0% of the activity of baseline to 500% of baseline over the course of the row.

Once all wells were prepared, hydrogen peroxide was added to all rows except E using a multichannel pipette in order to start the polymerization reaction. In row E, varying concentrations of H_2O_2 were added to each well in order to qualify the effect of varying H_2O_2 concentration on the resultant PANI. Qualitative changes in color and morphology of the resultant PANI were observed and documented in Figure 6.5H. Overall, increasing concentration of H_2O_2 generally improved the amount and quality of the PANI regardless of the other components of the solution. Lower concentrations of HRP were actually beneficial for the formation of PANI, producing larger aggregates (Figure 6.6) and suggesting that slower formation of the conducting polymer with an excess of H_2O_2 may be the optimal path.

Next, BG-11 agar plates were prepared and a "lawn" of 7942 was grown on the plates over the course of approximately 5 days. Once the 7942 had grown on the plates, a drop of each baseline mixture component (Figure 6.5B-F) was added to a separate plate, and the concentration at which a "dead zone" appeared after 60 minutes of incubation was noted on Figure 6.5H with red hashes. Finally, an alternate toxicity study was performed on the mixture components to determine if exposure to the components during

the log phase of growth would affect their ability to grow and propagate (Figure 6.5G). Samples of 7942 were collected and deposited in eppendorf tubes containing either a 1:10 dilution or a full strength solution of the baseline mixture components for varying amounts of time (1, 5, 10, and 60 minutes), then washed with BG-11 by centrifuging down and rinsing 3x prior to depositing a 15 μL drop of cell solution on a clean BG-11 agar growth plate and allowed to grow for 5 days. Of these mixture components, only one resulted in significant toxicity after 60 minutes (in any concentration), which was EDOT. Due to its extreme toxicity to the 7942, this component was disregarded as a possible pre-conductive monomer for future tests.

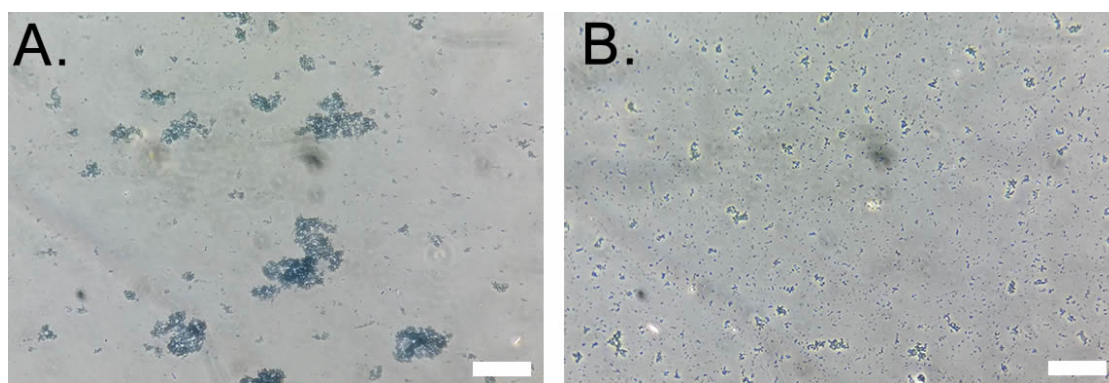


Figure 6.6: Morphological differences in enzymatically produced PANI. A) optical micrograph of the PANI produced from a solution of 0.1 M Aniline, 0.1 M pH 3.5 citrate buffer, 0.12M 10-CSA, **45 U/mL HRP**, and **1.176 mM H₂O₂**, and B) from a solution of 0.1 M Aniline, 0.1 M pH 3.5 citrate buffer, 0.12M 10-CSA, **9 U/mL HRP**, and **5 mM H₂O₂**. All scale bars: 100 μm

The result of these tests was a design space for the formulation of precursor solution (Table 6.3):

Table 6.3: Design space for the components of polyaniline precursor solution

Component	Concentration
Aniline	80-100 mM
Buffer	< 80 mM
Dopant	< 24 mM CSA or up to 100 mM of PSS
Enzyme	Lyngbya peroxidase, HRP, or SBP with activity 1-10 U/mL
H ₂ O ₂	> 500 μM

The baseline enzymatic oxidative polymerization reaction of aniline initiates im-

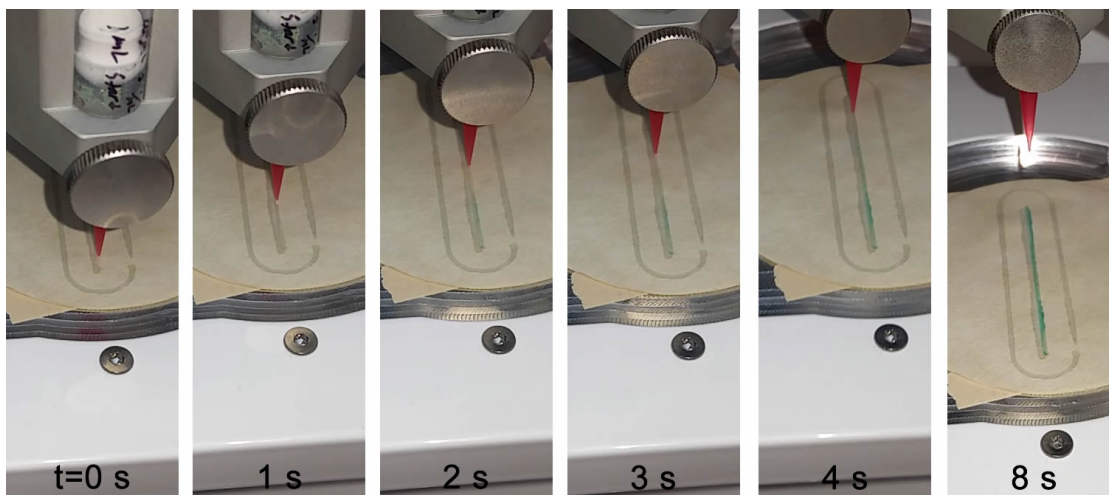


Figure 6.7: Time sequence of images showing the direct ink writing of a Cellink Start hydrogel with 5mM H_2O_2 being printed on a line next to an earlier print of Cellink Start hydrogel containing 0.1 M 97:2:1 (aniline:PPD:TPA) with other baseline components (0.1 M pH 3.5 citrate buffer, 0.12 M CSA (dopant), 45 U/mL HRP) incorporated into the Cellink Start hydrogel and loaded into a Cellink Inkredible+ DIW printer with 22ga nozzles.

mediately upon addition of H_2O_2 , but it requires a few minutes to go to completion. It was found that the reaction can be accelerated by the addition of crosslinking species (such as PPD or TPA) in a 97:2:1 (aniline:PPD:TPA) ratio in place of pure aniline. The use of such crosslinking species accelerates the aniline polymerization reaction to near-instantaneous. This enzymatic polymerization of **crosslinked** polyaniline is (at the time of writing) novel and not demonstrated in the literature, and enables the use of crosslinked PANI precursors in additive manufacturing applications (as demonstrated in Figure 6.7).

6.3.2 Optimizing Cyanobacterial Production of H_2O_2 in Response to Light

Once an optimal solution for the enzymatic polymerization of aniline was developed, the next task was to replicate the results of Stevens et al. [215] with respect to the cyanobacterial production of H_2O_2 in response to light - with the goal of increasing H_2O_2 production to the threshold required ($> 500 \mu M$) for effective formation of PANI through the earlier developed optimized enzymatic polymerization process.

In order to begin this phase of optimization, it was necessary to construct a light exposure chamber which could deliver a controllable light dosage to a sample of cyanobacteria. Such a system was constructed (Figure 6.8) and used for future testing as detailed in this section. The exposure chamber featured a power supply, 200W of potential light power emission (up to 7x sunlight), a water cooling system for the emitters, and heat sink below the cyanobacteria sample chamber in order to dissipate the heat from the intense light source and control the temperature of the samples.

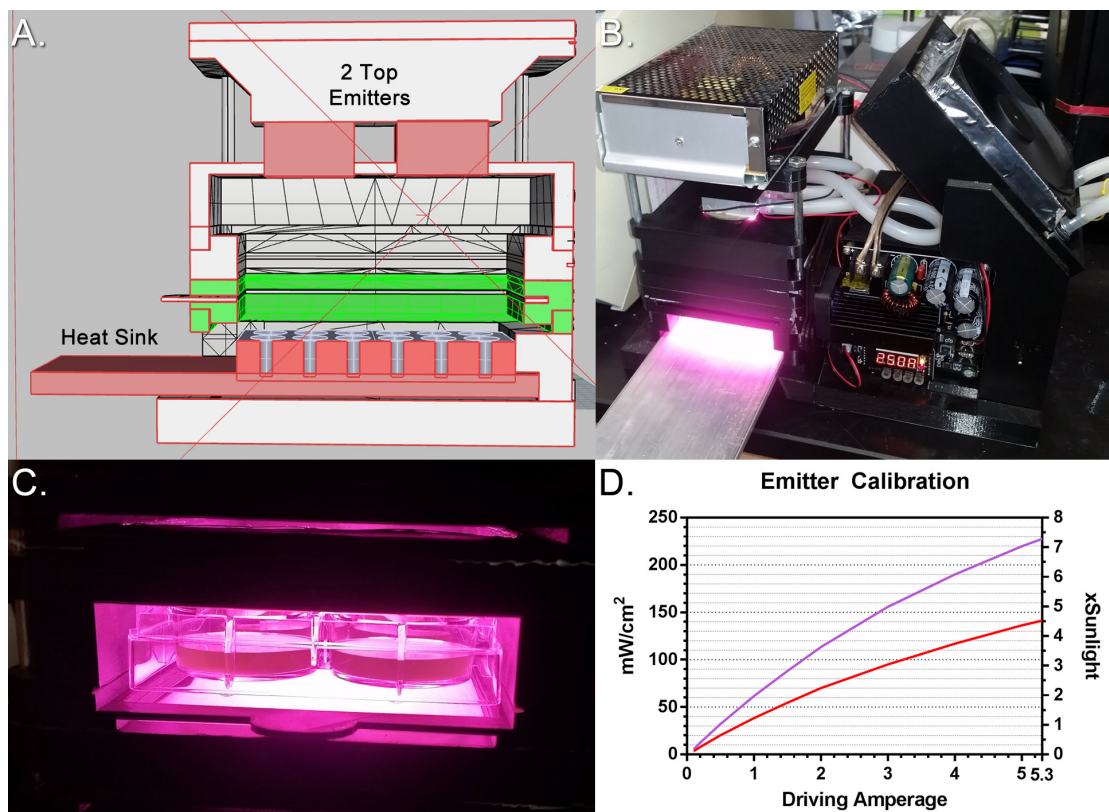


Figure 6.8: Design and construction of a high intensity LED light exposure chamber for the evaluation of cyanobacterial production of H_2O_2 . A) CAD design of the light box with two 100W 450/650nm optimized "grow LED" emitters for illumination of a standard 6, 12, or 24 well plate, B) photograph of the completed system, C) photograph of the illumination chamber with 6-well plate exposed to the light source, D) calibration curves showing the variable intensity capabilities of the light source from 0-230 mW/cm^2 and equivalent light dosage to daytime sunlight.

Next, a colony of wild-type (WT) 7942 cells were grown up in BG-11 media until they had reached the log phase of growth. At which point, 5mL samples of $OD_{750} = 0.5$ cyanobacteria were prepared in a 6 well plate and exposed to varying light intensities.100

μL samples were taken from the cells of the well plate at time intervals and placed in a 96 well plate pre-populated with a known concentration of HRP and ABTS. After each sample was taken, the 96-well plate was covered with aluminum foil and placed in a 4 °C refrigerator to reduce light exposure and prevent the generation of additional H_2O_2 . Once all samples had been collected, the OD405 was recorded for each timepoint and a calibration curve was generated using known concentrations of H_2O_2 to calculate the H_2O_2 concentration generated during the test. Further testing sought to include a known concentration of HRP within the samples under illumination and include ABTS in the test solution to give a real-time indication of the production of H_2O_2 *in-situ*. However, it was during this course of testing that a systemic error was discovered.

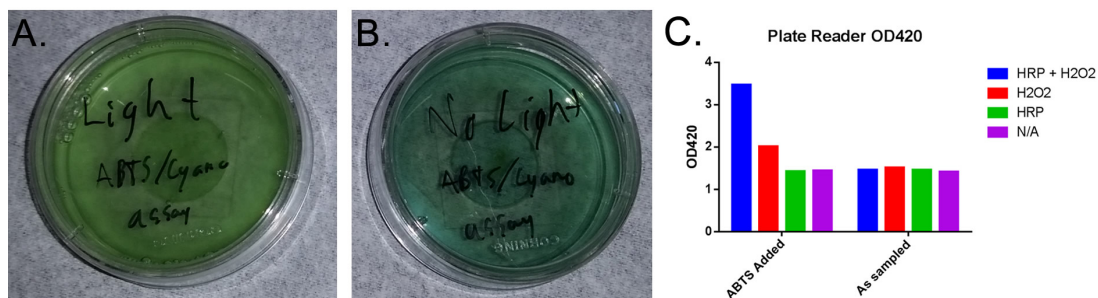


Figure 6.9: Evidence of ABTS as an unsuitable test for *in-situ* H_2O_2 production of biological organisms. A) sample of cyanobacteria exposed to light (3x sunlight for 60 minutes) with 45 U/mL HRP and 1.5 mM ABTS in solution during light exposure, B) sample of the same mixture as (A) but left in the dark for 60 minutes, showing blue coloration due to ABTS oxidation, C) plate reader OD₄₂₀ (indicating the presence of oxidized ABTS) of as-sampled mixture from (A) after each component was added back into solution and after each component **and additional ABTS** was added to the solution.

Two identical samples of OD₇₅₀=0.5 WT 7942 containing 45 U/mL HRP and 1.5 mM ABTS in solution with the 7942 were prepared. One sample was exposed to light for 60 minutes (Figure 6.9A) and the other was left in the dark (Figure 6.9B). A paradoxical result was observed. The sample exposed to sunlight showed no blue coloration (indicative of the presence of oxidized ABTS as a result of H_2O_2 production), but the sample left in the dark showed a blue coloration. Surprised by this result, degradation of one or more of the mixture components in the presence of intense light was suspected. Samples of the light-exposed mixture were extracted, and to each sample, HRP, H_2O_2 , or HRP+ H_2O_2 was added in order to determine which of the mixture

components had degraded in the presence of light. Again, surprisingly, none of the samples changed color (Figure 6.9C). This was confirmed by the plate reader OD₄₂₀ readings of the samples. Finally, 1.5 mM of ABTS was added to each of the samples and re-imaged in the plate reader and a conclusive result was obtained (Figure 6.9C). The addition of HRP had no effect on the OD₄₂₀, indicating that either 1) very little H₂O₂ was being produced, or 2) the HRP in solution was not significantly degrading over the course of 60 minutes illumination. When H₂O₂ was added, a small increase in OD₄₂₀ was observed, suggesting that some HRP remained in the mixture and the HRP was not completely degraded by the light. When HRP+H₂O₂ was added, the OD₄₂₀ more than doubled. When compared with the reactions in the mixture samples without ABTS added, the result is clear. ABTS was the primary component which degraded over the course of the illumination, but did not degrade in the sample left in the dark. It can be inferred that there was degradation of the HRP under illumination, and the production of H₂O₂ by WT 7942 is very low. It is unknown whether the 7942 consumed the ABTS due to the presence of bioavailable nitrogen, or whether the oxidized form absorbed more light and was subsequently inactivated via photobleaching, but the former is suspected.

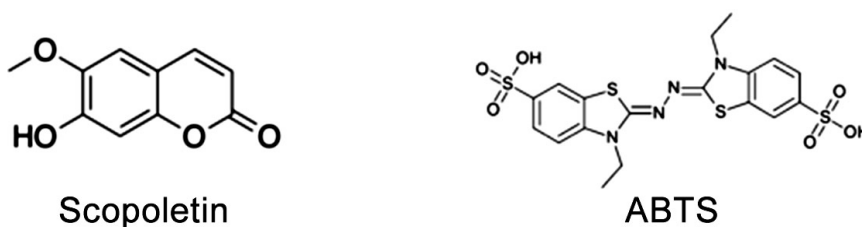


Figure 6.10: The molecular structures of scopoletin and ABTS

Scopoletin [231] is a naturally fluorescent dye which emits blue light under UV illumination but this UV fluorescence is quenched in the presence of H₂O₂. Higher concentrations of H₂O₂ lead to more quenching. Because there are no bioavailable nitrogens in the molecule, in contrast to ABTS (Figure 6.10), it is more suitable to *in-situ* quantification of cyanobacterial H₂O₂ production. A series of tests were performed using the method outlined in Section 6.5.3 to quantitatively determine the rate of production of H₂O₂ from WT 7942. A 96-well plate was prepared with wells containing an assay buffer of 20 μM scopoletin and 4 mU HRP. 100 μL samples were taken from a 6-well plate of OD₇₅₀=0.5 cyanobacteria culture under illumination at t=0, 20 s, 40 s, 1 min, 2 min, 5

min, 10 min, and 20 min of illumination at light intensities between 8.2 mW/cm² (lower bound of the emitter) to 16.4 W/cm² (samples placed directly on the emitter). The data from these preliminary quantitative tests is shown in Figure 6.11.

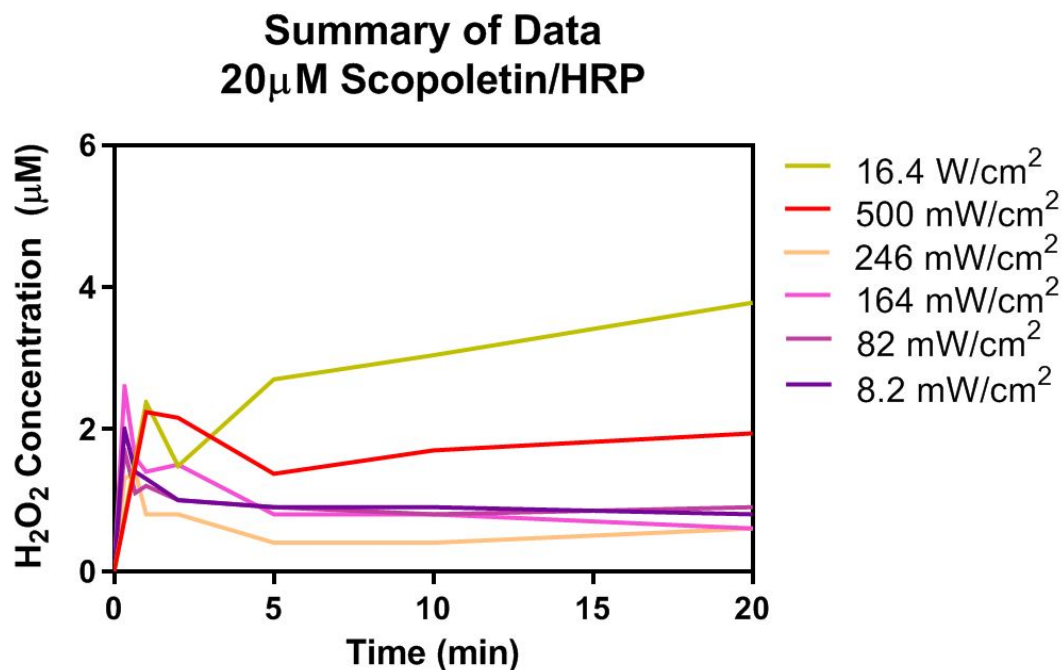


Figure 6.11: H₂O₂ production of WT 7942 cyanobacteria over time as a function of light intensity

From these preliminary quantitative findings it was apparent that even at extreme light intensities (sufficient to kill the cyanobacterial culture via heating), only minimal quantities (< 12 μ M/hr) of H₂O₂ were being generated. Therefore, alternative methods were considered in order to increase the peroxide production of cyanobacteria to a usable level.

Nevertheless, these initial results confirmed that a small amount of H₂O₂ was being produced from even the WT 7942, and thus could be used to polymerize aniline into PANI under the appropriate conditions. A solution of BG-11 buffer was prepared with 80 mM of aniline with 80 mM of PSS as a dopant species. 0.3 mg/mL of HRP (150 U/mg) was added to the buffer. Three 2 mL eppendorf tubes were prepared with 1 mL of OD₇₅₀=0.5 WT 7942 cyanobacteria which were pelleted at 10k rcf for 5 minutes and drained of their original media. The cells were each resuspended in 1mL of the

aniline/PSS/HRP buffer. Sample tube 1 was placed in a dark drawer for 5 days. Sample tube 2 was exposed to 3x sunlight for 10 minutes, then left exposed to ordinary room fluorescent light (roughly 100 lux) for 5 days. To sample tube 3, 1 mM H₂O₂ was added (as a positive control) and left on the bench beside tube 2 for 5 days. Samples from each of the tubes were analyzed via UV-Vis (Figure 6.12A) and their absorbance at 328/436/800 nm was compared (from the literature, the UV-Vis spectra of PANI:PSS has peak absorbance at 328, 436, and 848 nm [232]). Furthermore, a qualitative color between the three tubes could also be observed (Figure 6.12B).

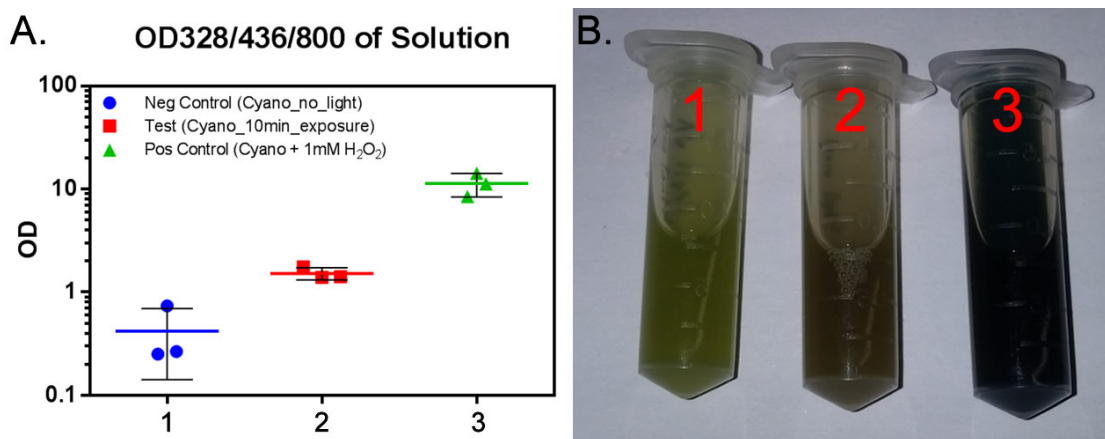


Figure 6.12: Evidence of enzymatic oxidative polymerization of aniline into PANI:PSS via HRP and photo-induced cyanobacterial biosynthesis of H₂O₂. A) comparative plot of UV-Vis OD values from sample tubes, B) photograph of sample tubes showing color difference between samples.

These results suggest that enzymatic oxidative polymerization of the aniline into PANI:PSS via cyanobacterially generated H₂O₂ occurred in response to light, a result not previously documented in the scientific literature.

The remainder of this chapter will focus on efforts to further refine and improve the process via chemical and recombinant techniques.

6.3.3 Recombinant Engineering of *PCC 7942* Cyanobacteria and Knock-Out of Catalase-Peroxidase

Perelman et al. suggested that it may be possible to create a recombinant (*katG*) mutant of *PCC 7942* which lacks the catalase-peroxidase gene suspected to be responsible for the removal of excess H₂O₂ from the media and cell environment. [222] The Golden

Lab fortuitously has already done much of the legwork in creating a library of knockout vectors for nearly every gene in the 7942 genome, as well as documenting the gene's necessity in terms of the mutant's survival. Through their CYANO-VECTOR system, it was documented that the catalase-peroxidase gene was NOT essential for survival, and cells could be successfully grown with that particular gene knocked out. The vector 8S2-N11 was used to remove Synpcc7942_1656 (CO) at position 144144-144152 in *PCC 7942* to create a recombinant mutant which lacks the ability to express catalase-peroxidase, hereafter referred to as Knock-Out Catalase-Oxidase (KOCO). The KOCO cells were difficult to grow in both liquid BG-11 media and on agar plates. Using excess sodium thiosulfate (up to 5 mM) in both the liquid media as well as the agar (Figure 6.13) tended to improve their growth rate, but even with excess thiosulfate their growth was substantially slower than that of the WT.

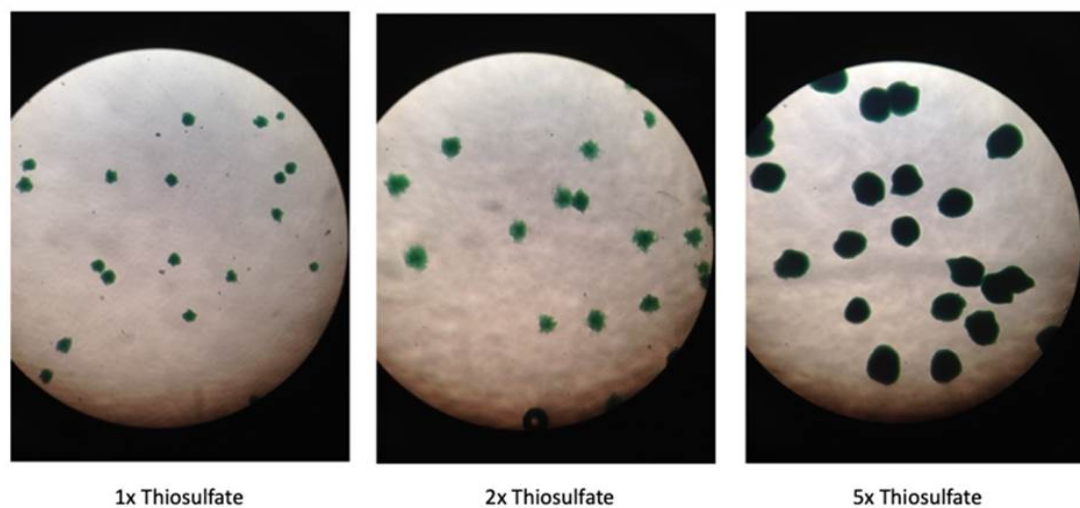


Figure 6.13: Optical micrographs of KOCO colonies grown on agar with varying concentrations of sodium thiosulfate (1 mM, 2 mM, and 5 mM), showing the comparative difference in growth after approx 2 weeks.

Nevertheless, it was possible to create a stable colony of KOCO cells in a BG-11 solution containing 5 $\mu\text{g}/\text{mL}$ kanamycin (Km) antibiotic and 1 mM sodium thiosulfate which grew in liquid culture at a rate comparable to that of WT in dim fluorescent room light (100 lux). 5mL samples of WT 7942 and the KOCO culture equalized to $\text{OD}_{750}=0.5$, the thiosulfate removed from the KOCO cells (by 3x washing/pelleting) and resuspended in fresh BG-11 buffer, then (Figure 6.14A) exposed in triplicate to 1.5x

sunlight (246 mW/cm^2) over the course of 60 minutes with $100 \mu\text{L}$ samples extracted from the illuminated cultures at timepoints 0, 1, 2, 5, 10, 20, 40, and 60 minutes. The $100 \mu\text{L}$ samples were placed in a 96 well plate with $20 \mu\text{M}$ scopoletin and 4 mU HRP buffer solution and the samples in the 96-well plate was read in a fluorometric plate reader after all samples had been collected, and after 18h incubation (in order to quantify whether the $100 \mu\text{L}$ samples taken from the exposure culture were changing significantly over time).

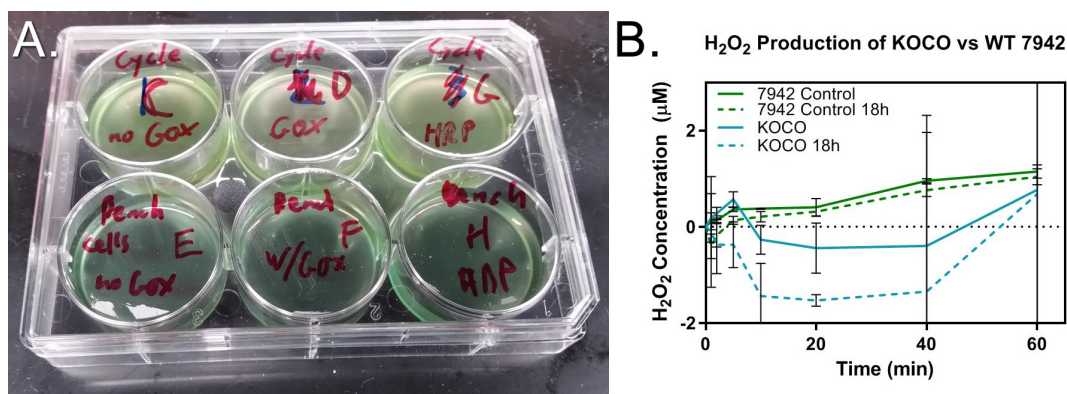


Figure 6.14: A) A notional photograph of a 6 well plate with (6) 5 mL samples of OD_{750} cyanobacterial culture prior to exposure inside the test apparatus of Figure 6.8, B) plot of H_2O_2 production of WT 7942 vs KOCO cyanobacterial cells after exposure to 246 mW/cm^2 light over the course of 60 minutes, and H_2O_2 concentration of the timepoint samples extracted into a 96 well plate after incubation for 18h.

Figure 6.14B shows the results of the scopoletin assay comparing the H_2O_2 production of KOCO vs WT 7942 cells at $1.5\times$ illumination. It is important to note the large error bars indicating the quantity of H_2O_2 produced in both KOCO and WT was largely below the threshold of measurement. It is also important to note that the $+18 \text{ hr}$ timepoints were not substantially different than the initial timepoints indicating that the method (taking plate reader fluorometric readings after all samples were collected) was likely sufficient for this preliminary analysis. The results of this study indicated that even with genetic modification of the WT 7942 to knock out catalase-(per)oxidase (KOCO), we hypothesize that there exist other ROS scavenger enzymes between the point of generation and the periplasm, specifically SOD. Knocking out SOD (while theoretically possible in some species of cyanobacteria under tightly controlled conditions [233, 234]) is largely considered to be detrimental to the cells' survivability and perhaps contrary

to the aims of the current work.

6.3.4 Utilization of ETC Inhibitors to Increase H_2O_2 Production of KOCO

In the interests of time, efforts to metabolically engineer enhanced H_2O_2 production into 7942 were eschewed in order to focus on other aspects of the project. One potential band-aid for the low H_2O_2 production of 7942 was to investigate the use of ETC inhibitors in order to dramatically increase photo-induced ROS production in order to overwhelm cellular defense mechanisms. This would of course damage the cells, but in pursuit of the goal of photo-induced expression of conductive PANI wires, having living cells within the conductive traces was not strictly required.

A number of preliminary studies were carried out to investigate the effect of different ETC inhibitors and different concentrations of ETC inhibitors on the production of extracellular H_2O_2 . The results from these studies are shown in Figure 6.15. The vast majority of tests showed no significant change in H_2O_2 production after 20 minutes for the use of ETC inhibitors in WT cells, however a slightly significant increase in concentration was observed with WT cells in the presence of DCMU after incubation post-exposure for 18 hrs (Figure 6.15C). This result led to further study on the effect of ETC inhibitors on KOCO cells.

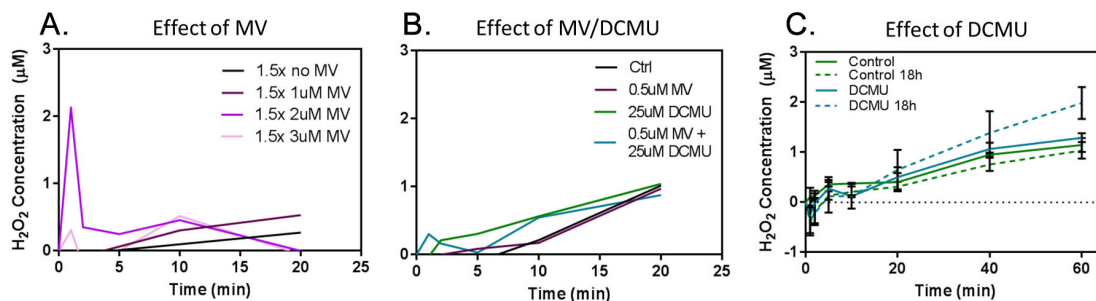


Figure 6.15: Preliminary studies on the H_2O_2 production of WT 7942 in the presence of ETC inhibitors during exposure to $246 \text{ mW}/\text{cm}^2$. A) Effect of varying concentrations of MV on the production of H_2O_2 over 20 minutes, B) effect of a combination of MV and DCMU on the production of H_2O_2 over 20 minutes, C) effect of $25 \mu\text{M}$ DCMU on the production of H_2O_2 over 60 minutes with H_2O_2 concentration readings repeated on the sample cells after 18 hrs.

Figure 6.16 demonstrates the effect of varying concentrations of DCMU on WT

and KOCO cells after exposure to 3x sunlight for 60 minutes and incubation post-exposure for 18 hrs. Where the WT 7942 cells showed no significant response to DCMU after incubation (in fact the amount of H_2O_2 actually decreased after letting them sit in the dark for 18 hrs), the KOCO cells showed dramatically increased H_2O_2 production after 18 hrs incubation. The 25 μM sample showed the best results and this concentration was selected for further testing. It is hypothesized that the 50 μM DCMU sample resulted in too much cell death and photobleaching and thus had a lower overall production of H_2O_2 .

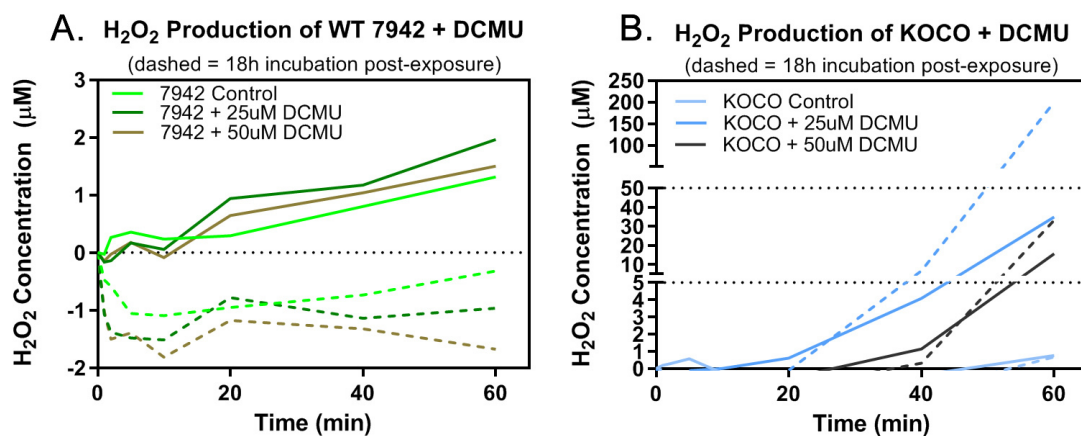


Figure 6.16: A) H_2O_2 production of WT 7942 cyanobacterial cells after exposure to 246 mW/cm^2 light over the course of 60 minutes with scopoletin assay timepoint readings of H_2O_2 production taken immediately after exposure (solid line) and after samples were incubated for 18 hrs in the dark (dashed line) B) H_2O_2 production of KOCO cyanobacteria using the same procedure as (A).

Figure 6.16 suggests that in KOCO cells, the amount of H_2O_2 increases even in the absence of light (unlike the WT 7942 cells which showed a reduction of any remaining H_2O_2 when the light source was removed). We hypothesize that this effect is due to the production of H_2O_2 largely inside the cells, but even though the H_2O_2 is being produced in large quantities, it still takes time for it to diffuse out of the cells and into the media. A follow on study was conducted to assess if a longer exposure to light would result in more H_2O_2 production in the catalase-peroxidase deficient cells because they lacked the enzyme necessary to remove it from the environment. Figure 6.17 shows the effect of the length of initial light exposure at 3x sunlight (4.5 mmol PPF or 492 mW/cm^2) for 60 minutes (Figure 6.17A) versus 120 minutes (Figure 6.17B) with the H_2O_2 concentration

assessed via scopoletin assay at 120 minutes and 18 hours after light exposure was started.

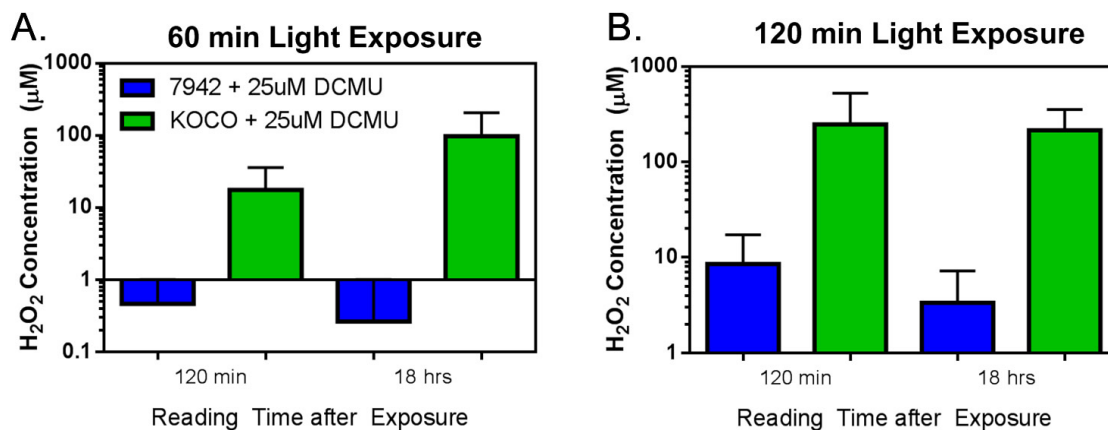


Figure 6.17: H₂O₂ production of WT 7942 vs KOCO cyanobacterial cells in the presence of 25 μM DCMU after exposure to 492 mW/cm² (4.5 mmol PPFD) light for A) 60 and B) 120 minutes. Both showing scopoletin assay results 120 min post-exposure and after samples were incubated for 18 hrs.

In light of these positive findings, attempts to replicate the results with biological replicants of the KOCO mutants produced additional difficulties. Subsequent catalase-peroxidase knock out cultures exhibited different ETC inhibitor responses. Figure 6.18 shows another KOCO culture that showed a resistance to DCMU and but still produced high concentrations of H₂O₂ when subjected to light exposure in the presence of MV.

While the WT 7942 cells still show very low H₂O₂ production even in the presence of MV, the KOCO cells are very sensitive to its presence. At concentrations as low as 100 nM, MV will cause KOCO cells to release ROS (which are then likely converted to H₂O₂ by SOD) even in the absence of light. Figure 6.19 shows the effect of incubation of KOCO and WT 7942 cells with different concentrations of MV -Figure 6.19A shows the absolute value concentration of H₂O₂ in the media after 90 min exposure, but Figure 6.19B shows the data of (A) with the H₂O₂ production of identical cultures kept in the dark, subtracted as a baseline from the data of (A). We can observe that in the sample containing 100 nM of MV, both the KOCO cultures kept in the dark and those exposed to light produced nearly the same amount of H₂O₂, so the relative difference in H₂O₂ production was low. From this data we can see that concentrations as low as 25 nM are required to achieve good contrast (in terms of H₂O₂ production) between samples kept in the dark and those that are exposed to light. Interestingly, with MV

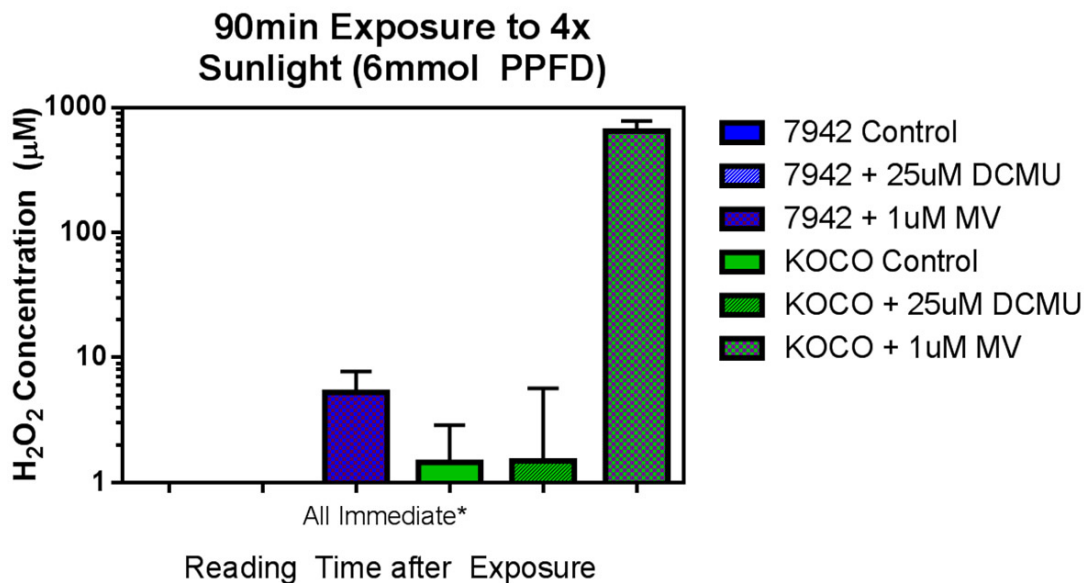


Figure 6.18: H₂O₂ production of WT 7942 and KOCO cyanobacterial cells in the presence of 25 µM DCMU and MV after exposure to 656 mW/cm² (6 mmol PPFd) light for 90 min

as the ETC inhibitor, the 18 hr incubation did not produce substantially more H₂O₂, and all concentration measurements shown in Figures 6.18, 6.19, and 6.20 were taken immediately after exposure to light.

Finally, an attempt was made to replicate the results of 6.12 using KOCO cells and ETC inhibitors. MV was chosen as the ETC inhibitor for this test as it seemed to produce the largest H₂O₂ production in some cultures. Figure 6.20 shows the result of this study where 2 mL samples of OD₇₅₀=0.5 standardized cultures of WT 7942 and KOCO cells were prepared in a 24-well plate with BG-11 buffer, 80 mM of aniline, 80 mM of PSS as a dopant species and in some samples 0.3 mg/mL of HRP (150 U/mg) and 50 nM of MV. The results of Figure 6.20B demonstrate a possible 6-fold increase in OD₃₂₈/OD₄₃₆ (corresponding to a 6-fold increase in PANI production) using a combination of KOCO cells and MV. However, at this time the results from this study are somewhat inconclusive as it is not presently known why the control samples lacking HRP in the composition displayed potential PANI production over those with 50 nM of MV and HRP. It is suspected that MV may have interfered in the polymerization of PANI:PSS or affected its UV-Vis absorbance such that it gave a false reading.

Nevertheless: Figure 6.17 and 6.19 present perhaps the clearest result yet that

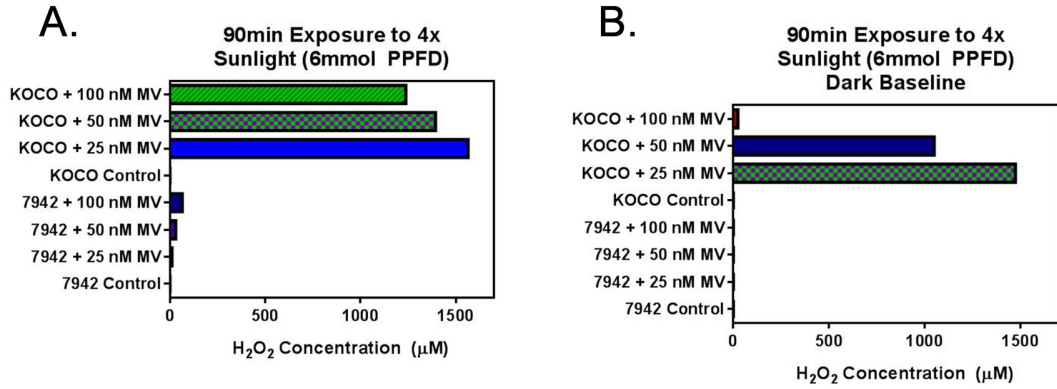


Figure 6.19: H₂O₂ production of WT 7942 vs KOCO cyanobacterial cells in the presence of 25-100nM MV after exposure to 656 mW/cm² (6 mmol PPFd) light for 90 min A) Absolute concentration of H₂O₂ produced after a 90 minute exposure B) difference in H₂O₂ concentration between a set of samples exposed to light (A) and an identical baseline set of samples kept in the dark, showing relative efficacy of MV concentrations to allow for photo-induced production of H₂O₂.

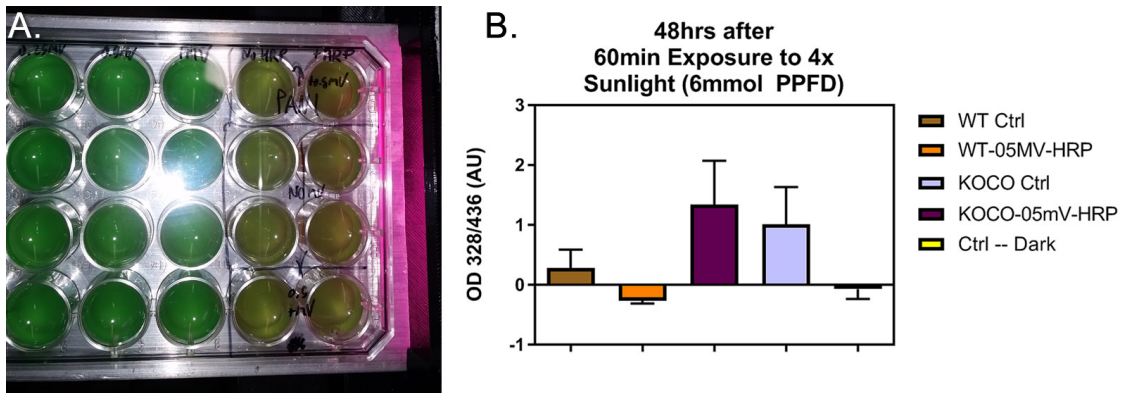


Figure 6.20: PANI production of WT 7942 vs KOCO cyanobacterial cells in the presence of 50 nM MV, and HRP 48 hrs after exposure to 656 mW/cm² (6 mmol PPFd) light for 60 min. A) Photograph of 24-well plate with 2 mL sample volumes after 60 minutes exposure B) Plot of summarized results showing a replication of Figure 6.12 (sample 2, WT 7942 with PANI buffer) sample shown in brown/orange, and similar sample compositions with KOCO cells shown in steel grey/burgundy.

the KOCO cells are capable of highly efficient photo-induced H₂O₂ production (up to 1500 μM in some samples) in the presence of ETC inhibitors and this component of the overall reaction is validated. Furthermore, it is suspected that with additional metabolic engineering, the use of ETC inhibitors to effect such production would no longer be

required and cleaner results confirming the high-yield production of PANI from such genetically engineered cells made possible, but such in-depth biological engineering is largely outside the scope of this work.

6.3.5 Transformation of Synthetic HRP-Coding Plasmid into *E. Coli* and Quantification of Peroxidase Expression

After achieving a somewhat successful result in the production of $> 1000 \mu\text{M}$ of H_2O_2 using a combination of genetically engineered KOCO cells and ETC inhibitors, attention was turned to the transformation of bacterial (and later cyanobacterial) cells with the genes necessary to biosynthesize HRP (or another peroxidase enzyme) capable of catalyzing the production of PANI from aniline and H_2O_2 .

This problem was broken down into two sub-problems. 1) Express a functional peroxidase enzyme in *E. coli*, and 2) express a functional peroxidase enzyme in *PCC. 7942*. The first problem was approached by attempting to re-create a sequence for functional HRP expression in *E. coli* patented in 2003 by Frances Arnold et al. [206] This sequence was extracted from the patent and inserted into a pET-26b(+) construct (Figure 6.21) with Kanamycin resistance and T7 expression which was synthesized by GenScript.

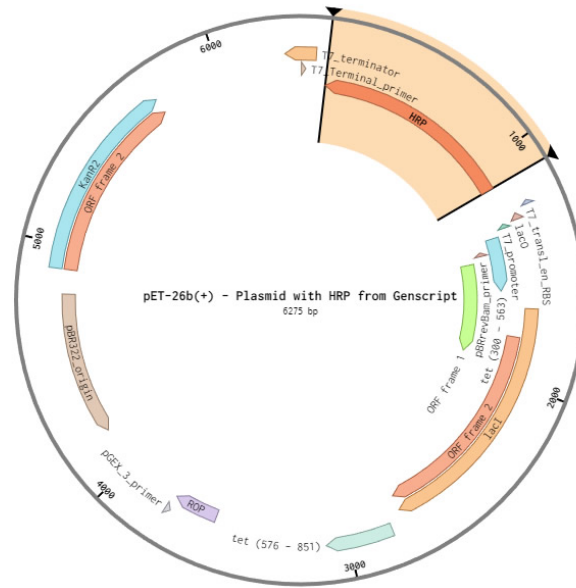


Figure 6.21: Synthetic pET-26b(+) construct for expression of functional HRP protein in *E. coli*

```

ATGCAGTTAA CCCCTACATT CTACGACAAT AGCTGTCCCA ACGTGTCCAA CATCGTTCGC
GACACAATCG TCAACGAGCT CAGATCCGAT CCCAGGATCG CTGCTTCAAT ATTACGTCTG
CACTTCCATG ACTGCTTCGT GAATGGTTGC GACGCTAGCA TATTACTGGA CAACACCACC
AGTTTCCGCA CTGAAAAGGA TGCATTCGGG AACGCTAACA GCGCCAGGGG CTTTCCAGTG
ATCGATCGCA TGAAGGCTGC CGTTGAGTCA GCATGCCAC TAACAGTCAG TTGTGCAGAC
CTGCTGGCTA TAGCTGCGCA ACAGAGCGTG ACTCTTGAG GCGGACCGTC CTGGAGAGTG
CCGCTCGGTC GACGTGACTC CCTACAGGCA TTCCCAGATC TGGCCAATGC CAACTTGCTT
GCTCCATTCT TCACCCTGCC CCAGCTGAAG GATAGCTTTA GAAACGTGGG TCTGAATCGC
TCGAGTGACC TTGTGGCTCT GTCCGGAGGA CACACATTTG GAAAGAACCA GTGTAGGTTT
ATCATGGATA GGCTCTACAA TTTCAGCAAC ACTGGGTTAC CTGACCCAC GCTGAACACT
ACGTATCTCC AGACTGAG AGGCTTGTGC CCACTGAATG GCAACCTCAG TGCACTAGTG
GACTTTGATC AGCGGACCCC AACCATCTTC GATAACAAGT ACTATGTGAA TCTAGAGGAG
CAGAAAGGCC TGATACAGAG TGATCAAGAA CTGTTTAGCA GTCCAAACGC CACAGACACC
ATCCCACTGG TGAGAAGTTT TGCTAACTCT ACTCAAACCT TCTTTAACGC CTTCGTGGAA
GCCATGGACC GTATGGGTAA CATTACCCCT CTGACGGGTA CCCAAGGCCA GATTTCGTCTG
AACTGCAGAG AGGTCAACAG CAACTCT

```

The synthetic plasmid was transformed into BL-21 cells and expressed using the method described in section 6.5.1. The patent and literature suggested that it was necessary to incubate the cells with hemin, which proved to be necessary in order to obtain any HRP activity in the resultant media. The cells were lysed and their peroxidase activity measured via ABTS assay (method described in section 6.5.2), and the results

are shown in Figure 6.22. Overall, some activity above the baseline was detected in the **uninduced** cultures incubated with heme, however no detectable enzyme activity was detected above the baseline (Heme+LB) for the induced cultures. The test was re-run with lower concentrations of IPTG (down to 100 μ M, but no improvement in enzymatic activity was observed in the induced samples.

One hypothesis for this phenomena is the “leakyness” of the T7 promoter. In *uninduced* cells, the HRP protein is expressed via very slowly, which may give it sufficient time to fold into its active conformation. Induction with IPTG causes the HRP protein to be expressed and excreted too fast for it to fold properly. However additional tests with even low concentrations of IPTG were largely inconclusive and there is limited evidence to evaluate this hypothesis. Overall, this HRP sequence was deemed to be too unreliable and attention was turned towards a relatively new *E. coli* expressible peroxidase: ascorbate pea coat peroxidase (APEX2).

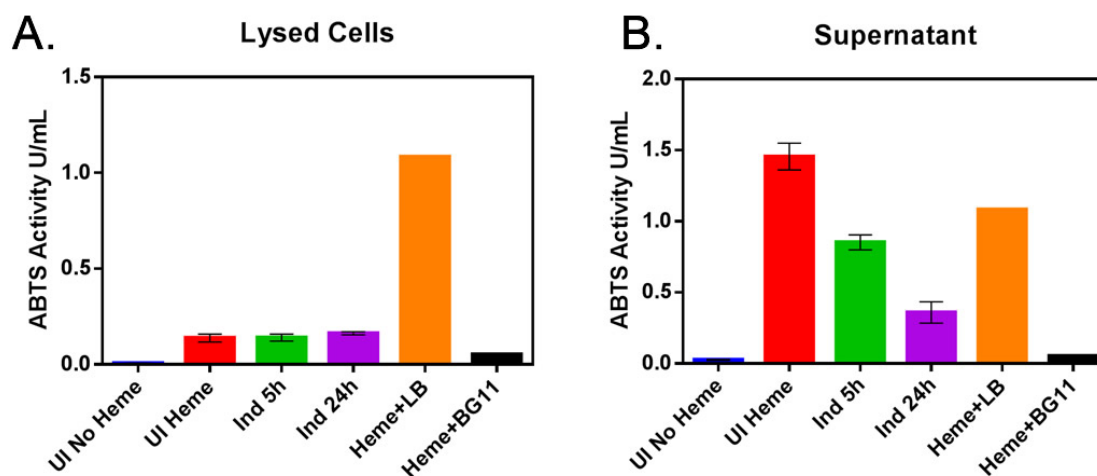


Figure 6.22: ABTS assay activity of expressed HRP protein in *E. coli* after transformation of the plasmid shown in Figure 6.21. A) ABTS activity of the lysed cells and B) supernatant media.

6.3.6 Expression of APEX2 in *E. Coli*

The APEX2 plasmid was published by Ganapathy et al. in 2018 and the functional plasmid published on AddGene which allowed for rapid procurement and testing. [212] One distinct advantage of the APEX2 over HRP is that it is advertised to be functionally expressible without the requirement of incubation with extracellular Hemin.

A sample of the APEX2 plasmid was obtained and transformed into New England Biolabs T7 Express cells in order to evaluate its claimed activity and functional expression capabilities. The results of this testing is summarized in Figure 6.23, and the results largely confirm the claims of the APEX2 study authors. The APEX2 plasmids possess significant activity when expressed via 0.1 mM IPTG at 30 °C, both the whole cell broth and media (although substantially less in the cell lysate, suggesting that the APEX2 is effectively transported into periplasm). The presence of hemin made no substantial difference to the activity of the APEX2 and there was little to no activity of the uninduced samples. These results are in contrast to the HRP samples which showed expression only in the hemin incubated uninduced samples, at a far lower activity level.

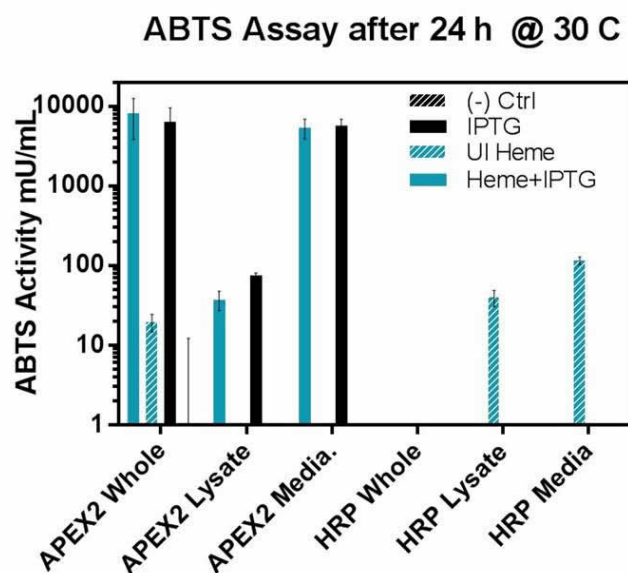


Figure 6.23: ABTS assay activity of expressed APEX2 and HRP proteins in *E. coli* (NEB T-7 Express and BL-21, respectively) after induction under the conditions stated for 24 hrs at 30 °C

However, despite the effectiveness of the APEX2 plasmid at expression of a functional peroxidase protein, follow-on tests of the protein showed that it was unable to catalyze the oxidative polymerization of PANI:PSS, likely due to insufficient electrochemical oxidative potential. It is unclear if the plasmid or functional protein can be genetically or chemically modified to remedy this shortcoming, but at the present, efforts to utilize APEX2 in the method of the current work have not proved fruitful.

6.3.7 Attempts at Recombinant Engineering of *PCC 7942* to Express Peroxidase Enzymes

In an attempt to bring the work full-circle and incorporate both a peroxidase and peroxide expression capability into one single organism, efforts were undertaken to insert either the HRP or APEX2 plasmids into the *PCC. 7942* genome and obtain a functional expression. Because the cyanobacteria does not possess the T7 RNA polymerase, we attempted to attach a PTRC promoter to a number of peroxidase enzymes including LsPOX, HRP, and APEX2, however after modification of the proteins, all failed to express properly in *E. coli*. Subsequent efforts to insert the modified or unmodified cassettes into *PCC. 7942* were also unfortunately unsuccessful.

6.4 Conclusion

We have investigated a novel method for the formation of conductive polymers using living systems incorporating a number of genetic and chemical techniques. While the optimization and incorporation of these separate processes into a single organism remains yet to be demonstrated, a number of novel demonstrations were conducted.

A knock out mutant of the *Synechococcus sp. (7942)* cyanobacteria deficient in its catalase-peroxidase enzyme (KOCO) was created which efficiently expressed H₂O₂ into the media. In the presence of 25 μ M DCMU or 25 nM of MV, the KOCO cells demonstrated the capacity to produce produced over 2 orders of magnitude more H₂O₂ than the WT cells or those cells which were kept in the dark, demonstrating effective photo-induced production of high concentrations of hydrogen peroxidase which may be useful for inducing oxidative polymerization, wastewater treatment, or production of oxidizer for aerospace applications via a self-replicating biological harvester. KOCO cultures exposed to concentrated light in the presence of 25 nM of MV expressed well over 11 μ M of hydrogen peroxide per minute and up to 1.4 mM after 90 minutes, well beyond the amount required in order to carry out the enzymatic oxidative polymerization of PANI:PSS.

Both the WT and KOCO cells, after exposure to concentrated light for 5-60 minutes in the presence of extracellular HRP, were demonstrated to be capable of polymerizing a conductive polymer (PANI:PSS) from a solution of aniline, PSS, and citrate buffer.

A functional HRP enzyme has been expressed in *E. coli* and a path forward towards functional expression in *PCC 7942* has been outlined.

6.5 Experimental Section

6.5.1 Method of ABTS Assay for Quantification of Enzymatic Peroxidase Activity

Cultures were started at standardized $OD_{600}=0.1$ and grown in LB with 50 μ M Kanamycin (HRP/APEX2) and 12 μ M Hemin was added. When cultures reached $OD_{600}=0.4-0.6$, they were induced with IPTG at a final concentration of 0.1 mM. ABTS assay of cultures was taken at $t=0$ and compared with assay results at 24 hrs.

6.5.2 Method of ABTS Assay for Quantification of Enzymatic Peroxidase Activity

ABTS assay procedure was based on the method documented by Cano, et al. [197]

Reaction mixture: 1.5mM ABTS (2 μ L of 75mM stock), 1.5mM H_2O_2 (1 μ L of 150mM stock) in pH 6 citrate buffer (98 μ L) for total buffer volume of (100 μ L) is placed into cells in a 96-well plate.

50 μ L cell stock is added to 96-well. ABTS pre-made buffer is transferred into the cell stock wells using a multi-channel pipette for a total rxn volume of 150 μ L.

Plate reader temperature is set to 25 °C with a 2 s pre-shake prior to imaging. OD_{405} reading is taken at initial $t=0$, $t=1$ min and $t=2$ min. $t=0$ OD reading is subtracted from $t=1$ min and $t=2$ min, and the ΔOD_{405} value per minute is computed for each set of datapoints and averaged.

A calibration curve is prepared using known activity HRP (150 U/mg) in a 3 mg/mL stock solution diluted to 90, 180, 270, 450 and 900 mU/mL in 50 μ L aliquots added to ABTS stock solutions and sampled using the above procedure and the calibration curve is used to correlate the ΔOD_{405} values of the unknown cell stock samples with known enzymatic activity values.

Enzyme activity of 1 U is defined as 1 μ mol substrate conversion per minute at pH 6, at 25 °C.

6.5.3 Method of Scopoletin Assay for Quantification of Hydrogen Peroxide Production

ABTS assay procedure was based on the method documented by Boveris and Paterson, et al. [231, 235] A 4mM scopoletin stock solution was created in DMSO. A second stock solution of HRP was created containing 4.5 U/mL.

20 μL of the HRP stock solution was added to 0.6 μL of scopoletin stock solution to create a single well of scopoletin buffer. If tests required 10 total timepoints, 200 μL of HRP stock would be prepared with 6 μL of scopoletin stock. If 100 total timepoints were required, 2 mL of HRP with 60 μL of scopoletin, etc.

For each sample volume, 5mL of cells were standardized to $\text{OD}_{750}=0.5$ and (if cultured in thiosulfate-rich media) washed 3x with fresh BG-11, then deposited into a 6-well plate under desired conditions (with or without ETC inhibitor under desired sunlight intensity to build up H_2O_2). At various timepoints of this incubation, 100 μL sample aliquots were taken of the cell stock solution and added to the wells of a 96-well plate. After each sample, the well plate is covered with tin foil and placed in a 4 °C refrigerator to prevent conditions in the 96-well from deviating excessively from the conditions under which the sample was taken. Once all 100 μL timepoint sample(s) have been collected in the 96-well plate, 20 μL of the catalyzed scopoletin stock solution is added to each of the 96-well plate samples and the 96-well plate inserted into plate reader.

Plate reader fluorescence assay was carried out on a a BioTek Synergy HT microplate reader with filter set: excitation 360/40, emission 460/40, top optics, gain 35, read speed normal, read height 1mm.

A calibration curve of known H_2O_2 concentration was created and plotted against measured scopoletin fluorescence at 460 nm emission. Using the stock solution described above this procedure should detect H_2O_2 in concentrations from 5-500 μM . To detect higher or lower quantities of H_2O_2 , the ratio of scopoletin to HRP, or the gain of the plate reader must be adjusted. Higher fluorescence readings indicate lower concentrations of H_2O_2 .

It was important to not use the outer rows (A and H) and columns (1 and 12) of the 96-well plate, as these wells tended to produce erroneous readings with our setup measuring fluorescence emission.

6.5.4 Preparation of BG-11 Media

BG-11 media was composed by adding 10 mL of BG-1 stock solution and 1 mL of the following BG-2 through BG-8 stock solutions (in numerical order) into 900 mL of DI water. After addition, the volume is raised to 1L and the pH is adjusted to 7.5 using pH paper strips or a pH meter using HCl or NaOH. The final mixture is then autoclaved for 30 min to sterilize.

BG-1: Sodium nitrate (NaNO_3) - stock solution: 150 g/L.

BG-2: Calcium chloride ($\text{CaCl}_2 \cdot 2\text{H}_2\text{O}$) - stock solution: 36 g/L.

BG-3: Ferric ammonium citrate and citric acid ($\text{C}_6\text{H}_9\text{FeNO}_7$ and $\text{C}_6\text{H}_8\text{O}_7$) - stock solution: 6 g/L of each, filter sterilize.

BG-4: EDTA \times Na_2 (EDTA disodium) - stock solution: 1 g/L (or 1.1 g/L if using the dihydrate)

BG-5: Potassium phosphate dibasic (K_2HPO_4) - stock solution: 40 g/L

BG-6: Magnesium sulfate (MgSO_4) - stock solution: 18.05 g/L (or 75 g/L if using the heptahydrate).

BG-7: Sodium carbonate (Na_2CO_3) - stock solution: 20 g/L, filter sterilize.

BG-8: Trace metals stock solution: 2.86 g/L boric acid (H_3BO_3), 1.81 g/L manganese (II) chloride tetrahydrate ($\text{MnCl}_2 \cdot 4\text{H}_2\text{O}$), 0.222 g/L zinc sulfate heptahydrate ($\text{ZnSO}_4 \cdot 7\text{H}_2\text{O}$), 0.39 g/L sodium molybdate dihydrate ($\text{Na}_2\text{MoO}_4 \cdot 2\text{H}_2\text{O}$), 79 **mg**/L copper (II) sulfate pentahydrate ($\text{CuSO}_4 \cdot 5\text{H}_2\text{O}$), 49 **mg**/L cobalt (II) nitrate hexahydrate ($\text{Co}(\text{NO}_3)_2 \cdot 6\text{H}_2\text{O}$). Filter sterilize.

6.5.5 Materials

Aniline (# 242284), triphenylamine (# T81604), p-phenylenediamine (# P6001), Horseradish peroxidase (HRP, # 77332), recombinant lyngbya peroxidase (# 04394), Laccase (# 38429), and EDOT (# 483028) were obtained from Sigma Aldrich.

Poly(styrene sulfonate) (PSS, $M_w=70k$ # AA4168818), and hydrogen peroxide (50wt% in water, # AC302865000) were obtained from Fisher Scientific. 10-camphorsulfonyl chloride (10-CSA, # C13085G) was obtained from TCI.

Bovine hemin (# H9039) was obtained from Sigma Aldrich and prepared as a 0.12 M stock solution solublized in 0.5 M NaOH.

Synthetic HRP plasmid was obtained from Genscript. APEX2 plasmid was obtained from Addgene (# 111702, IPTG-inducible expression of APEX2 in E. coli). Cata-

lase oxidase knock-out plasmid was obtained from the Golden Lab as well as a great deal of generous assistance and instruction regarding the of homologous recombination techniques for cyanobacteria.

T7 express competent *E. coli* (# C2566H), BL-21 competent *E. coli* (# C2530H), and NEB 5-alpha competent *E. coli* (# C2987H) were obtained from New England Biolabs.

BG-11 stock components (sodium nitrate, calcium chloride, etc.) were obtained from various sources and prepared in the Golden Lab with their generous assistance.

6.5.6 Instrumentation

Optical density (OD) measurements were taken with a BioTek Synergy HT microplate reader, 3D printing demonstrations were carried out on a Cellink Inkredible+ 3D direct ink writing bioplotter. UV-Vis absorbance spectra for the quantification and measurement of PANI:PSS was obtained using a Shimadzu BioSpecNano UV-vis spectrophotometer.

6.6 Acknowledgements

Chapter 6, is coauthored with Weiss, Elliot T.; Welkie, David; Pokorski, Jonathan K. The dissertation author was the primary investigator and author of this material.

Chapter 7

Conclusions and future work

Chapter 1 lays the framework for a generalized theory of additive manufacturing and outlines the limits and bottlenecks to current manufacturing systems. In the framework presented, the translation of digital information into physical structures at a high Structural Patterning Rate (SPR) depends chiefly on three factors:

1. Memory retrieval: The rate at which structural information can be retrieved from memory and passed to the metamorphic area to toggle the deposition or removal of material
2. Machine response: The rate at which the assembler's metamorphic area can move (v_t)
3. Material response: The rate at which the material inside the metamorphic voxel can accept information and undergo conformational change

If we consider memory retrieval to be the least restrictive bottleneck and also outside the scope of this work, we are left with limitations in machine and material which addressed throughout subsequent chapters. These efforts are summarized below, along with suggestions for future research.

7.1 Future Work on Self-expanding AM Polymeric Structures

7.1.1 Pushing the Envelope of Volumetric Build Rate for AM Systems

Chapter 2 attempts to improve the response rate of AM materials by allowing information to be accepted by a small volume of material followed by isotropic expansion of all voxels simultaneously. This approach allows a Masked SLA printer (possessing high SPR and high resolution) to construct structures up to 40x larger than the machine's OEM specifications, thereby increasing its effective volumetric build rate (V_s). Figure 7.1A adds the data from Chapter 3 to the chart of Chapter 1, showing how the addition of an isotropic expansion step allows for the production of objects at a record high volumetric build rate, exceeding even large FDM systems' V_s by nearly one order of magnitude. Figure 7.1B shows a different scatter plot of the same systems' SPR vs V_s , where our isotropic foam appears as the furthest top-right point. In both figures, we can see lines connecting the base MSLA systems to their datapoints after isotropic foaming techniques are used.

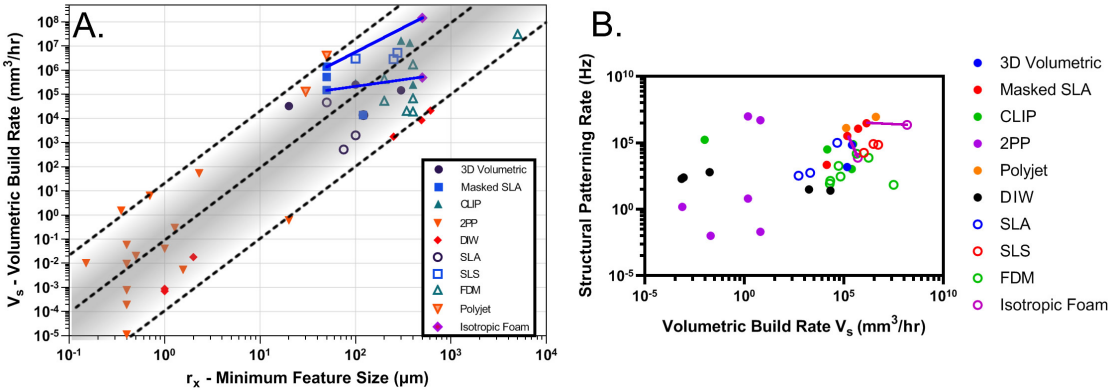


Figure 7.1: A) Scatter plot showing AM technologies demonstrating of various technologies demonstrates a roughly cubic relationship between minimum feature size and volumetric build rate, and B) showing a scatter plot of the same systems comparing their SPR and volumetric build rate. Full details for AM systems can be found in Table 1.1 and the data for isotropic foam can be found in Chapter 3.

In an idealized system, merely expanding the voxels by a given expansion percentage would result in a system with V_s increased by this percentage with a constant SPR, since no additional structural information is being input during the expansion

stage. However, the pHEMA resin takes considerably longer to cure than conventional acrylates, and the expansion step also takes time. Thus, more time is required to pattern the final structure on an isotropic foam than on a conventional MSLA print. So the SPR will always be lower.

On large machines, such as the Anycubic Mono X (top blue/purple line on Figure 7.1A/B), this inefficiency is relatively small (shown as a slope close to the idealized $\log V_s = 3 \log r_x$ on Figure 7.1A or a nearly flat line with slight negative slope on Figure 7.1B), but on smaller and less powerful machines such as the Anycubic Photon (the bottom line on both figures), the additional print time for pHEMA vs conventional resin results in a considerable inefficiency (represented by a considerably shallower slope on Figure 7.1A, and a significant negative slope on Figure 7.1B). If an isotropically expanding foam resin with a cure time similar to conventional MSLA resin could be developed, such a material could represent a considerable asset to future engineers since it would enable the production of large structures which take no more time to construct than small structures, merely trading off print resolution for size, without the need to change printer hardware.

An additional task on such an endeavor would be the synthesis or discovery of an alternate blowing agent since BOC_2O presents considerable toxicity in solution, and requires refrigeration to prevent the buildup of pressure within its container.

Finally, while the objective of freeing resultant final structure size from confinement of the printer's build volume was ultimately successful, the resultant structures are still limited by the size of the oven used to expand them. Future efforts could be directed at a RF-activated thermally expandable foaming resin in order to remove the requirement for large ovens to be used for foam expansion. Carbon micro or nanoparticles could be suspended in a resin in order to increase RF absorbance and a source of RF or microwave energy could be used to expand the foams rather than a conventional or convection oven. Structures fashioned in this way could be theoretically much larger than those fashioned with the method described in Chapter 2.

7.1.2 Improving the Strength of Expanded Polymeric Structures

The work in Chapter 3 is incomplete with respect to the final strength to weight ratio of produced structures. While great strides have been made in terms of improving the overall strength of the pHEMA foams from their baseline mechanical properties,

such structures are still weak compared to other AM methods even after coated with several layers of the high strength S100 resin. Future work on improving the strength (and strength to weight ratio) of expanded structures should ideally be directed at the refinement of polyurea coatings or the incorporation of composite materials (such as aramid or nylon) into the pHEMA base resin, however any modifications to the base resin (including crosslinkers, composite fibers, or high strength components) would likely pose a hindrance to expansion.

7.1.3 Novel Applications for Expanded Polymeric Structures

Cell scaffolding is another potential application for the novel pHEMA foam material developed in Chapter 2. The inclusion of 0.1 wt% GRGDS-Acrylate peptide in the base pHEMA resin (including 10 wt% BOC₂O), after expansion demonstrated substantial improvement in 3T3 cell attachment versus control samples (Figure 7.2). While such results are still preliminary, they demonstrate promise in the avenue of cell scaffolding with cell attachment peptide-containing pHEMA printed structures, and also back up claims regarding the complete degradation of BOC₂O and subsequent lack of toxicity of foams printed using this method after expansion.

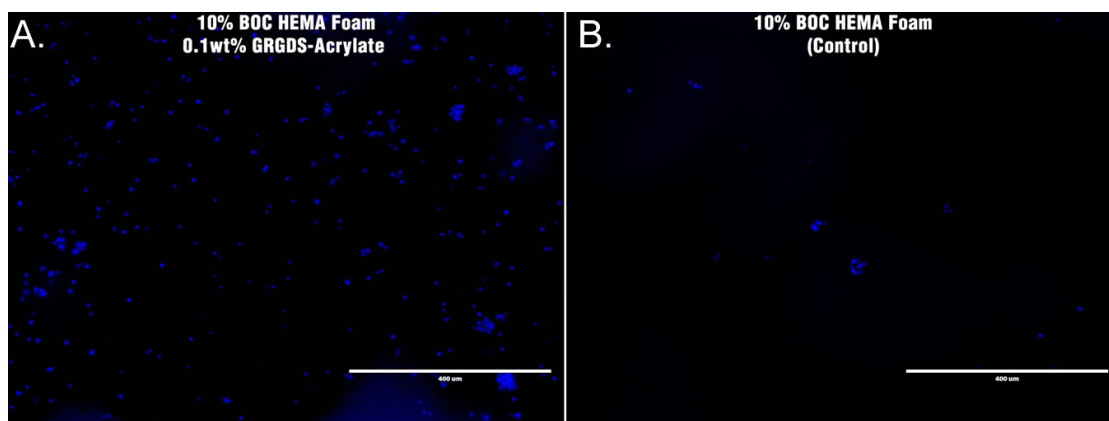


Figure 7.2: Preliminary tests showing the growth of NIH 3T3 cells on samples of pHEMA foam incorporating 0.1 wt% GRGDS-Acrylate. A) Fluorescence micrograph of 0.1 wt % GRGDS-Acrylate containing pHEMA foam cultured with 3T3 cells stained with Hoechst, B) Fluorescence micrograph of control pHEMA foam cultured with 3T3 cells stained with Hoechst. Scale bars: A) 400 μm , B) 100 μm .

7.2 Injection Molding of Controlled Release Devices

7.2.1 Efficacy of drug and vaccine loaded polymeric devices

In Chapter 4, attempts were made to re-engineer a conventional manufacturing technique (polymer extrusion, IM and melt processing) at a small scale in order to enable the solvent-free processing of high value polymers and biomaterials. *In-vivo* testing with such devices has been largely positive- implants fabricated using the melt processing system developed in Chapter 4 have resulted in positive improvements in the efficacy of single-dose HPV vaccines. [236]

The apparatus designed in Chapter 5 takes this concept a step further, towards the development of a scalable rapid manufacturing platform for customizable polymeric implants or dissolvable microneedle patches. However, challenges still remain regarding the stability of biomolecules processed via this technique. Injection molding of polymers generally results in substantially higher shear stresses than simple extrusion (likely as a result of the higher initial velocity required for the shot of molten polymer to penetrate the mold before solidifying). As a result, some of the more sensitive biomolecule payloads (such as Q β or VLPs) subjected to injection molding tended to degrade and attempts to reduce shear stresses during this process are still ongoing.

One potential avenue for remedy may be to modify the injection molding process to allow for longer shot times by incorporating thermoelectric heaters/coolers into the mold in order to keep the polymer molten throughout the shot, then electrically cool the mold in order to remove the devices.

Another option may be hot embossing. In a polymer hot embossing system, one or more sheets of polymer is pressed between two heated molds into cavities in a desired geometry. In such a process, shear stresses are much lower and higher viscosities can be tolerated- thus the temperatures used during such a process may be dramatically reduced. An injection/compression molding procedure could also be considered. [237]

7.2.2 Improving Sharpness of Injection Molded Microneedles

Another area for improvement on the work in Chapter 5 is the sharpness of MN tips. While a tip diameter of 60-90 μm could be reliably achieved in low viscosity PCL polymer, such tips are still over one order of magnitude duller than solvent-cast MN tips. This, combined with the softness of the PEG-100k/PVP polymer led to inconsistent

penetration in many tests. Alternate polymers such as PEOz (100k M_w) may offer improved dissolution in skin while also maintaining improved tip sharpness and strength. However, due to the high temperature required for PEOz processing and brittleness of the solidified polymer, additional work would be required to adapt it to the goals of this work. In a mass production environment, where cost is not an obstacle, such a mold insert could be made using electrochemical machining techniques from microporous stainless steel and the pre-vacuum applied through the bulk of the microporous insert to allow for even higher fidelity, repeatability and tip sharpness of molded dissolvable polymer microneedles. Other pathways forward to improve mold fidelity could include using ultrasonic energy during the injection of polymer to ensure complete dispersion into the small cavities. [238]

7.3 Directed Biological Polymerization of Conductive Polymers

Chapter 6 presents perhaps the most ambitious work contained in this text. Although much data was generated through the efforts documented herein and a great deal of research conducted on the potential paths forward, the work is still far from complete.

7.3.1 Cyanobacterial metabolic engineering

Perhaps the most obvious shortcoming of the work initiated and documented in Chapter 6 is the lack of success in metabolic and recombinant engineering of the cyanobacterial cells. While successful results were obtained in terms of H_2O_2 production with extracellular ETC inhibitors, and with production of peroxidase enzymes in *E. coli*, translating this peroxidase expression to the cyanobacteria was ultimately unsuccessful. The metabolic engineering of aniline or other pre-conductive monomers is also an important area of research not undertaken within the scope of this work but which may be necessary to fully utilize the potential of this novel method of bottom-up additive manufacturing.

Furthermore, engineering of the cyanobacteria to express H_2O_2 in the absence of ETC inhibitors necessitates further work. One potential avenue which could be explored in order to increase the photo-induced expression of H_2O_2 without the use of ETC

inhibitors may be co-culturing of the cyanobacteria with 5-Aminolevulinic acid (5-ALA). Co-culturing with extracellular 5-ALA may cause the cyanobacteria to accumulate toxic amounts of chlorophyll precursor species (such as protochlorophyllide) which may act as a photosensitizer and ROS-promoter. [239] If successful, a knockout could be performed on the rate-limiting mechanisms of chlorophyll precursor expression, resulting in the same internal cell conditions as co-culturing with extracellular 5-ALA.

7.3.2 Reductive Capabilities of *E. coli*

One peculiar phenomenon occurred during the investigation of HRP expression in *E. coli*. When ABTS assays were conducted to determine the peroxidase expression of the HRP plasmid *E. coli*, in some assays the initial concentration of peroxidase species appeared to be quite high (above 1 U/mL) and the ABTS solution turned a deep blue color indicating its oxidized state. However, when the well plates (with live cells) were left to sit on the bench, the wells which were once blue in color reverted to clear. Whereas the samples without live cells (media only or lysed cells) remained more or less the same color over the same period of time. This indicated that the *E. coli* cells were exhibiting *E. coli* reducing behavior despite their expression of HRP enzyme and the presence of high quantities of extracellular oxidizer. When additional ABTS was added to the well plates, no change in color occurred. When additional H₂O₂ was added, the blue color returned. An eppendorf tube was prepared with a sample of these HRP-expressing cells (cultured with 12 μ M hemin, 0 mM IPTG), to which was added 1 mM ABTS and 1 mM H₂O₂ (Figure 7.3A), and the eppendorf tube centrifuged at 10k rcf for 5 minutes to pellet the cells. After approximately 2 hours of incubation, the tube showed a gradient of oxidation. The cells were reducing the oxidized form of the ABTS, but the HRP expressed in solution was oxidizing the ABTS.

The action of a catalase enzyme was suspected. A second batch of cells was prepared in the same manner, except using 20 μ M scopoletin instead of ABTS. A drop of the cells was placed into a fluorescence microscope (Life Technologies EVOS FL 4300) and imaged (Figure 7.3B) - the fluorescence micrograph showed that not all of the *E. coli* cells were showing reducing phenomenon, but only some of the cells. The cause or implications of this phenomenon are unknown. While *E. coli* are known to express a number of naturally occurring oxidase enzymes, it is unclear why some cells were showing what appeared to be catalase-like activity and others showed no such activity.

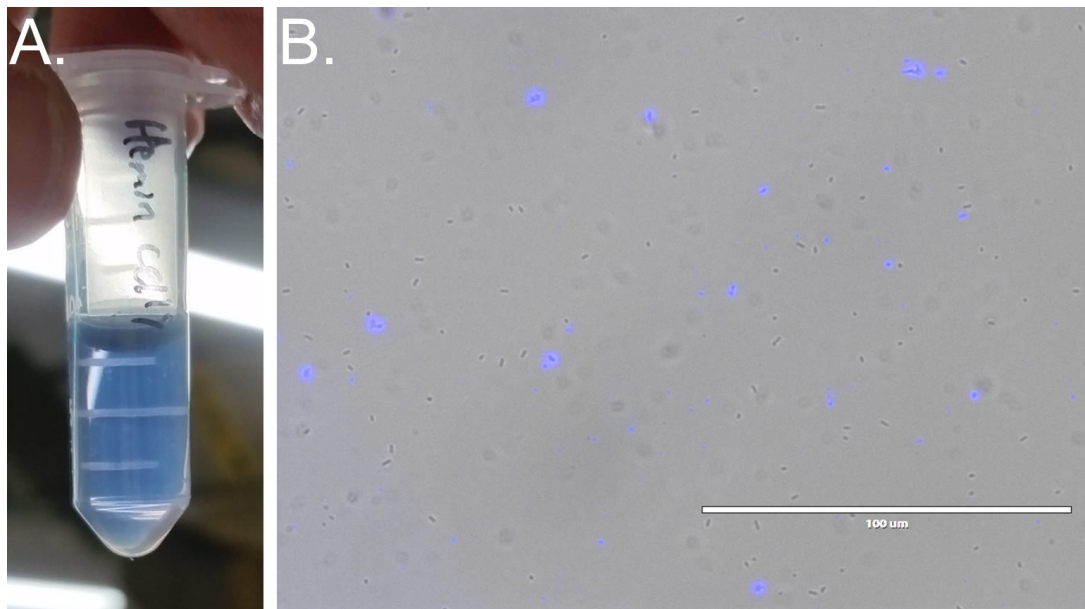


Figure 7.3: A) Photograph of a pelleted HRP-expressing *E. coli* culture in a 2 mL eppendorf tube with ABTS/H₂O₂ in solution showing reductive activity (solution turning clear) around the cell pellet, and B) Fluorescence micrograph of *E. coli* expressing HRP in a scopoletin/H₂O₂ solution showing reductive activity (scopoletin fluorescence around some individual cells, but not others). Scale bar: B) 100 μm .

Performance of a live-dead assay in combination with a scopoletin assay on similar cells expressing peroxidase enzymes may shed some light on the phenomenon.

7.3.3 Final Thoughts

In sum: the metabolic engineering of PSS and aniline, the optimization of H₂O₂ expression in the absence of ETC inhibitors, as well as the expression of all of these processes in a single organism remain as challenges for researchers in the future who choose to direct their efforts towards a self-assembling/self-replicating paradigm of manufacturing.

Bibliography

- [1] Charles W. Hull. Apparatus for production of three-dimensional objects by stereolithography, March 1986.
- [2] Xiaoxing Xia, Christopher M. Spadaccini, and Julia R. Greer. Responsive materials architected in space and time. *Nature Reviews Materials*, pages 1–19, June 2022.
- [3] J. J. Beaman, D. L. Bourell, C. C. Seepersad, and D. Kovar. Additive Manufacturing Review: Early Past to Current Practice. *Journal of Manufacturing Science and Engineering*, 142(11), September 2020.
- [4] Sunpreet Singh, Seeram Ramakrishna, and Rupinder Singh. Material issues in additive manufacturing: A review. *Journal of Manufacturing Processes*, 25:185–200, January 2017.
- [5] Patrick Holzmann, Robert J. Breiteneker, Aqeel A. Soomro, and Erich J. Schwarz. User entrepreneur business models in 3D printing. *Journal of Manufacturing Technology Management*, 28(1):75–94, January 2017.
- [6] Rafiq Noorani. *Rapid Prototyping: Principles and Applications* | Wiley. October 2005.
- [7] Maxim Shusteff. *Volumetric Additive Manufacturing of Polymer Structures by Holographically Projected Light Fields*. PhD thesis, MIT, 2017.
- [8] John R. Tumbleston, David Shirvanyants, Nikita Ermoshkin, Rima Januszewicz, Ashley R. Johnson, David Kelly, Kai Chen, Robert Pinschmidt, Jason P. Rolland, Alexander Ermoshkin, Edward T. Samulski, and Joseph M. DeSimone. Continuous liquid interface production of 3D objects. *Science*, 347(6228):1349–1352, March 2015.
- [9] David A. Walker, James L. Hedrick, and Chad A. Mirkin. Rapid, large-volume, thermally controlled 3D printing using a mobile liquid interface. *Science*, 366(6463):360–364, October 2019.
- [10] Brett E. Kelly, Indrasen Bhattacharya, Hossein Heidari, Maxim Shusteff, Christopher M. Spadaccini, and Hayden K. Taylor. Volumetric additive manufacturing via tomographic reconstruction. *Science*, 363(6431):1075–1079, March 2019.

- [11] Ze-Xian Low, Yen Thien Chua, Brian Michael Ray, Davide Mattia, Ian Saxley Metcalfe, and Darrell Alec Patterson. Perspective on 3D printing of separation membranes and comparison to related unconventional fabrication techniques. *Journal of Membrane Science*, 523:596–613, February 2017.
- [12] M. Fahad, P. Dickens, and M. Gilbert. Novel polymeric support materials for jetting based additive manufacturing processes. *Rapid Prototyping Journal*, 19(4):230–239, January 2013.
- [13] Jeffrey W. Stansbury and Mike J. Idacavage. 3D printing with polymers: Challenges among expanding options and opportunities. *Dental Materials*, 32(1):54–64, January 2016.
- [14] Rhys Jones, P. Haufe, E. Sells, P. Irvani, V. Olliver, Chris Palmer, and A. Bowyer. RepRap – the replicating rapid prototyper. *Robotica*, 2011.
- [15] Vincent Hahn, Pascal Kiefer, Tobias Frenzel, Jingyuan Qu, Eva Blasco, Christopher Barner-Kowollik, and Martin Wegener. Rapid Assembly of Small Materials Building Blocks (Voxels) into Large Functional 3D Metamaterials. *Advanced Functional Materials*, 30(26):1907795, 2020.
- [16] Jui-Teng Lin, Hsia-Wei Liu, Kuo-Ti Chen, and Da-Chuan Cheng. Modeling the Kinetics, Curing Depth, and Efficacy of Radical-Mediated Photopolymerization: The Role of Oxygen Inhibition, Viscosity, and Dynamic Light Intensity. *Frontiers in Chemistry*, 7, 2019.
- [17] Sam Kriegman, Douglas Blackiston, Michael Levin, and Josh Bongard. Kinematic self-replication in reconfigurable organisms. *Proceedings of the National Academy of Sciences*, 118(49), December 2021.
- [18] M. Schaechter, Joan P. Williamson, J. R. Hood, and A. L. YR 1962 Koch. Growth, Cell and Nuclear Divisions in some Bacteria. *Microbiology*, 29(3):421–434.
- [19] Alain Goriely. *The Mathematics and Mechanics of Biological Growth*. Springer, May 2017. Google-Books-ID: rgImDwAAQBAJ.
- [20] Onur Aydin, Austin P. Passaro, Ritu Raman, Samantha E. Spellicy, Robert P. Weinberg, Roger D. Kamm, Matthew Sample, George A. Truskey, Jeremiah Zartman, Roy D. Dar, Sebastian Palacios, Jason Wang, Jesse Tordoff, Nuria Montserrat, Rashid Bashir, M. Taher A. Saif, and Ron Weiss. Principles for the design of multicellular engineered living systems. *APL Bioengineering*, 6(1):010903, March 2022.
- [21] Satoshi Toda, Lucas R. Blauch, Sindy K. Y. Tang, Leonardo Morsut, and Wendell A. Lim. Programming self-organizing multicellular structures with synthetic cell-cell signaling. *Science*, 361(6398):156–162, July 2018.
- [22] John Jumper, Richard Evans, Alexander Pritzel, Tim Green, Michael Figurnov, Olaf Ronneberger, Kathryn Tunyasuvunakool, Russ Bates, Augustin Žídek, Anna

- Potapenko, Alex Bridgland, Clemens Meyer, Simon A. A. Kohl, Andrew J. Ballard, Andrew Cowie, Bernardino Romera-Paredes, Stanislav Nikolov, Rishub Jain, Jonas Adler, Trevor Back, Stig Petersen, David Reiman, Ellen Clancy, Michal Zielinski, Martin Steinegger, Michalina Pacholska, Tamas Berghammer, Sebastian Bodenstern, David Silver, Oriol Vinyals, Andrew W. Senior, Koray Kavukcuoglu, Pushmeet Kohli, and Demis Hassabis. Highly accurate protein structure prediction with AlphaFold. *Nature*, 596(7873):583–589, August 2021.
- [23] Joseph T. Toombs, Manuel Luitz, Caitlyn C. Cook, Sophie Jenne, Chi Chung Li, Bastian E. Rapp, Frederik Kotz-Helmer, and Hayden K. Taylor. Volumetric additive manufacturing of silica glass with microscale computed axial lithography. *Science*, 376(6590):308–312, April 2022.
- [24] Tiemo Bückmann, Nicolas Stenger, Muamer Kadic, Johannes Kaschke, Andreas Frölich, Tobias Kennerknecht, Christoph Eberl, Michael Thiel, and Martin Wegener. Tailored 3D Mechanical Metamaterials Made by Dip-in Direct-Laser-Writing Optical Lithography. *Advanced Materials*, 24(20):2710–2714, 2012.
- [25] Wei Chu, Yuanxin Tan, Peng Wang, Jian Xu, Wenbo Li, Jia Qi, and Ya Cheng. Centimeter-Height 3D Printing with Femtosecond Laser Two-Photon Polymerization. *Advanced Materials Technologies*, 3(5):1700396, 2018.
- [26] Qiang Geng, Dien Wang, Pengfei Chen, and Shih-Chi Chen. Ultrafast multi-focus 3-D nano-fabrication based on two-photon polymerization. *Nature Communications*, 10(1):2179, May 2019.
- [27] Jun-ichi Kato, Nobuyuki Takeyasu, Yoshihiro Adachi, Hong-Bo Sun, and Satoshi Kawata. Multiple-spot parallel processing for laser micronanofabrication. *Applied Physics Letters*, 86(4):044102, January 2005.
- [28] Xian-Zi Dong, Zhen-Sheng Zhao, and Xuan-Ming Duan. Micronanofabrication of assembled three-dimensional microstructures by designable multiple beams multiphoton processing. *Applied Physics Letters*, 91(12):124103, September 2007.
- [29] Joachim Fischer and Martin Wegener. Three-dimensional direct laser writing inspired by stimulated-emission-depletion microscopy [Invited]. *Optical Materials Express*, 1(4):614–624, August 2011.
- [30] Liang Yang, Ayman El-Tamer, Ulf Hinze, Jiawen Li, Yanlei Hu, Wenhao Huang, Jiaru Chu, and Boris N. Chichkov. Parallel direct laser writing of micro-optical and photonic structures using spatial light modulator. *Optics and Lasers in Engineering*, 70:26–32, July 2015.
- [31] Wensheng Yan, Benjamin P. Cumming, and Min Gu. High-throughput fabrication of micrometer-sized compound parabolic mirror arrays by using parallel laser direct-write processing. *Journal of Optics*, 17(7):075803, July 2015.
- [32] Benjamin W. Pearre, Christos Michas, Jean-Marc Tsang, Timothy J. Gardner, and Timothy M. Otchy. Fast micron-scale 3D printing with a resonant-scanning two-photon microscope. *Additive Manufacturing*, 30:100887, December 2019.

- [33] Sang-Hu Park, Tae-Woo Lim, Dong-Yol Yang, Jun-Ho Jeong, Ki-Don Kim, Kwang-Sup Lee, and Hong-Jin Kong. Effective fabrication of three-dimensional nano/microstructures in a single step using multilayered stamp. *Applied Physics Letters*, 88(20):203105, May 2006.
- [34] G. M. Gratson, F. García-Santamaría, V. Lousse, M. Xu, S. Fan, J. A. Lewis, and P. V. Braun. Direct-Write Assembly of Three-Dimensional Photonic Crystals: Conversion of Polymer Scaffolds to Silicon Hollow-Woodpile Structures. *Advanced Materials*, 18(4):461–465, 2006.
- [35] E. B. Duoss, M. Twardowski, and J. A. Lewis. Sol-Gel Inks for Direct-Write Assembly of Functional Oxides. *Advanced Materials*, 19(21):3485–3489, 2007.
- [36] Eric B. Duoss, Todd H. Weisgraber, Keith Hearon, Cheng Zhu, Ward Small IV, Thomas R. Metz, John J. Vericella, Holly D. Barth, Joshua D. Kuntz, Robert S. Maxwell, Christopher M. Spadaccini, and Thomas S. Wilson. Three-Dimensional Printing of Elastomeric, Cellular Architectures with Negative Stiffness. *Advanced Functional Materials*, 24(31):4905–4913, 2014.
- [37] Xiaoyu Zheng, Joshua Deotte, Matthew P. Alonso, George R. Farquar, Todd H. Weisgraber, Steven Gemberling, Howon Lee, Nicholas Fang, and Christopher M. Spadaccini. Design and optimization of a light-emitting diode projection micro-stereolithography three-dimensional manufacturing system. *Review of Scientific Instruments*, 83(12):125001, December 2012.
- [38] Herminso Villarraga-Gómez and Stuart T. Smith. Effect of the number of projections on dimensional measurements with X-ray computed tomography. *Precision Engineering*, 66:445–456, November 2020.
- [39] A. C. Kak and M. Slaney. *Principles of computerized tomographic imaging*. January 1988.
- [40] A. Wagner, A. M. Kreuzer, L. Göpperl, L. Schranzhofer, and C. Paulik. Foamable acrylic based ink for the production of light weight parts by inkjet-based 3D printing. *European Polymer Journal*, 115:325–334, June 2019.
- [41] George Wypych. *Handbook of Foaming and Blowing Agents - 1st Edition*. ChemTec Publishing, 1st edition, February 2017.
- [42] Ying Liu, John H. Campbell, Ori Stein, Lijia Jiang, Jared Hund, and Yongfeng Lu. Deformation Behavior of Foam Laser Targets Fabricated by Two-Photon Polymerization. *Nanomaterials*, 8(7):498, July 2018.
- [43] Wei Xiong, Ying Liu, Li Jia Jiang, Yun Shen Zhou, Da Wei Li, Lan Jiang, Jean-François Silvain, and Yong Feng Lu. Laser-Directed Assembly of Aligned Carbon Nanotubes in Three Dimensions for Multifunctional Device Fabrication. *Advanced Materials*, 28(10):2002–2009, 2016.
- [44] Bradley J. Sparks, Ethan F. T. Hoff, LaTonya P. Hayes, and Derek L. Patton. Mussel-Inspired Thiol–Ene Polymer Networks: Influencing Network Properties and

- Adhesion with Catechol Functionality. *Chemistry of Materials*, 24(18):3633–3642, September 2012.
- [45] Guoqi Zhang, Bing Wang, Li Ma, Linzhi Wu, Shidong Pan, and Jinshui Yang. Energy absorption and low velocity impact response of polyurethane foam filled pyramidal lattice core sandwich panels. *Composite Structures*, 108:304–310, February 2014.
- [46] Global Polymer Foam Market Size & Share | Industry Report, 2019-2025.
- [47] Qiyi Chen, Peng-Fei Cao, and Rigoberto C. Advincula. Mechanically Robust, Ultraelastic Hierarchical Foam with Tunable Properties via 3D Printing. *Advanced Functional Materials*, 28(21):1800631, 2018.
- [48] Qiyi Chen, Jiayu Zhao, Jingbo Ren, Lihan Rong, Peng-Fei Cao, and Rigoberto C. Advincula. 3D Printed Multifunctional, Hyperelastic Silicone Rubber Foam. *Advanced Functional Materials*, 29(23):1900469, 2019.
- [49] Ashish Kumar Singh, Balu Patil, Niklas Hoffmann, Brooks Saltonstall, Mrityunjay Doddamani, and Nikhil Gupta. Additive Manufacturing of Syntactic Foams: Part 1: Development, Properties, and Recycling Potential of Filaments. *JOM*, 70(3):303–309, March 2018.
- [50] Matteo Gregorio Modesto Marascio, Jens Antons, Dominique P. Pioletti, and Pierre-Etienne Bourban. 3D Printing of Polymers with Hierarchical Continuous Porosity. *Advanced Materials Technologies*, 2(11):1700145, 2017.
- [51] Claas Willem Visser, Dahlia N. Amato, Jochen Mueller, and Jennifer A. Lewis. Architected Polymer Foams via Direct Bubble Writing. *Advanced Materials*, 31(46):1904668, November 2019.
- [52] Xuan Song, Zhuofeng Zhang, Zeyu Chen, and Yong Chen. Porous Structure Fabrication Using a Stereolithography-Based Sugar Foaming Method. *Journal of Manufacturing Science and Engineering*, 139(3), March 2017.
- [53] Megan Carve and Donald Wlodkovic. 3D-Printed Chips: Compatibility of Additive Manufacturing Photopolymeric Substrata with Biological Applications. *Micromachines*, 9(2):91, February 2018.
- [54] Michael Ashby. *Materials Selection in Mechanical Design*. Elsevier, 3rd edition, 2005.
- [55] Chu Jing, Yasuhito Suzuki, and Akikazu Matsumoto. Thermal decomposition of methacrylate polymers containing tert-butoxycarbonyl moiety. *Polymer Degradation and Stability*, 166:145–154, August 2019.
- [56] Frederik Kotz, Karl Arnold, Werner Bauer, Dieter Schild, Nico Keller, Kai Sachsenheimer, Tobias M. Nargang, Christiane Richter, Dorothea Helmer, and Bastian E. Rapp. Three-dimensional printing of transparent fused silica glass. *Nature*, 544(7650):337–339, April 2017.

- [57] Carl J. Thrasher, Johanna J. Schwartz, and Andrew J. Boydston. Modular Elastomer Photoresins for Digital Light Processing Additive Manufacturing. *ACS Applied Materials & Interfaces*, 9(45):39708–39716, November 2017.
- [58] Wouter E. Roorda, Johanna A. Bouwstra, Mattina A. de Vries, and Hans E. Junginger. Thermal Behavior of Poly Hydroxy Ethyl Methacrylate (pHEMA) Hydrogels. *Pharmaceutical Research*, 5(11):722–725, November 1988.
- [59] Jiangtao Wu, Zeang Zhao, Craig M. Hamel, Xiaoming Mu, Xiao Kuang, Zaoyang Guo, and H. Jerry Qi. Evolution of material properties during free radical photopolymerization. *Journal of the Mechanics and Physics of Solids*, 112:25–49, March 2018.
- [60] J. Stehr. Chemical blowing agents in the rubber industry. Past – present – and future? *International Polymer Science and Technology*, 43(1), 2016.
- [61] Tarik Sadik, Caroline Pillon, Christian Carrot, and Jose-Antonio Reglero Ruiz. Dsc studies on the decomposition of chemical blowing agents based on citric acid and sodium bicarbonate. *Thermochimica Acta*, 659:74–81, January 2018.
- [62] Joel M. Williams and Debra A. Wroblewski. Microstructures and properties of some microcellular foams. *Journal of Materials Science*, 24(11):4062–4067, November 1989.
- [63] J. R. Meakin, D. W. L. Hukins, R. M. Aspden, and C. T. Imrie. Rheological properties of poly(2-hydroxyethyl methacrylate) (pHEMA) as a function of water content and deformation frequency. *Journal of Materials Science: Materials in Medicine*, 14(9):783–787, September 2003.
- [64] Mathias Celina. METHOD FOR EPOXY FOAM PRODUCTION USING A LIQUID ANHYDRIDE.
- [65] Masashi Iseki, Yuta Hiraoka, Chu Jing, Haruyuki Okamura, Eriko Sato, and Akikazu Matsumoto. Effect of glass transition temperature on heat-responsive gas bubbles formation from polymers containing tert-butoxycarbonyl moiety. *Journal of Applied Polymer Science*, 135(19):46252, 2018.
- [66] Christopher S. Dean, D. Stanley. Tarbell, and A. W. Friederang. Synthesis and kinetics of decomposition of di-tert-butyl tricarbonate, di-tert-butyl dithioltricarbonate, and the related dicarbonates. *The Journal of Organic Chemistry*, 35(10):3393–3397, October 1970.
- [67] A. R. Greenberg and R. P. Kusy. Influence of crosslinking on the glass transition of poly(acrylic acid). *Journal of Applied Polymer Science*, 25(8):1785–1788, 1980.
- [68] S.M. Walley and J.E. Field. Strain rate sensitivity of polymers in compression from low to high rates. *DYMAT Journal*, 1:211–227, January 1994.
- [69] Luca Di Landro, Giuseppe Sala, and Daniela Olivieri. Deformation mechanisms and energy absorption of polystyrene foams for protective helmets. *Polymer Testing*, 21(2):217–228, January 2002.

- [70] Jessica D. Kaufman, Gregory J. Miller, Elise F. Morgan, and Catherine M. Klapperich. Time-dependent mechanical characterization of poly(2-hydroxyethyl methacrylate) hydrogels using nanoindentation and unconfined compression. *Journal of materials research*, 23(5):1472–1481, May 2008.
- [71] Samuel Clark Ligon, Robert Liska, Jürgen Stampfl, Matthias Gurr, and Rolf Mülhaupt. Polymers for 3D Printing and Customized Additive Manufacturing. *Chemical Reviews*, 117(15):10212–10290, August 2017.
- [72] Tuan D. Ngo, Alireza Kashani, Gabriele Imbalzano, Kate T. Q. Nguyen, and David Hui. Additive manufacturing (3D printing): A review of materials, methods, applications and challenges. *Composites Part B: Engineering*, 143:172–196, June 2018.
- [73] Alberto Giarola. *Dynamic Elastography of Pre-Stressed Material with Multi-Directional Excitation in High Field MRI System*. PhD thesis, University of Illinois, Chicago, 2021.
- [74] Blu-Tough Resin By Siraya Tech.
- [75] Florent Monie, Thomas Vidil, Bruno Grignard, Henri Cramail, and Christophe Detrembleur. Self-foaming polymers: Opportunities for the next generation of personal protective equipment. *Materials Science and Engineering: R: Reports*, 145:100628, July 2021.
- [76] David M Wirth, Anna Jaquez, Sofia Gandarilla, Justin D Hochberg, Derek C Church, and Jonathan K Pokorski. Highly expandable foam for lithographic 3D printing. *ACS applied materials & interfaces*, 12(16):19033–19043, 2020.
- [77] P.S. Liu and G.F. Chen. *Porous Materials - Processing and Applications*. Butterworth-Heinemann, Imprint of Elsevier Inc., 2014.
- [78] Emmanuel O. Ogunsona, Koffi L. Dagnon, and Nandika Anne D’Souza. Multi-Fold Enhancement in Compressive Properties of Polystyrene Foam Using Pre-delaminated Stearate Functionalized Layer Double Hydroxides. *Polymers*, 12(1):8, January 2020.
- [79] James D. Dickson and Jonathan E. Clark. Design of a Multimodal Climbing and Gliding Robotic Platform. *IEEE/ASME Transactions on Mechatronics*, 18(2):494–505, April 2013.
- [80] Soyoung E. Seo, Younghoon Kwon, Neil D. Dolinski, Caitlin S. Sample, Jeffrey L. Self, Christopher M. Bates, Megan T. Valentine, and Craig J. Hawker. Three-Dimensional Photochemical Printing of Thermally Activated Polymer Foams. *ACS Applied Polymer Materials*, 3(10):4984–4991, October 2021.
- [81] FreeFoam | 3D Printable Foam Material for DLP 3D Printers.
- [82] Irina Gouzman, Nurit Atar, Eitan Grossman, Ronen Verker, Asaf Bolker, Mariana Pokrass, Shai Sultan, Omer Sinwani, Annika Wagner, Thomas Lück, and Christian

- Seifarth. 3D Printing of Bismaleimides: From New Ink Formulation to Printed Thermosetting Polymer Objects. *Advanced Materials Technologies*, 4(10):1900368, 2019.
- [83] Tao Wu, Pan Jiang, Xiaoqin Zhang, Yuxiong Guo, Zhongying Ji, Xin Jia, Xiaolong Wang, Feng Zhou, and Weimin Liu. Additively manufacturing high-performance bismaleimide architectures with ultraviolet-assisted direct ink writing. *Materials & Design*, 180:107947, October 2019.
- [84] Tengfei Shen, Dewen Zhou, Liyan Liang, Jie Zheng, Yanxun Lan, and Mangeng Lu. Synthesis and characterization of reactive blocked-isocyanate coupling agents from methyl ethyl ketoxime, ethyl cellosolve/e-caprolactam blocked aromatic and aliphatic diisocyanates. *Journal of Applied Polymer Science*, 122(2):748–757, 2011.
- [85] Marianne S. Rolph, Anna L. J. Markowska, Colin N. Warriner, and Rachel K. O’Reilly. Blocked isocyanates: from analytical and experimental considerations to non-polyurethane applications. *Polymer Chemistry*, 7(48):7351–7364, December 2016.
- [86] Kevin Injoe Jung, Beomjin Kim, Dong Geun Lee, Tae-Hee Lee, Seo Yeon Choi, Jin Chul Kim, Seung Man Noh, Young Il Park, and Hyun Wook Jung. Characteristics of dual-curable blocked isocyanate with thermal radical initiator for low-temperature curing of automotive coatings. *Progress in Organic Coatings*, 125:160–166, December 2018.
- [87] N. Iqbal, M. Tripathi, S. Parthasarathy, D. Kumar, and P. K. Roy. Polyurea spray coatings: Tailoring material properties through chemical crosslinking. *Progress in Organic Coatings*, 123:201–208, October 2018.
- [88] Brian J. Ramirez and Vijay Gupta. High tear strength polyurea foams with low compression set and shrinkage properties at elevated temperatures. *International Journal of Mechanical Sciences*, 150:29–34, January 2019.
- [89] Dr T., M. Anish, J. Jayaprabakar, Jeya Jeevahan, and Durairaj R B. Study on mechanical properties of polyurea coating with various process parameters. *Materials Research Innovations*, 25:1–7, June 2020.
- [90] Sachini D. Perera, Alejandra Durand-Silva, Ashele K. Remy, Shashini D. Diwakara, and Ronald A. Smaldone. 3D Printing of Aramid Nanofiber Composites by Stereolithography. *ACS Applied Nano Materials*, February 2022.
- [91] Ting Li, Zengxiao Wang, Hao Zhang, Zuming Hu, Junrong Yu, Yan Wang, and Jing Zhu. Non-destructive modification of aramid fiber by building nanoscale-coating solution to enhance the interfacial adhesion properties of the fiber-reinforced composites. *Journal of Composite Materials*, 55(13):1823–1834, June 2021.
- [92] Gerhard Kossmehl, Hans-Ingo Nagel, and Andreas Pahl. Cross-linking reactions on polyamides by bis- and tris(maleimide)s. *Die Angewandte Makromolekulare Chemie*, 227(1):139–157, 1995.

- [93] Changhai Chen, Ximeng Wang, Hailiang Hou, Yuansheng Cheng, Pan Zhang, and Jun Liu. Effect of strength matching on failure characteristics of polyurea coated thin metal plates under localized air blast loading: Experiment and numerical analysis. *Thin-Walled Structures*, 154:106819, September 2020.
- [94] Yinggang Miao, Hengning Zhang, He He, and Qiong Deng. Mechanical behaviors and equivalent configuration of a polyurea under wide strain rate range. *Composite Structures*, 222:110923, August 2019.
- [95] Lucia Zema, Giulia Loreti, Elena Macchi, Anastasia Foppoli, Alessandra Maroni, and Andrea Gazzaniga. Injection-Molded Capsular Device for Oral Pulsatile Release: Development of a Novel Mold. *Journal of Pharmaceutical Sciences*, 102(2):489–499, February 2013.
- [96] Parker Lee, Jenna Towslee, João Maia, and Jonathan Pokorski. PEGylation to Improve Protein Stability During Melt Processing. *Macromolecular Bioscience*, 15(10):1332–1337, 2015.
- [97] Parker W. Lee, Sourabh Shukla, Jaqueline D. Wallat, Chaitanya Danda, Nicole F. Steinmetz, Joao Maia, and Jonathan K. Pokorski. Biodegradable Viral Nanoparticle/Polymer Implants Prepared via Melt-Processing. *ACS Nano*, 11(9):8777–8789, September 2017.
- [98] Parker W. Lee, João Maia, and Jonathan K. Pokorski. Milling solid proteins to enhance activity after melt-encapsulation. *International Journal of Pharmaceutics*, 533(1):254–265, November 2017.
- [99] J. Snijder, I. L. Ivanovska, M. Baclayon, W. H. Roos, and G. J. L. Wuite. Probing the impact of loading rate on the mechanical properties of viral nanoparticles. *Micron*, 43(12):1343–1350, December 2012.
- [100] Qingping Guo. THERMOPLASTICS VISCOSITY MEASUREMENT COMBINING EXPERIMENTAL AND COMSOL SIMULATION RESULTS. In *Proceedings of the society of polymer engineers conference*, 2017.
- [101] J. Vlachopoulos. The Role of Rheology in Polymer Extrusion. 2012.
- [102] R. W. Warfield. Compressibility of bulk polymers. *Polymer Engineering & Science*, 6(2):176–180, 1966.
- [103] S. C. Lee, D. Y. Yang, J. Ko, and J. R. Youn. Effect of compressibility on flow field and fiber orientation during the filling stage of injection molding. *Journal of Materials Processing Technology*, 70(1):83–92, October 1997.
- [104] D. E. Dimla, M. Camilotto, and F. Miani. Design and optimisation of conformal cooling channels in injection moulding tools. *Journal of Materials Processing Technology*, 164-165:1294–1300, May 2005.
- [105] Ashis Gopal Banerjee, Xuejun Li, Greg Fowler, and Satyandra K. Gupta. Incorporating manufacturability considerations during design of injection molded multi-material objects. *Research in Engineering Design*, 17(4):207–231, March 2007.

- [106] Charles D. Ryder. Method of forming and injecting thermoplastic materials, June 1942.
- [107] Lucia Zema, Giulia Loreti, Alice Melocchi, Alessandra Maroni, and Andrea Gazzaniga. *Injection Molding and its application to drug delivery*, volume 159. January 2012.
- [108] *Handbook of Molded Part Shrinkage and Warpage*. Elsevier, 2013.
- [109] Wu Hong-wu, Zhang Shao-dan, Qu Jin-ping, and Xu Hai-hang. Measurement and Analysis of Cavity Pressure and Melt Filling Capacity During Injection Molding. *Polymer-Plastics Technology and Engineering*, 46(2):123–127, February 2007.
- [110] Julien Giboz, Thierry Copponnex, and Patrice Mélé. Microinjection molding of thermoplastic polymers: a review. *Journal of Micromechanics and Microengineering*, 17(6):R96–R109, May 2007.
- [111] David M. Wirth and Jonathan K. Pokorski. Design and fabrication of a low-cost pilot-scale melt-processing system. *Polymer*, 181:121802, October 2019.
- [112] Jicheng Yu, Yuqi Zhang, Yanqi Ye, Rocco DiSanto, Wujin Sun, Davis Ranson, Frances S. Ligler, John B. Buse, and Zhen Gu. Microneedle-array patches loaded with hypoxia-sensitive vesicles provide fast glucose-responsive insulin delivery. *Proceedings of the National Academy of Sciences*, 112(27):8260–8265, July 2015.
- [113] Zosano Pharma Announces FDA Acceptance of 505(b)(2) New Drug Application for QtryptaTM for the Acute Treatment of Migraine. Library Catalog: www.nasdaq.com.
- [114] Corium, Inc. Announces FDA Filing Acceptance of New Drug Application for ADLARITY[®] (donepezil transdermal system) for the Treatment of Alzheimer’s Disease. Library Catalog: www.biospace.com.
- [115] Rabinarayan Parhi. Review of Microneedle based Transdermal Drug Delivery Systems. 12(3):4511–24, June 2019.
- [116] Nadine G. Roupael, Michele Paine, Regina Mosley, Sebastien Henry, Devin V. McAllister, Haripriya Kalluri, Winston Pewin, Paula M. Frew, Tianwei Yu, Natalie J. Thornburg, Sarah Kabbani, Lilin Lai, Elena V. Vassilieva, Ioanna Skountzou, Richard W. Compans, Mark J. Mulligan, Mark R. Prausnitz, Allison Beck, Srilatha Edupuganti, Sheila Heeke, Colleen Kelley, and Wendy Nesheim. The safety, immunogenicity, and acceptability of inactivated influenza vaccine delivered by microneedle patch (TIV-MNP 2015): a randomised, partly blinded, placebo-controlled, phase 1 trial. *The Lancet*, 390(10095):649–658, August 2017. Publisher: Elsevier.
- [117] Jordan A. Stinson, Carter R. Palmer, David P. Miller, Adrian B. Li, Kandice Lightner, Heather Jost, William C. Weldon, M. Steven Oberste, Jonathan A. Kluge, and Kathryn M. Kosuda. Thin silk fibroin films as a dried format for temperature stabilization of inactivated polio vaccine. *Vaccine*, 38(7):1652–1660, February 2020.

- [118] Lucia Zema, Giulia Loreti, Alice Melocchi, Alessandra Maroni, and Andrea Gazzaniga. Injection Molding and its application to drug delivery. *Journal of Controlled Release*, 159(3):324–331, May 2012.
- [119] Douglas M Bryce. *Plastic injection molding: manufacturing process fundamentals Vol. 1, Vol. 1,*. Society of Manufacturing Engineers, Dearborn, 1996. OCLC: 840349052.
- [120] Musa Kamal. *Injection molding; technology and fundamentals*. Hanser Publications, 2009.
- [121] Shan Gao, Zhongjun Qiu, and Junhao Ouyang. The Improvement Effect and Mechanism of Longitudinal Ultrasonic Vibration on the Injection Molding Quality of a Polymeric Micro-Needle Array. *Polymers*, 11(1):151, January 2019.
- [122] H. Haugen, J. Will, W. Fuchs, and E. Wintermantel. A novel processing method for injection-molded polyether–urethane scaffolds. Part 1: Processing. *Journal of Biomedical Materials Research Part B: Applied Biomaterials*, 77B(1):65–72, 2006.
- [123] M. E. Gomes, A. S. Ribeiro, P. B. Malafaya, R. L. Reis, and A. M. Cunha. A new approach based on injection moulding to produce biodegradable starch-based polymeric scaffolds: morphology, mechanical and degradation behaviour. *Biomaterials*, 22(9):883–889, May 2001.
- [124] Firas Sammoura, JeongJin Kang, Young-Moo Heo, TaeSung Jung, and Liwei Lin. Polymeric microneedle fabrication using a microinjection molding technique. *Microsystem Technologies*, 13(5):517–522, March 2007.
- [125] Ying Zhang, Ken Brown, Kris Siebenaler, Amy Determan, Daniel Dohmeier, and Kris Hansen. Development of Lidocaine-Coated Microneedle Product for Rapid, Safe, and Prolonged Local Analgesic Action. *Pharmaceutical Research*, 29(1):170–177, January 2012.
- [126] R. Hoyle. Manufacturing components for a micro litre drug delivery system. *Eur. Med. Device Technol.*, 1(4), 2010.
- [127] Jone-Shin Deng, Marts Meisters, Luk Li, Jeff Setesak, Lee Claycomb, Youqin Tian, Dennis Stephens, and Matt Widman. The Development of an Injection-Molding Process for a Polyanhydride Implant Containing Gentamicin Sulfate. *PDA Journal of Pharmaceutical Science and Technology*, 56(2):65–77, March 2002.
- [128] M. Hecke and W. K. Schomburg. Review on micro molding of thermoplastic polymers. *Journal of Micromechanics and Microengineering*, 14(3):R1–R14, December 2003.
- [129] L Eith, R. F. T. Stepto, and I. Tomka. Injection-moulded drug-delivery systems. *Manuf. Chem.*, 58(1):21–25, 1987.
- [130] Christiane König, Kurt Ruffieux, Erich Wintermantel, and Jürg Blaser. Autosterilization of biodegradable implants by injection molding process. *Journal of biomedical materials research*, 38:115–9, June 1997.

- [131] Michael M Crowley, Feng Zhang, Michael A Repka, Sridhar Thumma, Sampada B Upadhye, Sunil Kumar Battu, James W McGinity, and Charles Martin. *Pharmaceutical Applications of Hot-Melt Extrusion: Part I*, volume 33. October 2007.
- [132] Michael A Repka, Soumyajit Majumdar, Sunil Kumar Battu, Ramesh Srirangam, and Sampada B Upadhye. *Application of hot-melt extrusion for drug delivery*, volume 5. January 2009.
- [133] Matthew D. Shin, Sourabh Shukla, Young Hun Chung, Veronique Beiss, Soo Khim Chan, Oscar A. Ortega-Rivera, David M. Wirth, Angela Chen, Markus Sack, Jonathan K. Pokorski, and Nicole F. Steinmetz. COVID-19 vaccine development and a potential nanomaterial path forward. *Nature Nanotechnology*, 15(8):646–655, August 2020.
- [134] L. Eith, R. F. T. Stepto, I. Tomka, and F. Wittwer. The Injection-Moulded Capsule. *Drug Development and Industrial Pharmacy*, 12(11-13):2113–2126, January 1986.
- [135] Herwig Juster, Bart van der Aar, and Hans de Brouwer. A review on microfabrication of thermoplastic polymer-based microneedle arrays. *Polymer Engineering & Science*, 59(5):877–890, 2019.
- [136] Bekir Bediz, Emrullah Korkmaz, Rakesh Khilwani, Cara Donahue, Geza Erdos, Louis D. Falo, and O. Burak Ozdoganlar. Dissolvable Microneedle Arrays for Intradermal Delivery of Biologics: Fabrication and Application. *Pharmaceutical research*, 31(1):117–135, January 2014.
- [137] N. R. Nair, V. C. Sekhar, K. M. Nampoothiri, and A. Pandey. 32 - Biodegradation of Biopolymers. In Ashok Pandey, Sangeeta Negi, and Carlos Ricardo Soccol, editors, *Current Developments in Biotechnology and Bioengineering*, pages 739–755. Elsevier, January 2017.
- [138] Poly(ethylene oxide) 181986.
- [139] N. Passerini and D. Q. Craig. An investigation into the effects of residual water on the glass transition temperature of polylactide microspheres using modulated temperature DSC. *Journal of Controlled Release: Official Journal of the Controlled Release Society*, 73(1):111–115, May 2001.
- [140] World Health Organization. WHO | Immunization supply chain and logistics IVB/14.05. Library Catalog: www.who.int Publisher: World Health Organization.
- [141] Population Division United Nations. WHO | Global Vaccine Action Plan 2019 Immunization coverage data. Library Catalog: www.who.int Publisher: World Health Organization.
- [142] Sayoni Ray, David M. Wirth, Oscar A. Ortega-Rivera, Nicole F. Steinmetz, and Jonathan K. Pokorski. Dissolving Microneedle Delivery of a Prophylactic HPV Vaccine. *Biomacromolecules*, 23(3):903–912, March 2022.

- [143] Ah-Young Jee, Hyemin Lee, Youmin Lee, and Minyung Lee. Determination of the elastic modulus of poly(ethylene oxide) using a photoisomerizing dye. *Chemical Physics*, 422:246–250, August 2013.
- [144] Miguel Angel Lopez-Ramirez, Fernando Soto, Chao Wang, Ricardo Rueda, Sourabh Shukla, Cristian Silva-Lopez, Daniel Kupor, David A. McBride, Jonathan K. Pokorski, Amir Nourhani, Nicole F. Steinmetz, Nisarg J. Shah, and Joseph Wang. Built-In Active Microneedle Patch with Enhanced Autonomous Drug Delivery. *Advanced Materials*, 32(1):1905740, 2020.
- [145] Christine E. Boone, Chao Wang, Miguel Angel Lopez-Ramirez, Veronique Beiss, Sourabh Shukla, Paul L. Chariou, Daniel Kupor, Ricardo Rueda, Joseph Wang, and Nicole F. Steinmetz. Active Microneedle Administration of Plant Virus Nanoparticles for Cancer In Situ Vaccination Improves Immunotherapeutic Efficacy. *ACS Applied Nano Materials*, 3(8):8037–8051, August 2020.
- [146] Shayan F. Lahiji, Manita Dangol, and Hyungil Jung. A patchless dissolving microneedle delivery system enabling rapid and efficient transdermal drug delivery. *Scientific Reports*, 5, January 2015.
- [147] Bernhard Brauner, Patrik Schwarz, Michael Wirth, and Franz Gabor. Micro vs. nano: PLGA particles loaded with trimethoprim for instillative treatment of urinary tract infections. *International Journal of Pharmaceutics*, 579:119158, April 2020.
- [148] Kate Duffy. Elon Musk says 194 billion hamsters can fit inside Tesla’s new Gigafactory in Texas, which is as big as 3 Pentagons.
- [149] E. Kinne-Saffran and R. K. Kinne. Vitalism and synthesis of urea. From Friedrich Wohler to Hans A. Krebs. *American Journal of Nephrology*, 19(2):290–294, 1999.
- [150] Manuel Schaffner, Patrick A. Rühls, Fergal Coulter, Samuel Kilcher, and André R. Studart. 3D printing of bacteria into functional complex materials. *Science Advances*, 3(12):eaao6804, December 2017.
- [151] Xiaofan Jin and Ingmar H. Riedel-Kruse. Biofilm Lithography enables high-resolution cell patterning via optogenetic adhesin expression. *Proceedings of the National Academy of Sciences of the United States of America*, 115(14):3698–3703, April 2018.
- [152] Jacob Koffler, Wei Zhu, Xin Qu, Oleksandr Platoshyn, Jennifer N. Dulin, John Brock, Lori Graham, Paul Lu, Jeff Sakamoto, Martin Marsala, Shaochen Chen, and Mark H. Tuszynski. Biomimetic 3D-printed scaffolds for spinal cord injury repair. *Nature Medicine*, 25(2):263–269, February 2019.
- [153] Nadav Noor, Assaf Shapira, Reuven Edri, Idan Gal, Lior Wertheim, and Tal Dvir. 3D Printing of Personalized Thick and Perfusable Cardiac Patches and Hearts. *Advanced Science*, 6(11):1900344, 2019.

- [154] Ludovico Cademartiri and Kyle J. M. Bishop. Programmable self-assembly. *Nature Materials*, 14(1):2–9, January 2015.
- [155] Daniel Wangpraseurt, Shangting You, Farooq Azam, Gianni Jacucci, Olga Gaidarenko, Mark Hildebrand, Michael Köhl, Alison G. Smith, Matthew P. Davey, Alyssa Smith, Dimitri D. Deheyn, Shaochen Chen, and Silvia Vignolini. Bionic 3D printed corals. *Nature Communications*, 11(1):1748, April 2020.
- [156] Anna M. Duraj-Thatte, Noémie-Manuelle Dorval Courchesne, Pichet Praveschotinunt, Jarod Rutledge, Yuhan Lee, Jeffrey M. Karp, and Neel S. Joshi. Genetically Programmable Self-Regenerating Bacterial Hydrogels. *Advanced Materials*, 31(40):1901826, 2019.
- [157] Pei Kun R. Tay, Peter Q. Nguyen, and Neel S. Joshi. A Synthetic Circuit for Mercury Bioremediation Using Self-Assembling Functional Amyloids. *ACS Synthetic Biology*, 6(10):1841–1850, October 2017.
- [158] Peter Q. Nguyen, Noémie-Manuelle Dorval Courchesne, Anna Duraj-Thatte, Pichet Praveschotinunt, and Neel S. Joshi. Engineered Living Materials: Prospects and Challenges for Using Biological Systems to Direct the Assembly of Smart Materials. *Advanced Materials (Deerfield Beach, Fla.)*, 30(19):e1704847, May 2018.
- [159] Xinyue Liu, Hyunwoo Yuk, Shaoting Lin, German Alberto Parada, Tzu-Chieh Tang, Eléonore Tham, Cesar de la Fuente-Nunez, Timothy K. Lu, and Xuanhe Zhao. 3D Printing of Living Responsive Materials and Devices. *Advanced Materials (Deerfield Beach, Fla.)*, 30(4), January 2018.
- [160] Liya Liang, Rongming Liu, Kyle E. O. Foster, AlakshChoudhury, Sherri Cook, Jeffrey C. Cameron, Wil V. Srubar, and Ryan T. Gill. Genome engineering of *E. coli* for improved styrene production. *Metabolic Engineering*, 57:74–84, January 2020.
- [161] Gang Fan, Austin J. Graham, Jayaker Kolli, Nathaniel A. Lynd, and Benjamin K. Keitz. Aerobic radical polymerization mediated by microbial metabolism. *Nature Chemistry*, 12(7):638–646, July 2020.
- [162] Guy della Cioppa, Stephen J. Garger, Genadie G. Sverlow, Thomas H. Turpen, and Laurence K. Grill. Melanin Production in *Escherichia coli* from a Cloned Tyrosinase Gene. *Bio/Technology*, 8(7):634–638, July 1990.
- [163] A. Bernardus Mostert, Ben J. Powell, Ian R. Gentle, and Paul Meredith. On the origin of electrical conductivity in the bio-electronic material melanin. *Applied Physics Letters*, 100(9):093701, February 2012.
- [164] Priti Pharkya. Microorganisms for the production of aniline, January 2017.
- [165] Seth C. Rasmussen. The Early History of Polyaniline: Discovery and Origins. *Substantia*, 1(2), October 2017.
- [166] H. Letheby. XXIX.—On the production of a blue substance by the electrolysis of sulphate of aniline. *Journal of the Chemical Society*, 15(0):161–163, January 1862.

- [167] Richard Balint, Nigel J. Cassidy, and Sarah H. Cartmell. Conductive polymers: Towards a smart biomaterial for tissue engineering. *Acta Biomaterialia*, 10(6):2341–2353, June 2014.
- [168] Jaroslav Stejskal and Jan Prokeš. Conductivity and morphology of polyaniline and polypyrrole prepared in the presence of organic dyes. *Synthetic Metals*, 264:116373, June 2020.
- [169] Feixue Zou, Luyan Xue, Xinxin Yu, Ying Li, Yin Zhao, Lu Lu, Xirong Huang, and Yinbo Qu. One step biosynthesis of chiral, conducting and water soluble polyaniline in AOT micellar solution. *Colloids and Surfaces A: Physicochemical and Engineering Aspects*, 429:38–43, July 2013.
- [170] Ryan Bouldin, Sethumadhavan Ravichandran, Akshay Kokil, Rahul Garhwal, Subhalakshmi Nagarajan, Jayant Kumar, Ferdinando F. Bruno, Lynne A. Samuelson, and Ramaswamy Nagarajan. Synthesis of polypyrrole with fewer structural defects using enzyme catalysis. *Synthetic Metals*, 161(15):1611–1617, August 2011.
- [171] Christopher T. Walsh, Sylvie Garneau-Tsodikova, and Annaleise R. Howard-Jones. Biological formation of pyrroles: Nature’s logic and enzymatic machinery. *Natural Product Reports*, 23(4):517–531, July 2006.
- [172] Andrew T. Cullen and Aaron D. Price. Digital light processing for the fabrication of 3D intrinsically conductive polymer structures. *Synthetic Metals*, 235:34–41, January 2018.
- [173] Jianjun Liao, Hwei Si, Xidong Zhang, and Shiwei Lin. Functional Sensing Interfaces of PEDOT:PSS Organic Electrochemical Transistors for Chemical and Biological Sensors: A Mini Review. *Sensors (Basel, Switzerland)*, 19(2):E218, January 2019.
- [174] Yi Zheng, Yangdong Wang, Fan Zhang, Shaomin Zhang, Kiryl D. Piatkevich, Nanjia Zhou, and Jonathan K. Pokorski. Coagulation Bath-Assisted 3D Printing of PEDOT:PSS with High Resolution and Strong Substrate Adhesion for Bioelectronic Devices. *Advanced Materials Technologies*, 7(7):2101514, 2022.
- [175] Hirokazu Yano, Kazuki Kudo, Kazumasa Marumo, and Hidenori Okuzaki. Fully soluble self-doped poly(3,4-ethylenedioxythiophene) with an electrical conductivity greater than 1000 S cm⁻¹. *Science Advances*, 5(4):eaav9492, April 2019.
- [176] Valérie Rumbau, Jose A. Pomposo, Aitziber Eleta, Javier Rodriguez, Hans Grande, David Mecerreyes, and Estibalitz Ochoteco. First enzymatic synthesis of water-soluble conducting poly(3,4-ethylenedioxythiophene). *Biomacromolecules*, 8(2):315–317, February 2007.
- [177] Sabrin R. M. Ibrahim, Abdelsattar M. Omar, Alaa A. Bagalagel, Reem M. Diri, Ahmad O. Noor, Diena M. Almasri, Shaimaa G. A. Mohamed, and Gamal A. Mohamed. Thiophenes-Naturally Occurring Plant Metabolites: Biological Activities and In Silico Evaluation of Their Potential as Cathepsin D Inhibitors. *Plants (Basel, Switzerland)*, 11(4):539, February 2022.

- [178] Ilaria Marotti, Mauro Marotti, Roberta Piccaglia, Anna Nastri, Silvia Grandi, and Giovanni Dinelli. Thiophene occurrence in different *Tagetes* species: agricultural biomasses as sources of biocidal substances. *Journal of the Science of Food and Agriculture*, 90(7):1210–1217, May 2010.
- [179] Eleni Stavrinidou, Roger Gabrielsson, K. Peter R. Nilsson, Sandeep Kumar Singh, Juan Felipe Franco-Gonzalez, Anton V. Volkov, Magnus P. Jonsson, Andrea Grimoldi, Mathias Elgland, Igor V. Zozoulenko, Daniel T. Simon, and Magnus Berggren. In vivo polymerization and manufacturing of wires and supercapacitors in plants. *Proceedings of the National Academy of Sciences*, 114(11):2807–2812, March 2017.
- [180] Muhammad Ovais, Ali Talha Khalil, Muhammad Ayaz, Irshad Ahmad, Susheel Kumar Nethi, and Sudip Mukherjee. Biosynthesis of Metal Nanoparticles via Microbial Enzymes: A Mechanistic Approach. *International Journal of Molecular Sciences*, 19(12):4100, December 2018.
- [181] Urartu Ozgur Safak Seker, Allen Y. Chen, Robert J. Citorik, and Timothy K. Lu. Synthetic Biogenesis of Bacterial Amyloid Nanomaterials with Tunable Inorganic–Organic Interfaces and Electrical Conductivity. *ACS Synthetic Biology*, 6(2):266–275, February 2017.
- [182] Esam M. Bakir, Nancy S. Younis, Maged E. Mohamed, and Nermin A. El Semary. Cyanobacteria as Nanogold Factories: Chemical and Anti-Myocardial Infarction Properties of Gold Nanoparticles Synthesized by *Lyngbya majuscula*. *Marine Drugs*, 16(6):E217, June 2018.
- [183] Yuanyuan Yang, Shaozhu Chen, and Lan Xu. Enhanced Conductivity of Polyaniline by Conjugated Crosslinking. *Macromolecular Rapid Communications*, 32(7):593–597, 2011.
- [184] Surajit Sinha, Sambhu Bhadra, and Dipak Khastgir. Effect of dopant type on the properties of polyaniline. *Journal of Applied Polymer Science*, 112(5):3135–3140, 2009.
- [185] Katarzyna Bednarczyk, Wiktor Matysiak, Tomasz Tański, Henryk Janeczek, Ewa Schab-Balcerzak, and Marcin Libera. Effect of polyaniline content and protonating dopants on electroconductive composites. *Scientific Reports*, 11(1):7487, April 2021.
- [186] R. A. de Barros, W. M. de Azevedo, and F. M. de Aguiar. Photo-induced polymerization of polyaniline. *Materials Characterization*, 50(2):131–134, March 2003.
- [187] Gordana Ćirić Marjanović, Budimir Marjanović, Patrycja Bober, Zuzana Rozlívková, Jaroslav Stejskal, Miroslava Trchová, and Jan Prokeš. The oxidative polymerization of p-phenylenediamine with silver nitrate: Toward highly conducting micro/nanostructured silver/conjugated polymer composites. *Journal of Polymer Science Part A: Polymer Chemistry*, 49(15):3387–3403, 2011.

- [188] Patrycja Bober, Jaroslav Stejskal, Miroslava Trchová, Jan Prokeš, and Irina Sapurina. Oxidation of Aniline with Silver Nitrate Accelerated by p-Phenylenediamine: A New Route to Conducting Composites. *Macromolecules*, 43(24):10406–10413, December 2010.
- [189] Jing Li, Heqing Tang, Aiqing Zhang, Xiantao Shen, and Lihua Zhu. A New Strategy for the Synthesis of Polyaniline Nanostructures: From Nanofibers to Nanowires. *Macromolecular Rapid Communications*, 28(6):740–745, 2007.
- [190] Xue Wang, Jinxing Deng, Xiaojuan Duan, Dong Liu, Jinshan Guo, and Peng Liu. Crosslinked polyaniline nanorods with improved electrochemical performance as electrode material for supercapacitors. *Journal of Materials Chemistry A*, 2(31):12323–12329, July 2014.
- [191] Euijin Shim, Jing Su, Jennifer Noro, Marta A. Teixeira, Artur Cavaco-Paulo, Carla Silva, and Hye Rim Kim. Conductive bacterial cellulose by in situ laccase polymerization of aniline. *PloS One*, 14(4):e0214546, 2019.
- [192] Galina Shumakovich, Alexander Streltsov, Elena Gorshina, Tatyana Rusinova, Victoria Kurova, Irina Vasil’eva, Grigory Otrokhov, Olga Morozova, and Alexander Yaropolov. Laccase-catalyzed oxidative polymerization of aniline dimer (N-phenyl-1,4-phenylenediamine) in aqueous micellar solution of sodium dodecylbenzenesulfonate. *Journal of Molecular Catalysis B: Enzymatic*, 69(3):83–88, May 2011.
- [193] V. S. Vasantha and K. L. N. Phani. Effect of hydroxypropyl- β -cyclodextrin on the electrochemical oxidation and polymerization of 3,4-ethylenedioxythiophene. *Journal of Electroanalytical Chemistry*, 520(1):79–88, February 2002.
- [194] Nigel C. Veitch. Horseradish peroxidase: a modern view of a classic enzyme. *Phytochemistry*, 65(3):249–259, February 2004.
- [195] Jose Neptuno Rodriguez-Lopez, David J. Lowe, Josefa Hernsandez-Ruiz, Alexander N. P. Hiner, Francisco Garcia-Csnavas, and Roger N. F. Thorneley. Mechanism of Reaction of Hydrogen Peroxide with Horseradish Peroxidase: Identification of Intermediates in the Catalytic Cycle. *Journal of the American Chemical Society*, 123(48):11838–11847, December 2001.
- [196] Jutta Vlasits, Christa Jakopitsch, Margit Bernroitner, Marcel Zamocky, Paul G. Furtmüller, and Christian Obinger. Mechanisms of catalase activity of heme peroxidases. *Archives of Biochemistry and Biophysics*, 500(1):74–81, August 2010.
- [197] Antonio Cano, Josefa Hernández-Ruíz, Francisco García-Cánovas, Manuel Acosta, and Marino B. Arnao. An end-point method for estimation of the total antioxidant activity in plant material. *Phytochemical Analysis*, 9(4):196–202, 1998.
- [198] F. Alyas, M. A. Zia, and University of Agriculture Khalil-ur Rehman. Extraction and purification of peroxidase from soybean seeds. *Pakistan Journal of Agricultural Sciences (Pakistan)*, 2002.

- [199] Peroxidase Type VI, essentially salt-free, lyophilized powder, main = 250units/mg solid using pyrogallol 9003-99-0.
- [200] Nabangshu Sharma and Ivanhoe K.H. Leung. Novel Thermophilic Bacterial Laccase for the Degradation of Aromatic Organic Pollutants. *Frontiers in Chemistry*, 9:711345, October 2021.
- [201] Peroxidase, Lyngbya sp., recombinant E. coli, = 1.0U/mg 9003-99-0.
- [202] Aaron Steevensz, Sneha Madur, Mohammad Mousa Al-Ansari, Keith E. Taylor, Jatinder K. Bewtra, and Nihar Biswas. A simple lab-scale extraction of soybean hull peroxidase shows wide variation among cultivars. *Industrial Crops and Products*, 48:13–18, July 2013.
- [203] Deborah K. Jones, David A. Dalton, Federico I. Rosell, and Emma Lloyd Raven. Class I Heme Peroxidases: Characterization of Soybean Ascorbate Peroxidase. *Archives of Biochemistry and Biophysics*, 360(2):173–178, December 1998.
- [204] Changqing Liu, Kai Zheng, Ying Xu, Lacmata Tamekou Stephen, Jiming Wang, Hongwei Zhao, Tongqing Yue, Rui Nian, Haibo Zhang, Mo Xian, and Huizhou Liu. Expression and characterization of soybean seed coat peroxidase in Escherichia coli BL21(DE3). *Preparative Biochemistry & Biotechnology*, 47(8):768–775, September 2017.
- [205] Arti Tewari, Akshay Kokil, Sethumadhavan Ravichandran, Subhalakshmi Nagarajan, Ryan Bouldin, Lynne A. Samuelson, Ramaswamy Nagarajan, and Jayant Kumar. Soybean Peroxidase Catalyzed Enzymatic Synthesis of Pyrrole/EDOT Copolymers. *Macromolecular Chemistry and Physics*, 211(14):1610–1617, 2010.
- [206] Frances Arnold and Zhanglin Lin. Expression of functional eukaryotic proteins, August 2003.
- [207] Z. Lin, T. Thorsen, and F. H. Arnold. Functional expression of horseradish peroxidase in E. coli by directed evolution. *Biotechnology Progress*, 15(3):467–471, June 1999.
- [208] Sushma Chauhan and Taek Jin Kang. Soluble expression of horseradish peroxidase in Escherichia coli and its facile activation. *Journal of Bioscience and Bioengineering*, 126(4):431–435, October 2018.
- [209] Alexey V Karamyshev, Sergey V Shleev, Olga V Koroleva, Alexander I Yaropolov, and Ivan Yu Sakharov. Laccase-catalyzed synthesis of conducting polyaniline. *Enzyme and Microbial Technology*, 33(5):556–564, October 2003.
- [210] Henry Joseph Oduor Ogola, Takaaki Kamiike, Naoya Hashimoto, Hiroyuki Ashida, Takahiro Ishikawa, Hitoshi Shibata, and Yoshihiro Sawa. Molecular Characterization of a Novel Peroxidase from the Cyanobacterium Anabaena sp. Strain PCC 7120. *Applied and Environmental Microbiology*, 75(23):7509–7518, December 2009.

- [211] Markus Auer, Clemens Gruber, Marzia Bellei, Katharina F. Pirker, Marcel Zamocky, Daniela Kroiss, Stefan A. Teufer, Stefan Hofbauer, Monika Souidi, Gianantonio Battistuzzi, Paul G. Furtmüller, and Christian Obinger. A stable bacterial peroxidase with novel halogenating activity and an autocatalytically linked heme prosthetic group. *The Journal of Biological Chemistry*, 288(38):27181–27199, September 2013.
- [212] Uday S. Ganapathy, Lu Bai, Linpeng Wei, Kathryn A. Eckardt, Clarissa M. Lett, Mary L. Previti, Isaac S. Carrico, and Jessica C. Seeliger. Compartment-Specific Labeling of Bacterial Periplasmic Proteins by Peroxidase-Mediated Biotinylation. *ACS infectious diseases*, 4(6):918–925, June 2018.
- [213] Jia Liu, Yoon Seok Kim, Claire E. Richardson, Ariane Tom, Charu Ramakrishnan, Fikri Birey, Toru Katsumata, Shucheng Chen, Cheng Wang, Xiao Wang, Lydia-Marie Joubert, Yuanwen Jiang, Huiliang Wang, Lief E. Fenno, Jeffrey B.-H. Tok, Sergiu P. Paşca, Kang Shen, Zhenan Bao, and Karl Deisseroth. Genetically targeted chemical assembly of functional materials in living cells, tissues, and animals. *Science*, 367(6484):1372–1376, March 2020.
- [214] Yasuhiro Shiraishi, Shunsuke Kanazawa, Yusuke Kofuji, Hirokatsu Sakamoto, Satoshi Ichikawa, Shunsuke Tanaka, and Takayuki Hirai. Sunlight-Driven Hydrogen Peroxide Production from Water and Molecular Oxygen by Metal-Free Photocatalysts. *Angewandte Chemie International Edition*, 53(49):13454–13459, 2014.
- [215] S. E. Stevens Jr., C. O. Pat Patterson, and Jack Myers. The Production of Hydrogen Peroxide by Blue-Green Algae: A Survey¹. *Journal of Phycology*, 9(4):427–430, 1973.
- [216] Julia M Diaz and Sydney Plummer. Production of extracellular reactive oxygen species by phytoplankton: past and future directions. *Journal of Plankton Research*, 40(6):655–666, November 2018.
- [217] You Chen, Arnaud Taton, Michaela Go, Ross E. London, Lindsey M. Pieper, Susan S. Golden, and James W. Golden. Self-replicating shuttle vectors based on pANS, a small endogenous plasmid of the unicellular cyanobacterium *Synechococcus elongatus* PCC 7942. *Microbiology*, 162(12):2029–2041, December 2016.
- [218] Martin Tichy and Willem Vermaas. In vivo role of catalase-peroxidase in *Synechocystis* sp. strain PCC 6803. *Journal of Bacteriology*, 181(6):1875–1882, March 1999.
- [219] Amel Latifi, Marion Ruiz, and Cheng-Cai Zhang. Oxidative stress in cyanobacteria. *FEMS Microbiology Reviews*, 33(2):258–278, March 2009.
- [220] Hamid Abdollahi, Kobra Erfaninia, Zahra Ghahremani, Jaber Nasiri, and Zeynab Salehi. Reactivation of electron flow in chloroplasts of in vitro shootlets of apple through elimination of carbon source and evaluation of its activity by inhibitors of electron transport chain and chlorophyll fluorescence quenching. *Plant Cell, Tissue and Organ Culture (PCTOC)*, 131(3):377–389, December 2017.

- [221] Inmaculada Morales and Francisco F. de la Rosa. Continuous photosynthetic production of hydrogen peroxide by the blue-green algae *Anacystis nidulans* R2 as a way to solar energy conversion. *Solar Energy*, 43(6):373–377, January 1989.
- [222] Alexander Perelman, Avraham Uzan, Dalia Hacoheh, and Rakefet Schwarz. Oxidative Stress in *Synechococcus* sp. Strain PCC 7942: Various Mechanisms for H₂O₂ Detoxification with Different Physiological Roles. *Journal of Bacteriology*, 185(12):3654–3660, June 2003.
- [223] M. Roncel, J. A. Navarro, and M. A. De la Rosa. Coupling of Solar Energy to Hydrogen Peroxide Production in the Cyanobacterium *Anacystis nidulans*. *Applied and Environmental Microbiology*, 55(2):483–487, February 1989.
- [224] Gadiel Saper, Dan Kallmann, Felipe Conzuelo, Fangyuan Zhao, Tünde N. Tóth, Varda Liveanu, Sagit Meir, Jędrzej Szymanski, Asaph Aharoni, Wolfgang Schuhmann, Avner Rothschild, Gadi Schuster, and Noam Adir. Live cyanobacteria produce photocurrent and hydrogen using both the respiratory and photosynthetic systems. *Nature Communications*, 9(1):2168, June 2018.
- [225] Marin Sawa, Andrea Fantuzzi, Paolo Bombelli, Christopher J. Howe, Klaus Hellgardt, and Peter J. Nixon. Electricity generation from digitally printed cyanobacteria. *Nature Communications*, 8(1):1327, November 2017.
- [226] Nikhil S. Malvankar, Tünde Mester, Mark T. Tuominen, and Derek R. Lovley. Supercapacitors based on c-type cytochromes using conductive nanostructured networks of living bacteria. *Chemphyschem: A European Journal of Chemical Physics and Physical Chemistry*, 13(2):463–468, February 2012.
- [227] L. An, T. S. Zhao, X. L. Zhou, X. H. Yan, and C. Y. Jung. A low-cost, high-performance zinc–hydrogen peroxide fuel cell. *Journal of Power Sources*, 275:831–834, February 2015.
- [228] Zhang Shimin, Jiang Jianhong, and Zhou Debi. Exploration of aqueous zinc–hydrogen peroxide batteries. *International Journal of Energy Research*, 36(9):953–962, 2012.
- [229] R. Hamlen, B. Rao, W. Halliop, and N. Fitzpatrick. Aluminum-hydrogen peroxide sea water battery. In *Proceedings of the 1987 5th International Symposium on Unmanned Untethered Submersible Technology*, volume 5, pages 128–140, June 1987.
- [230] Cyprien Verseux, Mickael Baqué, Kirsi Lehto, Jean-Pierre P. de Vera, Lynn J. Rothschild, and Daniela Billi. Sustainable life support on Mars – the potential roles of cyanobacteria. *International Journal of Astrobiology*, 15(1):65–92, January 2016.
- [231] A. Boveris, E. Martino, and A. O. M. Stoppani. Evaluation of the horseradish peroxidase-scopoletin method for the measurement of hydrogen peroxide formation in biological systems. *Analytical Biochemistry*, 80(1):145–158, May 1977.

- [232] Na Su. Polyaniline-Doped Spherical Polyelectrolyte Brush Nanocomposites with Enhanced Electrical Conductivity, Thermal Stability, and Solubility Property. *Polymers*, 7(9):1599–1616, September 2015.
- [233] S K Herbert, G Samson, D C Fork, and D E Laudenbach. Characterization of damage to photosystems I and II in a cyanobacterium lacking detectable iron superoxide dismutase activity. *Proceedings of the National Academy of Sciences of the United States of America*, 89(18):8716–8720, September 1992.
- [234] D. J. Thomas, T. J. Avenson, J. B. Thomas, and S. K. Herbert. A cyanobacterium lacking iron superoxide dismutase is sensitized to oxidative stress induced with methyl viologen but is not sensitized to oxidative stress induced with norflurazon. *Plant Physiology*, 116(4):1593–1602, April 1998.
- [235] C. O. Patterson and J. Myers. Photosynthetic Production of Hydrogen Peroxide by *Anacystis nidulans*. *Plant Physiology*, 51(1):104–109, January 1973.
- [236] Shuai Shao, Oscar A. Ortega-Rivera, Sayoni Ray, Jonathan K. Pokorski, and Nicole F. Steinmetz. A Scalable Manufacturing Approach to Single Dose Vaccination against HPV. *Vaccines*, 9(1):66, January 2021.
- [237] Keisuke Nagato. Injection Compression Molding of Replica Molds for Nanoimprint Lithography. *Polymers*, 6(3):604–612, March 2014.
- [238] Dennis E. Ferguson, Satinder K. Nayar, and Donald L. Pochardt. Method of molding a microneedle, August 2012.
- [239] Kiriakos Kotzabasis and Horst Senger. The Influence of 5-Aminolevulinic Acid on Protochlorophyllide and Protochlorophyll Accumulation in Dark-Grown *Scenedesmus*. *Zeitschrift für Naturforschung C*, 45(1-2):71–73, February 1990.